Monitoring structural and physiological properties of crop roots using spectral electrical impedance tomography

Maximilian Weigand

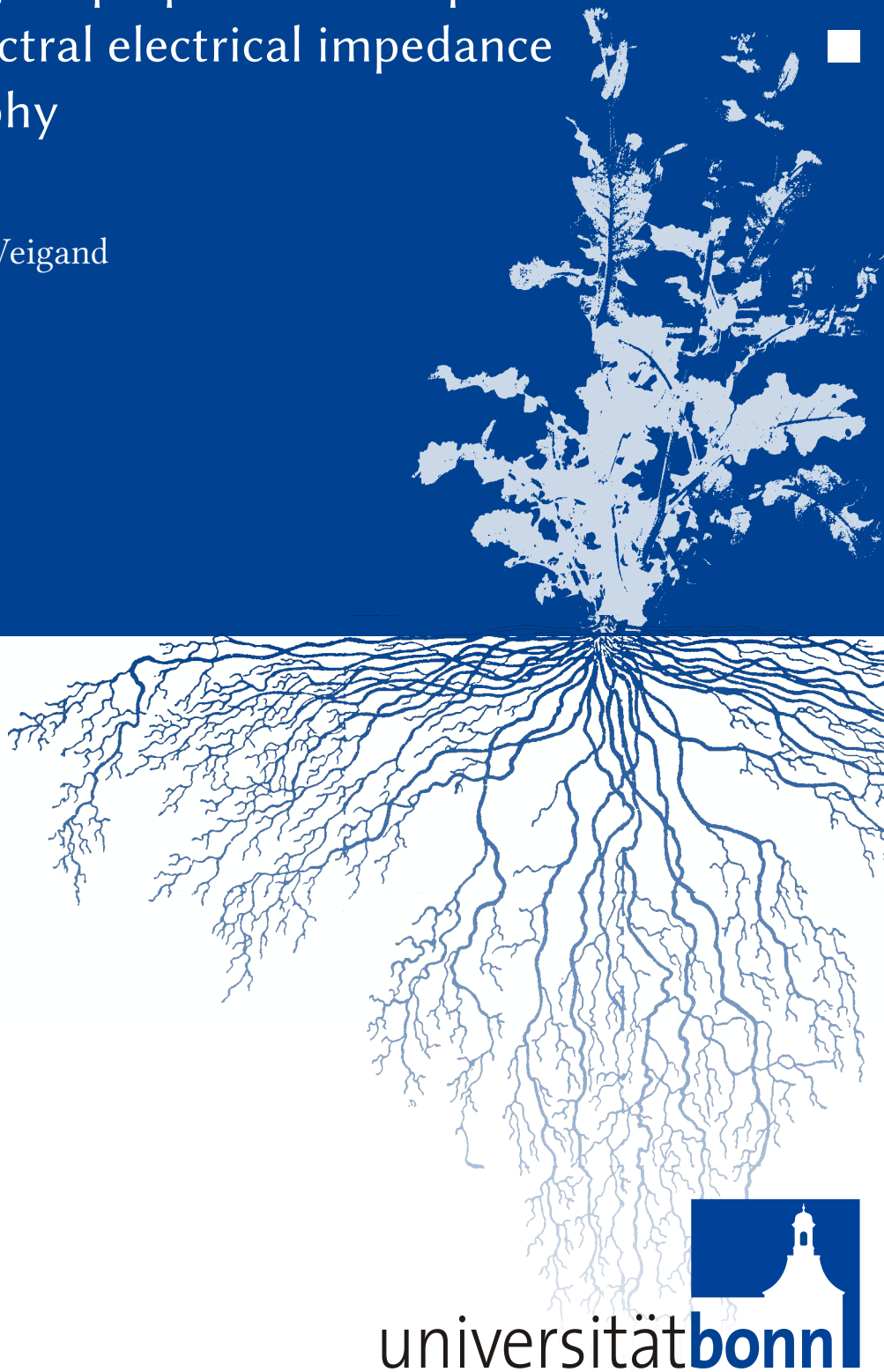

universitätbonn

Bibliographic data
Weigand, Maximilian: Monitoring structural and physiological properties of crop roots using spectral electrical impedance tomography, Ph.D. thesis, University of Bonn, doi:10.5281/zenodo.400833, urn:nbn:de:hbz:5n-46750, 2017

Monitoring structural and physiological properties of crop roots using spectral electrical impedance tomography

Dissertation

zur

Erlangung des Doktorgrades (Dr. rer. nat.)

der

Mathematisch-Naturwissenschaftlichen Fakultät

der

Rheinischen Friedrich-Wilhelms-Universität Bonn

vorgelegt von

Maximilian Weigand

aus

Viersen

Bonn 2017

Angefertigt mit Genehmigung der Mathematisch-Naturwissenschaftlichen Fakultät
der Rheinischen Friedrich-Wilhelms-Universität Bonn am Steinmann-Institut
für Geologie, Mineralogie und Paläontologie, Fachbereich Geophysik

1. Referent: Prof. Dr. A. Kemna
2. Referent: Prof. Dr. J.A. Huisman

Tag der Promotion: 7. Juli 2016
Erscheinungsjahr: 2017

“The right to search for the truth implies also a duty; one must not conceal any part of what one has recognized to be the truth.”

Albert Einstein

To my parents and my sister

Abstract

In this thesis I investigate the possibilities of using multi-frequency electrical impedance tomography (EIT) to characterize and monitor structural and physiological properties of crop root systems. Multi-frequency electrical material properties can be measured using electrical impedance spectroscopy (EIS) or using the imaging extension, EIT. Various studies have found that biological tissue, including crop roots, exhibit electrical polarization responses that can possibly be linked to structural and physiological properties.

This thesis has the primary objective to assess and adapt EIT to the biophysical field of crop root research. Up to now EIT has been commonly used in near-surface geophysical applications such as ore exploration and in hydrogeophysical setups. Applications on the small scale of crop roots are still very rare, as are studies involving the small signal strengths encountered in biological tissue. However, the non-invasive nature of EIT has the benefit of reducing workload and acquisition time considerably, compared to traditional invasive methods of root research.

The first three parts of this thesis deal with various aspects of the analysis of spectral signatures measured either directly with EIS or recovered from EIT images. At first an improved version of the Debye decomposition (DD) scheme is developed, characterized and extended to smooth results along the time domain, e.g., to filter noise components.

The second part compares the resulting model parameters to the de-facto standard, the Cole-Cole (CC) model. The CC chargeability can be underestimated by up to 80 per cent when the total chargeability of the DD is used to estimate total polarization responses. Even worse, the CC relaxation time can be under- oder overestimated by up to three orders of magnitude when the mean relaxation time from the DD is used. These findings must be considered if both models are used within the same study.

The third part of this thesis investigates the reconstruction quality of spectral parameters (either CC or DD parameters) in an imaging framework. The chargeability parameters show a strong dependence on decreasing sensitivity values, usually indicating a strong loss of resolution with increasing distance from the electrodes. Contrarily, relaxation times are much more resilient to de-

creasing sensitivity values and show good reconstruction quality over a large range of sensitivities.
The fourth and fifth parts of this thesis present various laboratory experiments on crop roots. A monitoring experiment on an oilseed plant shows that EIT can not only image the extension of root systems in watery solutions, but it can also monitor electrical polarization signals that decrease over time correspondingly to the decay of the plant in a nutrient deprived environment.
Further experiments demonstrate that electrical signals show a dependence on root mass and on other physiological factors, such as light or the addition of nutrients after a prolonged nutrient deprivation. However, additional experiments demonstrate that the reliable detection of the polarization signals of root systems is hindered by the growth medium used. Peat substrate shows significant polarization signatures by its own, and thus masks signals originating from roots. Also, spatially variable water content further complicates the successful imaging and characterization of crop roots grown in substrates.
Overall, I show that EIT can be successfully applied to characterize and monitor structural and physiological properties of crop roots in an laboratory environment. Although many challenges remain, establishing EIT as a reliable tool on the field scale is within reach.

Zusammenfassung

In dieser Arbeit untersuche ich die Charakterisierung und Überwachung von Nutzpflanzenwurzeln mit Hilfe der elektrischen Impedanztomographie (EIT). Elektrische Eigenschaften von Materialen können mit Mehrfrequenzmessungen der elektrischen Impedanz bestimmt werden. Diese Methode nennt man die elektrische Impedanzspektroskopie (EIS), deren bildgebende Erweiterung die EIT ist. Biologisches Material, unter anderem Pflanzenwurzeln, weisst eindeutige charakteristische Polarisationsignale auf, wie in diversen Studien belegt wurde. Zusätzlich werden Relationen zu strukturellen und physiologischen Eigenschaften der Wurzeln vermutet.

Die Hauptaufgabe dieser Arbeit ist die prinzipielle Evaluierung und Anpassung von EIT an das Themenfeld der Wurzelforschung. Bis jetzt ist EIT primär im Bereich der Erzexploration und hydrogeophysikalischen Themenstellungen auf größerer Skala benutzt worden. Anwendungen auf kleiner Skala mit den zusätzlich sehr kleinen Polarisationssignalen der Pflanzenwurzeln sind noch nicht weit verbreitet. Deshalb sind nur geringe Erfahrungen auf diesem Gebiet vorhanden. Eine erfolgreiche Anwendung würde jedoch signifikanten Mehrwert für die Wurzelforschung erbringen, da die nicht-invasive Natur von EIT Mess- und Arbeitszeit im Vergleich zu den destruktiven Standardmethoden minimieren würde.

In den ersten drei Teilen der Arbeit werden wichtige Aspekte der Auswertung von spektralen Impedanzsignaturen untersucht. Diese Signaturen können direkt am Objekt gemessen, oder aus tomographischen Ergebnissen extrahiert werden. Eine verbesserte und durch eine Zeitglättung erweitere Version der Debyezerlegung (DD) wird entwickelt und in Hinsicht auf wichtige Einstellungsparameter analysiert. Die Zeitglättung wird beispielsweise zur Unterdrückung von Rauschkomponenten verwendet.

Im zweiten Teil der Arbeit werden die Parameter der DD mit den Parametern des de-facto Standards zur Beschreibung von Impedanzspektren, dem Cole-Cole (CC) Modell, verglichen. Die CC-Aufladbarkeit wird hierbei um bis zu 80 % von dem analogen DD Parameter unterschätzt, und die mittlere Relaxationszeit der DD kann um bis zu drei Größenordnungen von der charakteristischen CC-Relaxationszeit abweichen. Dies zeigt die Wichtigkeit einer konsistenten

Datenauswertung und Datenbewertung auf, insbesondere bei Verwendung des CC Modells und der DD innerhalb einer Studie.
Der dritte Teil der Arbeit untersucht die Rekonstruktion von CC und DD Parametern innerhalb der Bildgebung, also den Fall, in dem Impedanzspektren aus EIT-Ergebnissen extrahiert und nachfolgend mit den Modellen ausgewertet werden. Hier zeigt sich, dass die Aufladbarkeit eine starke Abhängigkeit von der Sensitivität hat, also mit zunehmender Entfernung von den Messelektroden immer ungenauer rekonstruiert werden kann. Die Relaxationszeiten jedoch zeigen ein stabiles Rekonstruktionsverhalten über große Bereiche der Bildebene. Hieraus ergibt sich, dass hydrologische und biogeophysikalische Parameter, welche aus Relaxationszeiten bestimmt werden, stabiler aus EIT-Bildern rekonstruiert werden können, als solche aus Aufladbarkeitsparametern.
Der vierte und der fünfte Teil der Arbeit beschäftigen sich mit Laborexperimenten an Pflanzenwurzeln. Im vierten Teil wird detailliert ein Versuch mit Rapspflanzen vorgestellt, in dem mit EIT die elektrischen Signale der Wurzeln unter Nährstoffarmut aufgezeichnet wurden. Unter anderem konnte die Ausdehnung des Wurzelsystems durch die elektrischen Parameter räumlich abgebildet werden. Ferner wurde eine Abnahme der Gesamtpolarisation mit fortschreitendem Verfall der Pflanze gemessen.
Weitere Experimente zeigen eine Abhängigkeit elektrischer Eigenschaften von der Wurzelmasse und von physiologischen Effekten. Beispiele hierfür sind Reaktion auf Tag-/Nachtverhältnisse oder auf eine Nährstoffzugabe nach längerer Nährstoffarmut. Jedoch haben Experimente in Bodensubstraten gezeigt, dass die Wurzelsignale durch Signale der Substrate überlagert werden. Weiterhin hat der variable Wassergehalt in Zeit und Raum einen massiven Einfluss auf die gemessenen Signale, was eine zuverlässige Detektion der Wurzelsignale schwierig macht. Torferde hat sich bedingt durch starke Eigensignale des hohen Organikanteils als ungeeignet für EIT-Experimente gezeigt.
Insgesamt konnte ich in der Arbeit erfolreich die Erstanwendung von EIT auf die Charakterisierung von Pflanzenwurzeln aufzeigen. Strukturelle, sowie physiologische Eigenschaften haben in Laborexperimenten direkten Einfluss auf die gemessenen Polarisationeigenschaften gezeigt. Obwohl es noch viele ungeklärte Fragen gibt, ist die Etablierung von EIT als zuverlässiges Werkzeug auf der Feldskala in greifbare Nähe gerückt.

Contents

1 Introduction **1**

2 Debye decomposition of time-lapse spectral induced polarisation data **7**

2.1 Introduction 7
2.2 Methods 9
2.2.1 Debye decomposition 10
2.2.2 Integral parameters 12
2.2.3 Inverse approach 13
2.2.4 Extension to time-lapse inversion 19
2.3 Results and discussion 22
2.3.1 Relaxation times 23
2.3.2 Regularisation strategies 25
2.4 Conclusions 31

Appendices **33**

2.A Relationship between σ'' and m_n for a Debye response 33
2.B DD derivatives 34

3 Relationship between Cole-Cole model parameters and spectral decomposition parameters derived from SIP data **35**

3.1 Introduction 35
3.2 Methods 37
3.2.1 The Cole-Cole model 37
3.2.2 The Cole-Cole decomposition 38
3.3 Numerical experiments 39
3.4 Results 40
3.4.1 Chargeability recovery 40

3.4.2 Relaxation time recovery 40
3.5 Discussion 42
3.6 Conclusions 46

4 Reconstruction quality of SIP parameters in multi-frequency complex resistivity imaging 47
4.1 Introduction 47
4.2 Methods 49
4.2.1 Forward modeling and inversion 49
4.2.2 Cole-Cole model 49
4.2.3 Debye decomposition 50
4.3 Design of numerical experiments 51
4.3.1 Single-frequency reconstruction 53
4.3.2 Multi-frequency reconstruction 54
4.4 Results 57
4.4.1 Single-frequency results 57
4.4.2 Multi-frequency results 59
4.5 Discussion 64
4.5.1 Reconstruction quality of resistivity and polarization parameters 64
4.5.2 Reconstruction quality of spectral parameters 65
4.5.3 Application to more complex scenarios 67
4.6 Conclusions 69

Appendices 71
4.A Complex resistivity inversion 71
4.B Image appraisal 72

5 Multi-frequency electrical impedance tomography as a non-invasive tool to characterise and monitor crop root systems. 75
5.1 Introduction 75
5.2 Electrical properties and measurements of root systems 78
5.2.1 Electrical double layer polarization 79
5.2.2 Electrical measurements 79

5.2.3 Polarization of biomatter . . . 81
5.2.4 Working hypotheses . . . 83
5.3 Material and methods . . . 84
5.3.1 Electrical impedance tomography . . . 84
5.3.2 Debye decomposition . . . 85
5.3.3 Experimental setup . . . 87
5.3.4 Data processing . . . 88
5.4 Results . . . 93
5.4.1 Physiological response . . . 93
5.4.2 Impedance spectra . . . 93
5.4.3 Single-frequency imaging results . . . 95
5.4.4 Complex conductivity spectra recovered from imaging results . . . 96
5.4.5 Debye decomposition of recovered complex conductivity spectra . . . 98
5.4.6 Images of spectral parameters obtained from Debye decomposition . . . 99
5.5 Discussion . . . 102
5.5.1 Biological interpretation . . . 102
5.5.2 Geophysical methodology . . . 105
5.6 Conclusions . . . 107
5.7 Data Availability . . . 109

6 EIT on crop root systems in solutions and substrates 111
6.1 Introduction . . . 111
6.2 Measurements in aqueous solutions . . . 113
6.2.1 Mass dependence of EIS signals . . . 113
6.2.2 Imaging root growth in water . . . 116
6.2.3 Monitoring a decapitated root system in a nutrient-rich environment . . . 120
6.2.4 Monitoring nutrient deprivation in intact and decapitated plants . . . 123
6.2.5 Monitoring of day/night cycles with EIS . . . 130
6.2.6 Designing future experiments . . . 137

6.3 Imaging of crop roots in soil . . . 138
6.3.1 Introduction . . . 138
6.3.2 Field roots in top soil . . . 139
6.3.3 Monitoring root growth in a nutrient deprived environment . . . 143
6.3.4 Monitoring of oilseed growth in peat substrate: Experiment 1 . . . 152
6.3.5 Monitoring of oilseed growth in peat substrate: Experiment 2 . . . 156
6.4 Towards the field scale . . . 168
6.5 Discussion and conclusions . . . 171

Appendices **173**
6.A Tracer experiment in substrate growth experiment 1 . . . 173

7 Conclusions and future research perspectives **177**

References **202**

CHAPTER 1

Introduction

Root systems play a key role in the global ecosystem (e.g., White et al., 2013, and references therein). In many ways they form the primary connection between the subsurface and the atmosphere: They are an essential part in the global hydraulic circulatory system, taking up and transpiring large amounts of water (e.g., Tinker and Nye, 2000). In addition, most of the nutrients and toxins contained in our food chain are taken up by roots (e.g., Groff and Kaplan, 1988; Gregory, 2006). Root-soil interactions not only determine the development success of a plant, but they can also manipulate and permanently change the soil itself (Roose et al., 2016). Finally, they provide support for the topsoil in terms of erosion resistance (e.g., Groff and Kaplan, 1988). These, and many other minor functions, warrant a continuous and thorough investigation of root system development and functionality.

Traditional methods of root research are mostly destructive and require time intensive manual labor, which puts certain limits on the sampling intervals, as well as on quality and quantity of the results. Also, repeated analysis of intact plants is mostly impossible using these methods (e.g., Heřmanská et al., 2015). Non- or minimally invasive methods can improve measurement time, quality, and quantity by automating processes and reducing uncertainties introduced by manual processing steps. Among the growing number of emerging technologies are computed tomography (CT), nuclear magnetic resonance (NMR) and electrical methods (e.g., Gregory, 2006; Roose et al., 2016). These methods differ in their costs and constraints, such as upper radiation doses to not destroy the biological components, or the use of metal-free sample holders to not interfere with magnetic measurements. Yet, multi-scale imaging methods that provide spatial distributions of structural and chemical properties of the rhizosphere,

possibly non- or minimally invasive, are required for understanding and modeling the processes of the rhizosphere (e.g., Roose et al., 2016). In addition, there has yet to emerge a method that is established both on the laboratory and the field scale. With this in mind, electrical methods gain importance due to their low-cost, easy-to-use nature and applicability to both scales, and steady improvements in their adaption to biogeotechnical application fields. These fields include the possible characterization and monitoring of crop root systems, with the added benefit that electrical methods have shown a sensitivity to physiological processes and changes thereof (e.g., Cseresnyés et al., 2012, 2013).

This sensitivity originates in the internal structure and workings of plant roots. The roots consist of multiple layers of radially distributed tissue with specialized functionality vital to the plant root system (e.g., Gregory, 2006; Eshel and Beeckman, 2013). Of major importance is water and nutrient uptake, and subsequent translocation to the shoot and leave areas (e.g., Tinker and Nye, 2000). Transport and uptake can be passive or active, that is by energy conserving passive diffusion flow or by energy consuming active transport across cell membranes (Tinker and Nye, 2000; Gregory, 2006). Correspondingly, roots react to changes in their environment, e.g., to nutrient or water shortage, by influencing transport pathways. All these processes modify internal ion concentrations, which in turn directly or passively influence the electrical properties of root systems. These properties are determined by fluid conductivity, i.e. the concentration of various ions in the various structural parts and by the electrical double layers (EDLs) forming at various surface-fluid interfaces in and outside the root system, especially at ion-selective membranes (e.g., Lyklema, 2005).

Membranes in biomatter are usually negatively charged on their surface. Combined with charges of adsorbed ions this leads to a net charge on this surface, which in turn creates a diffusive concentration gradient towards the free fluid space. This double layer of fixed, adsorbed, and diffusive ions is called the EDL. As shown in numerous studies in colloid science and geophysical research the EDL is polarized in an external time-variable electrical field (e.g., Fixman, 1980; Lyklema, 2005). This polarization can be externally measured by means of non- or minimally invasive electrical impedance measurements.

The electrical impedance is a complex valued entity, which can be transferred into complex valued material properties by accounting for the geometry of the

measurement setup. For inhomogeneous materials a single measurement can produce only apparent, that is integrative, properties of the sample or subsurface due to the lack of spatial resolution. Spatial resolution can be achieved by subsequently changing the location of the measurement electrodes, and the final application of tomographic inversion algorithms (e.g., LaBrecque et al., 1996a; Kemna, 2000). Images of the electrical properties of the measured medium can thus be computed. This method is then called electrical impedance tomography (EIT). The real part of the electrical impedance denotes ohmic contributions, primarily controlled by fluid saturation and conductivity (in turn controlled by ion composition and conductivity). Imaginary parts, on the other hand, represent inductive and capacitive contributions, with EDL polarization being of a capacitive nature.

The impedance is usually frequency dependent, and in absence of tomographic measurements the measurement method is called electrical impedance spectroscopy (EIS) or spectral induced polarization (SIP). Multi-frequency measurements (usually in the mHz to low kHz range) can yield substantial information gains compared to measurements at a single frequency (e.g., Barsoukov and Macdonald, 2005; Kemna et al., 2012). The origin of the frequency dependence, which mainly manifests in the polarization, that is the imaginary part of the impedance, is manifold and highly dependent on the target medium.

In geophysical applications it is common to use phenomenological models in absence of physically motivated models to describe these complex impedance signatures. Among these models stand out the Cole-Cole model (Cole and Cole, 1941) and the Debye decomposition scheme (e.g., Uhlmann and Hakim, 1971; Lesmes and Morgan, 2001; Nordsiek and Weller, 2008), which both yield summarizing parameters that describe total polarization, as well as characteristic relaxation times of SIP signatures. Increasingly, they are also applied to signatures recovered from imaging results, providing spatially resolved multi-frequency summaries of target samples (e.g., Flores Orozco et al., 2012a, 2013; Günther and Martin, 2016).

Established theories link local polarization peaks to a length scale by means of an associated characteristic relaxation time (e.g., Schwarz, 1962). Length scales can include pore or grain radii in sedimentary materials, or bacterial diameters (e.g., Revil et al., 2012a). More broadly, a relationship between peak frequency

and the undisturbed dilation of the EDL is predicted. These theories, backed by a large number of published multi-frequency studies, can also be transferred to biological tissue. While research on EDL polarization in root systems is still in its infancy, the structural composition of roots with the large number of differently sized membranes suggests that multi-frequency electrical impedance measurements provide information also on the structural origins of root polarization signals.

Electrical measurements on the macro scale, i.e. the centimeter to decimeter scale, however, comprise the superposition of signals from a vast number of differently sized structures within root systems and their surroundings. A major methodological task is thus to understand and dissect these effective measurements to extract key information useful for root research (e.g., Dalton, 1995; Ozier-Lafontaine and Bajazet, 2005; Ellis et al., 2013). Understanding of electrical polarization properties of root systems can be approached from two directions: First, detailed physicochemical models can be formulated to describe the processes on a microscopic scale, and then be combined with upscaling models to compute effective macroscopic signatures. The second approach uses phenomenological models to summarize measured multi-frequency impedance signatures and compare the model parameters to certain environmental factors of the experiments (e.g., Ozier-Lafontaine and Bajazet, 2005).

Both approaches require carefully designed experiments to extract useful and exploitable results. However, due to the complex nature of the systems under investigation it is not yet possible to reliably formulate and test the detailed models that physically describe the involved processes, as discussed by Roose et al. (2016) for the modeling of non-electrical processes in the rhizosphere. Phenomenological models can help in building a large and robust database which will hopefully lead to the eventual emergence of physically correct models that yield reliable predictions of macroscopic measurements. This outcome can only to a certain extent be expected from phenomenological models.

While inherent uncertainties of electrical imaging methods, as well as uncertainties regarding the spectral models, have been investigated (e.g., Alumbaugh and Newman, 2000; Tarantola, 2005), little work has been conducted to assess combined uncertainties of spectral parameters recovered from imaging results. Also inter-model uncertainties, which arise when summarizing parameters from

multiple models are jointly used, have received very little attention. A better understanding of these uncertainties, and possible interpretation errors caused by them, will become even more crucial as the scope of EIS and EIT is extended to ever smaller targets with ever decreasing polarization strength. Crop root systems fall into these new emerging fields of application.
In summary, EIT, while established in the geophysical community, has the potential to be a robust tool for biological root research. It provides unique possibilities for a scale-independent characterization and monitoring of the rhizosphere and is potentially sensitive to both structural as well as physiological properties of root systems.
Contributing towards this goal this thesis investigates the possibilities and limits of applying modern EIT to the characterization and monitoring of crop root systems. Two main issues are addressed: First, improving and characterizing the robustness of phenomenological models used to describe SIP signatures in an EIT framework, and second, the application of EIT to crop root systems in controlled laboratory experiments to evaluate the characterization capabilities of EIT with regard to structural and physiological root properties. Methodological advancements are directly applied to the experimental results.

The thesis is structured as follows:

- Chapter 1 presents an improved version of the Debye decomposition procedure to describe multi-frequency complex resistivity signatures measured in a time-lapse setting. This method is extended to smooth results over time to account for noise components in monitoring data. Additionally, governing parameters of the decomposition scheme are analyzed with respect to result robustness.

- Chapter 2 investigates possible interpretation errors that occur if results of the Cole-Cole model and the Debye decomposition are jointly used within the same study.

- Chapter 3 presents numerical studies which examine the reconstruction properties of spectral electrical parameters in imaging applications.

- Chapter 4 presents a detailed case study of an application of multi-frequency EIT to crop root systems. Hydroponically grown oilseed plants were continuously monitored in a nutrient deprived environment over a three day period in a laboratory experiment. Data acquisition and processing steps are discussed in detail.
- Chapter 5 discusses multiple laboratory and field experiments on crop root systems, highlighting aspects of the EIT application to root systems. The feasibility to apply EIT to the field scale is discussed based on the available experimental evidence.
- Chapter 6 summarizes and concludes this thesis.

This chapter is based on the publication: Weigand, M. and Kemna, A. (2016). Debye decomposition of time-lapse spectral induced polarisation data. Computers and Geosciences, 86:34–45. doi:10.1016/j.cageo.2015.09.021.

CHAPTER 2

Debye decomposition of time-lapse spectral induced polarisation data

2.1 Introduction

Spectral induced polarisation (SIP) data consist of frequency dependent (typically 1 mHz - 10 kHz) electrical impedances or admittances. These complex-valued data can either be represented in terms of real and imaginary parts, or as magnitude and phase values. Using the geometrical location of the electrodes, complex resistivities or complex conductivities can be inferred. These properties reflect electrical conduction and polarisation processes, for instance electrochemical polarisation at the interface between the pore fluid and minerals in soils and rocks or between different cells in living tissue, as of interest in geophysics and biophysics. SIP data are usually analysed and related to petro-, hydro-, or biogeophysical properties by means of empirical or mechanistic models (see, e.g., Slater, 2007; Kemna et al., 2012; Bücker and Hördt, 2013b). While significant effort has been put into the development of mechanistic models over the last years (e.g., Revil and Florsch, 2010; Revil et al., 2012a), most studies still address the formulation of parameter relationships using empirical models (e.g., Weller et al., 2013).

Two types of empirical model approaches can be distinguished: The first type describes SIP data using one or a few polarisation peaks (i.e., local maxima) in

the absolute phase spectrum (or imaginary conductivity spectrum) with corresponding, distinct relaxation times. This includes the Debye model (Debye, 1960 [1929]; Böttcher and Bordewijk, 1978) and the class of Cole-Cole-type models (Cole and Cole, 1941; Pelton et al., 1978, see Dias (2000) for an overview). In general these models are overdetermined, containing far fewer model parameters than data points available. This, however, limits the flexibility regarding different shapes of the spectra and imposes strong data influence on fitting quality and robustness (Morgan and Lesmes, 1994).

The second approach describes the SIP response using a linear superposition of a large number of elementary Debye polarisation terms following a given distribution of relaxation times. The latter is commonly discretised in regular intervals. Thus, only the relative weights of the Debye contributions at discrete relaxation times are determined when fitting the observed polarisation response. This procedure of determining a relaxation time distribution (RTD) instead of a fixed number of relaxation times is referred to as Debye decomposition (DD). Contrary to the first type of models, the DD represents a strongly underdetermined inverse problem which requires some sort of regularisation to achieve a stable solution. A wide range of shapes of SIP spectra can be fitted using the DD approach, and more importantly, the approach does not require a certain number of polarisation peaks in the SIP data. However, representative (average or integral) parameters may be extracted from the RTD, also referred to as *integrating parameters* (Nordsiek and Weller, 2008) or *characteristic integral parameters* (Zisser et al., 2010a) in the literature.

The concept of the superposition of multiple polarisation terms goes back to v. Schweidler (1907), with the first proposition of a continuous RTD by Wagner (1913). One of the first published discrete decomposition procedures inverted the imaginary part of the complex permittivity (Uhlmann and Hakim, 1971), while later studies used the real part to fit permittivity spectra (Morgan and Lesmes, 1994; Lesmes and Morgan, 2001). It is noted here that because of the so-called Kramers-Kronig relationships (e.g., Macdonald, 1952) it is theoretically sufficient to only fit the real or imaginary part of the permittivity spectrum to infer the complete complex permittivity response (because both real and imaginary parts are related as a consequence of causality). Different implementations of the DD for time-domain data have been published (Tong et al., 2004;

Tarasov and Titov, 2007), and likewise formulations for frequency-domain resistance and resistivity instead of permittivity or conductivity have been presented (Nordsiek and Weller, 2008; Zisser et al., 2010a; Florsch et al., 2012; Keery et al., 2012). Keery et al. (2012) investigated uncertainties of the inferred DD parameters using a Markov-chain Monte Carlo method. Recently, Florsch et al. (2014) proposed a decomposition approach based on relaxation models other than the Debye model, such as the Cole-Cole model or Warburg model. In an accompanying work, Revil et al. (2014) promote the use of the Warburg model, arguing that the elementary response in a rock is less dispersive than a Debye response. Following the same reasoning, already Tarasov et al. (2003) used a decomposition based on a Cole-Cole model in accordance with the response of a theoretical model for the polarisation of a single pore (Titov et al., 2002).

Based on numerous previous works on the linkage of SIP parameters with textural and hydraulic characteristics (for an overview see Kemna et al., 2012, and references therein), more recently also relationships of DD parameters to various petrophysical parameters have been established, such as to slag mass and grain size of slag-sand mixtures (Nordsiek and Weller, 2008), permeability of sandstones (e.g., Weller et al., 2010a), water saturation of sand-clay mixtures (Breede et al., 2012), specific surface area per unit pore volume of sandstones and sand-iron/clay mixtures (e.g., Weller et al., 2010b), and to changes in water salinity of sandstones (e.g., Weller et al., 2011). Attwa and Günther (2013) found correlations between DD relaxation time and hydraulic conductivity for samples taken from a Quaternary aquifer. One of the few published applications to field-imaging results investigated the relationship between DD-derived integral parameters and BTEX (benzene, toluene, ethylbenzene, and xylenes) contamination (Flores Orozco et al., 2012a).

Despite the growing number of studies incorporating time-lapse SIP data (e.g., Breede et al., 2012; Flores Orozco et al., 2013) for monitoring purposes, we are not aware of any DD approaches incorporating time-lapse data sets in a single inversion problem, for instance to apply regularisation with respect to temporal changes. In this work we present an open source implementation of a DD for complex resistance/resistivity SIP time-lapse (monitoring) data which is capable of imposing smoothness constraints with respect to spectral variations as well as changes over time. The inversion methodology is developed in detail, and

integral parameters commonly extracted from DD results are briefly reviewed. Important aspects of the DD routine are examined, such as the choice of sampling (discretisation) of the relaxation time axis and the influence of regularisation strategies on the DD result. The source code (in the Python programming language) and corresponding documentation is available under an open source licence.

2.2 Methods

This section provides a detailed description of the DD methodology. Starting with the general formulation of the decomposition, the inversion algorithm is developed, including important implementation aspects, in particular the extension to invert time-lapse SIP data sets.

2.2.1 Debye decomposition

Fuoss and Kirkwood (1941) formulated the frequency response of the complex permittivity $\hat{\epsilon}$ using a continuous relaxation time distribution, $g(\tau)$, which describes the Debye contribution at different relaxation times τ:

$$\hat{\epsilon}(\omega) = \epsilon_\infty + (\epsilon_0 - \epsilon_\infty) \int_0^\infty \frac{g(\tau)}{1 + j\omega\tau} d\tau, \tag{2.1}$$

$$\int_0^\infty g(\tau) d\tau = 1, \tag{2.2}$$

with ϵ_0 and ϵ_∞ being the asymptotic permittivities at low and high frequencies, respectively, τ the relaxation time, ω the angular frequency, and $j = \sqrt{-1}$ the imaginary unit.

The Debye model follows from Eq. (2.1) for $g(\tau) = \delta(\tau - \tau_0)$, where δ denotes the Dirac delta function. In this case, τ_0 is inversely related to the frequency position (ω_{peak}) of the polarisation peak (in terms of imaginary part ϵ'') by $\tau_0 = 1/\omega_{\text{peak}}$. The discrete case can now be formulated either by expressing $g(\tau)$ by a weighted sum of δ functions, or by discretising the continuous integral in Eq. 2.1. The discrete (and fixed) τ_i values must sample at least the relaxation time range

implicitly defined by the frequency range spanned by the data (i.e., according to the inverse correlation $\tau_0 = 1/\omega_{\text{peak}}$) to facilitate an adequate approximation of the continuous case. SIP responses are now solely described by the weighting factors at the chosen relaxation times, representing a discrete RTD.
The analogon to the continuous formulation in Eq. (2.1) in terms of complex resistivity $\hat{\rho}(\omega)$ is given by

$$\hat{\rho}(\omega) = \rho_0 \left(1 - \sum_{k=1}^{N_\tau} m_k \left[1 - \frac{1}{1 + j\omega\tau_k} \right] \right), \tag{2.3}$$

with ρ_0 being the direct-current (DC) resistivity, N_τ the number of relaxation times, m_k the weighting factors, the so-called chargeabilities, corresponding to the relaxation times τ_k. This formulation is based on the resistivity formulation of the Cole-Cole model by Pelton et al. (1978):

$$\hat{\rho}(\omega) = \rho_{0,\text{cc}} \left(1 - m_{\text{cc}} \left[1 - \frac{1}{1 + (j\omega\tau_{\text{cc}})^{c_{\text{cc}}}} \right] \right), \tag{2.4}$$

where $\rho_{0,\text{cc}}$ is the DC resistivity, m_{cc} is the Cole-Cole chargeability, τ_{cc} is the Cole-Cole time constant (which has the meaning of an effective relaxation time), and c_{cc} is the frequency exponent, describing the strength of the frequency dependence (dispersion) (Figure 2.1). Eq. (2.4) simplifies to the Debye model in terms of resistivity for $c_{\text{cc}} = 1$. It should be noted that the discrete form of Eq. (2.1) and Eq. (2.3) are not fully equivalent to each other (Florsch et al., 2012; Tarasov and Titov, 2013), and care must be taken when comparing results obtained with the different formulations.
In this work, Eq. (2.4) is used to generate synthetic SIP data. Although in the literature the Debye decomposition has been mostly performed using the resistivity formulation (Eq. 2.3), results in this work are presented in terms of complex conductivity, $\hat{\sigma}(\omega) = 1/\hat{\rho}(\omega)$, which is commonly used as the basis for petrophysical interpretations (e.g., Revil and Florsch, 2010).

2.2.2 Integral parameters

From the RTD, different *integral parameters* can be derived, which provide information about the overall polarisation properties and relaxation time scales

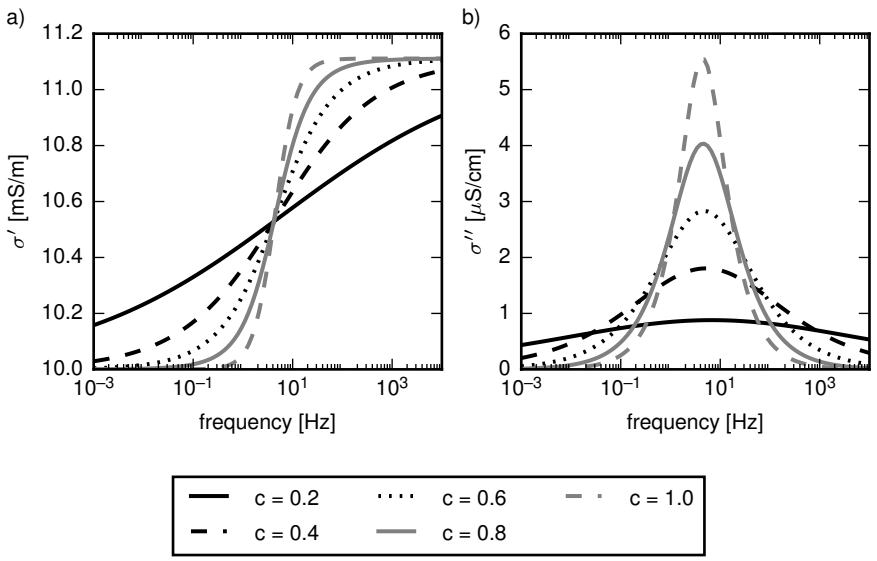

Figure 2.1: Exemplary Cole-Cole model responses ($\rho_0 = 100\,\Omega\text{m}, m = 0.1, \tau = 0.04$ s) for different c values. a) Real part of conductivity (σ'), b) imaginary part of conductivity (σ'').

of the medium. We here consider the following parameters, which have been used in previous works:

- The *total chargeability* $m_{\text{tot}} = \sum_{k=1}^{N_\tau} m_k$ (Nordsiek and Weller, 2008) is the analogon to the Cole-Cole chargeability m_{cc}. However, m_{tot} only accounts for polarisations within the considered frequency range of the DD, whereas m_{cc} also contains contributions from outside this range. Thus, not fully covered polarisation peaks imply an underestimation of the total chargeability m_{tot} of the system.

- The *normalised total chargeability* $m_{\text{n,tot}} = m_{\text{tot}}/\rho_0$ (Weller et al., 2010a) represents an extension of the normalised chargeability concept (e.g., Slater and Lesmes, 2002) to the total chargeability as derived from a DD. The normalised chargeability, $m_{\text{n}} = m/\rho_0$, is commonly considered as a more appropriate measure of the strength of polarisation. In 2.A we show for an individual Debye response according to Eq. (2.3) that the imaginary component of the complex conductivity, σ'', which represents

a direct measure of polarisation according to established petrophysical models (e.g., Revil and Florsch, 2010), indeed directly scales with m_n. For not too strong polarisations, i.e., $m \ll 1$, one obtains

$$\sigma''(\omega) \approx m_\mathrm{n} \frac{\omega\tau}{1 + (\omega\tau)^2}. \tag{2.5}$$

Hence it is physically plausible to consider the normalised total chargeability derived from the DD in Eq. (2.3) as a direct measure of the overall polarisation of the medium.

- The *cumulative relaxation time* τ_x denotes the relaxation time at which a certain percentage x of the total chargeability is reached (Nordsiek and Weller, 2008; Zisser et al., 2010a). Commonly used is τ_{50}, the median relaxation time of a given RTD.

- The *mean logarithmic relaxation time* τ_peak is the chargeability-weighted logarithmic mean value of the relaxation times (Nordsiek and Weller, 2008): $\tau_\mathrm{peak} = \exp\left(\sum_{k=1}^{N_\tau} m_k \log(\tau_k) / \sum_{k=1}^{N_\tau} m_k\right)$.

- As a generalisation of the maximum relaxation time τ_max (e.g., Attwa and Günther, 2013), we here introduce the relaxation time $\tau_{l,\mathrm{peak}}$, which refers to the l-th local maximum of the RTD, with numbering beginning at low frequencies (i.e., high τ values). This parameter is useful if multiple dominant relaxation phenomena are to be analysed in a given SIP spectrum. These polarisation peaks result in multiple peaks in the RTD, which cannot be tracked using integrative parameters such as τ_peak or τ_{50}.

- The *non-uniformity parameter* $U_\tau = \tau_{60}/\tau_{10}$ is a measure of the width of the RTD (Nordsiek and Weller, 2008).

For a complete list of implemented integral parameters, we refer to the source code documentation.

2.2.3 Inverse approach

The inversion is implemented using a Tikhonov regularisation scheme (e.g., Zhdanov, 2002; Menke, 2012) which minimises an objective function, Ψ, comprising data misfit, Ψ_y, and a model objective function, Ψ_x, balanced by a real-valued regularisation parameter, $\lambda_{\text{freq}} > 0$:

$$\Psi = \Psi_{\text{y}} + \lambda_{\text{freq}} \Psi_{\text{x}} \tag{2.6}$$

$$\text{with } \Psi_{\text{y}} = \left\| \underline{\underline{W}} (\underline{y} - \underline{f}(\underline{x})) \right\|_{L_2}^2 \tag{2.7}$$

$$\text{and } \Psi_{\text{x}} = \left\| \underline{\underline{R}} \underline{x} \right\|_{L_2}^2 , \tag{2.8}$$

where $\underline{x}$ is the model parameter vector, $\underline{y}$ is the data vector, and $\underline{f}(\underline{x})$ is the forward model response. We use individual data weighting factors which are stored in the diagonal matrix $\underline{\underline{W}}$. This corresponds to the assumption of uncorrelated data with Gaussian statistics, with the standard deviations of the data given by the inverse values of the diagonal entries of $\underline{\underline{W}}$. The regularisation term Ψ_x is chosen to force smooth solutions via a roughness matrix $\underline{\underline{R}}$, which evaluates either the first- or the second-derivative variation in the components of $\underline{x}$.

The inversion underlying the DD is formulated as a real-valued problem with real and (negative) imaginary components of the measured complex resistivity, $\rho'_{\text{obs}}(\omega_i)$ and $-\rho''_{\text{obs}}(\omega_i)$ (note that always $\rho' > 0$, and $-\rho'' > 0$ if polarisation is present), respectively, representing the data at the measurement frequencies ω_i. The model parameters are given by the log-transformed DC resistivity ρ_0 and the log-transformed chargeabilities m_k at the considered relaxation times τ_k. Our choice of using log-transformed chargeabilities in the parameterisation implies that relative changes in chargeability are equally weighted in the inversion, so that changes in the very low chargeability range still have importance in the inversion. Moreover, the log transform guarantees positive chargeability values. Ghorbani et al. (2007) suggest an alternative parameterisation of chargeability based on the *logit* function, which they argue is a mathematically more reasonable parameterisation also in the range towards the theoretical maximum value of chargeability (i.e. 1). However, since we are here not considering the

total chargeability (like for instance represented by the Cole-Cole chargeability m_{cc}) but the chargeability contributions at the different relaxation times τ_k, the values of m_k are typically very small (i.e. $\ll 1$) and we therefore consider the log transform being used here adequate as well. Thus, the model parameter vector $\underline{x}$, the data vector $\underline{y}$ (comprising one complex resistivity spectrum), and the forward model response $\underline{f}(\underline{x})$ are expressed as

$$\underline{x} = \begin{pmatrix} \log_{10}(\rho_0) \\ \log_{10}(m_1) \\ \vdots \\ \log_{10}(m_{N_\tau}) \end{pmatrix}, \tag{2.9}$$

$$\underline{y} = \begin{pmatrix} \rho'_{\mathrm{obs}}(\omega_1) \\ \vdots \\ \rho'_{\mathrm{obs}}(\omega_{N_f}) \\ -\rho''_{\mathrm{obs}}(\omega_1) \\ \vdots \\ -\rho''_{\mathrm{obs}}(\omega_{N_f}) \end{pmatrix}, \tag{2.10}$$

$$\underline{f}(\underline{x}) = \begin{pmatrix} \rho'(\omega_1) \\ \vdots \\ \rho'(\omega_{N_f}) \\ -\rho''(\omega_1) \\ \vdots \\ -\rho''(\omega_{N_f}) \end{pmatrix}, \tag{2.11}$$

with N_τ the chosen number of relaxation times, N_f the number of given frequencies, N_{x} the number of model parameters in $\underline{x}$ ($N_{\mathrm{x}} = 1 + N_\tau$), and N_{y} the number of data points in $\underline{y}$ ($N_{\mathrm{y}} = 2N_f$). The forward model response $\hat{\rho}(\omega_i) = \rho'(\omega_i) + j\rho''(\omega_i)$ is calculated according to Eq. (2.3).

The root-mean-square value of the misfit between data and model response for

the imaginary parts (i.e., the second half of $\underline{y}$ and $\underline{f}(\underline{x})$), RMS_{Im}, is used for assessing the quality of the inversion process:

$$RMS_{\mathrm{Im}} = \sqrt{\frac{1}{N_f}\sum_{i=1}^{N_f}\left|y_{N_f+i} - f_{N_f+i}(\underline{x})\right|^2}. \tag{2.12}$$

Jacobian

The Jacobian (or *sensitivity matrix*) corresponding to $\underline{f}(\underline{x})$ is defined as the $N_{\mathrm{x}} \times N_{\mathrm{y}}$ matrix

$$\underline{\underline{J}} = \frac{\partial \underline{f}}{\partial \underline{x}} = \begin{pmatrix} \frac{\partial \rho'(\omega_1)}{\partial \rho_0} & \frac{\partial \rho'(\omega_1)}{\partial m_1} & \cdots & \frac{\partial \rho'(\omega_1)}{\partial m_{N_\tau}} \\ \vdots & \vdots & \vdots & \vdots \\ \frac{\partial \rho'(\omega_{N_f})}{\partial \rho_0} & \frac{\partial \rho'(\omega_{N_f})}{\partial m_1} & \cdots & \frac{\partial \rho'(\omega_{N_f})}{\partial m_{N_\tau}} \\ -\frac{\partial \rho''(\omega_1)}{\partial \rho_0} & -\frac{\partial \rho''(\omega_1)}{\partial m_1} & \cdots & -\frac{\partial \rho''(\omega_1)}{\partial m_{N_\tau}} \\ \vdots & \vdots & \vdots & \vdots \\ -\frac{\partial \rho''(\omega_{N_f})}{\partial \rho_0} & -\frac{\partial \rho''(\omega_{N_f})}{\partial m_1} & \cdots & -\frac{\partial \rho''(\omega_{N_f})}{\partial m_{N_\tau}} \end{pmatrix}, \tag{2.13}$$

with the corresponding derivatives given in Eqs. (2.37)-(2.40) in 2.B.

A cumulated sensitivity (or *coverage*), $S_{\mathrm{Im},k}$, can be computed for each chargeability m_k:

$$S_{\mathrm{Im},k} = \sum_{i=1}^{N_f}\left|\frac{\partial \rho''(\omega_i)}{\partial m_k}\right|. \tag{2.14}$$

This cumulated sensitivity value is a measure of the overall change of the imaginary parts of the predicted data in response to changes of an individual chargeability value m_k, or in other words, how well the parameter m_k is *covered* by these data. Correspondingly, large values of $S_{\mathrm{Im},k}$ indicate chargeabilities with a high influence on the response ρ''.

Model update

Minimisation of Ψ leads to an iterative Gauß-Newton like scheme, in which a model update $\Delta \underline{x}_q$ is computed for each iteration q using the *normal equations*:

$$\left[\underline{\underline{J}}_q^T \underline{\underline{W}}^T \underline{\underline{W}} \underline{\underline{J}}_q + \lambda_{\text{freq}} \underline{\underline{R}}^T \underline{\underline{R}}\right] \triangle \underline{x}_q = \left[\underline{\underline{J}}_q^T \underline{\underline{W}}^T \underline{\underline{W}} (\underline{y} - \underline{f}(\underline{x}_q)) - \lambda_{freq} \underline{\underline{R}}^T \underline{\underline{R}} \underline{\underline{x}}_q\right]. \tag{2.15}$$

Successive iterations are computed by

$$\underline{x}_{q+1} = \underline{x}_q + \alpha \triangle \underline{x}_q, \tag{2.16}$$

with a real-valued parameter $\alpha \in [0, 1]$. The value of α is determined from a classical line search, explained further below, and the limitation $\alpha \leq 1$ prevents from overshooting (at the cost of potentially increasing the number of iterations until convergence is reached).

Starting model

The starting model for each spectrum is determined by testing a series of homogeneous RTDs for chargeability values between 10^{-12} and 1. The model yielding the minimal value of RMS_{Im} is then used as the starting model in the inversion.

Stopping criteria

The inversion is stopped when one or more of the following criteria are met:

- The RMS_{Im} does not change significantly (smaller than predefined percentage) between subsequent iterations.
- The RMS_{Im} decrease lies below a certain threshold value. An exception is the first iteration, where an RMS_{Im} increase of up to 100 % is allowed to account for a possible tuning-in phase based on the starting model.
- The update leads to a numerical error (e.g. overflow error).

Step-length selection

At each iteration an optimal step length parameter α (Eq. 2.16) is selected using a line search approach (e.g., Kemna, 2000; Günther, 2004): A parabola is fitted through three $\mathrm{RMS}_{\mathrm{Im}}$ values corresponding to the α values 0, 0.5, and 1, and the minimum of the parabola determines the step length $\alpha_{\min}$ for the model update. In case of a minimum above 1 the step length is set to 1. For $\alpha_{\min} \leq 0$, the model update does not lead to an improvement of $\mathrm{RMS}_{\mathrm{Im}}$ and the inversion is stopped.

Data weighting

The diagonal entries of $\underline{\underline{W}}$ compensate for different ranges of $\rho'(\omega)$ and $\rho''(\omega)$:

$$\underline{\underline{W}} = \begin{pmatrix} \underline{\underline{W}}^{\mathrm{Re}} & 0 \\ 0 & \underline{\underline{W}}^{\mathrm{Im}} \end{pmatrix}, \tag{2.17}$$

where $\underline{\underline{W}}^{\mathrm{Re}}$ is the unity matrix of size $N_f \times N_f$, and $\underline{\underline{W}}^{\mathrm{Im}}$ is a $N_f \times N_f$ diagonal matrix with entries $w = \sum_{i=1}^{N_f} |\rho'_i| / \sum_{i=1}^{N_f} |\rho''_i|$. This weighting scheme ensures that both real and imaginary parts are fitted to similar misfit levels irrespective of their values.

Regularisation

Smoothness constraints are applied to the chargeability values using first- and second-order finite-difference operators (e.g., Menke, 2012; Aster et al., 2013). The first-order smoothing operator is given by the $(N_\tau - 1) \times N_\tau$ matrix

$$\underline{\underline{D}}^{(1)} = \begin{pmatrix} -1 & 1 & 0 & \dots & 0 \\ 0 & -1 & 1 & \ddots & \vdots \\ \vdots & \ddots & \ddots & \ddots & 0 \\ 0 & \dots & 0 & -1 & 1 \end{pmatrix}, \tag{2.18}$$

and the second-order operator by the $(N_\tau - 2) \times N_\tau$ matrix

$$\underline{\underline{D}}^{(2)} = \begin{pmatrix} 1 & -2 & 1 & 0 & \dots & 0 \\ 0 & 1 & -2 & 1 & \ddots & \vdots \\ \vdots & \ddots & \ddots & \ddots & \ddots & 0 \\ 0 & \dots & 0 & 1 & -2 & 1 \end{pmatrix}. \tag{2.19}$$

As no smoothing between ρ_0 and the chargeabilities is imposed, the regularisation matrix $\underline{\underline{R}}$ of size $N_x \times N_x$ is chosen as

$$\underline{\underline{R}} = \begin{pmatrix} 0 & 0 \\ 0 & \underline{\underline{D}}^{(1),(2)} \end{pmatrix}, \tag{2.20}$$

with either $\underline{\underline{D}}^{(1)}$ or $\underline{\underline{D}}^{(2)}$.

Selection of τ values

Two parameters determine the discrete relaxation times used for the decomposition: The number of relaxation times per frequency decade, N_d, and the min/max limits for the relaxation times. The N_d parameter must provide enough degrees of freedom to fit the data (Uhlmann and Hakim, 1971). Minimal and maximal τ values can be inferred from the frequency limits of the data using the inverse correlation of τ and ω (Uhlmann and Hakim, 1971). These limits can be extended by multiplicative constants, defaulting to an extension of one frequency decade to either side of the data frequency limits. Integral parameters are only computed for the τ range defined by the data frequency range, irrespective of the actual range set for the decomposition.

Selection of λ_{freq} values

Three methods of selecting the regularisation parameter are implemented: A fixed value can be used for all iterations, the L-curve (e.g., Hansen, 1990; Florsch et al., 2014) can be used to infer an optimal regularisation parameter (Zisser et al., 2010b; Florsch et al., 2012), and a line search (simplified from the one used in Kemna (2000)) is implemented to automatically determine an optimal λ_{freq} value at each iteration. In the latter approach, the λ_{freq} value of the previous (q-th) iteration is used as a starting point and multiple new values in the

range between $0.1\lambda_{\text{freq}}$ and $10^4\lambda_{\text{freq}}$ are sampled. The value yielding the smallest RMS_{Im} value is then used to actually compute the model update. For the first iteration, the λ_{freq} value is set to the number of model parameters. The inversion results presented in the following were computed using this last approach of selecting λ_{freq}.

2.2.4 Extension to time-lapse inversion

Time-lapse data can be accounted for in the inversion scheme by extending the vectors and matrices to include all time steps. Based on the formulation for a single spectrum $\hat{\rho}(\omega)$ the new vectors sequentially contain the quantities for the different time steps, and the new matrices become block matrices with each block along the diagonal corresponding to a time step. In the following, the subscript $_d$ denotes the time index and N_{t} the total number of time steps.

The extended model vector $\underline{x}_{\text{all}}$, data vector $\underline{y}_{\text{all}}$, and model response $\underline{f}_{\text{all}}$ are thus given by

$$\underline{x}_{\text{all}} = \begin{pmatrix} \underline{x}_1 \\ \vdots \\ \underline{x}_{N_{\text{t}}} \end{pmatrix}, \tag{2.21}$$

$$\underline{y}_{\text{all}} = \begin{pmatrix} \underline{y}_1 \\ \vdots \\ \underline{y}_{N_{\text{t}}} \end{pmatrix}, \tag{2.22}$$

$$\underline{f}_{\text{all}}(\underline{x}_{\text{all}}) = \begin{pmatrix} \underline{f}(\underline{x}_1) \\ \vdots \\ \underline{f}(\underline{x}_{N_{\text{t}}}) \end{pmatrix}, \tag{2.23}$$

with $\underline{x}_{\text{all}}$ of size $N_{\text{x}} \cdot N_{\text{t}}$ (one parameter set for each time step), and $\underline{y}_{\text{all}}$ and $\underline{f}_{\text{all}}$ of size $2N_f \cdot N_{\text{t}}$ (real and imaginary parts for each frequency for each time step).

The corresponding Jacobian matrix can be assembled based on Eq. (2.13) for each time step:

$$\underline{\underline{J}}_{\text{all}} = \begin{pmatrix} \underline{\underline{J}}_1 & 0 & \dots & 0 \\ 0 & \underline{\underline{J}}_2 & \ddots & \vdots \\ \vdots & \ddots & \ddots & 0 \\ 0 & \dots & 0 & \underline{\underline{J}}_{N_\text{t}} \end{pmatrix}, \tag{2.24}$$

with the size $(N_\text{x} \cdot N_\text{t}) \times (2N_f \cdot N_\text{t})$.
The $\text{RMS}_{\text{Im}}^{\text{all}}$ value incorporates the misfits of the imaginary parts for all time steps:

$$\text{RMS}_{\text{Im}}^{\text{all}} = \sqrt{\frac{1}{N_\text{t} N_f} \sum_{d=1}^{N_\text{t}} \sum_{i=1}^{N_f} \left| y_{d,N_f+i} - f_{d,N_f+i}(\underline{x}_d) \right|^2}. \tag{2.25}$$

The regularisation term Ψ_x (Eq. 2.8) is now extended to include not only the frequency regularisation, but also time-regularisation terms for ρ_0 and the chargeabilities. Thus, the objective function with time regularisation, Ψ_time, becomes

$$\Psi_\text{time} = \Psi_\text{y} + \lambda_\text{f} \left\| \underline{\underline{R}}_\text{f} \underline{x}_\text{all} \right\|_{L_2}^2 + \lambda_{\rho_0} \left\| \underline{\underline{R}}_{\rho_0} \underline{x}_\text{all} \right\|_{L_2}^2 + \lambda_m \left\| \underline{\underline{R}}_\text{m} \underline{x}_\text{all} \right\|_{L_2}^2, \tag{2.26}$$

with the regularisation parameters $\lambda_\text{f}, \lambda_{\rho_0}, \lambda_\text{m}$ controlling the influence of the frequency regularisation operator $\underline{\underline{R}}_\text{f}$, the ρ_0-time regularisation operator $\underline{\underline{R}}_{\rho_0}$, and the chargeability-time regularisation operator $\underline{\underline{R}}_\text{m}$, respectively. Fixed values are used for λ_{ρ_0} and λ_m.
The extended frequency regularisation matrix $\underline{\underline{R}}_\text{f}$ is constructed as a $(N_\text{x} \cdot N_\text{t}) \times (N_\text{x} \cdot N_\text{t})$ block matrix containing the individual regularisation matrices $\underline{\underline{R}}$ (Eq. 2.20) for each time step:

$$\underline{\underline{R}}_{\text{t,f}} = \begin{pmatrix} \underline{\underline{R}} & 0 & 0 \\ 0 & \ddots & 0 \\ 0 & 0 & \underline{\underline{R}} \end{pmatrix}. \tag{2.27}$$

Depending on the type of regularisation used, $\underline{\underline{R}}$ is either based on $\underline{\underline{D}}^{(1)}$ (Eq. 2.18) or $\underline{\underline{D}}^{(2)}$ (Eq. 2.19).

The smoothness constraints along the time axis require some further consideration. The smoothing operator has to be applied to each parameter of $\underline{x}$ separately along the time axis, and thus correspondingly resized versions of Eqs. (2.18) and (2.19) are used, denoted by the matrices $\underline{\underline{T}}^{(1),(2)}$ of size $N_\mathrm{t} \times N_\mathrm{t}$. As the time-lapse entries of a specific parameter are non-continuously distributed in $\underline{x}_\mathrm{all}$, $\underline{\underline{T}}^{(1),(2)}$ must be projected into an extended matrix of size $(N_\mathrm{x} \cdot N_\mathrm{t}) \times (N_\mathrm{x} \cdot N_\mathrm{t})$, which is filled up with zeros. For the p-th parameter of $\underline{x}$, a given element $t_{l,m}$ of $\underline{\underline{T}}^{(1),(2)}$ is projected to the $[(l-1)N_\mathrm{x}+p, (m-1)N_\mathrm{x}+p]$-th element of this enlarged matrix, denoted by $\underline{\underline{R}}_p$. For $p = 1$, $\underline{\underline{R}}_{\rho_0}$ results, while $\underline{\underline{R}}_\mathrm{m}$ is obtained by summing up the regularisation matrices for all chargeabilities:

$$\underline{\underline{R}}_\mathrm{m} = \sum_{p=2}^{N_\mathrm{x}} \underline{\underline{R}}_p . \tag{2.28}$$

The scheme described above simplifies the implementation of the regularisation matrices, as only a *base* version (with variable size) has to be created for each regularisation type, which then can be applied to both frequency and time domains using the projection.

It is noted that so far the smoothing operators do not take the distance between adjacent parameters in the respective direction (frequency or time) into account. However, in particular for time-lapse measurements it is not uncommon to encounter irregular time intervals Δt. These time intervals can be used to weight the regularisation matrices by means of a diagonal time-weighting matrix $\underline{\underline{C}}_\mathrm{t}$:

$$\underline{\underline{C}}_\mathrm{t} = \begin{pmatrix} \frac{1}{t_2 - t_1} & 0 & 0 \\ 0 & \ddots & 0 \\ 0 & 0 & \frac{1}{t_{N_\mathrm{t}} - t_{N_\mathrm{t}-1}} \end{pmatrix}, \tag{2.29}$$

where t_d is the time (measured in an arbitrary unit) of the d-th time step. The original regularisation matrix is then transformed according to

$$\underline{\underline{T}}^{(1)}_{\mathrm{tw}} = \underline{\underline{C}}_t \underline{\underline{T}}^{(1)}, \tag{2.30}$$

with subscript tw indicating the time-weighted variant of the regularisation matrix. The time weighting can be disabled by setting the matrix $\underline{\underline{C}}_t$ to the unity matrix. In the current implementation, time weighting can only be applied in conjunction with first-order smoothing. However, in the future we plan to also extend it to second-order smoothing based on the implementation of the second-order derivative operator also for non-regularly sampled points.

2.3 Results and discussion

In this section the optimal selection of the number and range of τ values is examined, followed by an investigation of the effect of the regularisation, both in frequency and time domain.

2.3.1 Relaxation times

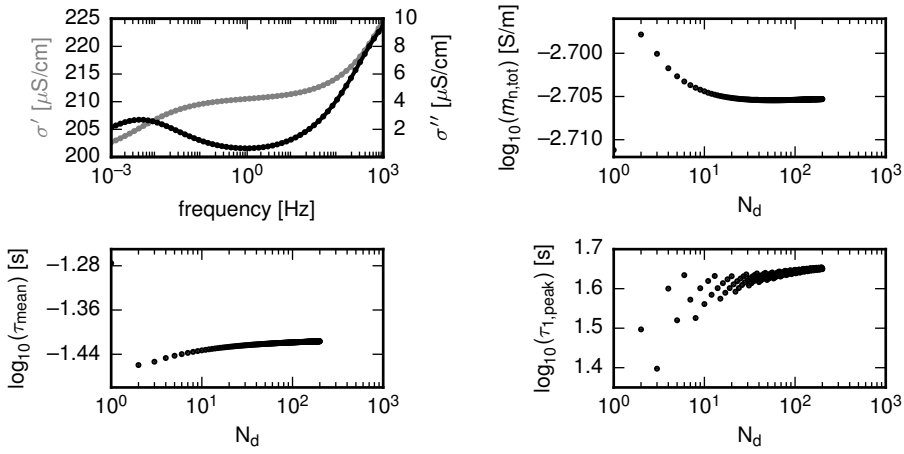

Figure 2.2: DD results in terms of inferred integral parameters for varying N_d values. a) Synthetic SIP data (grey: σ', black: σ''). b) $m_{\mathrm{n,tot}}$ results, c) τ_{peak} results, c) $\tau_{1,\mathrm{peak}}$ results. All fits were performed using a frequency regularisation parameter $\lambda = 100$.

The choice of relaxation times is crucial for the decomposition process. Using an exemplary bimodal SIP response (Fig. 2.2a), recovered integral parameters were investigated for various N_d values (in the literature, values for N_d range from 4 to 166 (Uhlmann and Hakim, 1971; Morgan and Lesmes, 1994; Nordsiek and Weller, 2008; Zisser et al., 2010a)). Figures 2.2b-d present the results for $m_{\mathrm{n,tot}}$, τ_{peak}, and $\tau_{1,\mathrm{peak}}$. A strong variation in the results can be observed for N_d values below 10. For larger values of N_d, the reconstructed values practically do not vary anymore and converge for $m_{\mathrm{n,tot}}$ and τ_{peak}, and $\tau_{1,\mathrm{peak}}$ only increases slightly beyond $N_d > 10$.

The response of even a single Debye term spreads significantly over a range of more than one frequency decade to both sides of its peak frequency (e.g., Florsch et al., 2014). Hence, τ values outside the data frequency range can influence the inverted RTD inside the data frequency range. To illustrate the effects of too narrow τ ranges, synthetic SIP data were generated in a frequency range between 10^{-3} Hz and 10^{3} Hz using a two-term Cole-Cole model (Fig. 2.3a), and subsequently the DD was applied using three different τ ranges: 1) the range was determined from the data frequencies, 2) the data frequency range was symmetrically extended by one frequency decade, and 3) the data frequency range was symmetrically extended by two frequency decades. In all cases, N_d was set to 20, and the data could be adequately fitted. However, the obtained RTDs vary considerably (Figs. 2.3b-d). Without any extension of the τ range (Fig. 2.3b), two peaks can be observed in the RTD (Fig. 2.3c), of which only one can be related to a polarisation peak in the SIP data (compare detected peaks, i.e., solid and dashed lines in Figs. 2.3a,b). However, when the τ range is increased (Figs. 2.3c,d), only the polarisation peak indeed present in the data is recovered. The high-frequency peak (low relaxation times) in the RTD (Fig. 2.3b) corresponds to a large increase in S_{Im} (Fig. 2.3e), indicating an over-proportional influence of the small τ values in the case of the insufficiently broad τ ranges. Note that, irrespective of the τ range used, large values of S_{Im} can be observed for the not fully covered high-frequency peak, suggesting a strong influence of the corresponding chargeabilities if polarisation peaks are not fully covered by the data. Based on the results (Figs. 2.2 and 2.3) we recommend to use a value of at least $N_d = 20$ for the DD, and to extend the τ range at least by one frequency decade to each side of the data frequency limits.

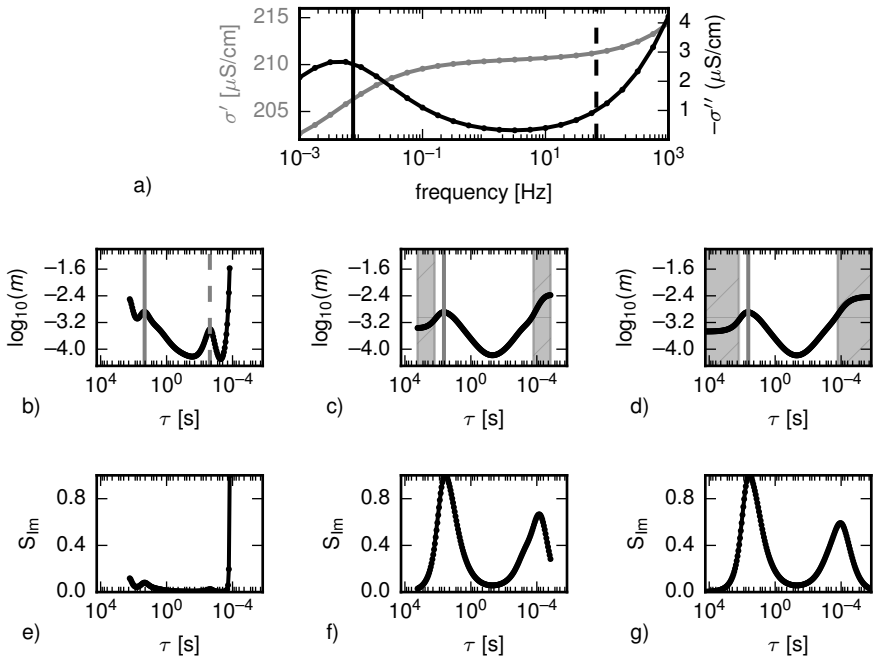

Figure 2.3: DD results using different τ ranges. a) Synthetic SIP data (dots) and fitting results (solid curves) (grey: σ', black: σ''). b,e): RTD and coverage S_{Im} using τ limits determined by data limits. c,f): RTD and coverage S_{Im} using τ limits extended by one frequency decade (shaded area) relative to the data limits. d,g) RTD and coverage S_{Im} using τ limits increased by two frequency decades (shaded area) relative to the data limits. All fits were performed using a frequency regularisation parameter $\lambda = 50$ and $N_d = 20$. Vertical lines mark peaks in the inverted RTD (see also discussion in the text).

2.3.2 Regularisation strategies

The effect of too weak or too strong (first-order) frequency regularisation is demonstrated using synthetic SIP data contaminated by normally distributed noise (this type of noise is in the following also referred to as *measurement noise*). Three DDs were performed using regularisation parameter values $\lambda = 1, 10^3$, and 10^5. The corresponding fitting results are shown in Figures 2.4a,c,e,

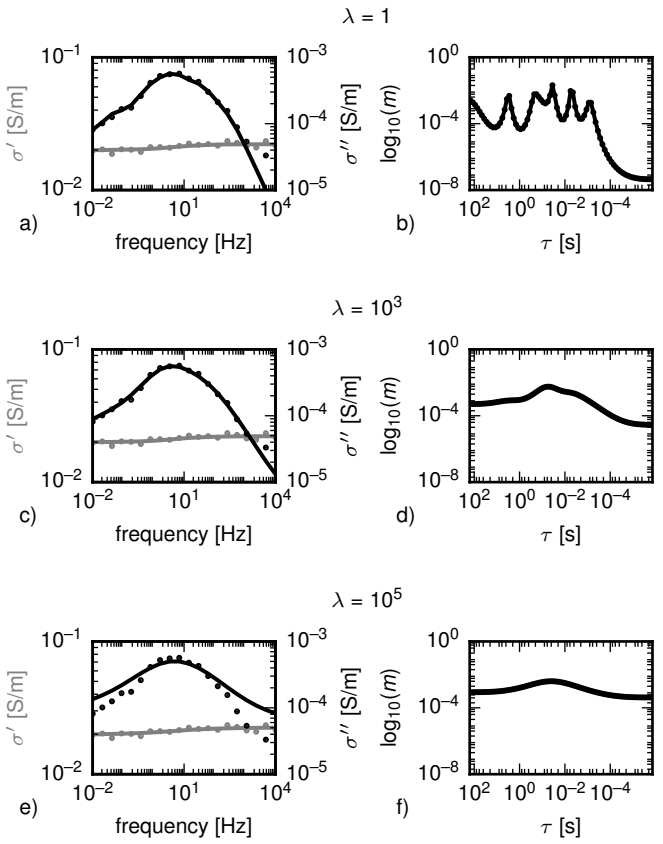

Figure 2.4: DD results for different values of the frequency regularisation parameter λ_{freq}. a,c,e) Synthetic SIP data (dots) and fitting results (solid curves) for λ_{freq} values of $1, 10^3$, and 10^5, respectively (grey: σ', black: σ''). Uncorrelated, normally distributed noise with standard deviations of 1.5 Ωm and 2 mrad for magnitude and phase of the complex resistivity, respectively, was added to the SIP data prior to DD. b,d,f) Corresponding RTDs, with $\log_{10}(m_{\text{n,tot}})$ values of $(-2.72, -2.71, -2.67)$ and $\log_{10}(\tau_{\text{peak}})$ values of $(-1.34, -1.36, -1.45)$.

with RTDs plotted in Figures 2.4b,d,f. For a λ value of 1, a relatively rough RTD is obtained, nonetheless adequately fitting the data. Due to the roughness of the RTD no clear peak relaxation time can be identified. The DDs performed with λ values of 10^3 and 10^5 show smooth RTD curves, each exhibiting a clear

peak. However, the larger regularisation parameter leads to a flat polarisation response which does not fit the SIP data (Fig. 2.4e). Thus, the used regularisation parameters should be verified to avoid situations as presented in Figs. 2.4b,f.

Considering the analysis of time-lapse data, no inherent constraints (or preferences) regarding the time evolution of the DD parameters can be inferred from the method itself. All such constraints must be based on some sort of a-priori information (e.g., on the type of polarisation or the type of process being investigated with SIP measurements). Therefore, a variety of regularisation operators can be used for time regularisation. However, it should be kept in mind that the different constraints reflect different a-priori information, which can have considerable influence on the resulting RTD.

The influence of time regularisation operators on the decomposition process is illustrated on a synthetic time-lapse SIP data set which comprises spectra at 20 (irregular) time steps created using a single-term Cole-Cole model response (Fig. 2.5). The chargeability values of the SIP spectra decrease linearly with time, imitating a corresponding time-dependent polarisation process (Fig. 2.5a, increasing opacity indicates increasing time). A small, normally distributed measurement noise component with a standard deviation of 0.5 mrad was added to each spectrum. Additionally, a time dependent, normally distributed noise component with a standard deviation of 5% was added to the Cole-Cole chargeability values to simulate variations in the underlying polarisation process (in the following also referred to as *process noise*). This second noise component does not distort the SIP spectra, however, the spectra are vertically shifted. This is the primary type of noise that can be smoothened out using a time-regularisation approach. Measurement noise would have to be very large in order to influence integral parameters such as m_{tot}. The $m_{\mathrm{n,tot}}$ values inferred from the inverted RTDs for different time-regularisation approaches in the DD are plotted in Figure 2.5b. For consistency, the DD without any time regularisation was performed with the same frequency regularisation parameter as the DD with time regularisation. The results show that time regularisation successfully smoothens the noise-induced roughness in the $m_{\mathrm{n,tot}}$ evolution compared to the DD results without time regularisation. Due to the non-regular spacing of the time-steps (as often found in long-term experiments, e.g. due to equipment failures or miscellaneous delays), the time-weighted regularisation scheme creates

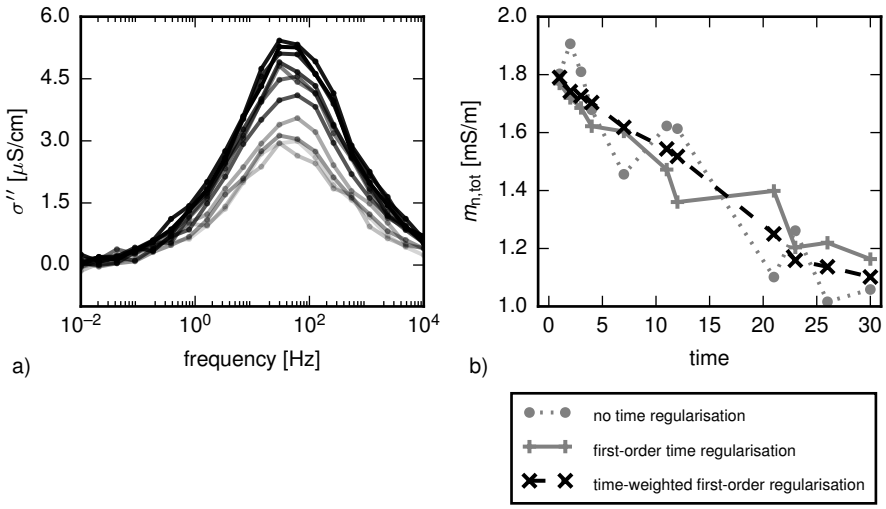

Figure 2.5: DD results in terms of inferred $m_{\mathrm{n,tot}}$ for different time regularisation approaches. a) Synthetic SIP data for all time steps, generated using a single-term Cole-Cole model. Amplitudes decrease with increasing time. Uncorrelated, normally distributed noise was added to the Cole-Cole chargeability (standard deviation 5%) prior to computation of the spectra, and frequency noise with a standard deviation of 0.5 mrad was added to the computed phase data for each time step. b) $m_{\mathrm{n,tot}}$ results without time regularisation, with first-order time regularisation, and with time-weighted first-order time regularisation (see legend).

smoother results in this example.

Time regularisation operates on the RTD, i.e., the chargeabilities at the discrete relaxation times. Smoothing of the chargeabilities thus directly influences the integral chargeability parameters m_{tot} and $m_{\mathrm{n,tot}}$, as shown above. Integral relaxation time parameters are only influenced implicitly due to the deformation of the RTD by the time regularisation. Nonetheless, time regularisation can improve the reconstruction quality of integral relaxation time parameters for noisy time-lapse SIP data. Here, measurement and process noise components are treated separately. Fig. 2.6a presents 20 single-term Cole-Cole model responses whose relaxation time changes linearly with time on a logarithmic scale (the

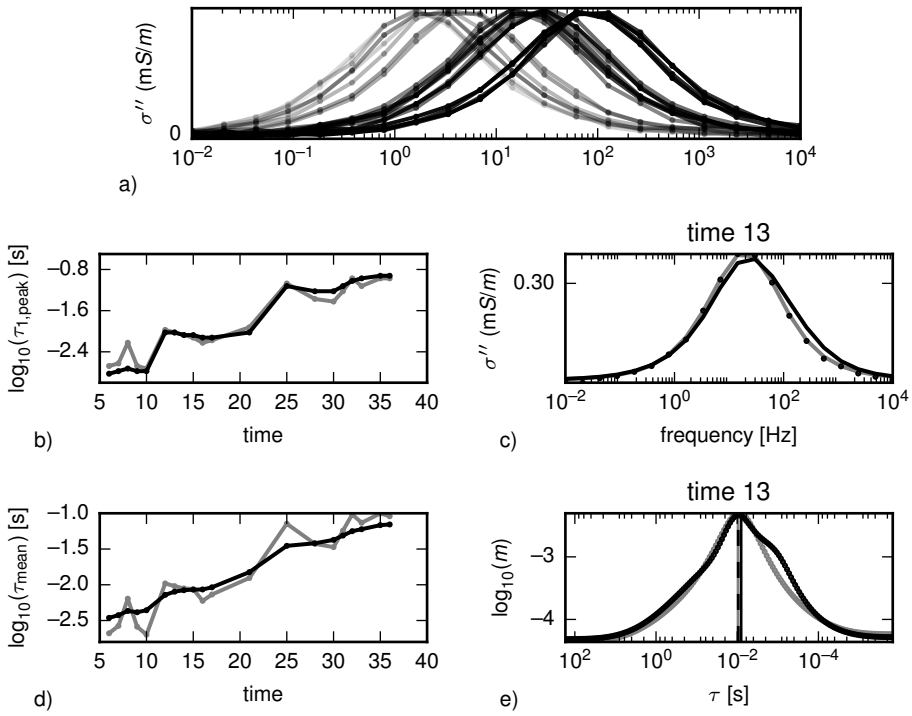

Figure 2.6: DD results in terms of inferred integral parameters $\tau_{1,\mathrm{peak}}$ and τ_{peak} without and with time regularisation. a) Synthetic SIP data in terms of σ''. Increasing opacity indicates increasing time. The data include uncorrelated, normally distributed measurement noise (standard deviation 0.5 mrad) added to the phase data for each time step prior to DD, as well as 20% process noise added to the Cole-Cole relaxation times before computation of the spectra. b) $\tau_{1,\mathrm{peak}}$ results, c) σ'' data (dots) and fitting results (solid lines) for time step 13 without (grey) and with (black) time regularisation. d) τ_{peak} results, e) RTD results for time step 13 without (grey) and with (black) time regularisation. Solid vertical lines indicate τ_{peak} results, while dashed lines indicate peak relaxation times.

simulated time steps, again, are not regularly spaced). A normally distributed process noise level of 20 % was added to the log-values of the relaxation times before computing the responses. This large noise level is justified by the large

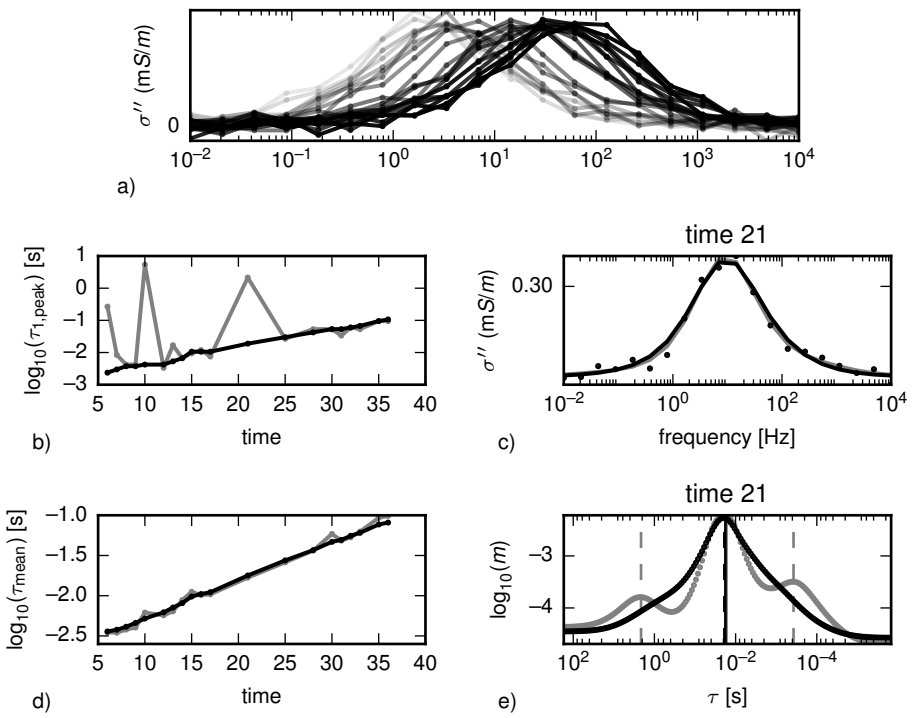

Figure 2.7: DD results in terms of inferred integral parameters $\tau_{1,\text{peak}}$ and τ_{peak} without and with time regularisation. a) Synthetic SIP data in terms of σ''. Increasing opacity indicates increasing time. The data include uncorrelated, normally distributed measurement noise (standard deviation 2 mrad) added to the phase data for each time step prior to DD. b) $\tau_{1,\text{peak}}$ results, c) σ'' data (dots) and fitting results (solid lines) for time step 21 without (grey) and with (black) time regularisation. d) τ_{peak} results, e) RTD result for time step 21 without (grey) and with (black) time regularisation. Solid vertical lines indicate τ_{peak} results, while dashed lines indicate peak relaxation times.

possible dynamics that can be observed for relaxation times. Additionally, a small measurement noise level of 0.5 mrad was added to the generated spectra. The time evolution of the integral parameters $\tau_{1,\text{peak}}$ and τ_{peak}, inferred from the obtained RTDs, is presented in Figures 2.6b and 2.6d, respectively. Time regularisation greatly improves the quality of the τ_{peak} results, while the $\tau_{1,\text{peak}}$

results are only slightly improved. This can be explained by the nature of the data noise: Process noise components in τ directly translate to changes in the peak position of the RTD, without affecting the smoothness of the spectrum and the RTD. Time regularisation strategies thus have to move the RTD peak in order to change $\tau_{1,\mathrm{peak}}$ results, but only have to change the shape of the RTD in order to influence τ_{peak}. This is illustrated in Figures 2.6c and 2.6e. Time regularisation changes the model response only slightly, but deformes the RTD enough to influence τ_{peak} (Fig. 2.6c, black curve).

However, $\tau_{1,\mathrm{peak}}$ results can be heavily improved by time regularisation schemes, if the data are primarily influenced by measurement noise. This effect is illustrated in Figure 2.7, which shows a simulation similar to the previous one (presented in Fig. 2.6). However, no process noise component was added to the Cole-Cole relaxation time, and the standard deviation of the measurement noise was increased to 2 mrad. As can be observed in Fig. 2.7b, $\tau_{1,\mathrm{peak}}$ is heavily influenced by these noise components, while τ_{peak} is only slightly affected. This result can be explained by the resulting RTDs (Fig. 2.7e), where the noise produces misdirecting peaks which get smoothed out by the time regularisation.

Note, again, that $\tau_{1,\mathrm{peak}}$ is usually only interesting if multiple dominating polarisation responses are present in the SIP spectra, and only a subset is analysed. In other cases a more robust relaxation time parameter such as τ_{peak} should be preferred.

The presented results (Figs. 2.4 – 2.7) illustrate that care must be taken with respect to both, adequately balancing regularisation versus data misfit, as well as adequately balancing time versus frequency regularisation. The former issue can be addressed by, for example, performing a line search at each iteration of the DD to find the regularisation parameter value which locally minimises the data misfit, or by using the L-curve criterion. For the present inverse problem, however, it was found that the latter approach may yield varying results. To ensure a good balance between frequency and time regularisation, the involved regularisation parameters should be chosen such that the norms of the different regularisation terms in Eq. 2.26, i.e. $\underline{\underline{R}}_{\mathrm{f}}\underline{x}_{\mathrm{all}}$, $\underline{\underline{R}}_{\rho_0}\underline{x}_{\mathrm{all}}$, and $\underline{\underline{R}}_{\mathrm{m}}\underline{x}_{\mathrm{all}}$, yield values of similar order of magnitude, so that the dominance of a single term over the others is avoided.

2.4 Conclusions

The presented Debye decomposition procedure is a robust and versatile tool to describe and analyse time-lapse SIP data. The implementation of the procedure available under an open source licence facilitates further development and an easy adaptation to specific data types and fields of application. Time-regularisation strategies yield improved results for a better interpretation of monitoring measurements, especially when peak relaxation times are considered. The number of relaxation times per frequency decade should be larger than 20, and the range of relaxation times should be extended by at least one frequency decade beyond the limits given by the data frequencies. In addition, as with all regularised inversion problems, the choice of regularisation type and strength can significantly influence the results of the Debye decomposition. Future developments of the DD implementation will include the incorporation of specific polarisation terms, for example to represent higher-frequency electromagnetic coupling responses, as well as the inclusion of spatial regularisation for an improved analysis of SIP imaging results.

The code described in this study is maintained and developed at https://github.com/m-weigand/ccd_tools

Appendix

2.A Relationship between σ'' and m_{n} for a Debye response

The imaginary component of a complex resistivity Debye response according to Eq. (2.3) is given by

$$-\rho''(\omega) = \rho_0 m \frac{\omega\tau}{1+(\omega\tau)^2}. \tag{2.31}$$

With $\sigma'' = -\rho''/|\hat{\rho}|^2$ (since $\hat{\sigma} = 1/\hat{\rho}$) we obtain for the imaginary component of the complex conductivity

$$\sigma''(\omega) = \frac{\rho_0 m}{|\hat{\rho}(\omega)|^2} \frac{\omega\tau}{1+(\omega\tau)^2}. \tag{2.32}$$

Since $\rho_\infty = \rho_0(1-m)$ (see, e.g., Tarasov and Titov, 2013), with the high-frequency asymptotic resistivity ρ_∞, and $\rho_\infty < |\hat{\rho}(\omega)|$, we can write $|\hat{\rho}(\omega)| = \rho_0[1 - f(\omega)m]$, with some real-valued function $f(\omega) \in [0,1]$. Substitution into Eq. (2.32) yields

$$\sigma''(\omega) = \frac{1}{\rho_0} \frac{m}{[1-f(\omega)m]^2} \frac{\omega\tau}{1+(\omega\tau)^2}. \tag{2.33}$$

If we now assume that the polarization is not too strong, i.e., $m \ll 1$, expand the term $m/[1-f(\omega)m]^2$ into a Taylor series and neglect higher-order terms in m, we obtain

$$\sigma''(\omega) \approx \frac{m}{\rho_0} \frac{\omega\tau}{1+(\omega\tau)^2}, \tag{2.34}$$

which relates σ'' with the normalised chargeability $m_n = m/\rho_0$ (Eq. (2.5)).

2.B DD derivatives

The real and imaginary parts of the complex resistivity, as described by Eq. (4.2), are given by (e.g., Nordsiek and Weller, 2008)

$$\rho'(\omega) = \rho_0 - \rho_0 \sum_{k=1}^{N_\tau} m_k \frac{(\omega\tau_k)^2}{1 + (\omega\tau_k)^2}, \tag{2.35}$$

$$-\rho''(\omega) = \rho_0 \sum_{k=1}^{N_\tau} m_k \frac{\omega\tau_k}{1 + (\omega\tau_k)^2}. \tag{2.36}$$

The corresponding partial derivatives with respect to the model parameters used here are given by

$$\frac{\partial \rho'(\omega)}{\partial \log_{10}(\rho_0)} = \log(10) \cdot \rho_0 \left(1 - \sum_{k=1}^{N_\tau} m_k \frac{(\omega\tau_k)^2}{1 + (\omega\tau_k)^2}\right), \tag{2.37}$$

$$\frac{\partial \rho'(\omega)}{\partial \log_{10}(m_k)} = -\log(10) \cdot m_k \cdot \rho_0 \frac{(\omega\tau_k)^2}{1 + (\omega\tau_k)^2}, \tag{2.38}$$

$$-\frac{\partial \rho''(\omega)}{\partial \log_{10}(\rho_0)} = \log(10) \cdot \rho_0 \sum_{k=1}^{N_\tau} m_k \frac{\omega\tau_k}{1 + (\omega\tau_k)^2}, \tag{2.39}$$

$$-\frac{\partial \rho''(\omega)}{\partial \log_{10}(m_k)} = \log(10) \cdot m_k \cdot \rho_0 \cdot \frac{\omega\tau_k}{1 + (\omega\tau_k)^2}. \tag{2.40}$$

This chapter is based on the publication: Weigand, M. and Kemna, A. (2016). Relationship between Cole-Cole model parameters and spectral decomposition parameters derived from sip data. Geophysical Journal International. doi:10.1093/gji/ggw099

CHAPTER 3

Relationship between Cole-Cole model parameters and spectral decomposition parameters derived from SIP data

3.1 Introduction

Over the last decade the spectral induced polarisation (SIP) method has seen a rapid increase of its use in hydrogeological and environmental studies (e.g., Kemna et al., 2012). SIP data are given as frequency dependent electrical impedance or admittance measurements that can be converted to resistivities or conductivities by accounting for the measurement geometry.

Two basic types of phenomenological models are in use for the quantitative description of SIP data. The Cole-Cole (CC) model and its variants (e.g., Cole and Cole, 1941; Pelton et al., 1978; Dias, 2000) are typically used if the spectrum exhibits a distinct peak. Here three parameters, the CC relaxation time, the CC chargeability and the CC frequency exponent, account for the position of the peak along the frequency axis, the magnitude and the frequency dispersion of the response, respectively.

Alternatively, SIP data can be decomposed into individual responses of a chosen elementary relaxation model, mathematically acting as kernel in the involved

integral, based on a broad range of relaxation times. A frequently used kernel function is the Debye model (e.g., Uhlmann and Hakim, 1971; Lesmes and Morgan, 2001; Tarasov et al., 2003; Nordsiek and Weller, 2008), the special case of the CC model with strongest possible frequency dispersion. However, also the CC model with some other a priorly specified frequency dispersion (e.g., the Warburg model with intermediate frequency dispersion) has been proposed as kernel in the decomposition (Tarasov et al., 2003; Florsch et al., 2014; Revil et al., 2014). The choice of the latter follows pore-scale modelling results, which indicate that the elementary polarisation response of a single pore or grain exhibits a broader frequency dispersion than the Debye model response (e.g., Wong, 1979; Titov et al., 2002; Bücker and Hördt, 2013a). Therefore a Cole-Cole decomposition (CCD) (with fixed frequency dispersion) seems to be more adequate from a petrophysical point of view. The decomposition approach yields a relaxation time distribution (RTD) from which integral spectral parameters similar to those of the CC model can be computed, especially a mean relaxation time and a total chargeability.

It is important to note that the decomposition of SIP spectra based on CC-type kernel functions is highly ambiguous and the resultant RTD depends on the frequency dispersion of the kernel. For instance the equivalent representation of a CC model response as a superposition of Debye model responses based on an appropriate RTD was already recognised by Cole and Cole (1941). However, even if the frequency dispersion of the kernel is fixed in the decomposition, which is commonly done due to this inherent equivalence, the resulting inverse problem typically still is ill-posed, requiring regularisation (Florsch et al., 2012, 2014; Weigand and Kemna, 2016b). This leads to considerable uncertainties in the decomposition results on top of the contribution on the account of data errors. Several studies have assessed uncertainties in the estimation of spectral parameters for the CC model (Ghorbani et al., 2007; Chen et al., 2008) and the Debye decomposition (DD) (Florsch et al., 2012; Keery et al., 2012) in detail.

With the growing number and sophistication of SIP studies relating phenomenological model parameters to petrophysical properties, for example to permeability (e.g., Binley et al., 2005; Zisser et al., 2010a; Revil and Florsch, 2010; Weller et al., 2015), consistency of data analysis procedures becomes important to ensure comparability of results. However, the variety of different models in use

today is quite large, and formulations based on either resistivity or conductivity further complicate the interpretation of results across studies. For example, Revil et al. (2015) used four different approaches to determine characteristic relaxation times from SIP data. As pointed out by Weller et al. (2015), the total chargeability derived from the DD is biased by the shape of the spectrum and the analysed frequency range, while the CC chargeability accounts for all frequencies. Gurin et al. (2015) also mention that the total chargeability from the DD is not comparable to the CC chargeability, and is dependent on the position of the spectral peak and the frequency range covered by the data.
Despite these insights, to our knowledge it has not yet been systematically studied how the total chargeability and the mean relaxation time derived from the CC decomposition (including the Debye and Warburg cases) of CC-type data deviate from the original CC chargeability and CC relaxation time. We here investigate these relationships based on synthetic SIP data sampled from an ideal CC response for a broad range of CC parameter values. The results of our study yield quantitative information on the possible over- or underestimation of chargeability and relaxation time when different models are used to analyse SIP data.

3.2 Methods

3.2.1 The Cole-Cole model

Based on the original formulation of Cole and Cole (1941), the complex conductivity ($\hat{\sigma}$) formulation of the CC model is given as (e.g., Tarasov and Titov, 2013)

$$\hat{\sigma}(\omega) = \sigma_\infty \left(1 - \frac{m}{1 + (j\omega\tau_{(\sigma)})^c}\right), \tag{3.1}$$

with ω denoting the angular frequency, σ_0 and σ_∞ the conductivity in the low- and high-frequency limit, respectively, $m = (\sigma_\infty - \sigma_0)/\sigma_\infty$ the chargeability, j the imaginary unit, $\tau_{(\sigma)}$ the CC relaxation time, and c the CC frequency exponent.
An alternative formulation in terms of complex resistivity ($\hat{\rho}$) was proposed by

Pelton et al. (1978) as

$$\hat{\rho}(\omega) = \rho_0 \left(1 - m \left[1 - \frac{1}{1 + (j\omega\tau_{(\rho)})^c}\right]\right), \tag{3.2}$$

$$m = \frac{\sigma_\infty - \sigma_0}{\sigma_\infty} = \frac{\rho_0 - \rho_\infty}{\rho_0}, \tag{3.3}$$

with $\rho_0 = 1/\sigma_0$ being the DC resistivity, $\rho_\infty = 1/\sigma_\infty$, and $\tau_{(\rho)}$ the CC relaxation time in the resistivity formulation. Importantly, from $\hat{\rho}(\omega) = 1/\hat{\sigma}(\omega)$ it follows that $\tau_{(\sigma)}$ and $\tau_{(\rho)}$ are not identical but related by (Florsch et al., 2012)

$$\tau_{(\sigma)} = \tau_{(\rho)}(1 - m)^{1/c}. \tag{3.4}$$

It is easy to show that the peak frequencies of the imaginary components of $\hat{\sigma}(\omega)$ and $-\hat{\rho}(\omega)$ are related to the relaxation times $\tau_{(\sigma)}$ and $\tau_{(\rho)}$ according to

$$f_{\text{peak}}^{(\sigma'')} = \frac{1}{2\pi\tau_{(\sigma)}} \quad \text{and} \quad f_{\text{peak}}^{(-\rho'')} = \frac{1}{2\pi\tau_{(\rho)}}. \tag{3.5}$$

In combination with eq. (3.4) this implies that $\sigma''(\omega)$ and $-\rho''(\omega)$ peak at different frequencies (with $''$ denoting the imaginary component).

3.2.2 The Cole-Cole decomposition

Based on a broad range of relaxation times spanned by N discretised values τ_k, the discrete form of the CCD in conductivity and resistivity formulation, respectively, can be written as

$$\hat{\sigma}(\omega) = \sigma_\infty \left(1 - \sum_{k=1}^{N} \frac{m_k^{(\sigma)}}{1 + (j\omega\tau_k)^{\tilde{c}}}\right), \tag{3.6}$$

$$\hat{\rho}(\omega) = \rho_0 \left(1 - \sum_{k=1}^{N} m_k^{(\rho)} \left[1 - \frac{1}{1 + (j\omega\tau_k)^{\tilde{c}}}\right]\right), \tag{3.7}$$

where the kernel (assumed elementary relaxation model) is adopted from the CC model in eqs. (3.1) and (3.2), respectively. In eqs. (3.6) and (3.7), $m_k^{(\sigma)}$

and $m_k^{(\rho)}$ denote the chargeability weights at the sampled relaxation times τ_k in conductivity and resistivity formulation, respectively. Usually the relaxation time range is chosen to cover at least the measurement frequency (f) range of the data according to the inverse relationship $\tau = 1/(2\pi f)$ (e.g., Weigand and Kemna, 2016b). The frequency dispersion of the kernel functions in the decompositions is controlled by the chosen fixed value for $\tilde{c}$, with the DD resulting for $\tilde{c} = 1$ and a Warburg decomposition (Revil et al., 2014) resulting for $\tilde{c} = 0.5$. The RTD is given by the distribution $m_k^{(\sigma)}(\tau_k)$ or $m_k^{(\rho)}(\tau_k)$, respectively, from which the following integral parameters can be derived:

- The *total chargeability* $m_{\text{tot}} = \sum_{k=1}^{N} m_k$ (e.g., Nordsiek and Weller, 2008) is the analogon to the chargeability m in eqs. (3.1) and (3.2) when a single CC model is used to describe SIP data. However, in the typical case that the fixed value of $\tilde{c}$ in the decomposition is considerably larger than the c value of a single CC model describing the same SIP data, i.e. if the elementary relaxation model has a much stronger frequency dispersion than the given data, m_{tot} primarily accounts for polarisation within the considered frequency range of the decomposition (spanned by the chosen τ_k values), whereas m also contains significant contributions from outside this range.

- The *median relaxation time* τ_{50} is the relaxation time at which 50 % of the total chargeability is reached (Nordsiek and Weller, 2008; Zisser et al., 2010a).

- The *mean logarithmic relaxation time* τ_{mean} is the chargeability-weighted logarithmic mean value of the RTD (Nordsiek and Weller, 2008):

$$\tau_{\text{mean}} = \exp\left(\frac{\sum_{k=1}^{N} m_k \log(\tau_k)}{\sum_{k=1}^{N} m_k}\right).$$

- The arithmetic mean of the RTD is given by $\tau_a = \frac{\sum_{k=1}^{N} m_k \tau_k}{\sum_{k=1}^{N} m_k}$ (Tong et al., 2004).

Although originally proposed for the DD, the above parameters can be computed analogously from the RTD of the CCD.

3.3 Numerical experiments

Synthetic SIP data were generated assuming a CC model response in resistivity formulation (eq. (3.2)) by systematically varying $\tau_{(\rho)}$ in the range from $1.59 \cdot 10^{-5}$ s to 159.15 s and c from 0.05 to 1. Assumed measurement frequencies were selected using eq. (3.5) such that the polarisation peaks lie within the frequency range covered by the data, with 30 frequencies in total. CCDs of the resulting spectra were performed for the $\tilde{c}$ values 0.3, 0.5, and 1.0, according to eq. (3.7) (resistivity formulation), using the open-source code from Weigand and Kemna (2016b), with 20 relaxation times per decade, and two decades of relaxation times outside the low- and high-frequency limits of the data (222 relaxation times in total, 140 representing the data frequency range).

The input CC chargeability m was compared to the m_{tot} parameters computed from the CCD results. For the relaxation times, the three parameters τ_{mean}, τ_{50}, and τ_a based on the decomposition with $\tilde{c} = 1$ (DD) were related to the input CC parameter $\tau_{(\rho)}$. In addition, τ_{mean} resulting from the CCD for the $\tilde{c}$ values 0.3 and 0.5, respectively, was compared to $\tau_{(\rho)}$. Finally, the analogon of eq. (3.4) for the mean relaxation times $\tau_{\text{mean}}^{(\sigma)}$ and $\tau_{\text{mean}}^{(\rho)}$ obtained from the DD ($\tilde{c} = 1$) in conductivity (eq. (3.6)) and resistivity (eq. (3.7)) formulation, respectively, was evaluated for different input CC chargeability values in terms of $\tau_{\text{mean}}^{(\sigma)} / \tau_{\text{mean}}^{(\rho)}$.

3.4 Results

3.4.1 Chargeability recovery

Original CC chargeabilities m are increasingly underestimated by $m_{\text{tot}}^{(\rho)}$ by up to 80 % for decreasing c values, i.e. decreasing frequency dispersion of the data, and for $\tau_{(\rho)}$ approaching either the low or high relaxation time limit in the decomposition (Fig. 3.1). This behaviour is found for different $\tilde{c}$ values in the range $c < \tilde{c}$.

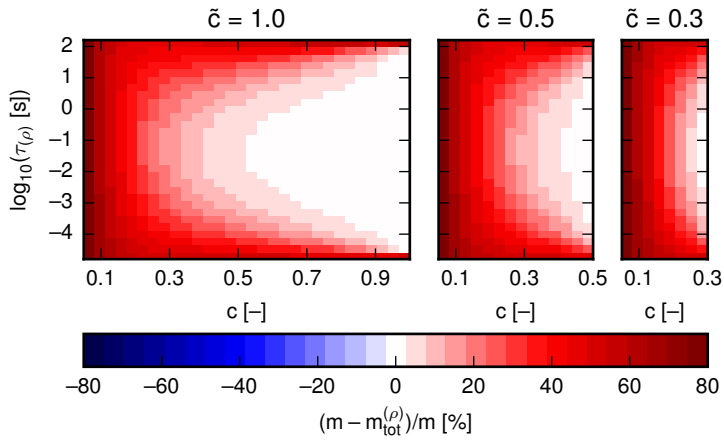

Figure 3.1: Relationship between original CC chargeability m and CCD-derived total chargeability $m_{\mathrm{tot}}^{(\rho)}$ using the indicated values of $\tilde{c}$ for varying values of input CC time constant $\tau_{(\rho)}$ and CC frequency exponent c ($< \tilde{c}$). A fixed value $m = 0.5$ was used in the CC model to generate the SIP data. The resistivity formulations of both the CC model and the DD scheme were used.

3.4.2 Relaxation time recovery

The relaxation times $\tau_{\mathrm{mean}}^{(\rho)}$ and $\tau_{50}^{(\rho)}$ recovered from the CCD (eq. (3.7)) over- or underestimate the original CC relaxation time $\tau_{(\rho)}$ by up to three orders of magnitude for $\tau_{(\rho)}$ approaching the high or low relaxation time limit, respectively, and for decreasing c values (Fig. 3.2). The absolute deviation patterns are similar to those obtained for $m_{\mathrm{tot}}^{(\rho)}$ (Fig. 3.1). The arithmetic mean relaxation time ($\tau_a^{(\rho)}$) shows only a narrow band of CC parameters where the agreement with the original $\tau_{(\rho)}$ value is good; outside this range, deviations up to three orders of magnitude exist.

The deviation of the CCD-derived (eq. (3.7)) relaxation time $\tau_{\mathrm{mean}}^{(\rho)}$ for different values of $\tilde{c}$ exhibits a similar pattern as the corresponding $m_{\mathrm{tot}}^{(\rho)}$ results (Fig. 3.1). The absolute deviation from the original $\tau_{(\rho)}$ value increases with decreasing c ($< \tilde{c}$) and with $\tau_{(\rho)}$ approaching one of the relaxation time limits (Fig. 3.3).

The ratio between the DD-derived relaxation times $\tau_{\mathrm{mean}}^{(\sigma)}$ and $\tau_{\mathrm{mean}}^{(\rho)}$ (using eqs. (3.6) and (3.7), respectively) diverts from the behaviour of the CC counterparts

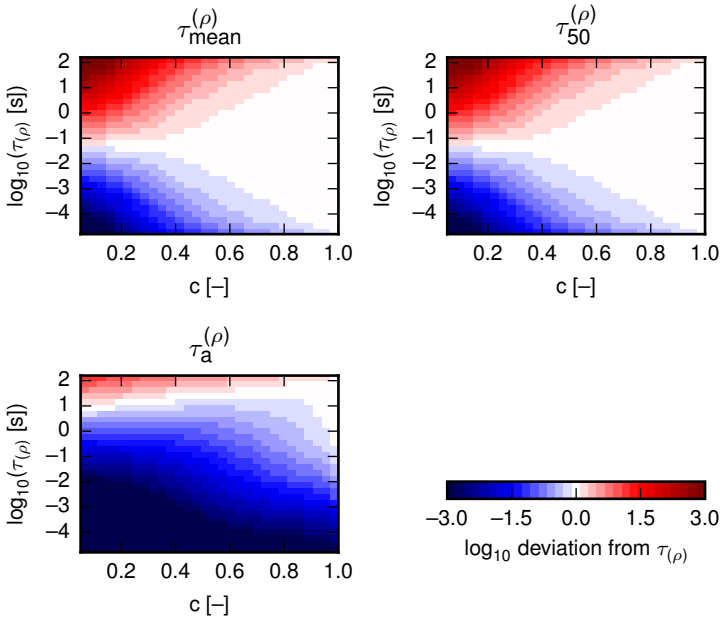

Figure 3.2: Relationship between original CC relaxation time $\tau_{(\rho)}$ and the indicated DD-derived relaxation times for varying values of input CC parameters $(\tau_{(\rho)}, c)$. A fixed value $m = 0.5$ was used for the input CC chargeability. Displayed is the $\log_{10}$-difference between $\tau_{(\rho)}$ and the DD-derived relaxation times. The resistivity formulations of both the CC model and the DD scheme were used.

$\tau_{(\sigma)}$ and $\tau_{(\rho)}$ (described by eq. (3.4)) and shows much less dependence on m (Fig. 3.4). However, the ratio deviates from 1 (the value which indicates perfect agreement between $\tau_{(\sigma)}$ and $\tau_{(\rho)}$) for larger m values and also depends on $\tau_{(\rho)}$, i.e. the position of the peak in the spectrum relative to the analysed frequency range.

3.5 Discussion

The CCD-derived parameters m_{tot}, τ_{mean}, and τ_{50} increasingly diverge from the original CC model parameters with decreasing values of c and for $\tau_{(\rho)}$ approaching the relaxation time limits in the decomposition. This result can be mostly

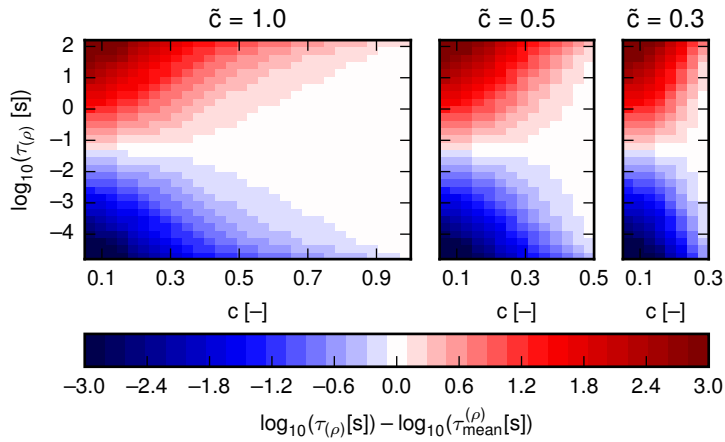

Figure 3.3: Relationship between original CC relaxation time $\tau_{(\rho)}$ and CCD-derived relaxation time $\tau^{(\rho)}_{\text{mean}}$ for different values of $\tilde{c}$. The resistivity formulations of both the CC model and the DD scheme were used.

attributed to the limited frequency range covered by the data, and thus the limited relaxation time range considered in the CCD. Outside the data frequency range the CCD response decreases faster than the original CC response (Fig. 3.5a,c) (if the used kernel has a stronger frequency dispersion than the data), which causes a bias in the inferred mean and median relaxation times towards the center of the RTD. However, a non-zero response outside the data range always remains due to the spectral width of the response of even a single kernel term, which can extend over more than one decade beyond the data frequency limits (increasing with decreasing $\tilde{c}$ value, cf. Figs. 3.5a,c). One decade can also be considered as the approximate theoretical resolution limit below which two peaks in a spectrum can no longer be distinguished (Florsch et al., 2014). Since the deviations of the CCD-derived relaxation times can easily exceed one decade, they must be considered significant and therefore should to be taken into account when analysing SIP data.

As noticeable in the RTD results in Fig. 3.5b, in this example the CCDs for $\tilde{c} = 1$ (DD) and $\tilde{c} = 0.5$ (Warburg decomposition) yield similar chargeability weights at the data frequency edges, which explains the larger spread of the response outside the data frequency range for the $\tilde{c} = 0.5$ case (Fig. 3.5a). However, with

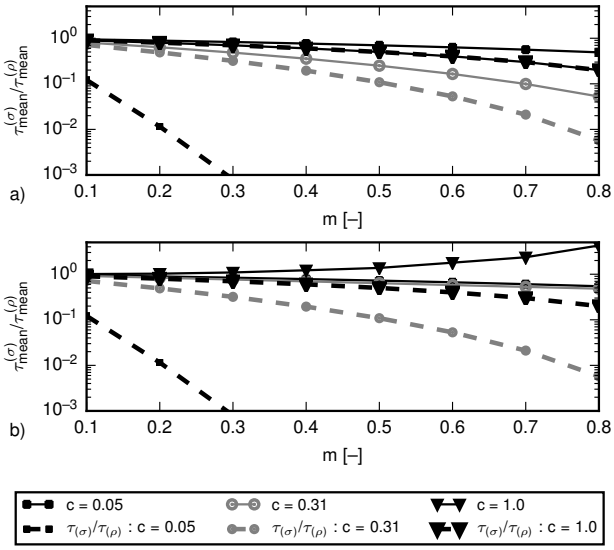

Figure 3.4: Relationship between $\tau^{(\sigma)}_{\text{mean}}$ and $\tau^{(\rho)}_{\text{mean}}$ obtained from DD results in conductivity and resistivity formulation, respectively, for different values of input CC frequency exponent c (0.05, 0.31, 1) and CC relaxation time $\tau_{(\rho)}$ (0.038 s (a), $1.59 \cdot 10^{-5}$ s (b)) plotted as ratio $\tau^{(\sigma)}_{\text{mean}}/\tau^{(\rho)}_{\text{mean}}$ (solid curves). For comparison the relationship between the corresponding CC relaxation times $\tau_{(\sigma)}$ and $\tau_{(\rho)}$ according to eq. (3.4) is shown (dashed curves).

increasing original c value the contribution outside the data frequency range decreases, and thus the underestimation of m is also reduced (Figs. 3.5c,d). In fact for the trivial, but practically irrelevant, case of a decomposition kernel with identical frequency dispersion like the data (i.e. $\tilde{c} = c$), the derived parameters m_{tot}, τ_{mean}, and τ_{50} perfectly resemble the original CC parameters if the spectral peak lies well within the analysed data frequency range (cf. Figs. 3.1 – 3.3).

The observed variation in the reconstruction quality of chargeabilities and relaxation times also influences the relationship between the mean relaxation times derived from the CCD in conductivity and resistivity formulations (Fig. 3.4). We found that $\tau^{(\sigma)}_{\text{mean}}$ and $\tau^{(\rho)}_{\text{mean}}$ agree only within one order of magnitude over the whole range of c values. Therefore, should $\tau^{(\sigma)}_{\text{mean}}$ and $\tau^{(\rho)}_{\text{mean}}$ be compared or jointly used in a study, the discrepancy between both quantities should be taken

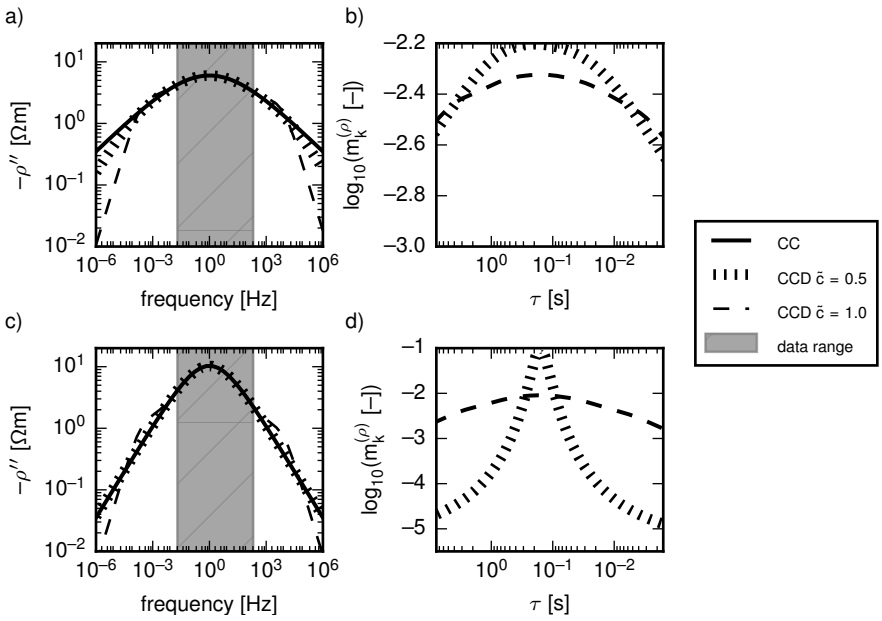

Figure 3.5: Debye versus Warburg decomposition of two CC model responses with different frequency dispersion. Decompositions are based on the shaded frequency range only (a,c). Original CC chargeability is $m = 0.5$ and CC relaxation time $\tau_{(\rho)} = 0.159$ s. a) Responses of input CC model for $c = 0.3$ and CCD results for $\tilde{c} = 1$ ($m_{\text{tot}}^{(\rho)} = 0.30$) and $\tilde{c} = 0.5$ ($m_{\text{tot}}^{(\rho)} = 0.35$). b) RTDs of the CCDs from a). c) Responses of input CC model for $c = 0.5$ and CCD results for $\tilde{c} = 1$ ($m_{\text{tot}}^{(\rho)} = 0.41$) and $\tilde{c} = 0.5$ ($m_{\text{tot}}^{(\rho)} = 0.50$). d) RTDs of the CCDs from c). The resistivity formulations of both the CC model and the DD scheme were used.

into account. However, we again stress that errors can be much larger when CC and CCD-derived parameters are jointly interpreted and their systematic deviations ignored—no matter if conductivity or resistivity formulations are used.

We finally note that the CCD scheme depends on various settings which can have significant influence on the results, with the selected range of relaxation times having the strongest effect. As shown in previous work (Weigand and Kemna, 2016b), the relaxation time range should extend by at least one order of magnitude (better two) to both sides of the data frequency limits. The amount

of regularisation, here a smoothness constraint imposed on the RTD, has from our experience only marginal influence on the derived integral parameters m_{tot} and τ_{mean}. However, regularisation at all is crucial to overcome the inherent ill-posedness of the problem (Florsch et al., 2014).

3.6 Conclusions

In this study we investigated the relationships of chargeability and relaxation time parameters recovered from a spectral decomposition of synthetic CC-type SIP data with the corresponding CC input parameters. As kernel function in the decomposition we considered CC models with different frequency dispersion, including the Debye model and the Warburg model. We found that total chargeability and mean relaxation time derived from the decomposition results can deviate significantly from their CC model counterparts, as well as among each other for different decomposition approaches. Total chargeability was underestimated by up to 80 % and mean relaxation time varied by up to three orders of magnitude compared to the CC input parameters. The deviations depend on the frequency dispersion of the analysed spectrum and the proximity of its peak to the frequency range limits considered in the decomposition. This behaviour is found for all considered kernels (Debye, Warburg, CC), except for the trivial, and practically irrelevant, case of a CC kernel with a frequency dispersion identical to the one of the data. Importantly, our results do not promote the use of a particular kernel function, which should be chosen based on the physics of the underlying polarisation mechanism in the given application.

We conclude that a quantitative comparison of SIP parameters across different studies, or the adoption of parameter relationships from other studies, is only possible on the basis of a consistent, well documented spectral analysis procedure. This is especially important when comparing effective CC parameters with spectral parameters derived from decomposition results. Non-adherence to a consistent analysis procedure can result in severe misinterpretations in the growing field of applications, for example when linking SIP parameters to textural, hydraulic, or (bio)geochemical properties, or when transferring laboratory results to the field.

*T*his chapter is based on the publication:
Weigand, M., Flores Orozco, A., and Kemna, A.: Reconstruction quality of SIP parameters in multi-frequency complex resistivity imaging, Near Surface Geophysics, **15**, 187–199, doi:10.3997/1837-0604.2016050, 2017

CHAPTER 4

Reconstruction quality of SIP parameters in multi-frequency complex resistivity imaging

4.1 Introduction

The induced polarization (IP) method yields images of the complex resistivity (CR) of the subsurface, which provides information about the conduction and polarization properties of the measured soils or rocks. The measurements can be performed at different frequencies (typically below 10 kHz), in the so-called spectral IP (SIP) method, to obtain information about the frequency dependence of the CR.

Due to its simplicity, the Cole-Cole (CC) model is widely used to describe the SIP response (e.g., Pelton et al., 1978; Luo and Zhang, 1998). In recent years the Debye decomposition (DD) approach has been promoted as a robust and flexible alternative to the CC model in (near-surface) geophysical applications (e.g., Lesmes and Morgan, 2001; Nordsiek and Weller, 2008; Florsch et al., 2014; Weigand and Kemna, 2016b).

While initially the IP method has been mainly used for the prospection of ore deposits (e.g., Pelton et al., 1978), over the last 15 years the potential of CR imaging has also been demonstrated for various hydrogeological and environmen-

tal applications, including lithological discrimination (e.g., Kemna et al., 2004; Mwakanyamale et al., 2012), mapping and quantification of hydraulic conductivity (e.g., Kemna et al., 2004; Hördt et al., 2007), monitoring the integrity and performance of reactive barriers (Slater and Binley, 2006), mapping and characterization of contaminant plumes (e.g., Kemna et al., 2004; Flores Orozco et al., 2012a), monitoring of sulphide mineral precipitation (e.g., Williams et al., 2009; Flores Orozco et al., 2013), as well as monitoring of micro-particle injection and movement (Flores Orozco et al., 2015). These field-scale applications have also prompted the development of models describing the link between the CR response and lithologic, textural, hydraulic, or geochemical soil/rock properties (see, e.g., Slater (2007); Kemna et al. (2012) and references therein). The potential of the SIP method has also been demonstrated for applications in the emerging field of biogeophysics (e.g., Atekwana and Slater, 2009). Examples include the detection of alterations at mineral-fluid interfaces due to microbial growth (e.g., Abdel Aal et al., 2004) or biostimulated mineral precipitation (e.g., Williams et al., 2009; Flores Orozco et al., 2011), detection of biofilm formation (e.g., Ntarlagiannis et al., 2005; Davis et al., 2006), and characterization of tree roots (e.g., Zanetti et al., 2011) or crop roots (Weigand and Kemna, 2016a). The variety of these studies demonstrates the growing interest in the application of CR (or SIP) imaging.

It is well known that electrical images are characterized by spatially variable image resolution (e.g., Oldenburg and Li, 1999; Friedel, 2003; Binley and Kemna, 2005), which needs to be taken into account in the interpretation of the resulting images. Day-Lewis et al. (2005) found a spatially variable reconstruction quality of water content determined from electrical measurements, with an increasing inaccuracy of the inferred water content estimates with decreasing image resolution. This resolution-related phenomenon was referred to by the authors as 'correlation loss', as it can be considered as loss of information in the resistivity images due to poor resolution. Kemna (2000) demonstrated that the analysis of the cumulated sensitivity can provide insight into the variable image resolution. Nguyen et al. (2009) found, for regions with cumulated sensitivity below some threshold value, an increase in the correlation loss for the mass fraction between fresh water and seawater reconstructed from electrical resistivity imaging results. However, even if the problem of correlation loss has been pointed out

for conventional resistivity imaging, it has not yet been addressed for single- or multi-frequency (spectral) IP imaging. The assessment of correlation loss is critical for the desired application of petrophysical models established on the basis of laboratory studies to imaging results obtained in the field.
We here investigate, by means of numerical simulations, the reconstruction quality of CC model and DD parameters recovered from multi-frequency CR images. We consider a standard dipole-dipole surface survey over a homogeneous, non-polarizable half-space containing a two-dimensional polarizable anomaly, whose vertical position is systematically varied to investigate its reconstruction in areas with different sensitivity in the inversion. Hereafter, we refer to reconstruction quality as the deviation of the recovered model parameters from their original values. We analyze and compare the reconstruction quality of single- and multi-frequency (spectral) IP parameters as a function of cumulated sensitivity. We also investigate the impact of data noise on the reconstruction quality, considering that data quantification is critical for quantitative IP imaging applications (Flores Orozco et al., 2012b; Kemna et al., 2012).

4.2 Methods

4.2.1 Forward modeling and inversion

Synthetic data, i.e., complex transfer impedances, are computed using the 2.5D finite-element modeling code CRMod (Kemna, 2000). CRMod solves the underlying 2.5D forward problem (Helmholtz equation) for a given 2D CR distribution. For details of the implementation, we refer to Kemna (2000). Data noise is added from a normally distributed ensemble of random numbers. In order to provide comparable results, all simulations are conducted using the same ensemble of random numbers, scaled by previously chosen standard deviations.
The noise-contaminated data are inverted using CRTomo (Kemna, 2000), a smoothness-constraint, Gauss-Newton-type inversion scheme. The data are weighted in the inversion by individual errors (see Appendix 4.A).
Image appraisal is done using the L_1- and L_2-normed cumulated sensitivity (coverage) and the diagonal entries of the model resolution matrix (see Appendix 4.B). Throughout this study normalized cumulative, error-weighted sensitivities

(hereafter simply referred to as sensitivity) are presented, as they offer better comparability.

4.2.2 Cole-Cole model

The frequency-dependent electrical properties of soils and rocks are often described by the empirical Cole-Cole (CC) model (Cole and Cole, 1941). In terms of CR, $\rho(\omega)$, with angular frequency ω, the CC model can be expressed after Pelton et al. (1978) as

$$\rho(\omega) = \rho_0 \left(1 - m \left[1 - \frac{1}{1 + (j\omega\tau)^c}\right]\right), \tag{4.1}$$

where ρ_0 is the DC resistivity (low-frequency asymptote), m the CC chargeability, τ the CC relaxation time, c the CC exponent, and j the imaginary unit. The parameter ρ_0 defines the amplitude of the magnitude spectrum ($|\rho(\omega)|$), while the parameter m determines the amplitude of the phase spectrum ($\phi(\omega)$). The parameter c describes the asymptotic slope of the symmetric phase spectrum (in log-log representation), i.e., the degree of frequency dispersion, and the parameter τ is inversely related to the peak frequency of the imaginary part of the resistivity, $\omega_{\max,\,\rho''}$, by $\omega_{\max,\,\rho''} = 1/\tau$. Values of m and c range from 0 to 1, while τ values may span several orders of magnitude (e.g., Pelton et al., 1978; Vanhala, 1997; Luo and Zhang, 1998).

4.2.3 Debye decomposition

The Debye decomposition (DD) scheme describes the CR spectrum using a superposition of a large number of Debye polarization terms (e.g., Nordsiek and Weller, 2008):

$$\rho(\omega) = \rho_{0,\mathrm{DD}} \left(1 - \sum_{k=1}^{N} m_k \left[1 - \frac{1}{1 + j\omega\tau_k}\right]\right), \tag{4.2}$$

where N is the number of relaxation times (i.e., Debye polarization terms) used for the superposition, m_k is the k-th chargeability corresponding to the k-th relaxation time τ_k, and $\rho_{0,\mathrm{DD}}$ is the DC resistivity (as obtained from the DD). The relaxation times are chosen to cover the frequency range spanned by the

data according to the inverse relationship $\tau = 1/\omega_{\max,\,\rho''}$ (e.g., Weigand and Kemna, 2016b). For each frequency decade 20 relaxation times are used, and the relaxation time range is extended by two orders of magnitude at each end of the covered frequency range, as suggested by Weigand and Kemna (2016b,c). The resulting distribution of relaxation times $m_k(\tau_k)$ is called the relaxation time distribution, from which parameters similar to the CC parameters are derived:

- The *total chargeability*, $m_{\text{tot}} = \sum_{k=1}^{N} m_k$, provides an analog to the CC chargeability m. However, m_{tot} only accounts for polarization contributions within the data frequency range due to the much narrower spectral shape of the Debye response compared to typical CC responses (with $c < 1$).

- The *mean logarithmic relaxation time*, τ_{mean}, denotes the chargeability-weighted logarithmic mean value of the DD relaxation times (Nordsiek and Weller, 2008):
  $\tau_{\text{mean}} = \exp\left(\frac{\sum_{k=1}^{N} m_k \log(\tau_k)}{\sum_{k=1}^{N} m_k}\right)$.

4.3 Design of numerical experiments

The numerical experiments are conducted on a model domain of 80 m by 17 m (as depicted in Fig. 4.1a), with the underlying finite-element mesh consisting of 3128 rectangular cells, each composed of four triangular elements. Forty electrodes are located at the surface with an equidistant spacing of 1 m. Only the quadratic fine-element cells below the electrodes are used for the analysis, and they are equally sized with an edge length of 0.5 m. To increase modeling accuracy, additional elements with exponentially increasing width are used at both sides of the grid. Simulations are performed using a dipole-dipole measurement scheme composed of skip-0,1,2,3 configurations, resulting in 1944 measurements. The 'skip-number' refers to the dipole length, indicating the number of electrodes 'skipped' between the two current electrodes and the two voltage electrodes, respectively. For instance, the skip-0 configuration uses adjacent electrodes for current injection and voltage measurement. Resistance

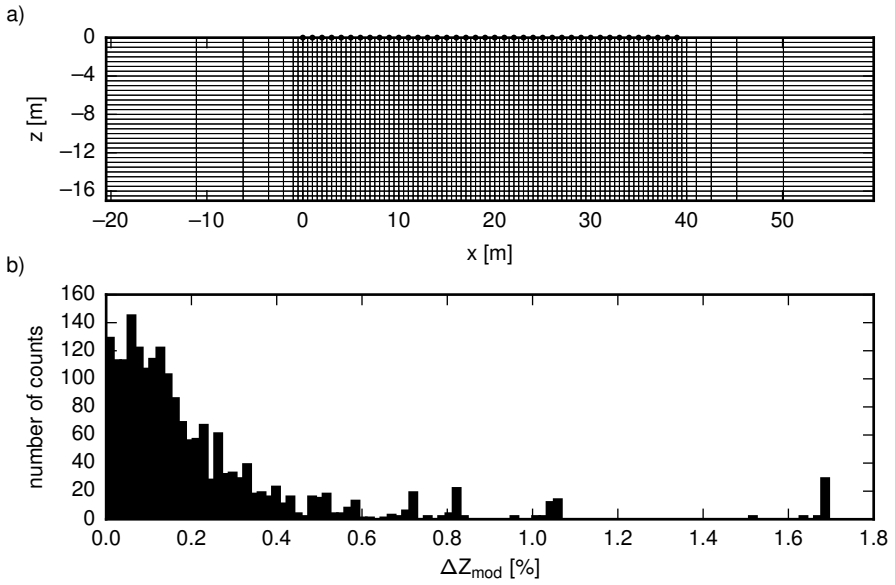

Figure 4.1: a) Finite-element grid used for the forward modeling. b) Distribution of percentage errors of modelled impedance magnitude values (ΔZ_{mod}) for all used measurement configurations, determined for a homogeneous resistivity model (half-space).

(impedance magnitude) modeling errors for a homogeneous half-space lie below 2% for all measurement configurations (Fig. 4.1b).

The surface electrode configuration used in this study exhibits a cumulative sensitivity distribution that decreases monotonically with depth (Fig. 4.2b). Thus, an anomaly placed at different depths in the subsurface (Fig. 4.2a) is associated with different cumulative sensitivity. The CR model used to compute synthetic data is defined as a homogeneous background ($|\rho| = 100\ \Omega\text{m}, \phi = 0$ mrad) containing an anomalous body (4 by 4 model cells, corresponding to a size of 2 m by 2 m) with varying resistivity magnitude and phase values. Since the spatial extension of the anomaly is relatively small (given the modeling domain and the used measurement configurations), and since anomalous resistivity magnitude values were only varied within one order of magnitude relative to the background value, the current density (and sensitivity) distributions do not differ significantly from the distribution for a homogeneous model. Therefore,

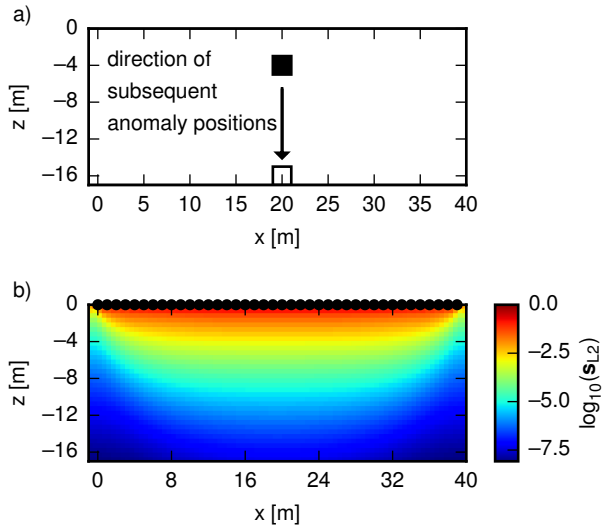

Figure 4.2: Model used for the numerical simulations (a) and corresponding (L_2-normed) cumulated sensitivity distribution (normalized to 1) (b). The model consists of a homogeneous half-space ($|\rho| = 100\,\Omega$m, $\phi = 0$ mrad) with an embedded polarizable anomaly (indicated by the black rectangle), the depth position of which is varied in the simulations. The positions of the surface electrodes are indicated by black dots. Outer elements of the modeling grid are not shown (cf. Fig. 4.1a).

we use the sensitivity values of the homogeneous model in the analysis of the reconstruction quality of the CC parameters for models containing the polarizable anomaly. However, the diagonal entries of the model resolution matrix, $\underline{\underline{R}}$ (see Appendix 4.B), are computed after the final iteration of the inversion process. As the final values of the regularization parameter λ differ for the different anomaly locations, also the computed diagonal entries of $\underline{\underline{R}}$ vary on this account (cf. Eq. (4.10)). Although this makes a quantitative comparison for the different anomaly locations difficult, the diagonal entries of $\underline{\underline{R}}$ are presented in the following sections to show their general behavior in comparison with cumulated sensitivity.

4.3.1 Single-frequency reconstruction

In a first step we investigate the reconstruction quality of resistivity magnitude and phase values in the region of the anomaly, i.e., the deviation between original and recovered values, for a single-frequency data set. In the single-frequency studies we investigate three scenarios: (i) 10 Ωm, −30 mrad (conductive, polarizable anomaly); (ii) 100 Ωm, −30 mrad (polarizable anomaly); and (iii) 1000 Ωm, −30 mrad (resistive, polarizable anomaly). Figure 4.3 shows exemplary inversion results for the second scenario for two depths of the anomaly. A small, stabilizing noise component of 0.1% Gaussian noise is added to the impedance magnitude data, and Gaussian noise with a standard deviation of 0.5 mrad is added to the impedance phase data. The error estimate in the inversion assumes 3% relative and 0.001 Ω absolute error for the impedance magnitude (resistance), and 1% relative and 0.5 mrad absolute error for the impedance phase.

The inverted resistivity magnitude and phase values of the anomaly pixels (i.e., model cells within the anomaly region) are averaged (arithmetic mean of log magnitude and phase, respectively), and the deviations from the original values are calculated as a measure of reconstruction quality. These deviations are analyzed against the averaged (arithmetic mean of log values) cumulative sensitivity values ($\underline{s}_{\mathrm{L1}}$ and $\underline{s}_{\mathrm{L2}}$), as well as against the diagonal entries of the model resolution matrix ($\mathrm{diag}(\underline{\underline{R}})$), for the different anomaly locations.

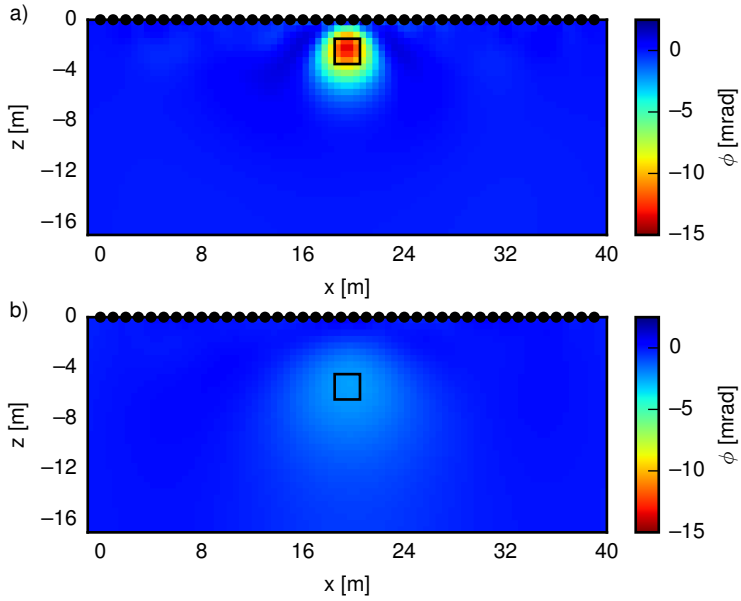

Figure 4.3: Resistivity phase imaging results for the model shown in Figure 4.2a for two different depths of the polarizable (−30 mrad) anomaly. The position of the anomaly is marked by the black rectangle.

4.3.2 Multi-frequency reconstruction

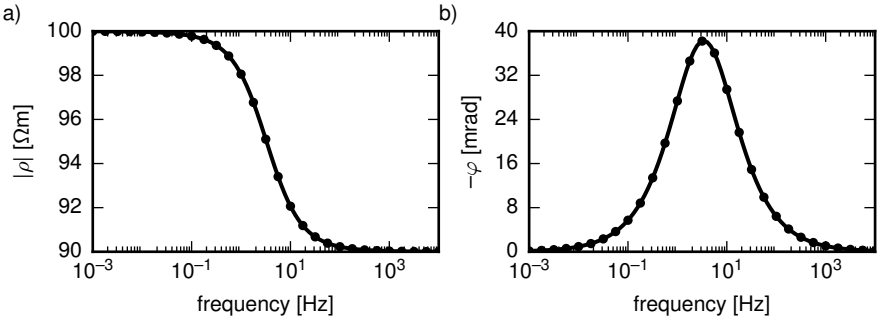

Figure 4.4: Complex resistivity magnitude (a) and phase (b) CC model response of the polarizable anomaly simulated in this study (for CC parameters $\rho_0 = 100\,\Omega\text{m}$, $m = 0.1$, $\tau = 0.049\,\text{s}$, $c = 0.8$). The dots indicate the considered measurement frequencies.

The next step in our study is to examine the reconstruction quality of the CC model parameters inferred from multi-frequency imaging results. The original CC parameters of the anomaly are chosen as $\rho_0 = 100\,\Omega\text{m}, m = 0.1, \tau = 0.049\,\text{s}$, and $c = 0.8$, so that the peak of the phase response occurs in the center of the considered frequency range (at approximately 3 Hz). Based on these parameters, impedance measurements at 29 frequencies between 10^{-3} Hz and 10^4 Hz (equally spaced on a logarithmic scale) are numerically computed, as illustrated in Figure 4.4. The model background is set to 100 Ωm and 0 mrad for all frequencies. CR models are created for each of the 29 frequencies and used to model synthetic data sets, which are then independently inverted. Following this, a CC model is fitted to the CR spectra extracted from the multi-frequency images for each of the anomaly pixels (hereafter referred to as intrinsic spectra). Likewise the DD is applied to the obtained intrinsic spectra. In a last step, the arithmetic mean values of the resultant spectral model parameters $(\log(\rho_0), m, \log(\tau), m_{\text{tot}}, \log(\tau_{\text{mean}}))$ are computed. Thus, for each vertical anomaly position, one set of averaged spectral model parameters is obtained.

In order to assess the reconstruction quality, the deviations between the recovered and original values are analyzed against the $\underline{s}_{\text{L1}}$, $\underline{s}_{\text{L2}}$, and $\text{diag}(\underline{\overline{R}})$ values, averaged (arithmetic mean of log values) over the anomaly pixels. The following parameters denote the percentage deviation of the recovered parameters from the original CC parameters, representing a measure of reconstruction quality:

$$\eta_{\text{m}} = \frac{m_{\text{orig}} - m}{m_{\text{orig}}} \cdot 100, \tag{4.3}$$

$$\eta_{\text{mtot}} = \frac{m_{\text{orig}} - m_{\text{tot}}}{m_{\text{orig}}} \cdot 100, \tag{4.4}$$

$$\eta_{\tau} = \frac{\tau_{\text{orig}} - \tau}{\tau_{\text{orig}}} \cdot 100, \tag{4.5}$$

$$\eta_{\tau,\text{mean}} = \frac{\tau_{\text{orig}} - \tau_{\text{mean}}}{\tau_{\text{orig}}} \cdot 100, \tag{4.6}$$

$$\eta_{\text{c}} = \frac{c_{\text{orig}} - c}{c_{\text{orig}}} \cdot 100, \tag{4.7}$$

with the subscript $_{\text{orig}}$ denoting the original CC parameters used to generate the

CR response in the forward model. The other parameters are recovered from the CC fit and the DD of the imaging results.
A stabilizing noise component of 0.1% Gaussian noise is added to the impedance magnitude data, and an impedance magnitude (resistance) error estimate comprising 3% relative error and 0.001 Ω absolute error is used in the inversions to account for numerical errors in the forward solution. Gaussian noise of different levels (0.05 mrad, 0.1 mrad, and 0.5 mrad) is added to the impedance phase data sets to investigate the effects of data noise and error estimation on the reconstruction of the CC and DD parameters. Here, at first, phase error estimates equal to the actual noise level in the phase data are assumed in the inversion, thus adequately accounting for the added noise. In subsequent inversions the actual phase noise level is deliberately underestimated by up to one order of magnitude to investigate the effect of over-fitting on the reconstruction quality.
In a final numerical simulation we investigate the quality of reconstructed τ and τ_{mean} values for different degrees of frequency dispersion (i.e., different c values) and different spectral positions of the phase peak (i.e., different τ values) in the original CC model response of the anomaly.

4.4 Results

4.4.1 Single-frequency results

The reconstruction quality of resistivity magnitude decreases with decreasing sensitivity for anomalies with a contrasting magnitude value, compared to the background magnitude (Figs. 4.5a,c). The contrast between anomaly and background values, i.e., whether the anomaly is conductive or resistive, determines the sign of the deviation, for over- or underestimated values. If no contrast is present in the magnitude, reconstruction quality is independent of sensitivity (Fig. 4.5b). The phase reconstruction curves do not show such a dependency on the magnitude contrast (Figs. 4.5d-f). The three cases, referring to the same value of the phase anomaly ($\phi = -30$ mrad), reveal a monotonic decrease in reconstruction quality with decreasing sensitivity ($s_{\text{L1}}, s_{\text{L2}}$) and resolution ($\text{diag}(\underline{\underline{R}})$) values. Reconstruction quality curves in Figure 4.5 also reveal

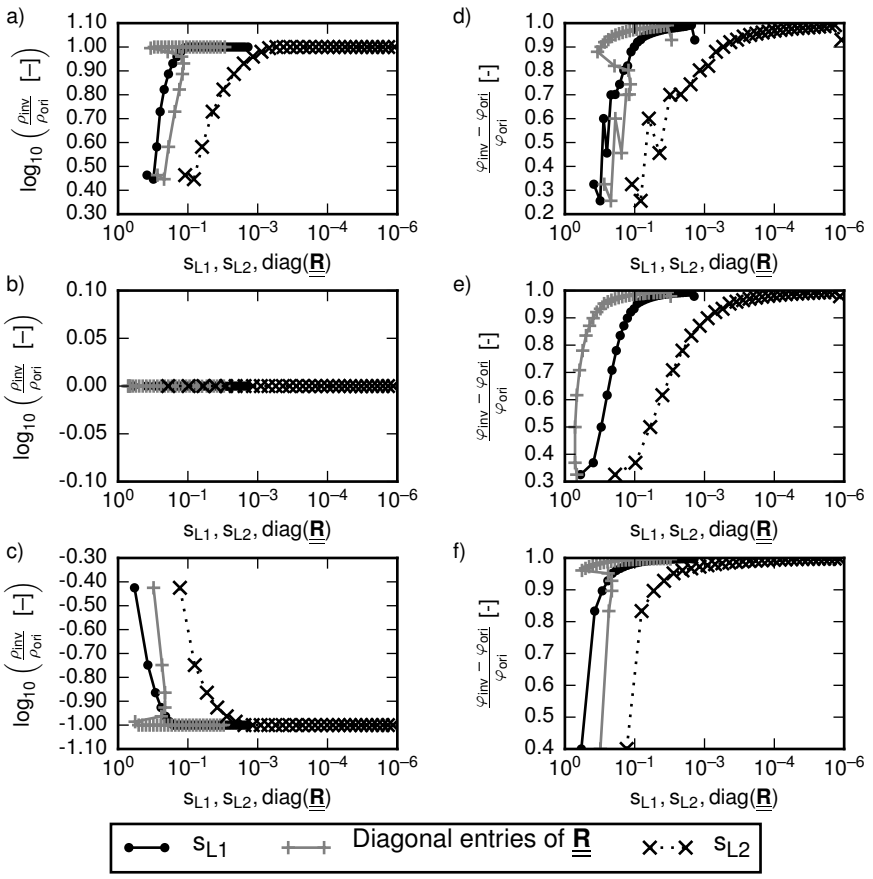

Figure 4.5: Deviation between recovered and original resistivity magnitude (a, b, c) and phase (d, e, f) values in the anomaly region. Results are presented for different depth positions of the anomaly (indicated by the markers along each curve), plotted as a function of L_1 cumulated sensitivity (s_{L1}), L_2 cumulated sensitivity (s_{L2}), and resolution (i.e., diagonal entry of model resolution matrix) in the anomaly region. Results are shown for three scenarios: a conductive, polarizable anomaly (model values 10 Ωm, −30 mrad) (a, d); a solely polarizable anomaly (model values 100 Ω, −30 mrad) (b, e; cf. Fig. 4.3); and a resistive, polarizable anomaly (model values 1000 Ωm, −30 mrad) (c, f), each embedded in a homogeneous background (model values 100 Ωm, 0 mrad). The reconstructed values are extracted from the corresponding (single-frequency) complex resistivity imaging results, and averaged over the 16 model cells that comprise the anomaly. A phase noise level of 0.5 mrad is assumed in the inversion.

a slightly different behavior depending on whether the anomaly is conductive or resistive. In particular, for the same depth position of the anomaly a smaller deviation of the reconstructed phase values is observed in case of a conductive anomaly (Fig. 4.5d) in comparison to a resistive anomaly (Fig. 4.5f). This indicates an improved phase reconstruction capability in conductive regions, where current flow is focused. Furthermore, Figure 4.5 reveals a similar qualitative behavior with respect to sensitivity (for both L_1 and L_2 curves) and resolution (diag($\underline{R}$)), demonstrating that (cumulated) sensitivity is an adequate proxy to evaluate image resolution.

4.4.2 Multi-frequency results

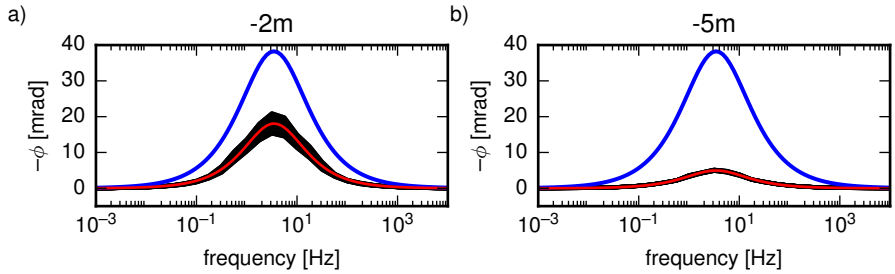

Figure 4.6: Recovered phase values for all 16 elements (black lines), the corresponding original spectral response (blue curve), and the response of the fitted CC model (red curve) in the anomaly region for 2 m depth (a) and 5 m depth (b) of the anomaly (referring to the top boundary of the anomaly) (cf. Fig. 4.3).

Figure 4.6 shows the recovered spectral phase response for the anomaly located at 2 m and 5 m depth, respectively, and, thus, associated with different sensitivity (resolution). Both reconstructed spectra exhibit an underestimation of the absolute phase values in comparison with the original values. This underestimation is larger for the deeper anomaly position (Fig. 4.6b) associated with a lower sensitivity. An additional effect caused by the underestimated phase values is the change of the slope of the recovered phase spectrum for different depth positions, which affects the fitting of the CC exponent c (describing the

degree of dispersion). This spectral distortion effect is more pronounced for the deeper anomaly position (Fig. 4.6b), associated with regions of lower sensitivity. Intrinsic spectra recovered for the shallower anomaly position exhibit a larger spread within the anomaly (Fig. 4.6a, black curves), indicating a stronger variation of the sensitivities in the anomaly region.

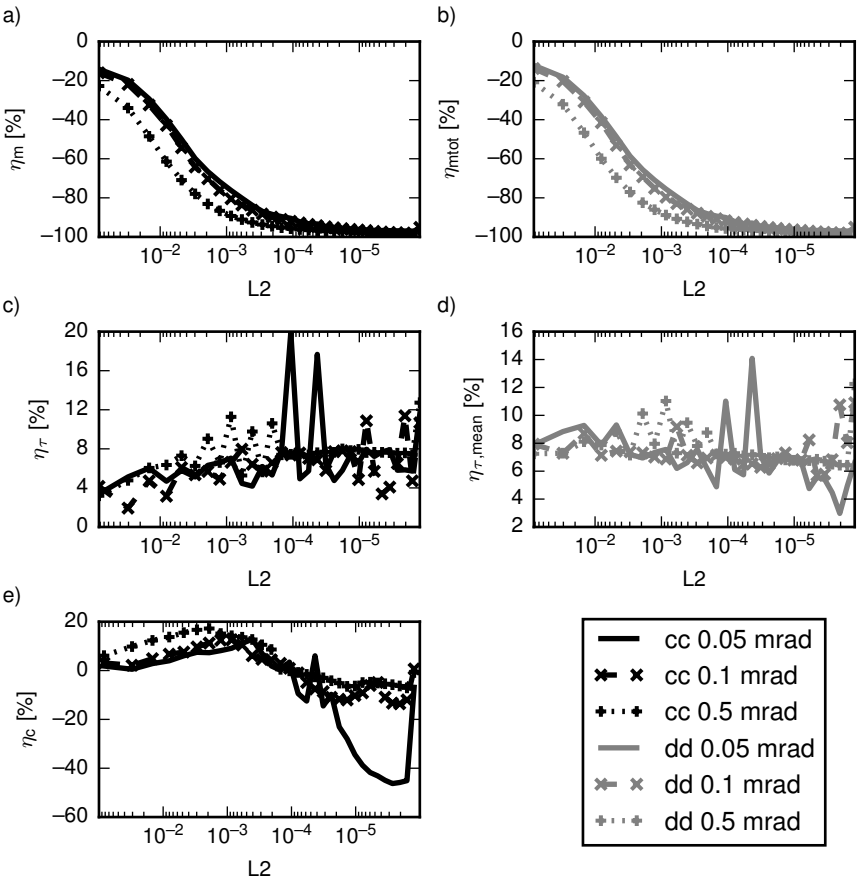

Figure 4.7: Reconstruction quality parameters for recovered CC and DD parameters of the anomaly pixels, plotted versus decreasing sensitivity values ('L_2'), i.e., increasing depth locations of the anomaly. a) η_m, b) η_{mtot}, c) η_τ, d) $\eta_{\tau,mean}$, e) η_c. Simulations were performed for a phase data noise level of 0.05, 0.1, and 0.5 mrad, respectively. The phase error estimate in the inversions was chosen accordingly.

Reconstruction quality of m decreases with decreasing sensitivity (Fig. 4.7a), similar to the behavior observed for the reconstruction of the (single-frequency) phase value (cf. Fig. 4.5). The reconstruction curves for m also reveal a dependence on the level of noise in the phase data, with larger deviations between recovered and original values for higher noise levels and thus lower contrast in the inversion results. The DD parameter m_{tot} (Fig. 4.7b) shows a reconstruction behavior similar to the one of m (Fig. 4.7a).

The reconstruction quality of c shows a dependence on sensitivity, but not a monotonic one (Fig. 4.7e). While m and m_{tot} are underestimated over the whole sensitivity range (Fig. 4.7a,b), c reconstruction varies widely and shows smaller deviations for more noisy data and thus a lower degree of fitting (Fig. 4.7e).

The reconstruction quality of τ and τ_{mean} differs significantly from that for m, m_{tot}, and c, as the reconstruction quality curves of the relaxation times show no systematic dependence on sensitivity. However, small noise levels of 0.05 mrad lead to some erratic behavior for low sensitivity values below 10^{-4} (normalized L_2 value), showing variations up to 20 % (Fig. 4.7c,d).

If the level of phase data noise is underestimated in the inversion, m and m_{tot} reconstruction curves are shifted to smaller sensitivities, that is for the same sensitivity (depth) the recovered contrast is slightly increased when noise is underestimated (on the account of over-fitting the data) (Figs. 4.8a,b). The reconstruction curves of τ and τ_{mean} become more erratic for increasing underestimation of the data noise level (Fig. 4.8c,d), and also c reconstruction quality decreases (Fig. 4.8e), especially at low sensitivities. However, reconstructed relaxation time values stay within 60% of the original τ value for a ten-fold underestimation of the actual phase data noise level in the inversion.

The reconstruction quality of CC relaxation time τ decreases for decreasing c values, i.e., decreasing frequency dependence in the spectrum (Figs. 4.9a,c). Corresponding recovered DD relaxation times τ_{mean}, however, stay within 16% of the original τ values (Fig. 4.9e). For different positions of the phase peak, i.e., different original τ values (Fig. 4.9b), reconstruction quality of CC relaxation time does vary only within 14% (Fig. 4.9d). Corresponding DD relaxation times τ_{mean} show deviations from the original τ values that increase enormously at lower sensitivities (Fig. 4.9f), which is an effect of the strong dependence of the DD results on the position of the spectral response in the analyzed frequency

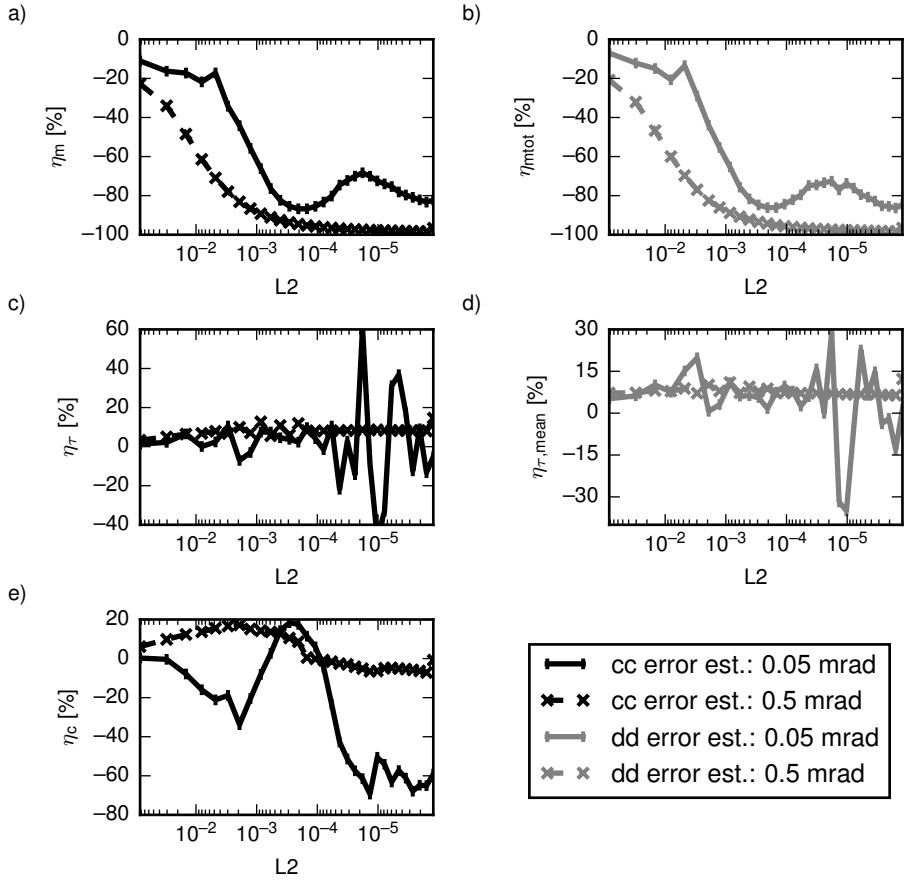

Figure 4.8: Reconstruction quality parameters for recovered CC and DD parameters of the anomaly pixels, plotted versus decreasing sensitivity values ('L_2'), i.e., increasing depth locations of the anomaly. a) η_{m}, b) η_{mtot}, c) η_τ, d) $\eta_{\tau,\mathrm{mean}}$, e) η_{c}. Results are averaged over the 16 pixels of the anomaly. Simulations were performed for a phase data noise level of 0.5 mrad and two different phase error estimates used in the inversions, corresponding to an underestimation of noise (0.05 mrad error) and the correct estimation of noise (0.5 mrad error).

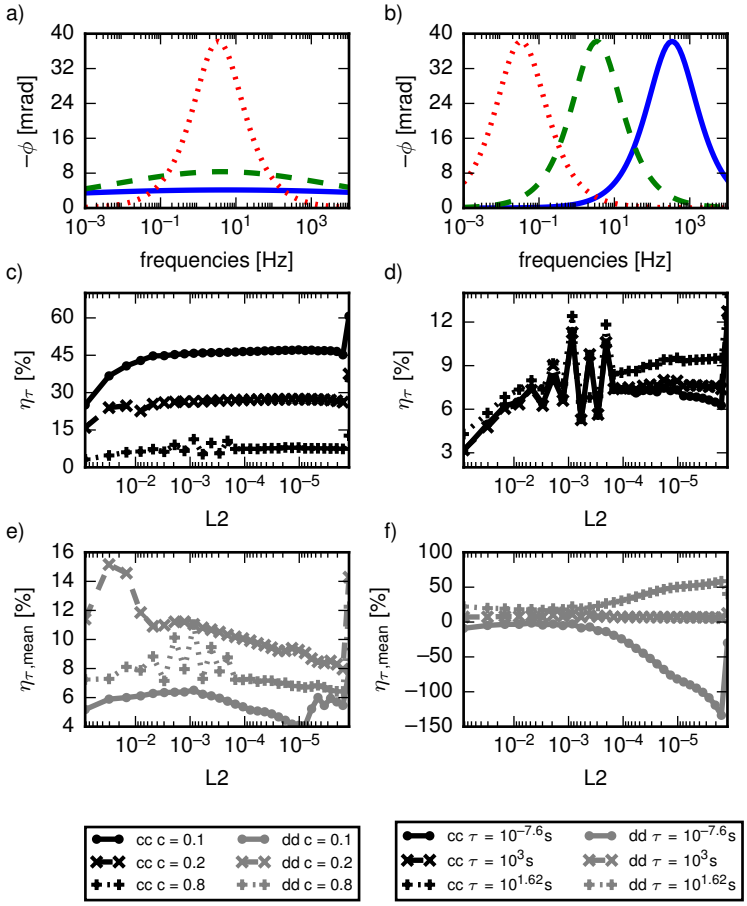

Figure 4.9: a) CC model phase responses for different values of c ($c = 0.1$: blue, $c = 0.2$: green, $c = 0.8$: red) with $\tau = 0.049\,\mathrm{s}$, $\rho_0 = 100\,\Omega\mathrm{m}$, and $m = 0.1$. b) CC model phase responses for different values of τ ($\tau = 5\,\mathrm{s}$: red, $\tau = 0.049\,\mathrm{s}$: green, $\tau = 5 \cdot 10^{-4}\mathrm{s}$: blue) with $c = 0.8$, $\rho_0 = 100\,\Omega\mathrm{m}$, and $m = 0.1$. c-f) Reconstruction quality parameters for recovered CC and DD relaxation time parameters of the anomaly pixels for different original CC parameter values of c and τ, respectively, plotted versus decreasing sensitivity values ('L_2'), i.e., increasing depth locations of the anomaly. c,d) η_τ; e,f) $\eta_{\tau,\mathrm{mean}}$.

range (Weigand and Kemna, 2016b).

4.5 Discussion

4.5.1 Reconstruction quality of resistivity and polarization parameters

To understand the reconstruction behavior of SIP parameters it is important to also understand the reconstruction quality of the single-frequency magnitude and phase values. Pelton et al. (1978) already noted that the parameter m is primarily sensitive to the phase angle ϕ, and thus it is not surprising that the reconstruction curves (i.e., the reconstruction quality as a function of cumulated sensitivity) of m and ϕ are similar in their shape (cf. Figs. 4.5e and 4.7a,b). We explain the loss of reconstruction quality of ϕ (and m, m_{tot}) with the (non-linearly) decreasing signal-to-noise ratio (SNR) with deeper anomaly position (cf. Fig. 4.2b). This effect is well known for DC resistivity imaging. Although the loss of sensitivity and resolution with depth is inherent to the method and thus inevitable, a careful design of the electrode layout and measurement configurations may help to mitigate this effect. This also holds for cross-borehole imaging applications, where the loss of sensitivity/resolution is related to the distance to the boreholes. Another factor contributing to the SNR is the given phase contrast of the anomaly relative to the background. An anomaly with a large phase contrast will be better resolved than one with only a weak contrast.

As observed in Figures 4.7 and 4.8, data error quantification and its adequate consideration in the inversion play a significant role in the quantitative imaging of CC parameters. The addition of noise to the phase data, or the inversion of the data to an inadequate noise level, affects the reconstruction curve for ϕ (and m, m_{tot}). We explain this as the result of over/under-fitting the data in the inversion. While underfitting the data can produce larger contrasts in the inversion results (Figs. 4.8a,b), it also introduces artifacts in the images and amplifies noise components. This comes into effect for the reconstruction of relaxation times (Figs. 4.8c,d).

4.5.2 Reconstruction quality of spectral parameters

Regarding the shape of the spectral response, the c reconstruction curve can be divided into two parts: For high sensitivities the c values are correctly (or slightly over-) estimated, and below a certain sensitivity threshold value they are underestimated (Fig. 4.7e). To understand this pattern, it is necessary to consider the reconstructed phase values in the different regions of the spectrum. As previously discussed, due to variations in the SNR, large (absolute) phase values that form the phase peak will be better reconstructed than smaller (absolute) phase values at the spectral edges of the CC model response (Fig. 4.6). We explain the behavior observed in Figure 4.7e as follows: In high-sensitivity regions, the loss of reconstruction quality for the edge values dominates over the loss of reconstruction quality for the peak values (see changing slope of the curve in Fig. 4.5e), resulting in steeper slopes of the recovered spectral response and thus an overestimation of c. With decreasing sensitivity, at some point the loss of reconstruction quality for the peak values will lead to a flattened spectral response with c values smaller than the original ones. This behavior can be expected, with certain variations due to changing SNR, for different anomaly parameterizations, phase error estimations, and noise levels. However, as observed in Figure 4.8e an underestimation of data noise level leads to an unpredictable reconstruction behavior of c, possibly due to stronger influence of noise components in inversion. This in turn has a direct influence on the slope of the intrinsic spectra, and correspondingly on the parameter c. The reconstruction of the c parameter, and to a certain extent the chargeabilities m and m_{tot}, can possibly be improved by using a frequency regularization scheme in the inversion (e.g., Kemna et al., 2014; Günther and Martin, 2016): If a smoothness of suitable strength is imposed on the spectrum, then its original form can be retained over a larger SNR bandwidth, i.e., down to larger depths.

The reconstruction quality of the CC relaxation time τ and the DD relaxation time τ_{mean} differ significantly from the results for ρ_0, m, m_{tot}, and c, revealing a stable, i.e., sensitivity-independent, reconstruction quality over a large range of sensitivity values. This can be explained by the direct relation of τ to the frequency position of the phase peak, which is more robust to data noise, error underestimation, and small sensitivities than the other features of the spectral

CR response used to determine ρ_0, m, m_{tot}, and c. The relaxation time is (inversely) proportional to the peak frequency, i.e., the frequency at which the strongest polarization response is observed (e.g., Pelton et al., 1978). Hence, this parameter is only dependent on the position of the peak in the spectrum, but not on the resistivity or phase values. Therefore, under/over-fitting in the inversion should not impact the reconstruction quality of τ and τ_{mean}, as long as the peak in the spectrum is not strongly distorted (cf. Fig. 4.6). Also, the interpretation of τ and τ_{mean} results will not be influenced (to a certain degree) by the varying image resolution or different noise levels, as would be the other parameters (cf. Fig. 4.7). This result is extremely important for SIP imaging applications as it implies that the recovered relaxation time values will be less dependent on the electrode configuration of the survey and of similar quality over a large sensitivity (and thus image) region. Merely the underestimation of data noise has a larger effects on recovered relaxation times (Fig. 4.8c,d). However, the observed 60% deviation are still relative small, compared to the overall dynamics of multiple magnitudes that can be observed for relaxation times (e.g., Pelton et al., 1978).

Quantitative imaging of CC parameters may play a significant role in the characterization of processes relevant in hydrogeological and environmental studies. However, petrophysical relationships are still required to derive information of interest from CC/DD parameters. For instance, recent studies have demonstrated a strong correlation between hydraulic conductivity (or permeability), governing groundwater flow, and the length scale at which the polarization takes place, i.e., a characteristic relaxation time τ (e.g., Binley et al., 2005; Revil and Florsch, 2010; Zisser et al., 2010a). However, several works have also investigated the link between a single-frequency CR parameter and important textural properties, such as surface-area-to-pore-volume ratio (e.g., Börner et al., 1996; Slater and Lesmes, 2002; Weller et al., 2010b), which could also be used to estimate hydraulic conductivity. While both, single-frequency and multi-frequency CR imaging may thus be used to estimate the same parameter (e.g., hydraulic conductivity), the results presented in our study suggest that, for imaging surveys, petrophysical relationships relying on relaxation times (τ, τ_{mean}) are better suited than those based on m, m_{tot}, or ϕ, given the better reconstruction quality of τ. We have shown that the τ reconstruction quality is

robust with respect to different noise levels in the data; however, it is important that the considered frequency range is wide enough to capture the spectral behavior. Hence, we also conclude that the quality of the reconstruction will benefit from the acquisition of broadband CR measurements, preferably with dense spectral sampling.

4.5.3 Application to more complex scenarios

In this study we consider a simple model of a polarizable anomaly with a CC model response in a homogeneous, unpolarizable background. This setting is transferable to only a limited number of real-life scenarios. For example, certain tracer tests could provide a situation in which the results of this study can be directly applied. In general, the subsurface will exhibit a more complex, heterogeneous structure, and other aspects, such as shielding effects of high-resistive layers, will become important. Also, with increasing inhomogeneity of a given subsurface resistivity distribution, regularization effects will influence inversion results to a much larger degree. Analyzing such scenarios would greatly overreach this study and is left for future studies. However, as a preview on possible research directions, Figure 4.10 shows the reconstruction curves of CC and DD parameters for a setting similar to the one presented in Figure 4.7. Data noise with a standard deviation of 0.5 mrad is added to the data, and corresponding error estimates are used in the inversion. Intrinsic spectra are extracted from 2 m $\times$ 2 m areas successively moved to deeper locations, as it is done in the previous simulations. However, instead of considering a local anomalous block, the whole depth layer is parameterized with a given CC model response. Thus a simple layered structure is simulated, as for example found when sedimentary layers are investigated. Intrinsic spectra are only extracted from the center of the modeling grid to exclude boundary effects of the regularization. Reconstruction of m and m_{tot} is greatly improved over the non-layered case (Fig. 4.10a,b), while relaxation times do not show large variations (below 10%) from each other (Fig. 4.10c,d). Merely c reconstruction shows differences in its reconstruction behavior (Fig. 4.10e), whose origin is not yet clear and must be addressed in future work.

We believe that our results on the reconstruction quality of CC and DD pa-

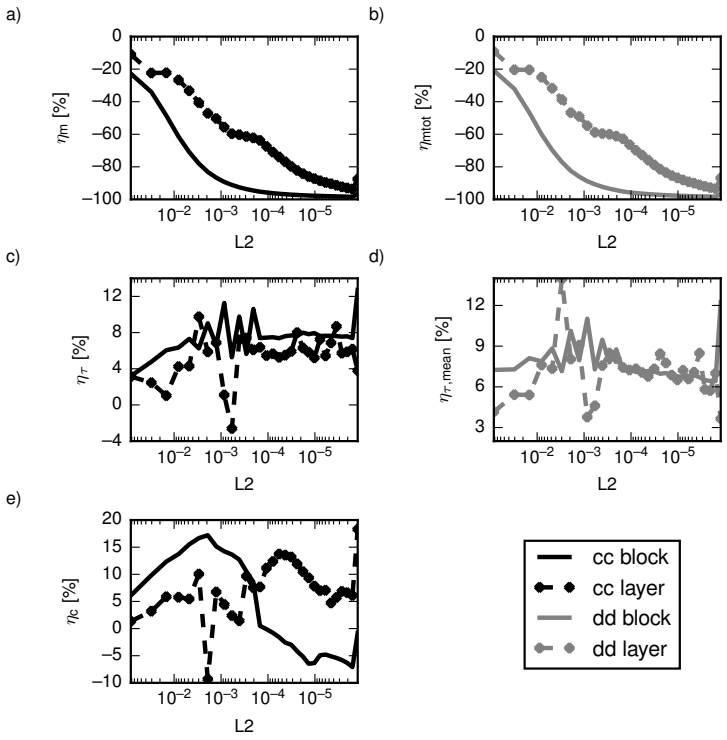

Figure 4.10: Reconstruction quality parameters for recovered CC and DD parameters of the anomaly pixels, plotted versus decreasing sensitivity values ('L_2'), i.e., increasing depth locations of the anomaly. a) η_m, b) η_{mtot}, c) η_τ, d) $\eta_{\tau,mean}$, e) η_c. Results for a block anomaly ('block', cf. Fig. 4.8) and a layered anomaly ('layer') are compared. Simulations were performed for a phase data noise level of 0.5 mrad and a corresponding error estimate in the inversion.

rameters as a function of sensitivity are still applicable to more heterogeneous situations, at least if the given spectral signatures are close to CC type. Hence, considering our results, we can also suggest that sensitivity values can be used to assess the reliability of the reconstructed parameters in single- and multi-frequency CR imaging. Our results also show that (cumulated) sensitivity can be a sufficient parameter to address reconstruction quality, compared to other, computationally more expensive approaches based on resolution matrix.

4.6 Conclusions

We investigated the reconstruction quality of Cole-Cole (CC) model and Debye decomposition (DD) parameters based on multi-frequency complex resistivity (CR) imaging by means of numerical simulations. Our results show that the reconstruction quality of the CC parameters m and c, as well as the DD parameter m_{tot}, vary strongly across the imaging plane, with reconstructed values deviating considerably from the original values for lower sensitivities. The reconstruction quality of m and m_{tot} decreases monotonically with decreasing sensitivity, while c shows inconclusive behavior that cannot be explained yet for all scenarios. The same dependence in the reconstruction quality curves is observed for the diagonal entries of the model resolution matrix. Therefore, based on our results, cumulated sensitivity (regardless of whether its L_1 or its L_2 measure is used) appears to be an adequate, computationally inexpensive proxy for image resolution. Opposite to this, the reconstruction quality of the CC relaxation time τ and the DD relaxation time τ_{mean} is only weakly dependent on sensitivity, resulting in fair quantitative reconstructions even in regions with relatively low sensitivity (deviation less than 20% from the original value down to normalized L_2 cumulated sensitivity values of 10^{-4}).

Our results suggest that a quantitative interpretation of relaxation time parameters (either from CC model fit or DD), and any parameters derived from them using established petrophysical relationships, is also possible in a multi-frequency CR imaging framework. The recovery of chargeabilities m or m_{tot}, as well as the CC exponent c, on the other hand, is highly affected by the imaging characteristics (sensitivity, resolution), which must be carefully taken into account if a quantitative interpretation is intended. Given the strong correlation between CC model parameters (and corresponding DD parameters) and various petrophysical properties of relevance in hydrogeological and environmental applications, as demonstrated by a large number of studies over the last years, our findings are of outermost importance for the successful quantitative application of multi-frequency CR imaging for improved subsurface characterization.

Appendix

4.A Complex resistivity inversion

Complex resistivity images are computed using the inversion code of Kemna (2000). The code computes the distribution of complex resistivity ρ (expressed in magnitude ($|\rho|$) and phase (ϕ)), in a 2D (x, z) image plane from a given data set of complex transfer impedances Z_i (expressed in magnitude ($|Z_i|$) and phase (φ_i)) under the constraint of maximum smoothness. The algorithm iteratively minimizes a cost function $\Psi(\underline{m})$ which is composed of the measures of data misfit and model roughness, with both terms being balanced by a (real-valued) regularization parameter λ:

$$\Psi(\underline{m}) = \left\| \underline{\underline{W}}_{\mathrm{d}} (\underline{d} - \underline{f}(\underline{m})) \right\|^2 + \lambda \left\| \underline{\underline{W}}_{\mathrm{m}} \underline{m} \right\|^2, \tag{4.8}$$

where $\underline{d}$ is the data vector (log impedance data), $\underline{m}$ the model vector (log complex resistivities of parameter cells (lumped elements of underlying finite-element mesh)), $\underline{f}(\underline{m})$ the operator of the forward model, $\underline{\underline{W}}_{\mathrm{d}}$ a data weighting matrix, and $\underline{\underline{W}}_{\mathrm{m}}$ a (real-valued) matrix evaluating the first-order roughness of $\underline{m}$. Under the assumption that the data errors are uncorrelated and normally distributed, $\underline{\underline{W}}_{\mathrm{d}}$ is a diagonal matrix given by

$$\underline{\underline{W}}_{\mathrm{d}} = \begin{pmatrix} \frac{1}{\epsilon_1} & 0 & 0 \\ 0 & \ddots & 0 \\ 0 & 0 & \frac{1}{\epsilon_n} \end{pmatrix}, \tag{4.9}$$

where ϵ_i is the complex error estimate (standard deviation) of the i-th datum, $d_i = \ln(Z_i) + j\phi_i$ (with j denoting the imaginary unit). At each iteration step of the inversion, a univariate search is performed to find the maximum value of the regularization parameter λ which locally minimizes the data misfit.

In complex resistivity inversion, the data misfit is typically dominated by the real component of the complex data (that is log impedance magnitude). In order to take the misfit in the phase (imaginary component of the data) properly into account, subsequent to the complex inversion additional inversion iterations are run only for the phase (i.e., as a real-valued inverse problem with the impedance phase values as data and the complex resistivity phase values as parameters). Here the resistivity magnitude image from the complex inversion is kept unchanged, and the same smoothness-constrained inversion procedure is used. For more details on the implementation of the inversion, we refer to Kemna (2000).

4.B Image appraisal

Electrical resistivity images exhibit a variable spatial resolution (e.g., Oldenburg and Li, 1999; Friedel, 2003; Binley and Kemna, 2005). A common approach for the quantification of this variable resolution uses the diagonal entries of the model resolution matrix, $\underline{\underline{R}}$ (e.g., Alumbaugh and Newman, 2000), which for the complex case is given by

$$\underline{\underline{R}} = \left[\underline{\underline{A}}^H \underline{\underline{W_\mathrm{d}}}^H \underline{\underline{W_\mathrm{d}}} \underline{\underline{A}} + \lambda \underline{\underline{W_\mathrm{m}}}^T \underline{\underline{W_\mathrm{m}}}\right]^{-1} \left[\underline{\underline{A}}^H \underline{\underline{W_\mathrm{d}}}^H \underline{\underline{W_\mathrm{d}}} \underline{\underline{A}}\right], \tag{4.10}$$

where $\underline{\underline{A}} = \frac{\partial \underline{f}(\underline{m})}{\partial \underline{m}}$ is the complex Jacobian matrix (for its computation, see Kemna, 2000). The model resolution matrix is usually evaluated at the end of the iterative inversion process. Due to its lower computational cost compared to $\underline{\underline{R}}$, the cumulative (and error-weighted) sensitivity, $\underline{s}_{\mathrm{L2}}$, has been alternatively used (e.g., Kemna et al., 2002; Nguyen et al., 2009). Using the L_2-norm, its components are given by Kemna (2000) as

$$(\underline{s}_{\mathrm{L2}})_k = \mathrm{diag}\left(\underline{\underline{A}}^H \underline{\underline{W}}_d^H \underline{\underline{W}}_d \underline{\underline{A}}\right) = \sum_i \frac{|a_{ik}|^2}{|\epsilon_i|^2}, \tag{4.11}$$

where a_{ik} is the i,k-th element of the Jacobian matrix $\underline{\underline{A}}$, i.e., the sensitivity of the i-th datum with respect to the k-th parameter cell. Note that also for the complex case, $\underline{s}_{\mathrm{L2}}$ is a real-valued vector. The cumulated sensitivity is a measure

of how much an entire data set changes due to a changing model cell. Given the correspondence between cumulated sensitivity and the diagonal of the model resolution matrix, the cumulated sensitivity can be used as a proxy for model resolution. We emphasize here that a large cumulated sensitivity does not necessarily imply a good resolution; however, good resolution cannot be expected for model cells exhibiting small cumulative sensitivities (Kemna, 2000).
In addition to the L_2-normed cumulated sensitivity, in our study we also compute the L_1-normed cumulated sensitivity based on the sum of the absolute values of the sensitivities (weighted by the absolute error of the corresponding measurement):

$$(\underline{s}_{\mathrm{L1}})_k = \sum_i \frac{|a_{ik}|}{|\epsilon_i|}. \tag{4.12}$$

This chapter is based on the publication
Weigand. M, and Kemna. A.
Multi-frequency electrical impedance tomography as a non-invasive tool to characterise and monitor crop root systems, Biogeosciences, **14**, 4, 921–939, doi:10.5194/bg-14-921-2017, 2017.

CHAPTER 5

Multi-frequency electrical impedance tomography as a non-invasive tool to characterise and monitor crop root systems.

5.1 Introduction

Interest in and development of non-invasive methods for the structural and functional characterization and monitoring of root systems and the surrounding rhizosphere has substantially increased in recent years (e.g., Heřmanská et al., 2015, and references therein). This trend is driven mostly by the need to improve crop management and breeding techniques, and to reduce fertiliser usage (e.g., Heege, 2013). In this context, various non-invasive methods for the investigation and characterization of crop root systems have been proposed (for a comprehensive overview of current methods, both for laboratory and field studies, see Mancuso, 2012). These methods include light transmission tomography (e.g., Pierret et al., 2003), X-ray computer tomography (e.g., Gregory et al., 2003; Pierret et al., 2003), neutron radiography (e.g., Willatt et al., 1978), magnetic resonance imaging (e.g., Metzner et al., 2015, and references therein), electrical resistivity tomography (ERT) (e.g., Mancuso, 2012), electrical capacitance

measurements, and electrical impedance spectroscopy (EIS) (see Mancuso, 2012; Anderson and Hopmans, 2013, and references therein). However, most of these methods can not, or only under special circumstances, be used at the field scale, or they lack sensitivity to structural or physiological features of the rhizosphere (e.g., Mancuso, 2012).

Electrical methods, including both tomographic and spectroscopic approaches, are gaining importance among these methods due to their universal applicability at different scales and the recognized potential to provide pertinent information on root systems via their electrical properties. Advances in measurement accuracy (Zimmermann et al., 2008) and large-scale deployments (e.g., Johnson et al., 2012; Loke et al., 2013) allow imaging studies with high spatial and temporal resolution at both laboratory and field scales (see, e.g., Kemna et al., 2012; Singha et al., 2014).

Electrical resistance measurements on root systems have been related to root age (Anderson and Higinbotham, 1976), to absorbing root surfaces of trees (Aubrecht et al., 2006; Čermák et al., 2006), and to surface area in contact with the ambient solution (Cao et al., 2010). The measured resistances are usually interpreted by means of equivalent electrical circuit models of the root-soil continuum, and relations to biological properties are analyzed in terms of the circuit model parameters. Electrical imaging applications on crop root systems, however, are relatively rare. ERT has been used to map root zones (al Hagrey, 2007; Amato et al., 2008, 2009; al Hagrey and Petersen, 2011; Rossi et al., 2011) and to monitor water content in maize fields (Srayeddin and Doussan, 2009; Beff et al., 2013) and under an apple orchard (Boaga et al., 2013). Whalley et al. (2017) showed that ERT can be used in the field to indirectly phenotype root systems by monitoring water content distributions over time.

As pointed out by Urban et al. (2011), resistance methods for root characterization suffer from an inherent ambiguity of effective conductivity (or resistivity), making interpretation difficult. Polarization properties, on the other hand, provide valuable additional information, in particular if their spectral variation is explored. In geophysics, corresponding measurement approaches are referred to as induced polarization (IP) or spectral induced polarization (SIP) methods, since the polarization is provoked by an impressed electric field. A wide range of studies have investigated electrical polarization properties of plant root sys-

tems, mostly in terms of capacitances, using alternating-current measurements at some frequency (e.g., Walker, 1965; Chloupek, 1972; Dvořák et al., 1981; Dalton, 1995; Aulen and Shipley, 2012; Dietrich et al., 2013). Correlations of varying strength have been found between measured capacitances and root (dry) mass, root surface, and various attributes associated with physiological processes such as root development. For example, Ellis et al. (2013) used an improved measurement setup to investigate the relation of electrical capacitances to root mass, root surface area, and root length in soil experiments. For an overview of studies using electrical capacitance measurements on root systems, we refer to Kormanek et al. (2015). While in the above-mentioned studies single-frequency capacitance measurements were used, more recent studies also focused on the analysis of spectral measurements covering a broad frequency range, in terms of both capacitances (Ozier-Lafontaine and Bajazet, 2005) and impedances (Ozier-Lafontaine and Bajazet, 2005; Cao et al., 2011; Zanetti et al., 2011; Cseresnyés et al., 2013; Repo et al., 2014).

Research has also been conducted on electrical properties at the cellular scale, including electrical surface properties of cell membranes (also called plasma membranes) (e.g., Kinraide, 1994; Wang et al., 2011). An electrical double layer (EDL) forms at an electrically charged surface in contact with an electrolyte (e.g., Lyklema, 2005). This EDL gives rise to electrical polarizability (e.g., Lyklema et al., 1983), that can be measured with EIS or electrical impedance tomography (EIT). Accordingly, variations in the EDL characteristics related to structural or functional changes in the root system should manifest in electrical impedance measurements. According to Kinraide et al. (1998) cell walls can be assumed to be near ionic equilibrium with the surrounding electrolyte and thus do not contribute to the formation of EDLs in biomaterial.

Imaging of IP or SIP parameters has so far, to our knowledge, not been applied to the field of root research. However, various applications in near-surface petro- and biogeophysics have been successful. For example, spectral (i.e., multi-frequency) EIT was used to map subsurface hydrocarbon contamination at an industrial site (Flores Orozco et al., 2012a) and to monitor uranium precipitation induced by bacterial injections within the frame of contaminated site remediation (Flores Orozco et al., 2013)—both studies demonstrating the field-scale applicability of the method for subsurface (bio)geochemical characterization. Martin and

Günther (2013) applied EIT to investigate fungus infestation of trees; however, in the imaging they did not take the spectral variation into account.
In the present work we propose broadband (mHz – kHz) multi-frequency EIT as an imaging tool for the physiological, i.e., functional, characterization of crop root systems. This novel approach for functional root imaging combines the spatial resolution benefits of EIT with the diagnostic capability of EIS, and builds upon instrumentation and processing tools that have been developed in recent years. Analogous to the now widely accepted interpretation of SIP signatures of soils and rocks in terms of textural and mineral surface characteristics, we hypothesize that the SIP response of crop root systems, which is imaged with the proposed methodology, is directly related to physico-chemical processes in the vicinity of electrical double layers forming in association with root physiological activity (e.g., nutrient uptake) at specific scales of the root system.
Besides the spatial delineation and monitoring of active root zones in terms of polarization magnitude, we aim at the analysis of the imaged SIP response in terms of relaxation times, which provides information on the spatial length scale at which the underlying processes occur. Relaxation times are determined using the Debye decomposition scheme, a phenomenological model that can describe a wide variety of SIP signatures (e.g., Nordsiek and Weller, 2008; Weigand and Kemna, 2016b). A similar procedure to analyse SIP signatures is also proposed by Ozier-Lafontaine and Bajazet (2005) for the analysis of SIP signatures measured on root systems.
To demonstrate the proposed methodology we conducted a laboratory experiment on oilseed plants grown in hydroponics. The plants were placed in a rhizotron container filled with tap water and monitored using multi-frequency EIT in the course of prolonged nutrient deficiency. The recovered spectral electrical signatures at various time steps were analyzed with regard to total polarization strength and dominant relaxation time scales, and qualitatively related to the macroscopic reaction of the root system to the induced stress situation.
The next section shortly reviews electrical measurements on, and corresponding polarization properties of root systems. Then the geophysical methods used in the presented study are described, followed by the experimental setup and data acquisition/processing steps. The last two sections present the results and discuss methodological and biological aspects of the experiment.

5.2 Electrical properties and measurements of root systems

This section develops our working hypotheses regarding the electrical polarization of crop root systems. A more detailed description of the EDL is given and linked to the measurement methodology. We moreover shortly review previous works on small-scale (cells and cell suspensions) polarization of biomatter and the approaches used to analyze polarization measurements on whole root systems.

5.2.1 Electrical double layer polarization

Electrical conduction properties of soils are primarily determined by electrolytic soil water conductivity, i.e., ion concentration and mobility, and interface conduction processes at water-mineral interfaces. Electrical polarization properties originate mainly in ion accumulation processes in constrictions of the pore network and at water-mineral interfaces. If surfaces are electrically charged and in contact with an electrolyte, as for example found at mineral grain surfaces or cell membranes, electrical double layers (EDLs) form, which comprise the so-called Stern layer of bound counterions and the so-called diffusive layer. The latter forms in equilibrium of electromigrative and diffusive ion fluxes and is characterized by ion concentration gradients. The EDL is affected by external electric fields, manifesting an induced polarization (IP), and takes a finite time (relaxation time) to reach equilibrium again once an impressed external field is turned off (e.g., Lyklema, 2005). Models of both Stern layer polarization (build-up of counterion concentration gradients in the Stern layer in the direction of the external electric field) (e.g., Schwarz, 1962; Leroy et al., 2008) and diffuse layer polarization (build-up of counterion and coion concentration gradients in the diffuse layer in the direction of the external electric field) (e.g., Dukhin et al., 1974; Fixman, 1980) have been developed, as well as models considering both Stern layer and diffuse layer (e.g., Lyklema et al., 1983; Razilov and Dukhin, 1995). In a porous system, such as soil, diffuse layer polarization is also referred to as membrane polarization since the resultant ion concentration gradients, for instance along a pore constriction, have an effect similar to an ion-selective

membrane (e.g., Bücker and Hördt, 2013b). Strength and relaxation behavior of EDL polarization are, among other factors, influenced by background ion concentration in the pore water and surface charge density (e.g., Lyklema, 2005). Importantly, the relaxation time is related to the spatial length scale of the polarization process and the ionic diffusion coefficient in the EDL, which may be different for Stern layer and diffuse layer polarization (e.g., Lyklema et al., 1983). The relationship between relaxation time and characteristic length scale for induced polarization in soils and sediments has been investigated in many studies (e.g., Titov et al., 2002; Binley et al., 2005; Kruschwitz et al., 2010; Revil and Florsch, 2010; Revil et al., 2014).

5.2.2 Electrical measurements

Electrical methods measure the conduction and polarization properties of a medium. In the frequency domain, the measured quantity is the complex-valued impedance, with the real (ohmic) part accounting for conduction, and the imaginary part accounting for polarization (capacitive) effects.

The electrical impedance, $\hat{Z}$, at some measurement (angular) frequency ω is defined as the ratio of the complex voltage $\hat{U}$ to the current $\hat{I}$, and can be represented by a real part Z' and an imaginary part Z'':

$$\hat{Z}(\omega) = \frac{\hat{U}(\omega)}{\hat{I}(\omega)} = Z'(\omega) + jZ''(\omega), \tag{5.1}$$

with j denoting the imaginary unit. The inverse of the impedance is the admittance $\hat{Y}(\omega) = 1/\hat{Z}(\omega) = Y'(\omega) + jY''(\omega)$. Impedances, or admittances, can be translated to effective material properties by means of a (real-valued) geometrical factor K, which takes into account the geometric dimensions of the measurement (in particular electrode positions):

$$\hat{\rho}_a(\omega) = K\hat{Z}(\omega) = \frac{K}{\hat{Y}(\omega)}, \tag{5.2}$$

$$\hat{\sigma}_a(\omega) = \frac{\hat{Y}(\omega)}{K} = \frac{1}{K\hat{Z}(\omega)} = \frac{1}{\hat{\rho}_a(\omega)}, \tag{5.3}$$

with $\hat{\rho}_a$ and $\hat{\sigma}_a$ being the apparent complex resistivity and apparent complex conductivity, respectively. These quantities are referred to as "apparent" because they do only represent the true properties if the medium under investigation is homogeneous. Otherwise they represent an effective (average) value. Spatial discrimination of electrical properties can be achieved by the use of multiple measurements with different electrode locations, which also form the basis for tomographic processing (inversion), i.e., imaging.

Impedance measurements can be conducted using only two electrodes for a combined current and voltage measurement, or by using four electrodes (quadrupole measurements, also called four-point spreads) with separate current and voltage electrode pairs. In the latter case the contact impedance between electrode and medium, which becomes significant towards lower measurement frequencies, has practically no influence on the voltage measurement (e.g., Barsoukov and Macdonald, 2005).

5.2.3 Polarization of biomatter

Polarization phenomena of biomatter are commonly classified into three frequency regions with different polarization sources, namely the α, β and γ regions (e.g., Schwan, 1957; Prodan et al., 2008). While overlapping, the low-frequency α polarization is thought to extend into the lower kHz range, followed by the β polarization up to about 100 MHz, and joined by the γ polarization at higher frequencies (e.g., Repo et al., 2012). Controlled by the mobility of the charge carriers, the α-range is assumed to be associated with electrochemical polarization (i.e. the build-up and relaxation of ionic concentration gradients, as found in EDLs, in an electric, time-variable field), the β-range by the Maxwell-Wagner polarization of composite media (e.g., Prodan and Prodan, 1999; Prodan et al., 2008), and the γ-range by molecular, ionic and atomic polarization. The different processes lead to different current flow paths within biomatter for different frequencies (Repo et al., 2012). These observations have been primarily made on cell suspensions and various kinds of tissue, which exhibit structures much more homogeneous than fully developed plant and root systems. Polarization processes in plant roots are assumed to originate, among others, in the cell membranes, the apoplast and the symplast (Repo et al., 2014). The

frequency-dependence of published multi-frequency measurements (e.g., Ozier-Lafontaine and Bajazet, 2005; Repo et al., 2014) indicates multiple length scales, and associated structures, as the origin of electrical polarization responses.

On a cellular, or multi-cellular, level, much work has been conducted to gain information about the electrical surface characteristics of cells (cell structures). A Gouy-Chapman-Stern model relating surface charges to external ion concentrations has been formulated and subsequently improved (Kinraide et al., 1998; Kinraide, 1994; Wang et al., 2011). Using this model, ion activity at membrane surfaces can be computed and analyzed for the investigation of physiological effects. These, and following, studies regarding ion toxicity and related surface electric potential have provided further evidence that certain surface potentials can be linked to physiological states and processes (for example, ion availability and uptake) (Wang et al., 2009; Kinraide and Wang, 2010; Wang et al., 2011, 2013). Li et al. (2015) estimated the electric potential at rice-root surfaces of macroscopic root segments using measurements of the electrokinetic Zeta-potential. The Zeta-potential is the experimentally accessible electric potential at some distance from the surface where slipping in the electrolyte occurs upon a flow-driving pressure gradient.

The EDL is the source of polarization responses in the low-frequency range usually measured with EIS/EIT. It is sensitive to physiological processes that affect ion (nutrient) availability in the vicinity of, and ion fluxes across, charged cell membranes. The key function of roots is the uptake of water and nutrients, which is highly dependent on nutrient availability, demand, and stress factors (e.g., Claassen and Barber, 1974; Delhon et al., 1995; Hose et al., 2001). Nutrient availability can influence water (and nutrient) transport within plant systems (e.g., Clarkson et al., 2000; Martínez-Ballesta et al., 2011), and nutrient availability within roots can fluctuate in response to certain depletion situations (e.g., Benlloch-González et al., 2010). Also, the distribution of stress hormones such as ABA increases in response to stress situations, possibly inducing the aforementioned reactions (e.g., Schraut et al., 2005). The formation and properties of large-scale ion-selective structures such as endodermis and hypodermis are also directly influenced by the growth environment, and can change in response to external stress factors (Hose et al., 2001). In addition, Dalton (1995) noted that electrical polarization effects originate in the 'active' parts of a root system only,

which change according to age, nutrient availability, and other stress factors (see also Anderson and Hopmans, 2013).

The majority of studies concerning full root systems work with equivalent electrical circuit models to describe the measured signals of various biostructures (see Repo et al., 2012, and references therein). The scale and composition of these models vary considerably. For example, Dalton (1995) equates root segments with cylindrical capacitors, whose conducting plates are formed by the inner xylem and the fluid surrounding the root segment, with root cortex acting as a dielectric. Kyle et al. (1999) proposed a simplified model of cell polarization in root systems, in which the cell membrane acts as a dielectric between the conducting inner and outer regions of the cells, thus representing a classical capacitor. Equivalent circuit representations inherently depend on the assumed flow paths of the electric current. For instance, impedance measurements using the stem as one pole for current injection and the medium surrounding the roots as the other pole (as frequently being done, e.g., Chloupek, 1976; Dietrich et al., 2013; Repo et al., 2014) force the current to cross all radial layers of the roots. However, even for stem injection, equivalent circuit models considerably simplify the true electrical processes in the root and root-rhizosphere system, and it is questionable whether these models can be transferred between different experimental setups (as evident from the large number of slightly different models that were proposed, e.g., Dalton, 1995; Ozier-Lafontaine and Bajazet, 2005; Dietrich et al., 2013). A purely phenomenological analysis is made by Repo et al. (2014), who use a classification approach to analyze spectral impedance data measured on pine roots infested with mycorrhizal fungi.

5.2.4 Working hypotheses

We propose to describe and interpret low-frequency (< 1 kHz) polarization processes in biomatter using concepts similar to those established for soils and rocks in recent years, under the assumption that the observed responses originate from the polarization of EDLs present in the biomatter. Accordingly, it should be possible to link the polarization magnitude to the average EDL thickness (which depends on the electric potential drop between the charged surface/membrane and the background ambient electrolyte), and characteristic re-

laxation times to the length scales at which the polarization processes take place. Given the to-date observations and understanding of electrical polarization processes in biomatter, as reviewed in the previous section, our hypotheses are:

1. The magnitude of the low-frequency polarization response of roots is related to the overall surface area comprised by EDLs in the root-rhizosphere system, including the inner root structure. EDLs may form at Casparian strips (e.g., hypodermis and endodermis) and plasma membranes.

2. The characteristic relaxation times of the low-frequency polarization response of roots provide information on the length scales at which the polarization processes take place. While it is not clear to which extent a discrimination of specific polarization processes (e.g., plasma membrane polarization and polarization of the hypodermis) is possible, changes in the relaxation times should indicate changes in the length scale of the polarizing structures.

3. EDLs in the inner root system are influenced by ions (nutrients) in the sap fluid, EDLs at the outer root surface are influenced by ion concentrations in the external fluid. Thus, physiological processes that influence the availability, usage and translocation of ions directly influence the low-frequency polarization response.

4. Spectral EIT is a suitable non-invasive method to image and monitor magnitude and characteristic relaxation times of the low-frequency polarization response of root systems.

In the present study we address the second part of hypothesis 3, as well as hypothesis 4. Hypotheses 1 and 2 are based on the synthesis of existing works, but can neither be validated nor invalidated by the present study.

5.3 Material and methods

5.3.1 Electrical impedance tomography

The EIS (or SIP) method involves the measurement of impedances at multiple frequencies (usually in the mHz to kHz range). It can be extended by utilizing

electrode arrays consisting of tens to hundreds of electrodes to collect numerous, spatially distributed four-point impedance measurements. From such data sets images of the complex conductivity (or its inverse, complex resistivity) can be computed using tomographic inversion algorithms (e.g., Kemna, 2000; Daily et al., 2005). This method is called complex conductivity (or complex resistivity) imaging, or electrical impedance tomography (EIT) and refers to both single- and multi-frequency (spectral) approaches. EIT images are characterized by a spatially variable resolution, which decreases with increasing distance from the electrodes (e.g., Alumbaugh and Newman, 2000; Friedel, 2003; Binley and Kemna, 2005; Daily et al., 2005). The method has its primary fields of application in near-surface geophysics (e.g. Binley and Kemna, 2005; Daily et al., 2005; Revil et al., 2012b) and medical imaging (e.g., Bayford, 2006).
Spectral EIT measurements presented in this study were conducted using the 40-channel EIT-40 impedance tomograph (Zimmermann et al., 2008), which was configured in a monitoring setup to acquire up to seven EIT data sets (frames) on a mini-rhizotron container per day.

2D forward modeling

Synthetic impedance data, required in the tomographic inversion process, were modeled using the finite-element (FE) forward modeling code of Kemna (2000). The code solves the Poisson equation for a 2D complex conductivity distribution and 2D source currents in a tank of given thickness (Flores Orozco et al., 2012b). At the boundaries of the 2D modeling domain now-flow Neumann conditions are imposed, which do not allow any current flow out of the modeling domain. Details of the implementation can be found in Kemna (2000).
A sketch of the FE grid (also used for the inversion and presentation of imaging results) resembling the rhizotron container is shown in Fig. 5.1b along with the position of 38 electrodes. The grid consists of 60 elements in x-direction, and 157 elements in z-direction (9,420 elements in total).

2D tomographic inversion

Complex conductivity images at multiple measurement frequencies were computed using the smoothness-constraint inversion code of Kemna (2000). The

code computes the distribution of complex conductivity $\hat{\sigma}$ (expressed in either magnitude ($|\hat{\sigma}|$) and phase (ϕ), or real component (σ') and imaginary component (σ'')), in the 2D (x, z) image plane from the given set of complex transfer impedances $\hat{Z}_i$ (expressed in magnitude ($|\hat{Z}_i|$) and phase (φ_i)) under the constraint of maximum model smoothness. Log-transformed impedances and log-transformed complex conductivities (of the individual elements of the grid) are used as data and model parameters, respectively, in the inversion. The iterative, Gauss-Newton-type inversion scheme minimizes an objective function composed of measures of data misfit and model roughness. The data misfit is weighted by the (real-valued) magnitudes of individual complex-valued data errors (see Kemna, 2000), which, however, are dominated by the resistance errors since the phase values are relatively small for the measurements considered here. Therefore the resistance error model (LaBrecque et al., 1996b)

$$\Delta|\hat{Z}_i| = a|\hat{Z}_i| + b, \tag{5.4}$$

can be used in the complex inversion for the weighting of the complex data (including the phase), with $\Delta|\hat{Z}_i|$ being the error of impedance magnitude (resistance) $|\hat{Z}_i|$, a a relative error contribution and b an absolute error contribution. For more details on the inversion scheme we refer to Kemna (2000). The inversion is performed for each frequency of the given data set separately.

5.3.2 Debye decomposition

The Debye decomposition (DD) approach (e.g., Uhlmann and Hakim, 1971; Lesmes and Frye, 2001) was used to analyze the complex conductivity spectra recovered from the multi-frequency EIT inversion results. The approach yields integral parameters describing the spectral characteristics of the SIP signature. The complex conductivity spectrum is represented as a superposition of a large number of Debye relaxation terms at relaxation times τ_k (suitably distributed over the range implicitly defined by the data frequency limits, see Weigand and Kemna (2016b)):

$$\hat{\sigma}(\omega) = \sigma_\infty \left[1 - \sum_k \frac{m_k}{1 + j\omega\tau_k}\right], \tag{5.5}$$

with σ_∞ being the (real-valued) conductivity in the high-frequency limit, and m_k the k-th chargeability, describing the relative weight of the k-th Debye relaxation term in the decomposition. The chargeabilities m_k at the different relaxation times τ_k form a relaxation time distribution (RTD), from which the following descriptive parameters are computed (e.g., Nordsiek and Weller, 2008):

- The normalized total chargeability $m_{\text{tot}}^{\text{n}}$ is a measure of the overall polarization reflected in the spectrum (e.g., Tarasov and Titov, 2013; Weigand and Kemna, 2016b):

$$m_{\text{tot}}^{\text{n}} = \sigma_0 \sum_k m_k, \tag{5.6}$$

  with σ_0 being the (real-valued) conductivity in the low-frequency limit.

- The mean logarithmic relaxation time τ_{mean} represents a weighted mean of the RTD:

$$\tau_{\text{mean}} = \exp\left(\frac{\sum_k m_k \log(\tau_k)}{\sum_k m_k}\right). \tag{5.7}$$

- The uniformity parameter $U_{60,10}$ describes the frequency dispersion of the spectrum:

$$U_{60,10} = \frac{\tau_{60}}{\tau_{10}}, \tag{5.8}$$

  with τ_{10} and τ_{60} being the relaxation times at which the cumulative chargeability reaches 10 % and 60 %, respectively, of the total chargeability sum.

The implementation of Weigand and Kemna (2016b) was used for the DD analysis. The iterative inversion scheme balances between (error-weighted) data fitting and smoothing requirements.

5.3.3 Experimental setup

Rhizotron

The experiment was conducted using a mini-rhizotron container with the dimensions of 30 cm width, 78 cm height, and 2 cm thickness, and a transparent

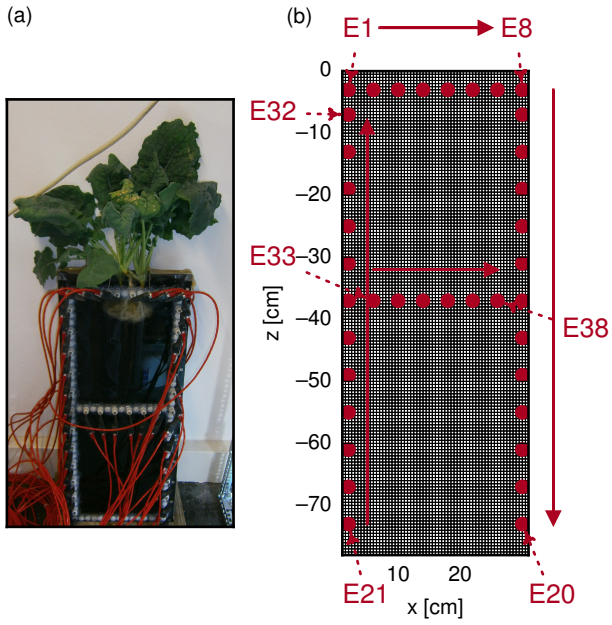

Figure 5.1: a) Experimental setup of plant root systems in water filled rhizotron. b) Corresponding finite-element grid used for electrical modeling and imaging. Red dots indicate position of electrodes. Red arrows indicate the ascending order of electrode numbering, some of which are marked using the notation E1 - E38.

front plate (Fig. 5.1). The front of the rhizotron is equipped with 38 brass pins of 5 mm diameter as electrodes, which do not extend into the rhizotron inner volume. A growth lamp was installed above the rhizotron and turned on during daylight hours.

Plant treatment

Oilseed plants had been grown in nutrient solution prior to the experiment. To increase the root mass, three plants were tied together and centrally placed at the top of the rhizotron (Fig. 5.1), which before had been filled with tap water. No water was added to the rhizotron during the experiment, nor was the water in the rhizotron disturbed in any way. Thus it is possible that at some point

anaerobic conditions manifested.

Data acquisition

Over the course of 3 days 21 EIT data sets at 35 frequencies between 0.46 Hz and 45 kHz were collected in regular intervals, starting right after the placement of the plant system in the rhizotron. A total of 1,158 quadrupoles were measured for each data set, involving 74 individual current injections (plus 767 reciprocal configurations, where current and voltage electrode pairs are interchanged, for quality assessment), requiring less than four hours acquisition time. These quadrupoles consisted mostly of skip-0 and skip-2 (numbers of electrodes between the two electrodes used for current injection and voltage measurement, respectively) dipole-dipole configurations, as well as quadrupoles with current electrodes on opposite sides (left and right) of the rhizotron and skip-0 voltage readings.

5.3.4 Data processing

Selection of impedance data

The inversion scheme assumes normally distributed and uncorrelated data errors and is very sensitive to outliers (e.g., LaBrecque and Ward, 1990). Outliers are usually associated with low signal-to-noise ratios or systematic errors due to missing or bad electrode contacts. Outliers can either be removed from the data set prior to inversion, or accounted for by sophisticated, 'robust' inversion schemes (LaBrecque and Ward, 1990). In these robust schemes, the weighting of individual data points is iteratively adapted, which can lead to a reduction of spatial resolution as well as recovered contrast in the imaging results. However, usually this does not change the qualitative results of the inversion. In the present study we sought to analyze data across the frequency and time domains, which requires a careful and consistent analysis of the inversion data. Thus, to prevent introducing unnecessary variations between time-steps and frequencies, we opted to remove outliers using the criteria described below and use individual, but consistent, data weighting schemes for all measurements.
The measured impedance data (also referred to as 'raw data', in contrast to com-

plex conductivity data recovered from the imaging results, referred to as 'intrinsic data') were screened (filtered) for outliers and faulty data according to multiple criteria: First, outliers were identified for each frequency and time step and removed from the data set. Due to the underlying physical principles, EIT measurements usually do not show strong variations when electrode positions are only slightly shifted. The exception here are measurements with electrodes located close to the plant stem system, where a very localized anomalous response is expected in the data. Accordingly, care was taken not to remove these data as outliers. Following this selection process, only impedance spectra were kept that retained more than 90 % of the original data points below 300 Hz and showed consistency over several time steps. To avoid errors due to electromagnetic coupling effects (e.g., Pelton et al., 1978; Zhao et al., 2013), only data below 220 Hz were considered for the imaging. Measurements at 50 Hz were discarded due to powerline noise.

The applied data selection criteria resulted in small variations of the number of measurements actually used for the inversions for the different time steps, ranging between 530 and 555 measurements per data set and frequency. The average injected current strength of the measurements at each time step increased slightly over time from approximately 1.0 mA to 1.2 mA.

Correction of impedance data for imperfect 2D situation

Since the electrodes do not extend across the entire depth (i.e., horizontal direction perpendicular to the image plane) of the rhizotron the electric current and potential field distributions in the rhizotron are not perfectly 2D, as is assumed in the forward modeling. Therefore measurements were conducted on a rhizotron solely filled with tap water of known conductivity. By comparing the latter with the apparent conductivity (Eq. (5.3)) derived from the measured impedance and the numerically determined geometric factor (obtained from running the forward model for a homogeneous case) for each measurement configuration, correction factors were computed and applied to all measured impedances.

From a theoretical point of view, these correction factors are independent of the conductivity value of a homogeneous distribution (since measured resistance

and resistivity (inverse of conductivity) are linearly related for a homogeneous distribution). Significant changes in the correction factors can only occur for strong spatial conductivity variations, in particular across the thickness of the rhizotron (2D/3D effects). However, even if present, such effects in the correction factors would primarily result in inaccuracies in the inverted conductivity magnitude image, while the conductivity phase image, and also the DD-derived spectral parameters (total chargeability, relaxation time), are relatively robust against magnitude, i.e., correction factor, errors. We therefore, for the small to moderate conductivity variations observed in the experiment in the upper region of the rhizotron, assume that the conducted calibration survey, i.e., one universal set of correction factors, was actually sufficient.

In Fig. 5.2 the effect of this correction procedure on the EIT inversion result is shown. Without correction the obtained image exhibits an artificial pattern (Fig. 5.2a), while with correction a practically homogeneous distribution is recovered, in agreement with the conductivity of the tap water (Fig. 5.2b).

The inversion was conducted using the error parameter values $a = 0.5$ % and $b = 0.012$ Ω (cf. Eq. (5.4)). These values were found to be appropriate and were also used in the inversions of which the results are shown in the following.

Adaptation of modeling domain to changing water table

Due to evaporation and root water uptake the water table fell by ca. 2 cm over the course of the monitoring experiment. This was not problematic in terms of electrode contact as electrodes always remained in the water. However, the changing water table has to be accounted for in the EIT inversion by means of an adapted modeling domain, i.e., by adapting the position of of the top boundary of the FE modeling grid, where no-flow conditions are assumed. Otherwise, as we checked in numerical experiments, significant artifacts appear in the inversion results (Fig. 5.3).

From the known water tables at the beginning and end of the experiment, and the average time when each EIT data set was collected, the positions of the top boundary of the individual grids used for the inversion of each data set were determined by linear interpolation.

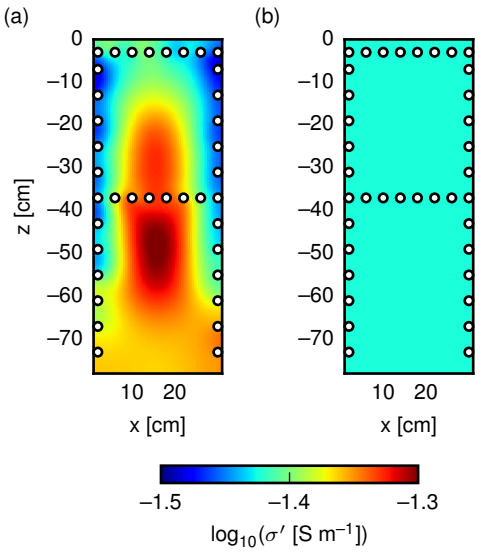

Figure 5.2: EIT inversion results (real component of complex conductivity) for measurements on a rhizotron filled with water of known conductivity (375 µS/cm = $10^{-1.43}$ S/cm) without (a) and with (b) correction of the impedance data for the imperfect 2D situation.

Analysis of spectral imaging results

The spectral imaging results were analyzed by means of pixel-wise application of the Debye decomposition scheme. As water exhibits no significant polarization response in the examined frequency range, the area free of roots from 20 cm to 78 cm depth of the rhizotron was used to quantify a $m^{\mathrm{n}}_{\mathrm{tot}}$ threshold value below which polarization is considered insignificant. Based on this threshold value the entire images of spectral parameters obtained from the Debye decomposition, i.e., including the top 20 cm of the rhizotron, were partitioned into pixels with and without significant polarization. The observed polarization can be fully attributed to the root system (no polarization is expected from the surrounding water in the examined frequency range) and thus the corresponding pixels delineate polarizable areas of the root system, which we refer to the root pixel group.

To analyze the temporal evolution of the overall root system polarization (in

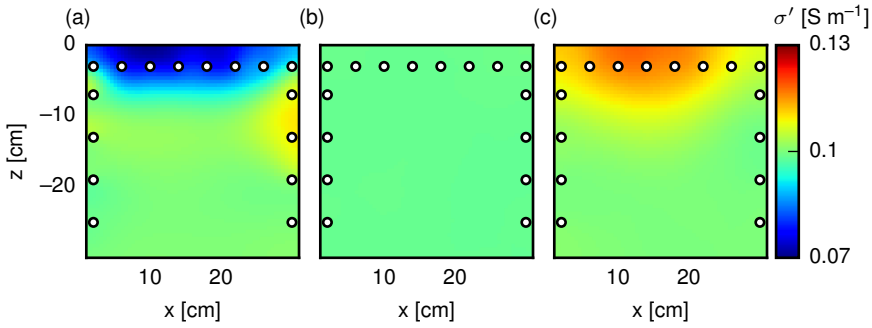

Figure 5.3: EIT inversion results (real component of complex conductivity) obtained from synthetic data using a modeling grid in the inversion with 1.5 cm lower (a), identical (b), and 1.5 cm higher (c) position of the top boundary compared to the grid used to simulate (forward model) the data. The forward model was homogeneously parameterized with a conductivity distribution of 0.1 S/m. Only the upper part of the modeling domain (rhizotron) is shown. Electrode positions and measurement configurations are the same for all three cases.

terms of normalized total chargeability) the root pixel group was determined for the first time step, and then kept fix for the following time steps. Relaxation times, however, can only be reliably extracted from SIP signatures if they show significant polarization. Therefore, for the relaxation time analysis (in terms of mean relaxation time and uniformity parameter) the root pixel groups were determined for each time step individually.

5.4 Results

5.4.1 Physiological response

Photographs of the plant systems at the beginning and the end of the experiment are shown in Figure 5.4. As is evident from the photographs, the plants significantly reacted to the nutrient stress situation (and possibly anaerobic conditions) and degraded over time. The root systems extended down to a depth of approximately 13 cm, with an approximate maximum lateral extension of 13

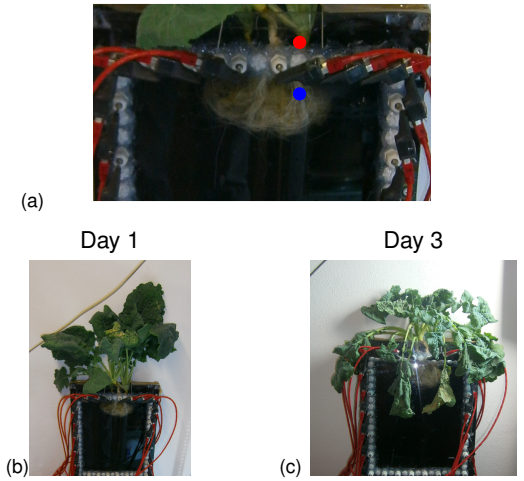

Figure 5.4: Photographs of the oilseed plants during the experiment: a) close-up of the root systems in the rhizotron container, b) day 1, c) day 3. The colored dots in a) indicates the approximate position at which intrinsic signatures, recovered from tomographic inversion results, are investigated; red: stem area, blue: fine root area.

cm (cf. Fig. 5.1).

5.4.2 Impedance spectra

In Figure 5.5 the temporal evolution of the raw data spectra in terms of apparent complex conductivity (Eq. (5.3)) is shown for two exemplary measurement configurations: a quadrupole with electrode pairs on both sides of the rhizotron located directly above the root system, i.e., with sensitivity to the root system, and a quadrupole with electrodes from the horizontal electrode line at 37 cm depth, i.e., located relatively far away from the root system and thus sensitive only to the water. The real component of apparent complex conductivity shows a smooth, consistent behavior across the time and frequency domains for both "with roots" and "water-only" responses (Figs. 5.5a,b). However, the conductivity decreases for the quadrupole around the root system, while it increases in the 'water-only' quadrupole. The imaginary components, i.e., the polarization re-

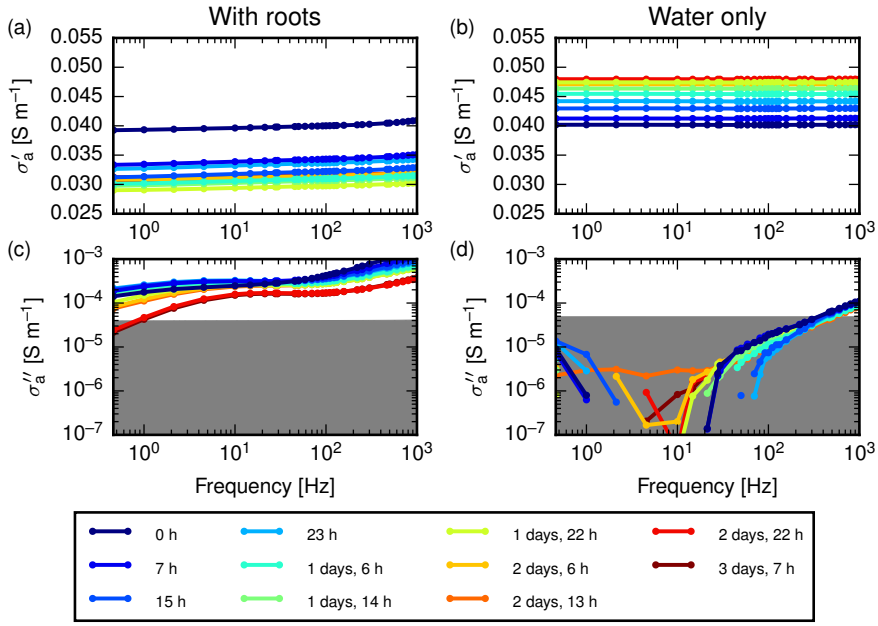

Figure 5.5: Temporal evolution of raw data spectra, plotted as real (a,b) and imaginary (c,d) components of apparent complex conductivity (Eq. (5.3)), for two exemplary measurement configurations: a,c) current injection between electrodes 3 and 4 and voltage measurement between electrodes 5 and 6 (quadrupole located directly above the root system, i.e., response "with roots"); b,d) current injection between electrodes 34 and 35 and voltage measurement between electrodes 36 and 37 (quadrupole located in an area relatively far away from the root system, i.e., "water-only" response). For electrode numbering, see Fig. 5.1b. Blue color indicates early measurements, while later ones are shown in red. Values of σ'' that lie below the measurement accuracy of the system (1 mrad phase shift at 1 kHz for water, see Zimmermann et al. (2008)) are indicated by gray areas.

sponses, with roots (Fig. 5.5c) are also consistent, and show changes, especially in the lower-frequency range, over time. The water-only measurements, on the other hand, exhibit only negligible polarization responses, likely dominated by measurement errors and noise (Fig. 5.5d). The polarization magnitudes, on one

hand, lie well below the signal threshold that can be reliably measured with the EIT-40 system (Zimmermann et al., 2008). The jittery shape of these signatures (Fig. 5.5d) is attributed to the logarithmic scale of the plot. On the other hand, measured root signatures lie clearly above the measurement threshold of the system (Fig. 5.5c).

5.4.3 Single-frequency imaging results

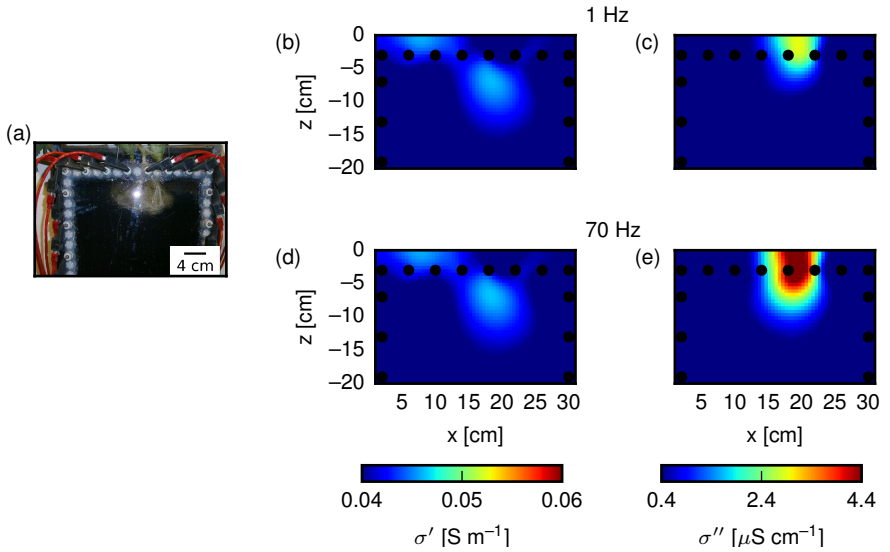

Figure 5.6: Single-frequency inversion results in terms of real (b,d) and imaginary (c,e) components of complex conductivity for 1 Hz (b,c) and 70 Hz (c,e) at the first time step. The photograph of the root system at this time (a) shows the same area of the rhizotron as the inversion results.

The spatial variability of the electrical response was assessed using the complex conductivity imaging results, i.e., σ' and σ'', at the first time step for the two frequencies 1 Hz and 70 Hz (Fig. 5.6). Only weak variations in the real component (in-phase conductivity) can be observed at the location of the root system (Fig. 5.6b,d). However, a significant polarization response in the imaginary component (Fig. 5.6c,e) coincides with the extension of the root system. The frequency dependence previously found in the apparent complex conductivity spectra (cf.

Fig. 5.5) is also revealed in the imaging results, with a stronger response at 70 Hz than at 1 Hz. It manifests both in signal strength and in the spatial extension of the polarizable anomaly associated with the root system.

5.4.4 Complex conductivity spectra recovered from imaging results

Complex conductivity spectra were extracted from the multi-frequency imaging results at three locations: near the stem area of the root system, from the lower area of the root system, and from the lower half of the rhizotron, where no root segments were present. The two locations near the root system are indicated in Fig. (5.4)a. These locations thus represent areas with, respectively, relatively thick root segments, thin root segments, and no root segments (water only) at all. Figure 5.7 shows the temporal evolution of the spectral response for the three locations. The real component of complex conductivity (σ') increased over the course of the experiment for all three locations (Fig. 5.7a-c). The imaginary component of complex conductivity (σ'') reveals a frequency-dependent polarization response at the root segment locations for all time steps (Fig. 5.7d,e). The polarization magnitude decreases over time, and changes in the shape of the spectra can be observed for later time steps. These changes are most pronounced for the location near the stem (Fig. 5.7a). The polarization signatures recovered at the bottom of the rhizotron (water only) show almost two orders of magnitude smaller magnitudes (Fig. 5.7f), compared to those in the root system areas; they are more noisy and do not exhibit a clear frequency trend.

5.4.5 Debye decomposition of recovered complex conductivity spectra

The Debye decomposition scheme was applied to the complex conductivity spectra recovered from multi-frequency EIT to quantify the overall polarization (normalized total chargeability $m^{\mathrm{n}}_{\mathrm{tot}}$) and the characteristic relaxation time (mean relaxation time τ_{mean}), as well as the uniformity parameter $U_{60,10}$. By means of this analysis, the intrinsic spectra can be assessed with respect to the magnitude

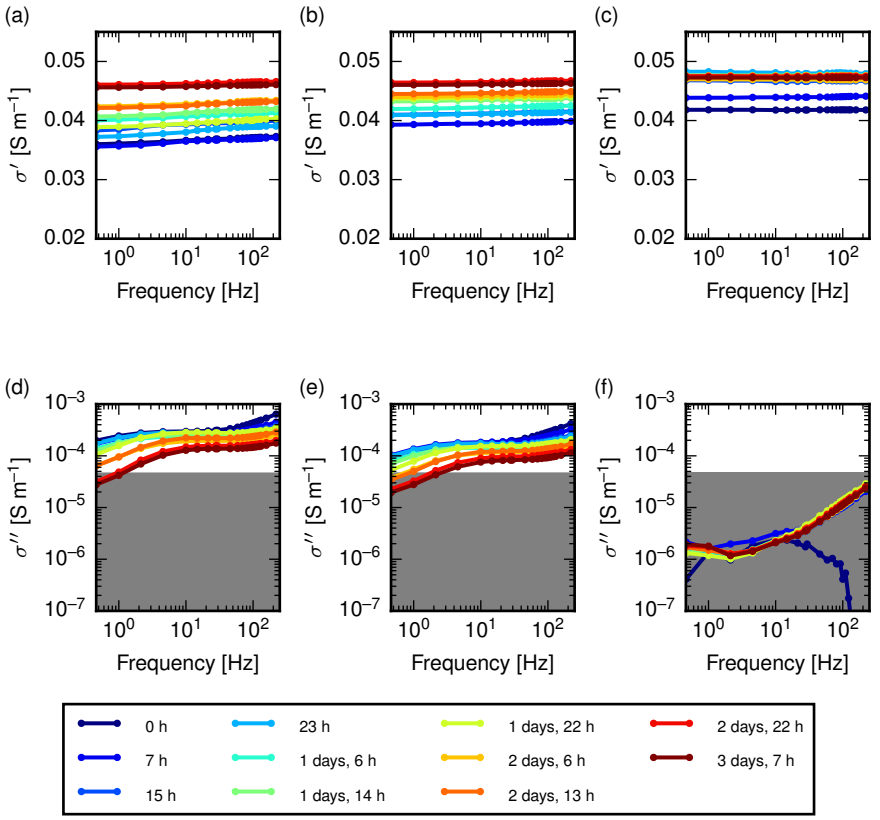

Figure 5.7: Intrinsic complex conductivity spectra (in terms of real component σ' and imaginary component σ'') for all time steps (indicated by color of the curves) recovered from the multi-frequency inversion results at different locations in the rhizotron: a,d) stem area (x position: 20.25 cm, z position: −0.75 cm); b,e) bottom of the root system (x position: 20.25 cm, z position −6.25 cm); c,f) water-only location (x position: 20.25 cm, z position: −50.25 cm). Positions for a/d and b/e are also indicated in Fig. 5.4a. Values of σ'' that lie below the measurement accuracy of the system (1 mrad phase shift at 1 kHz for water, see Zimmermann et al. (2008)) are indicated by gray areas.

and shape of the polarization response for all pixels at each time step. Figure 5.8 shows a decomposition result for a pixel from the stem area for the first time

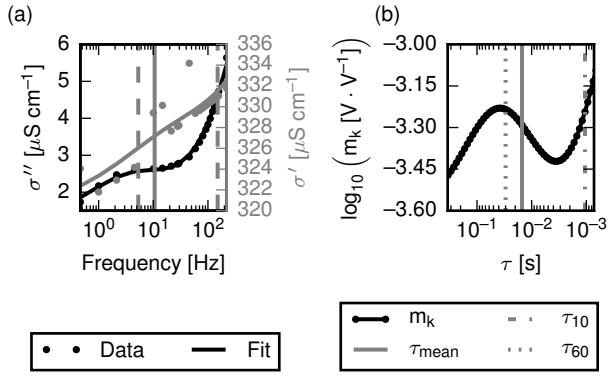

Figure 5.8: Debye decomposition of the recovered complex conductivity spectrum for a pixel from the stem area with maximum polarization response (cf. Figs. 5.5 and 5.7): a) complex conductivity (gray: real component, black: imaginary component) from spectral EIT (dots) and fitted DD response (solid curves); b) corresponding relaxation time distribution. Vertical gray solid lines indicate τ_{mean}, and the dashed vertical lines indicate τ_{10} and τ_{60}, respectively.

step, corresponding to the spectrum plotted in Fig. 5.7a,d at "0 hours" (dark blue curve). The complex conductivity spectrum was fitted by means of 96 Debye relaxation terms (Fig. 5.8a), yielding a relaxation time distribution (RTD) (Fig. 5.8b), from which τ_{mean}, τ_{10} and τ_{60} can be determined (Fig. 5.8a,b). We note that τ_{mean} does not coincide with the RTD peak, which only happens if the RTD shows a perfect symmetry (in log scale), which is not the case here.

5.4.6 Images of spectral parameters obtained from Debye decomposition

Images depicting the DD-derived total polarization ($m^{\text{n}}_{\text{tot}}$) results of the complex conductivity spectra (obtained from multi-frequency EIT) for selected time steps are presented in Figure 5.9. The extension of the root system against the surrounding water (characterized by low polarization) is clearly delineated in the images, and a continuous decrease in polarization strength is observed over time.

For further analysis, the complex conductivity spectra (also referred to as pixel

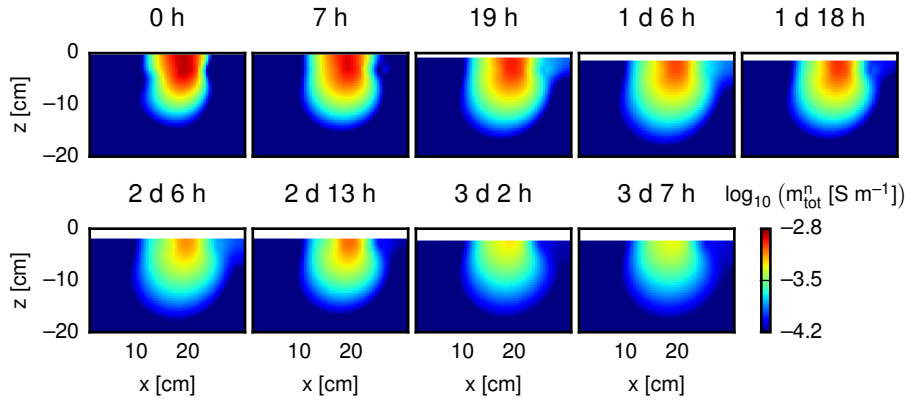

Figure 5.9: Spatial distribution of DD-derived parameter m^{n}_{tot} for selected time steps. The top boundary is adjusted according to the estimated water table for each measurement time.

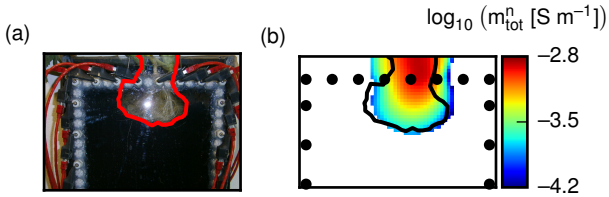

Figure 5.10: Comparison of root extension inferred from the photograph (a), indicated by overlaid solid lines, and m^{n}_{tot} results (b) for the first time step. Plotted in b) are only pixels from the root zone, i.e., pixels with a polarization response above the identified σ'' threshold value.

spectra) were classified into two categories, with and without root segments, as described in Section 5.3.4. The resulting "root system spectra" were then processed separately, and care was taken that the selected spectra exhibit a sufficiently strong and consistent polarization response to allow a reliable relaxation time analysis. Figure 5.10 shows the comparison of the m^{n}_{tot} results for the first time step with the extension of the root system according to the photograph. The root system area reconstructed from the spectral EIT results shows a good agreement with the known outer boundaries of the root system. Systematic changes in the overall root system response were analyzed by averaging the

$m^{\mathrm{n}}_{\mathrm{tot}}$ pixel values in the root system zone (Fig. 5.11). This average polarization response shows a steady decrease over time.

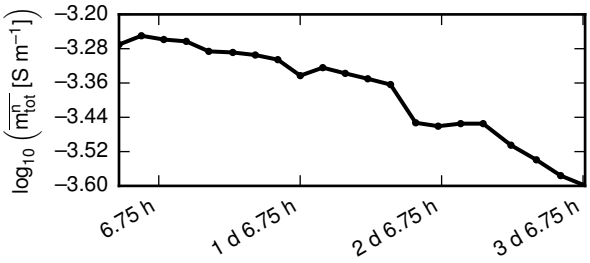

Figure 5.11: Mean value of DD-derived total chargeability $m^{\mathrm{n}}_{\mathrm{tot}}$ plotted versus time after start of the experiment. Average values were computed based on all pixels belonging to the root system zone.

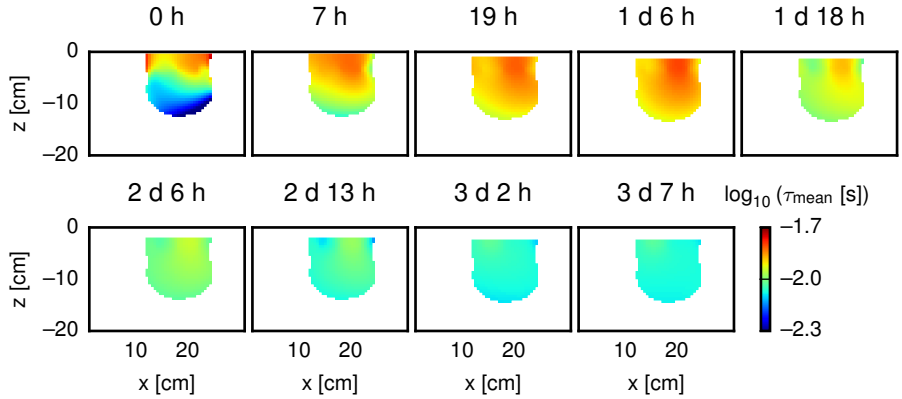

Figure 5.12: Spatial distribution of the DD-derived parameter τ_{mean} for selected time steps. Only pixels belonging to the root system zone are plotted. Masked (white) pixels were classified as water. The top boundary is adjusted according to the estimated water table for each measurement time.

Images of the DD-derived mean relaxation time τ_{mean} are presented in Fig. 5.12 for selected time steps. Spatial variations within the root system zone can be observed for each time step, as well as changes between time steps. Noticeable

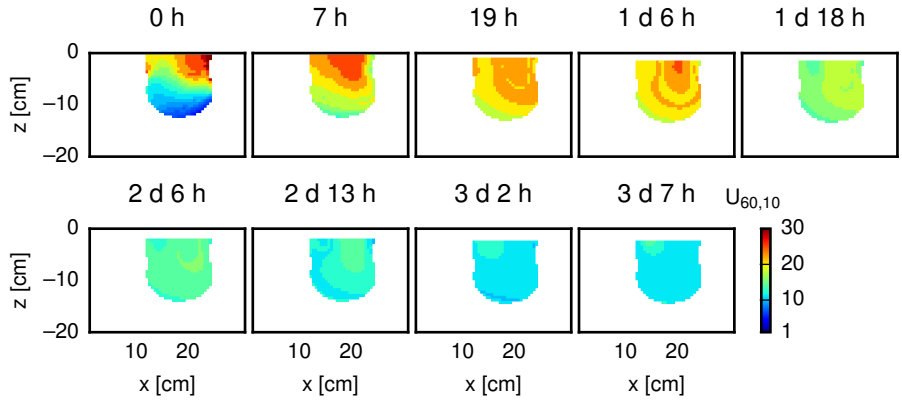

Figure 5.13: Spatial distribution of the DD-derived parameter $U_{60,10}$ for selected time steps. Only pixels belonging to the root system zone are plotted. Masked (white) pixels were classified as water. The top boundary is adjusted according to the estimated water table for each measurement time.

is a general trend from larger relaxation times (up to 18 ms) to smaller relaxation times (down to 9 ms) over the course of the experiment. Corresponding images of the uniformity parameter $U_{60,10}$ are shown in Fig. 5.13. Observed variations within images and between time steps indicate changes in the shape of the pixel spectra. Values approaching 1 indicate a stronger spectral dispersion, i.e., a focusing of the spectral polarization response in a narrower frequency band.

5.5 Discussion

The following discussion is divided into two parts: the biological discussion of the experiment, and the assessment of the geophysical methodology for crop root investigations.

5.5.1 Biological interpretation

In the course of the experiment a conductivity increase is observed (Fig. 5.7a-c), which originated at the bottom of the rhizotron and continuously migrated upwards (see supplement 1 for conductivity images of the whole rhizotron). This spatial pattern rules out the root system as the cause of the conductivity increase, and we attribute it to the dissolution and subsequent upwards diffusion of impurities at the bottom of the rhizotron frame. While a certain influence on the spectral parameter results (Figs. 5.9 and 5.12) is possible, we believe the impact to be relatively small for two reasons: First, the observed time evolution of $m^{\mathrm{n}}_{\mathrm{tot}}$ shows changes more or less centered around the stem region, not following the distribution pattern of the conductivity increase. Second, we observe changes in the spectral behavior of the signatures (in terms of τ_{mean}), which can not be explained by an increase in conductivity. However, in future experiments the background conditions should be monitored and the plant only inserted once equilibrium of the system has been reached.

The physiological response of the root system to the imposed nutrient deprivation and possible anaerobic conditions is reflected by a decreasing overall polarization response (Figs. 5.9 and 5.11). Note that it is highly unlikely that the dropping water table caused this decrease in polarization, as more current is forced through the main bulk of the root system with the dropping water table. Thus should actually increase the polarization response, assuming that this response does not change due to physiological reactions in the root system. Note that the water table always remains above the actual root system and only drops in the stem area. We attribute the observed decrease in polarization to a general weakening of the EDLs present in the root system. The cause of this EDL weakening can be manifold and can not be isolated in this study. In the following we shortly discuss two (possibly superimposing) approaches to

interpretation:
The first approach is to consider ion (nutrient) concentration in the fluid phase of the EDL. Plant-root systems represent a hydraulically connected system whose water potential is primarily controlled by water transpiration at the leaves. In case of intact hydraulic connectivity in the plant, a decrease in water potential due to transpiration causes water and solute uptake by the roots, and water and solute flow from the roots to the leaves (Tinker and Nye, 2000). While it is possible that solutes were taken up by the plant in our experiment, no nutrients were available to the plant. Accordingly, we expect for our experiment that the root regions farther away from the stem, that is the regions with highest water potentials, were depleted of nutrients first, as the available nutrients were translocated to the stem and the leaf areas, following the (negative) water potential gradient. Especially, if dynamic responses are considered, plants can sense, and react to, stress situations and can initiate changes in solute transport and hydraulic membrane conductivity properties (e.g., Clarkson et al., 2000; Schraut et al., 2005). As a result, without being able to pinpoint the exact cause, the ion concentration could have decreased in the vicinity of cell membranes in these depleted areas, leading to a weakening of associated EDLs, in turn implying a decreased polarization response. The second approach is to consider changes in the electrical surface characteristics of cell membranes in reaction to the imposed physiological stress situation. These surface characteristics could have changed in response to certain active triggers, such as stress hormones, or as a result of balancing processes across the membranes. In light of these considerations, the stem should retain a more stable electrical polarization as it is likely not as much affected by physiological responses as the other, smaller, root segments (in terms of larger nutrient storage capability, better air availability, and general metabolic activity). This is consistent with the time-lapse imaging results, which show more stable polarization responses in the stem area (Fig. 5.9).
Another indication of the physiological stress response are the changes in the shape of the spectra (Figs. 5.12 and 5.13). Relative changes in the relaxation time contributions suggest changes in the underlying structures that control the polarization response at certain time steps. These changes might be related to new or ceased ion fluxes and their varying pathways within the root systems, as well

as to varying surface charges at various structures such as the endodermis. If these structures change, or break down, in response to stress situations, corresponding changes in the electrical properties can be expected. However, given its spatial resolution limits, EIT does not allow to distinguish these different structures directly.

Assuming that relaxation times can be linked to length scales of the underlying polarization processes, the observed signatures indicate multiple polarizable structures. However, the methodology applied here prevents further investigations in this direction. In contrast to most of the existing studies, we did not inject current directly in the stem, and correspondingly the explicit current pathways are much less defined in our approach. This prevents (at this stage) a simple formulation of an equivalent lumped electrical circuit model. Comparison of measurements using the procedure presented here with a stem-injection approach could, however, help elucidating the origin of polarization and its length-scale characteristics. Current injection into the stem forces the current to flow through the root system and through all radial layers of the root segments, and thus a stronger polarization response from inside the root segment can be expected, as well as the polarization of additional membrane structures. Additional experiments could focus on establishing relationships between recovered spectral polarization parameters and root specific parameters, such as surface area and root length density. The use of sophisticated electrical models, coupled to existing macroscopic root development and nutrient uptake models (e.g., Dunbabin et al., 2013; Javaux et al., 2013), could provide further insight to identify the key processes that control the electrical polarization signatures of root systems. While this study focused on establishing the EIT methodology for crop root research, in future studies also physiological plant parameters should be monitored, such as, for example, leave transpiration rates, which could help to identify the key processes that control electrical polarization signatures.

As already pointed out by Repo et al. (2012), single-frequency measurements are of limited value to determine electrical polarization properties of root systems, both in terms of spatial distribution and polarization strength, and our spectral EIS results (Figs. 5.5, 5.7, 5.12, and 5.13) support this finding. It becomes even more obvious when interpreting the polarization signature as an EDL response, which typically exhibits a strong frequency dependence. It should be

noted that the frequency range analyzed here in an imaging framework (0.46 Hz to 220 Hz) does not cover the full bandwidth that could be, in principle, measured with the presented setup, and corresponding advances are within easy reach (e.g., Huisman et al., 2015). However, reliable measurements at lower and higher frequencies will require careful adaptations in measurement and data processing procedures.

The classification of image pixels into two classes can not, and should not, be treated as an universal analysis procedure. For the simple conditions in this experiment a clear distinction between root system area and surrounding medium could be made, which facilitated the assessment of the method (e.g., Fig. 5.11), and can potentially be used for further experiments with root systems in aqueous solutions. However, the primary results of this study do not rely on this specific classification, and likewise soil-based experiments could be conducted with the measurement setup.

This study does not involve any kind of granular substrate and thus excludes possible influences from such a background material. In fact, significant additional electrical polarization can be expected when soil surrounds the root system, which will superimpose on the root system response. Organic matter and micorrhiza may also contribute to the overall electrical signature. Finally, a variable water content can significantly influence the electrical response of the soil and the root system, either directly by influencing present EDLs, or indirectly by inducing physiological processes such as nutrient uptake, which in turn can affect the electrical signatures of the EDLs.

5.5.2 Geophysical methodology

The observed polarization response of the root system is relatively weak and its measurement requires a corresponding accuracy of the measurement instrument. This accuracy is provided by the EIT-40 tomograph that was used in this study (Zimmermann et al., 2008). The high accuracy of the instrument was recenty also demonstrated in an imaging study on soil columns (Kelter et al., 2015).

If a fixed data weighting is used, which we believe to produce more reliable and consistent results for multi-frequency time-lapse data, data selection, i.e., filter-

ing, becomes a relevant step in the processing pipeline before the inversion and subsequent spectral analysis. While it is common to remove outliers from geophysical data prior to inversion, filtering becomes challenging if multiple time steps are to be analyzed in a consistent way. The number of retained data points varied slightly between time steps, although the same filtering criteria were applied. This can be explained by data noise and varying contact impedances at the electrodes. However, data quality was sufficient enough to produce consistent imaging results for all time steps and frequencies, as is evident from the impedance spectra (Fig. 5.5).

Another important issue is the data processing flow in the imaging framework, coupled with the spectral analysis based on the Debye decomposition. The inversion algorithm produces spatially smooth images; however, the images were computed for each frequency separately, and thus no smooth variation between adjacent frequencies is enforced in the inversion, although physically expected. Corresponding inversion algorithms have been developed recently (Kemna et al., 2014; Günther and Martin, 2016) and could lead to a further improvement of the multi-frequency imaging results. However, a similar constraint is introduced by the Debye decomposition, where smoothness is imposed along the relaxation time axis (which directly corresponds to the frequency axis). Minor noise components can thus be expected to be smoothed out both spatially and spectrally.

EIT applications in pseudo-2D rhizotron containers require specific processing steps. The determination and testing of correction factors accounting for modeling errors due to an imperfect 2D situation (Fig. 5.2) is as important as the correct representation of the rhizotron in terms of the FE grid underlying the inversion process (Fig. 5.3). Not taking these aspects into account can produce artefacts in the imaging results that can easily be misinterpreted in biological terms. Similarly, data errors should not be underestimated, as this can also produce misleading imaging results when data are overfitted (e.g., Kemna et al., 2012). Contrarily, an overestimation of data errors can mask information present in the data. Among others, raw (impedance) data and imaging (complex conductivity) data should be checked for consistency and plausibility by taking into account the much lower spatial resolution of the raw data (cf. Figs. 5.5 and 5.7).

Electrical imaging results exhibit a spatially variable resolution, which usually decreases with increasing distance from the electrodes. One could question the usefulness of such a method if the resolution can not be clearly determined. Nonetheless, even limited spatial information allows for a distinction of polarizing and non-polarizing regions in the investigated object. This is not possible with spectroscopic measurements, and correspondingly it is more difficult with such measurements to analyze spatially distributed root systems. We suspect that some of the reported inconsistencies in electrical capacitance relationships with biological parameters (e.g., Kormanek et al., 2015, and references therein) can be ascribed to missing spatial information in the measurement data. The resolution of EIT is not sufficient to image microscopic current flow paths in the root system, but the imaged macroscopic electrical properties can be compared for different regions of the root system, for instance the (older) top part of the root system compared to the younger lower part. Future improvements in experimental setups (electrode distribution and spacing) and measurement configurations will most probably lead to increased spatial resolution.

Another advantage of the EIT approach presented in this study is the possibility of arbitrarily placed electrodes (as long as the resulting geometrical arrangement allows for a sufficient measurement coverage of the root system), in contrast to using stem electrodes as commonly done in previous studies. If the stem of a plant is used to inject current into the root system, measurements, and resulting correlations to biological parameters, are highly sensitive to the electrode position above the stem base (Dalton, 1995; Ozier-Lafontaine and Bajazet, 2005). Another problem is that electrodes can not be inserted into the stem if damage of the plant is to be avoided. However, injections can also be realized by use of non-invasive clamps.

Also important for the experimental design is the time scale of the physiological response to be monitored. It took approximately three and a half hours to complete a single time frame of the spectral EIT measurements presented here. Physiological processes taking place on a shorter time span can thus not be resolved. Reducing the data acquisition time can be achieved by either reducing the number of low-frequency measurements or the number of current injections. This can result in a loss of spectral and spatial resolution if measurement configurations are not suitably optimized to compensate for the lost number of

measurements.

5.6 Conclusions

The goal of this study was to investigate and establish spectral (i.e., multifrequency) EIT as a non-invasive tool for the characterization and monitoring of crop root systems. Based on working hypotheses derived from the state of science in the involved fields, including geophysics and plant science, we designed and conducted a controlled experiment, in which the root systems of oilseed plants were monitored in a 2D, water-filled rhizotron container. Since water does not exhibit a significant polarization response in the considered frequency range, the observed electrical polarization response could be attributed to the root systems.

The spectral EIT imaging results revealed a low-frequency polarization response of the root system, which enabled the successful delineation of the spatial extension of the root system. Based on a pixel-based Debye decomposition analysis of the spectral imaging results, we found a mean relaxation time of the root system's polarization signature in the covered frequency range of the order of 10 ms, corresponding to a frequency of the order of 15 Hz. Importantly, upon ongoing nutrient deprivation (with possibly anaerobic conditions) the magnitude of the overall polarization response steadily decreased and the spectral characteristics systematically changed, indicating changes in the length scales on which the polarization processes took place in the root system. The spectral EIT imaging results could be explained by the macroscopically observed and expected physiological response of the plant to the imposed stress situation. The identification of the root structures and processes controlling the root electrical signatures, however, was beyond the scope of this study given the inherent spatial resolution limits of EIT. Nonetheless the recovered electrical signatures could be used in the future to develop and calibrate improved macroscopic root electrical models which incorporate microscopic processes.

We showed, for the first time (to the best of our knowledge), that spectral EIT is a capable non-invasive method to image root system extension as well as to monitor changes associated with root physiological processes. Given the applicability of the method at both laboratory and field scale, our results suggest

an enormous potential of spectral EIT for the structural and functional imaging of root systems for various applications. In particular at the field scale, non-invasive methods for root system characterization and imaging are lacking and EIT seems to be a very promising method to fill this gap. In future studies we will aim at further proving the suitability of spectral EIT to monitor physiological responses in different situations and to different stimuli, at both laboratory and field scales.

5.7 Data Availability

Measured raw data, electrical imaging data, spectral analysis results, and Python scripts used to generate the figures can be accessed at https://doi.org/10.5281/zenodo.260087

CHAPTER 6

EIT on crop root systems in solutions and substrates

6.1 Introduction

Chapter 5 presented a detailed case study of using EIT to characterize crop root systems. These results also show that EIT can be used to monitor root systems with regard to certain physiological changes. This directly raises questions about the biological possibilities and restrictions of this method. What processes can be monitored, with what spatial and temporal resolution? Which ambiguities exist between processes, i.e., which physiological processes in root systems can be distinguished by electrical polarization measurements? Ultimately these questions can only be answered by a widespread adoption of EIT and integration in biological studies. Experiments must provide reliable information gathered by means of established methods, while still allowing for an optimal assessment of EIT in this setting.

With these goals in mind, this chapter presents various laboratory experiments on crop root systems, highlighting additional aspects of EIT measurements in connection with crop root systems not addressed in the previous chapter. The experiments highlight the versatility of EIT, showing different responses to various external physiological stimuli such as nutrient deprivation and decapitation. Also, measurements in substrates, such as topsoil and peat, are presented. Experimental procedures largely follow those already described in chapter 5, unless otherwise noted. However, the experiments were conducted over the span of multiple years, and certain aspects mirror the corresponding development – and evolution – of EIT in this biological setting. These aspects include

measurement frequency ranges and frequency densities that were unsuitable for a spectral analysis, i.e., an analysis using the Debye decomposition scheme. The presentation style of this chapter aims to highlight the various electrical signatures measured in response to the external stimuli, and does not aim at presenting the full geophysical analysis procedure of each experiment.

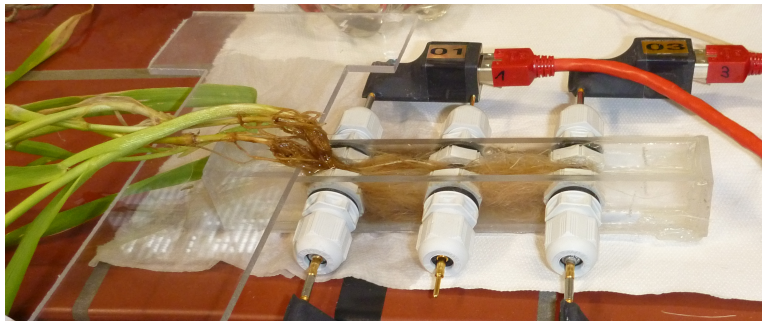

Figure 6.1: Measurement setup for four-point EIS measurements. Photograph by Matthias Kelter.

6.2 Measurements in aqueous solutions

6.2.1 Mass dependence of EIS signals

Root systems can be imaged using EIT, as shown in chapter 5. While a systematic dependence of the polarization magnitude on the physiological state of the root system was found, the fact that the extension of the root system could be imaged indicates a direct relationship of polarization magnitude to the effectively polarizable EDL area within the root system. Here another experiment is conducted which examines the dependence of polarization magnitude on root mass. The root mass serves as a direct measure of active EDL area, assuming only minor variations in root diameters between the measured root systems.
Correspondingly it is assumed that more root mass under investigation, i.e., more root mass located in the current path ways, should also lead to an increase in measured polarization strength. Three barley root systems of different mass are measured using EIS in a small measurement container (Fig. 6.1). To increase the available masses, five combinations of these plants are measured (Table 6.1). Mass numbers refer to the root mass after drying. All plants were grown in hydroponics, and correspondingly there is a large (unfortunately unspecified) age difference between plants 1 and plants 2/3. Results in this subsection were already partially presented in Kelter (2011) and Kemna et al. (2011).
Conductivity spectra for the water background and all root combinations show no differences in the real part of the apparent conductivity σ'_a (Fig. 6.2a). How-

ever, polarization (σ_a'') signatures show a clear spectral behavior, and overall polarization increases significantly with increasing root mass (Fig. 6.2b). The subsequent application of the Debye decomposition scheme shows a consistent increase in $m_{\text{tot}}^{\text{n}}$ values with increasing root mass (Fig. 6.2c), corresponding to an increase in overall polarization signatures. All three investigated relaxation times (τ_{mean}, τ_{50}, and τ_{peak}^{1}) increase with root mass, too, although with much larger variations (Fig. 6.2d).

The dependence of polarization magnitude on root mass supports the hypothesis that polarization signals increase with increasing EDL surface size. The results also agree with a linear relationship between measured capacitance and root fresh weight that is reported by, among others, Ozier-Lafontaine and Bajazet (2005) and Dietrich et al. (2013). However, if relaxation times are assumed to be proxies to length scales of the polarization processes, then a mixing of root systems should not increase characteristic relaxation times beyond those observed for the single root systems, that is, a mixing of materials with different characteristic relaxation times should only result in the superposition of relaxation processes, unless a significant interaction between the mixed agents occurs. It is highly unlikely that roots of different plants interact in such a short time span. Possible explanations for the nonetheless measured increase in relaxation times for mixed plant systems include a denser packing of roots, which could cause a better connection between individual roots and the corresponding emergence of continuous large-scale EDLs, and physiological responses of the plants between the measurements that were not accounted for (e.g., decay, growth, stress).

plant specifier	weight [mg]
barley 1	12.8
barley 2	103.3
barley 3	124.4
barley 2+3	227.7
barley 1,2,3	240.5

Table 6.1: Fresh weights of the plant combinations used for EIS measurements. The mass of combined roots is calculated from the individual weights.

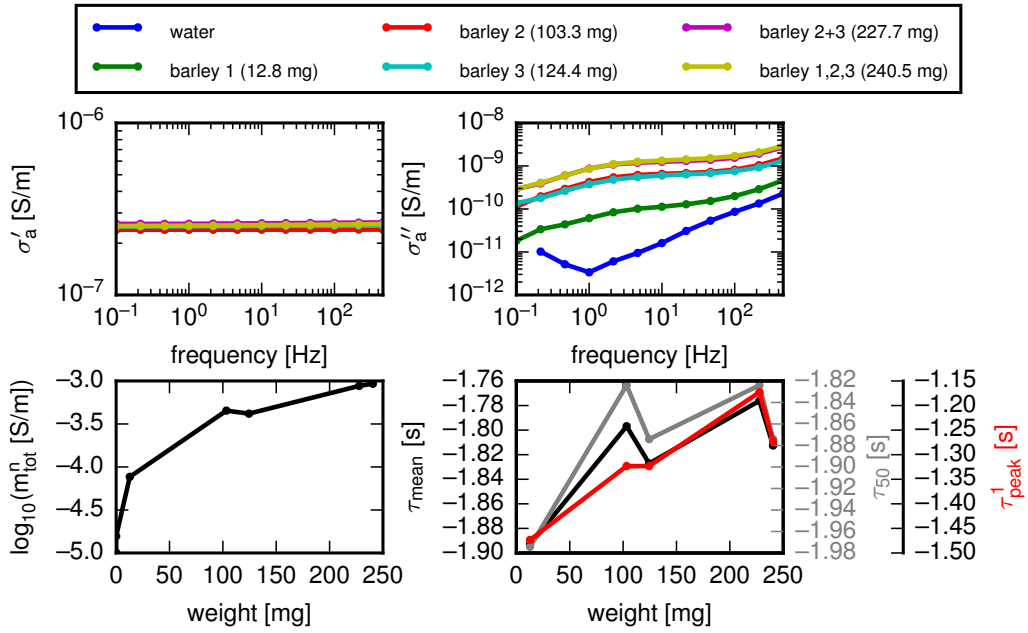

Figure 6.2: Apparent conductivity spectra measured on barley root systems: a) σ'_a b) σ''_a. Corresponding Debye decomposition results: c) total, normalized chargeability m^n_{tot} d) relaxation times (τ_{mean}: black, τ_{50}: gray, τ^1_{peak}: red). The water measurement is not shown here due to negligible polarization strength.

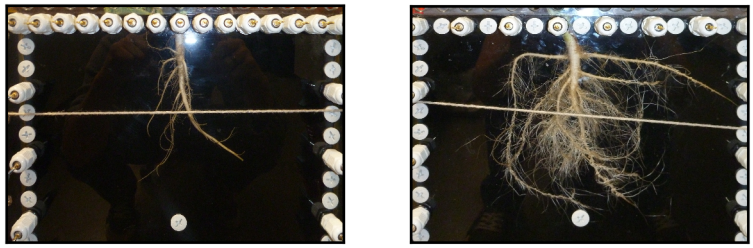

Figure 6.3: Photographs of the oilseed root system 11 days apart. The horizontal thread is used to hold the rhizotron in the measurement position.

6.2.2 Imaging root growth in water

Similar to the polarization increase observed for increasing root mass of different plant root systems, root growth was also monitored using EIS (Kelter, 2011). In the following the results with regard to spatial, i.e., imaging, processing are presented. An oilseed plant was initially taken from the field and then kept in a hydroponic solution. EIT measurements were conducted at day one and at day 11 (Fig. 6.3). Before each measurement the plant was rinsed with tap water to remove residual nutrient solution. Measurements were conducted in tap water, and imaging analysis, including the Debye decomposition of intrinsic pixel spectra, was done in accordance to the procedures described in chapter 5. Early results of this experiment were presented in Kelter (2011) and Kemna et al. (2011).

The plant showed a significant increase in root mass during the experiment (Fig. 6.3). The diameter of the tap root and larger lateral roots increased, as did the amount of finer roots.

The apparent in-phase conductivity σ'_a, as measured directly above the root system, shows a decrease between measurements (Fig. 6.4a). However, σ''_a shows an increase in polarization strength over the whole frequency bandwidth. In addition, changes in the spectral behavior can be observed (Fig. 6.4b). Inversion results show corresponding results, both in σ' and σ'' (Fig. 6.5). Additionally an increase of the polarized area is observed between measurements (Fig 6.5). Recovered intrinsic spectra from a pixel located in the stem area show results

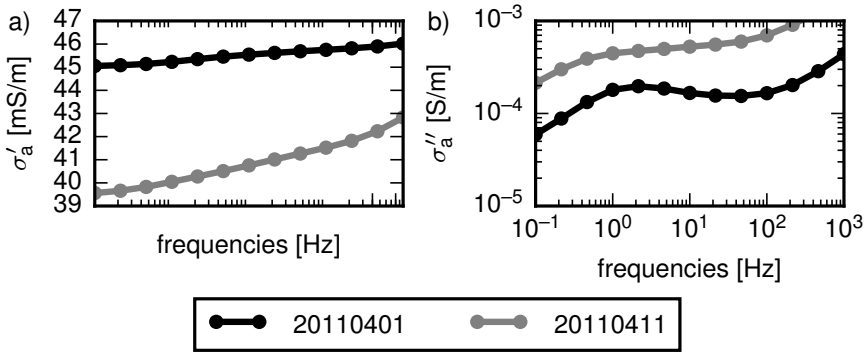

Figure 6.4: Apparent conductivity spectra measured on a dipole-dipole configuration directly above the root system for the two growth states.

in accordance with the raw data results (cf. Figs. 6.4 and 6.6). Debye decomposition results show changes in characteristic relaxation times τ_{mean} and τ_{50} (Fig. 6.7).

These results indicate that the growth evolution of the root system can be characterized using EIT. An increase in root mass and extension was mirrored in the increased σ'' signature strengths. In comparison to barley (Section 6.2.1) the oilseed plant investigated here evolved primary and secondary roots, resulting in a larger distribution of root diameters. While a certain spectral dynamic was observed, results did not differ very much in comparison to barley root measurements (cf. Fig. 6.2). Changes in the real part of the conductivity between measurements can be attributed to a change in salinity of the tap water used. In addition, the amount of ions from the nutrient solution still present on the root surface can vary between measurements.

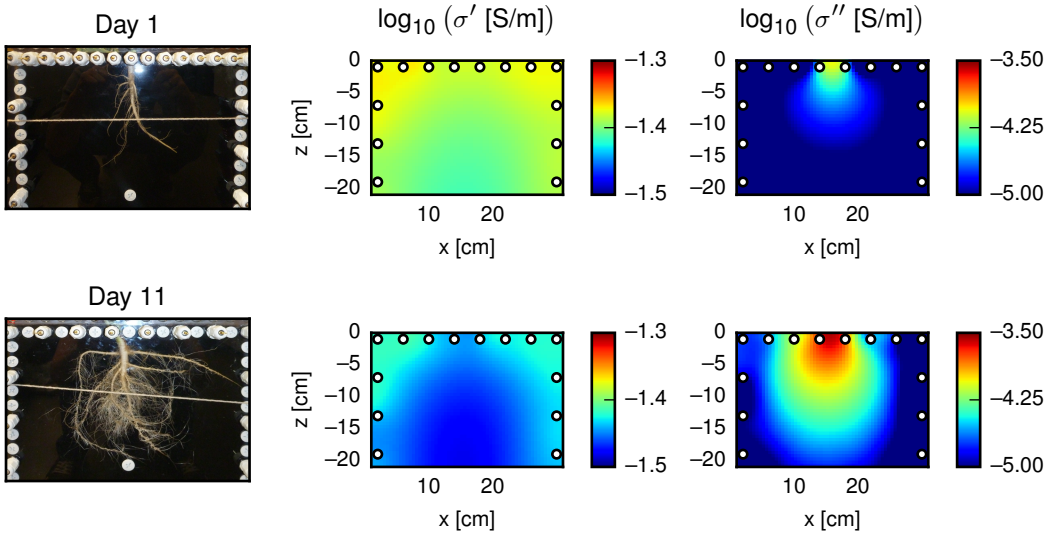

Figure 6.5: Inversion results (4.64 Hz) for the two growth states.

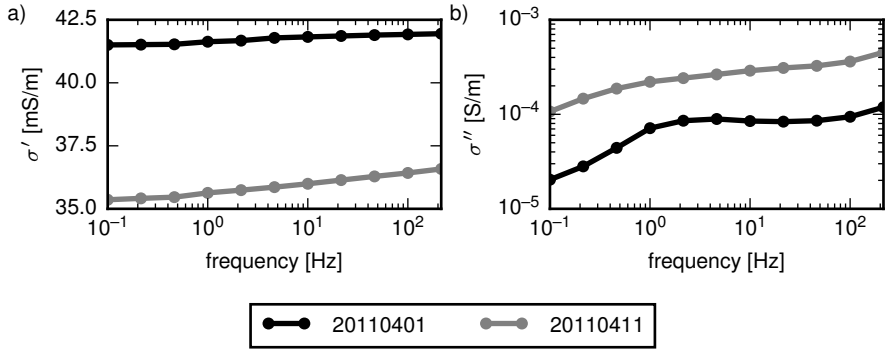

Figure 6.6: Intrinsic spectra recovered from imaging results. A pixel directly located beneath the stem area was extracted.

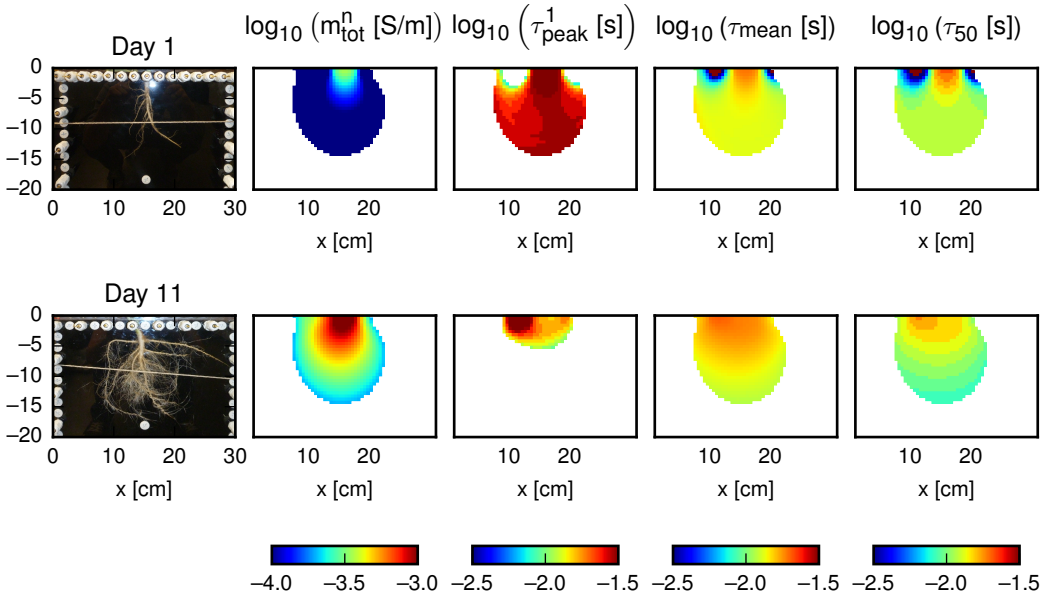

Figure 6.7: Debye decomposition results for the two growth stages. Results for τ^1_{peak} are only reported where distinct peaks could be recovered from the relaxation time distributions.

6.2.3 Monitoring a decapitated root system in a nutrient-rich environment

The oilseed plant already used in subsection 6.2.2 was furthermore cultivated in hydroponics. The stem was cut off after 53 days, and the subsequent electrical response of the root system was monitored using EIT. Measurements took place in tap water, but the root system was kept in nutrient solution between measurements.

Measured apparent conductivity signatures show slight increases in in-phase conductivity over the measurement period (Fig. 6.8a), while polarization responses decrease over the whole frequency band (Fig. 6.8b) with time. Inversion results show that in-phase conductivity changes cannot be clearly attributed to the root system, while polarization anomalies map well to the placement and extension of the root system in the rhizotron (Fig. 6.9, cf. Fig. 6.3). The polarization anomaly decreases in extension and strength over time. Debye decomposition results confirm the decrease in polarization response, but also show distinct changes in the relaxation times τ_{mean} and τ^1_{peak} (Fig. 6.10, third and fourth rows). From a physiological point of view, cutting off the stem stops the symbiotic interaction between leaf area and root system. No sugar can be synthesized without using photosynthesis, which has a major impact on the energy supply that is required for growth processes. Also, water transport by means of transpiration is completely interrupted, preventing any effective long-distance nutrient translocation within the remaining root system (Tinker and Nye, 2000). Consequently, remaining nutrient supplies will be either stored or used in place, and eventually the remaining root system will die off. We interpret the observed decrease in polarization response over time as the decrease of EDL polarization strength induced by these physiological reactions. The decrease in spatial polarization response could indicate that the thicker central root elements remain structurally and physiologically intact over a longer time span, thus sustaining EDL strength and continuity over a longer time span. However, changing relaxation times were observed for the whole root system. This in turn could indicate that physiological processes, perhaps nutrient translocation and consumption, occur even in the larger, more stable root element areas nearer located to the stem.

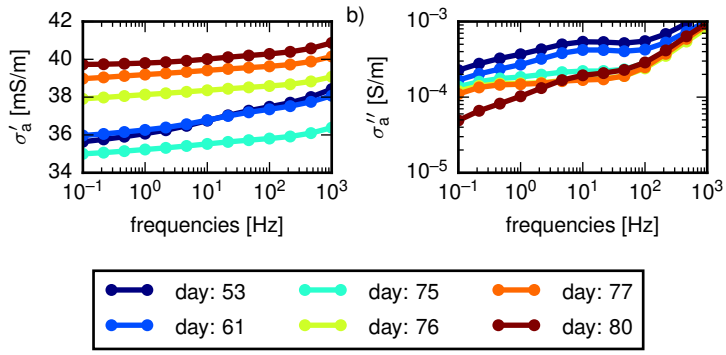

Figure 6.8: Apparent conductivity spectra measured above the root system after stem was cut off.

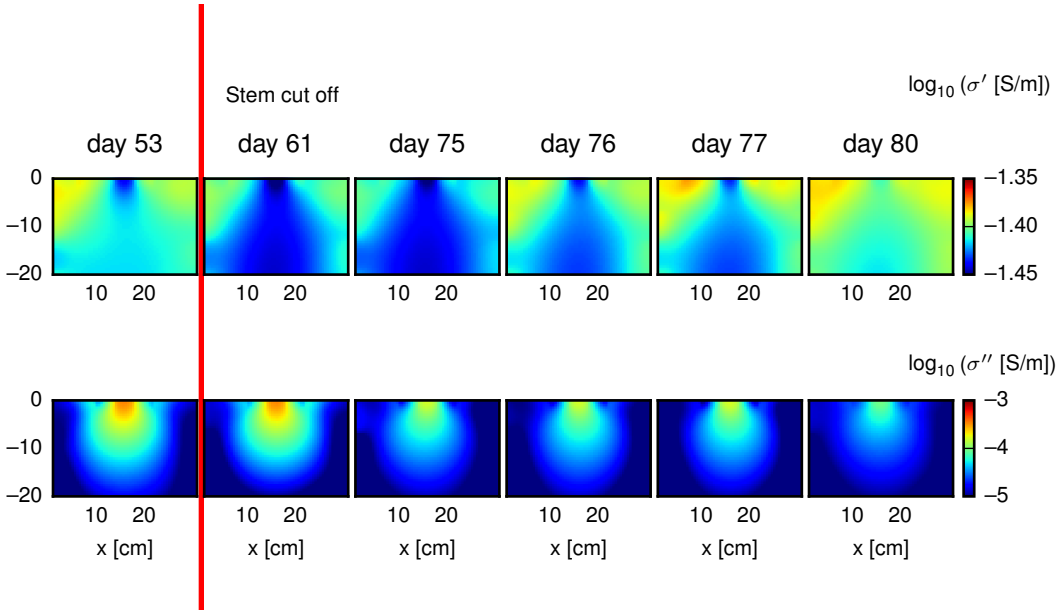

Figure 6.9: Inversion results (4.6 Hz) following the decapitation of the oilseed plant.

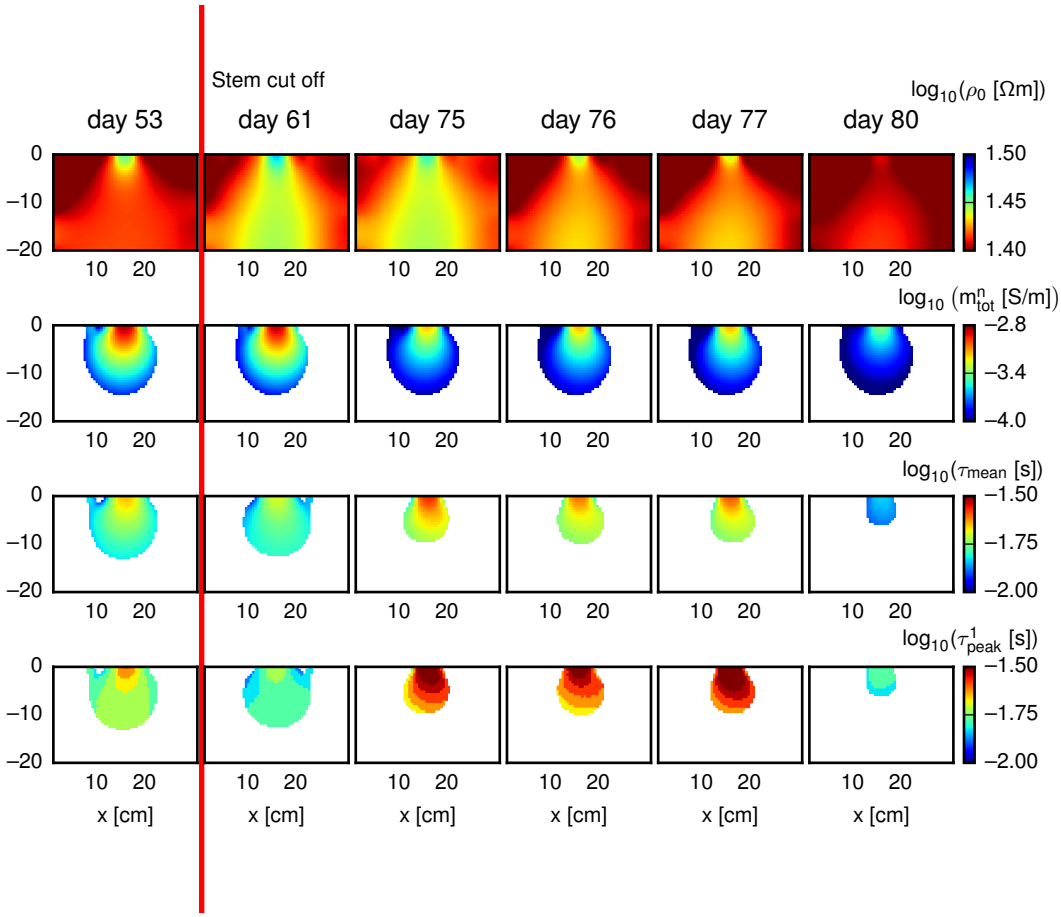

Figure 6.10: Debye decomposition results for time steps after decapitation. Only pixels classified as root are shown. Classification is done by applying a threshold to $m^{\mathrm{n}}_{\mathrm{tot}}$ determined from the lower part of the rhizotron, which is guaranteed to be free of root elements.

6.2.4 Monitoring nutrient deprivation in intact and decapitated plants

Figure 6.11: Setup of EIT measurements with two oilseed plants in one rhizotron. Left: Initial setup with uncovered root systems. Right: measurement setup with decapitated plant and covered root systems.

The previous sections presented the monitoring of plants under nutrient deprivation (section 5) and after decapitation (section 6.2.3). One logical continuation is now to combine these two experiments to investigate the behavior of electrical signatures of an intact plant in comparison with a decapitated plant under nutrient deprivation. Therefore, an experiment comprising the simultaneous monitoring of two oilseed plants within one rhizotron was conducted. Similar to the experiment in section (6.2.3), two plants were taken from the field (Klein-Altendorf test site, Meckenheim, Germany) and kept in hydroponics before the experiment. Both plants were placed next to each other in a rhizotron filled with tap water and EIT measurements were conducted continuously for 7 days (Fig. 6.11). The right plant was decapitated on day 1, and both plants were illuminated with a growth lamp for 12 hours a day. Water was circulated using an air ventilation system between EIT measurements. In addition, on day 5 both plants were taken out of the rhizotron and placed in a nutrient solution for 20 hours. Afterwards they were relocated to the rhizotron and EIT monitoring was

resumed. The experiment had four objectives:

1. Establishing the possibility of concurrent monitoring of two root systems in one rhizotron container.

2. Monitoring of an intact plant under nutrient stress with high temporal and spectral resolution, similar to the experiment already discussed in chapter 5. However, a plant originating from the field was used in this new experiment, showing more pronounced primary tap root elements.

3. Monitoring of a decapitated plant under nutrient stress analog to section 6.2.3, with increased temporal and spectral resolution.

4. Monitoring of possible reactions of both root systems to nutrient availability after prolonged nutrient stress.

Measurements and subsequent analysis procedures were applied as already presented in chapter 5, unless otherwise noted. In total 40 measurements with an individual measurement time of approximately four hours were conducted over 7 days. This resulted in an approximate measurement interval of 5 hours. Measurements were conducted at 35 frequencies between 0.46 Hz and 45 kHz. Based on the intrinsic spectra recovered from imaging results, the subsequent Debye decomposition was done using data up to 300 Hz (Fig. 6.12).
Total polarization responses decreased for the intact plant during the experiment (Fig. 6.13 left), while polarization did not vary much for the decapitated plant system (Fig. 6.13 right). No clear trend can be observed for the measurements before and after the 20 hours that the plants were kept in nutrient solution (between hours 98 and 118). However, a large jump towards smaller relaxation times is observed for the intact plant after the time in nutrient solution (Fig. 6.14 left). No clear trend is visible in the first 88 hours, and relaxation times slowly relax back towards the values of the pre-nutrient solution (at hours 152 and 156). The decapitated plant does not show any variations over the course of the experiment (Fig. 6.14). When pixels of the root area are averaged for each time step, it can be observed that the decrease in total polarization response is delayed for the time the intact plant spent in nutrient solution (Fig. 6.15a). The

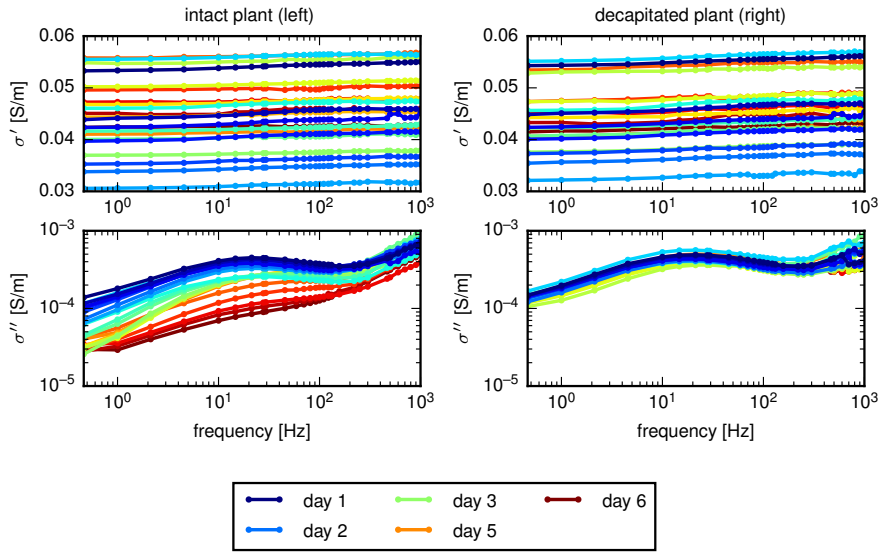

Figure 6.12: Intrinsic pixel spectra recovered from imaging results for two pixels exemplary for the intact plant (left) and the decapitated plant (right).

decapitated plant, again, shows no trend in the averaged values (Fig. 6.15b). Averaged relaxation times, however, exhibit a jump in values during the time the plants spent in nutrient solution (Fig. 6.15c), while the decapitated plant does not show any trend in relaxation times, either (Fig. 6.15d).

As the experiment presented in chapter 5 monitored the physiological reaction of an intact plant to nutrient deprivation, results can be directly compared to those of the intact plant. The only difference between those two experiments is the origin of the plants: Chapter 5 monitored a plant completely grown in hydroponics, while the present experiment investigated a field plant. This resulted in more pronounced tap roots of the latter root system. Also, in the former experiment the rhizotron was not ventilated between measurements. Both plants show a continuous decrease in polarization response both in the total polarization (by means of $m^{\mathrm{n}}_{\mathrm{tot}}$) and in the spatial domain, i.e., detected root area (cf. Figs. 5.9 and 6.13). While relaxation times generally decreased in the hydroponically grown root system (Fig. 5.12) they did not change considerably in the field plant,

unless treated with nutrient solution (Fig. 6.13). Corresponding polarization responses indicate that in both plants EDL polarization broke down over time. In combination with the relatively stable polarization response observed for the decapitated plants this suggests that an intact plant system exhibits a faster decrease of EDL polarization strength under nutrient deprivation, compared to the EDL polarization in decapitated plants. One major difference here is that intact plants govern water transport by inducing a negative water potential through evaporation at the leaves, which leads to an effective water/nutrient flow from the roots to the leave area (Tinker and Nye, 2000). Thus the intact plant is still capable of translocating water and nutrients effectively within the whole plant, leading to an optimal consumption of all available nutrients. However no new nutrients enter the system and only tap water is taken up by the roots in order to transport nutrients. In comparison, the decapitated plant has no significant water circulation going on (diffusive and osmotic processes are only effective over small length scales or large time scales) and due to the missing stem there is a strong reduction in nutrient consumption. Therefore it can be assumed that nutrients stay within the root system and are not diluted by large quantities of nutrient deficient tap water entering the system. It is thus feasible to assume that the EDLs at the cell membranes can be sustained for a longer time and exhibit stronger polarization signals compared to the double layers in the intact plant. However, even the decapitated root system will at some point degrade, which could be indicated by changes in the relaxation times, which in turn indicate changes in the length scales of the polarization signals. This behavior was observed in the decapitation experiment in section 6.2.3, which ran for a much longer time, and correspondingly captured the eventual decay of the decapitated plant. The hypothesis that nutrient translocation and consumption drives the decreasing polarization signals in the intact root system is supported by the last part of the experiment, where both plant systems were put into a nutrient solution for 20 hours. Only the intact plant shows changes in the polarization response, while the decapitated root system does not react to the temporary nutrient supply. Changes in recovered relaxation times of the intact plant additionally suggest a reaction to the nutrients. However, polarization strengths did not return to the initial magnitudes, indicating a too large decay of the intact plant to recover completely.

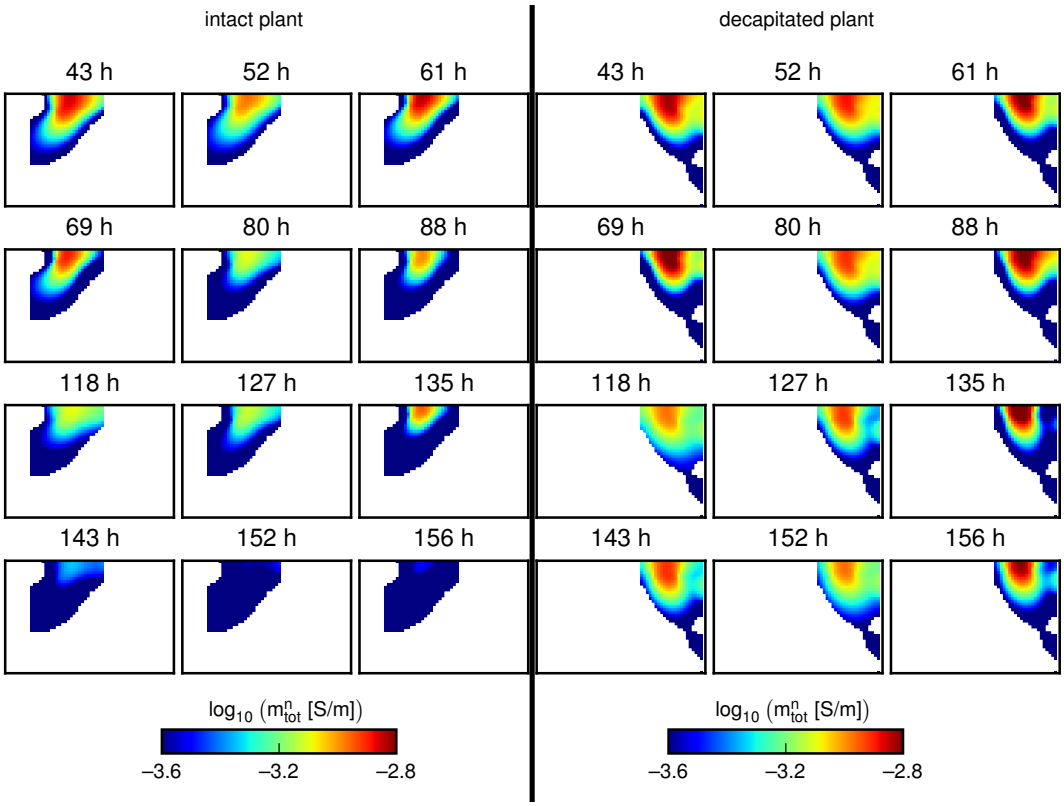

Figure 6.13: Total chargeability (m^{n}_{tot}) results for selected time steps. Results for both plants are shown (left: intact, right: decapitated plant). Placement of both root systems in nutrient solution was commenced between measurements at 98 and 110 hours. Pixels not classified as root system are masked.

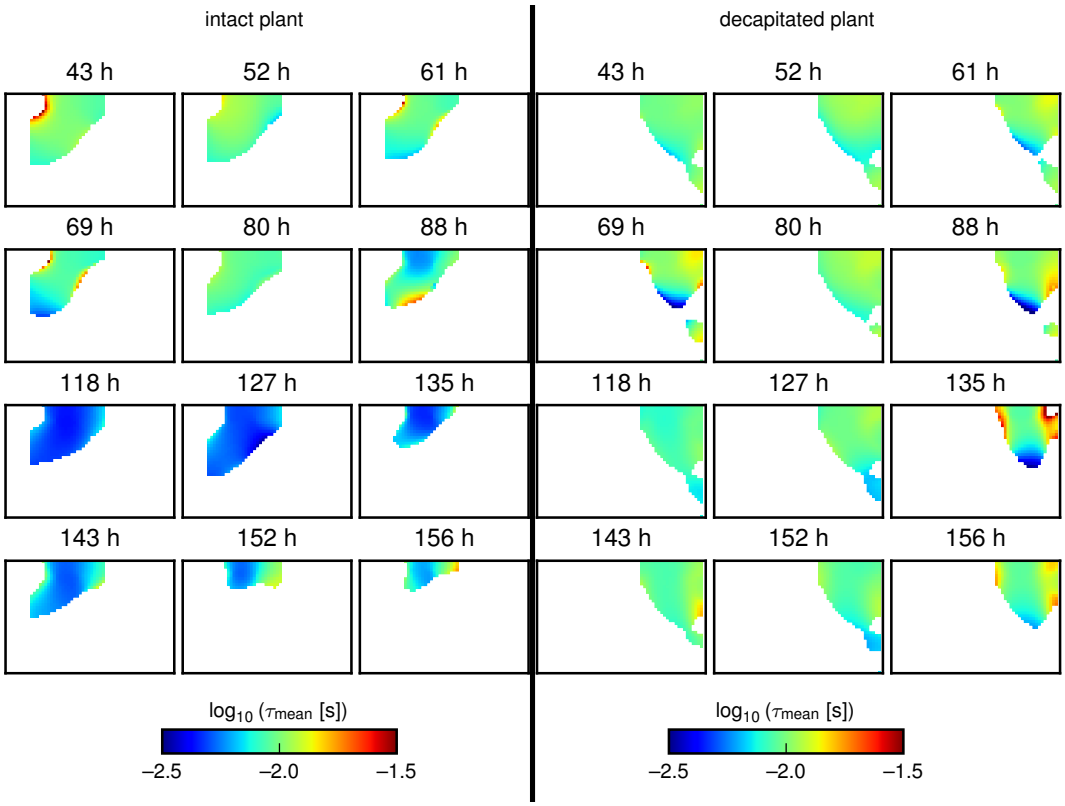

Figure 6.14: Mean relaxation time (τ_{mean}) results for selected time steps. Results for both plants are shown (left: intact, right: decapitated plant). Placement of both root systems in nutrient solution was commenced between measurements at 98 and 110 hours. Pixels not classified as root system are masked.

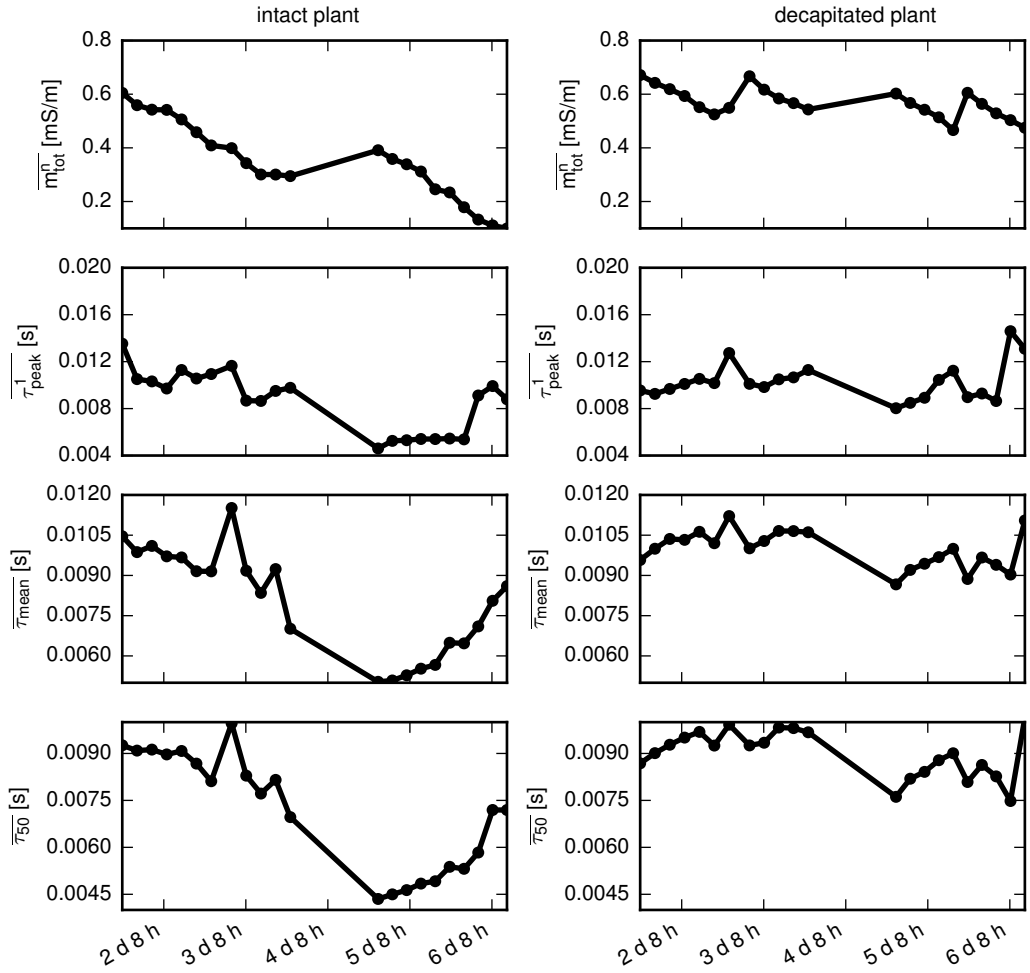

Figure 6.15: Averaged spectral SIP parameters recovered from the Debye decomposition of individual pixels. Only pixels classified as root pixels are taken into account.

6.2.5 Monitoring of day/night cycles with EIS

Figure 6.16: Measurement setup of EIS monitoring of day/night cycles on an oilseed root system.

The final experiment on plant root systems in aqueous solution presents the spectral monitoring with very high temporal resolution (Stamm et al., 2016). One hydroponically grown oilseed plant was placed in nutrient solution ($\sigma \approx 1000\,\mu$S/cm) for multiple days, and spectral measurements between 0.1 Hz and 45 kHz were conducted every 14 minutes. No reciprocal or tomographic data were acquired due to the requirement of high-speed measurements. Only one four-point spread located directly above the plant stem, previously selected to yield reliable and strong polarization signals, was captured. Spectral signatures were analyzed with respect to the change of spectral characteristics of oilseed rape root systems in response to changing light stimuli, i.e., day and night patterns. Light was switched on for 11.5 hours per day (7:30 a.m. to 7 p.m.). In

order to prevent large variations in the water table (due to evaporation and root water uptake), as observed in the experiment presented in chapter 5, a compensating water reservoir was connected to the rhizotron. Thus variations could generally be limited to a few mm. Temperatures were not regulated, but varied only within 2° Celsius within one day/night cycle. The experiment was run for 27 days with the following events:

- Light was not switched on on days 14 and 18.
- On day 22 the plant was decapitated. Light cycles were continued for the remaining 5 days of the experiment.

Spectral analysis of the multi-frequency signatures was done using the Debye decomposition scheme, resulting in parameters for the direct current resistivity (ρ_0), the total polarization magnitude ($m^{\mathrm{n}}_{\mathrm{tot}}$), and two types of characteristic relaxation times (τ_{mean} and τ^{1}_{peak}).

General results

The complete time series of the experiment is shown in Figure 6.17. Daily variations with variable amplitude dynamics can be observed in all SIP parameters (ρ_0, $m^{\mathrm{n}}_{\mathrm{tot}}$, τ_{mean}, τ^{1}_{peak}). In addition, long-term trends are visible. The daily variations in conductivity for each day/night cycle, with increased conductivity in daylight hours, are presented in more detail in Figs. 6.18a. Changes in the direction of the curves, i.e., changes from decreasing to increasing conductivities, and vice versa, coincide with changes of the light conditions. Electrical polarization responses exhibit cyclic variations, too (Fig. 6.17b, 6.18b). However, their minima and maxima are shifted with respect to the day/night cycle pattern: polarization is at a low during daylight hours. Small, but consistent, changes in relaxation times are observed, too (Figs. 6.17c,d and 6.18c,d). The peak relaxation time τ^{1}_{peak} shows a more or less binary behavior, with large relaxation times during night and small relaxation times during day (Fig. 6.18d).

Prolonged darkness

Suspending light for one day induces a saturation at night-time levels of polarization, and a somewhat reduced shift of relaxation times (Fig. 6.19).

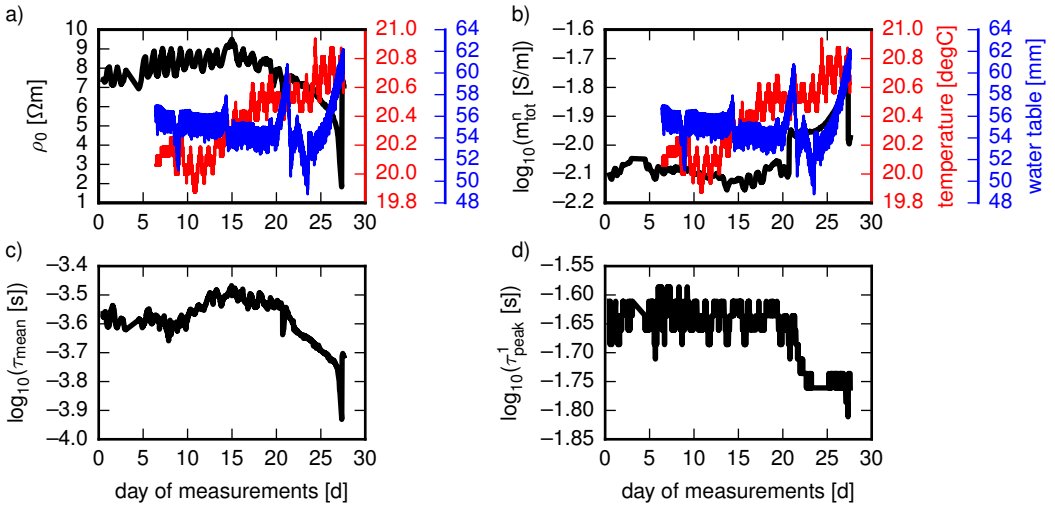

Figure 6.17: Temporal evolution of spectral parameters during the experiment. a) DC resistivity ρ_0, b) total normalized chargeability a) and b): Ambient temperature is plotted in red, water table fluctuations in blue. The values of the water table sensor are measured to an arbitrary reference point and not in reference to the rhizotron top. m^n_{tot}, c) mean relaxation time τ_{mean}, d) τ^1_{peak}. Parameters were computed using the resistivity formulation of the Debye decomposition.

Decapitation of plant

Decapitation of the plant leads to a continuous increase of polarization magnitude with time, and a corresponding decrease in relaxation times (Fig. 6.20). However, changes in light conditions do not lead to corresponding changes of the polarization response anymore, as was observed for light-darkness cycles of the intact plant (Fig. 6.18).

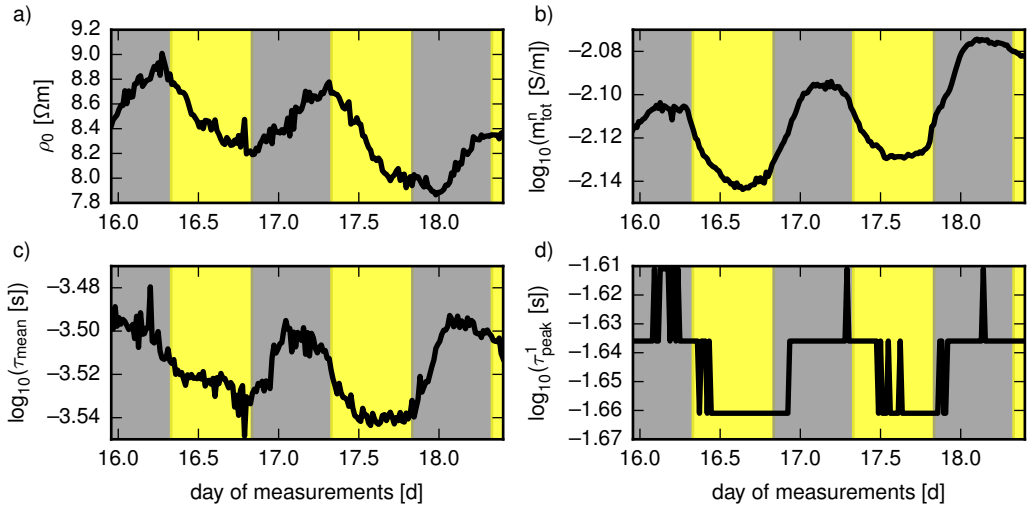

Figure 6.18: Spectral parameters for an arbitrary time span of 2.5 days, taken from the full time series. Parameters as in Figure 6.17.

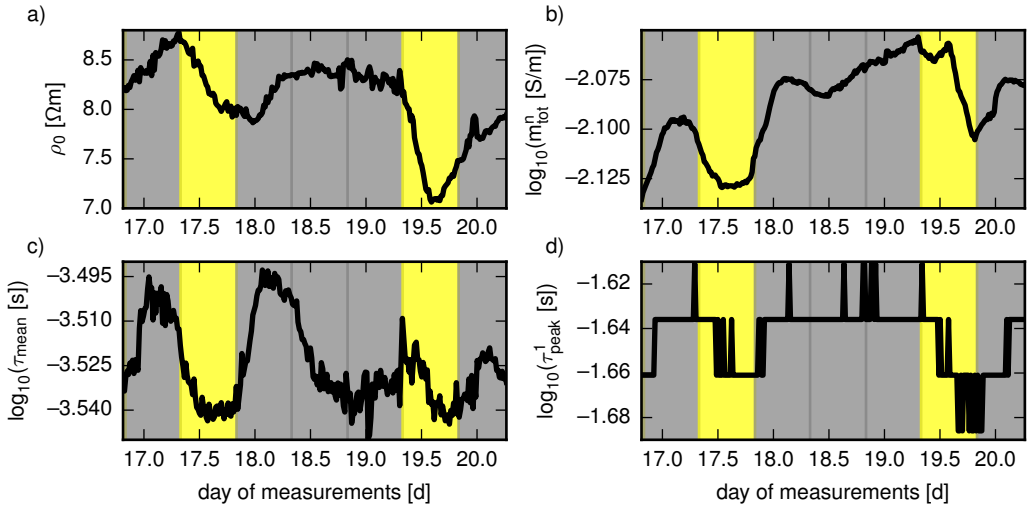

Figure 6.19: Spectral parameters for the time before, during, and after one full day of darkness. Parameters as in Figure 6.17.

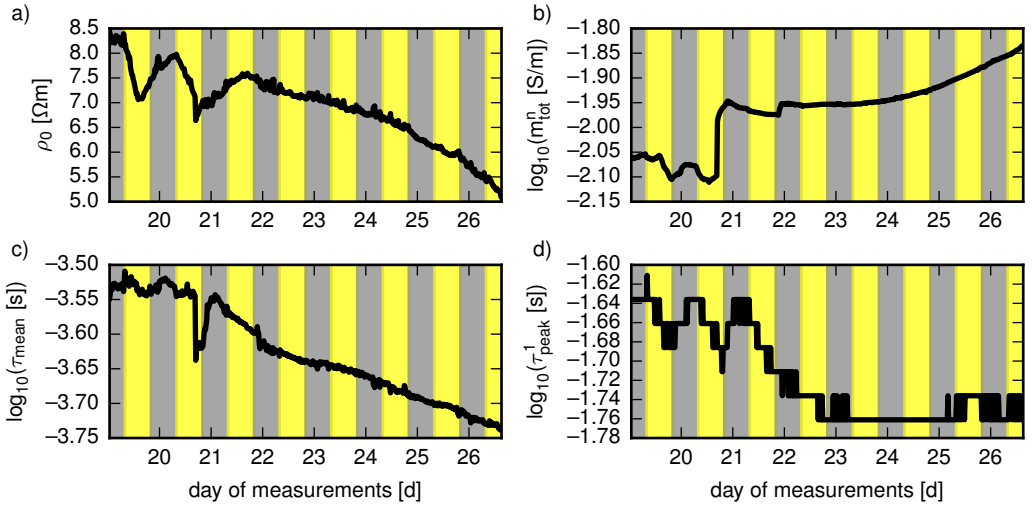

Figure 6.20: Spectral parameters for the time before and after decapitation of plant. Parameters as in Figure 6.17.

Discussion

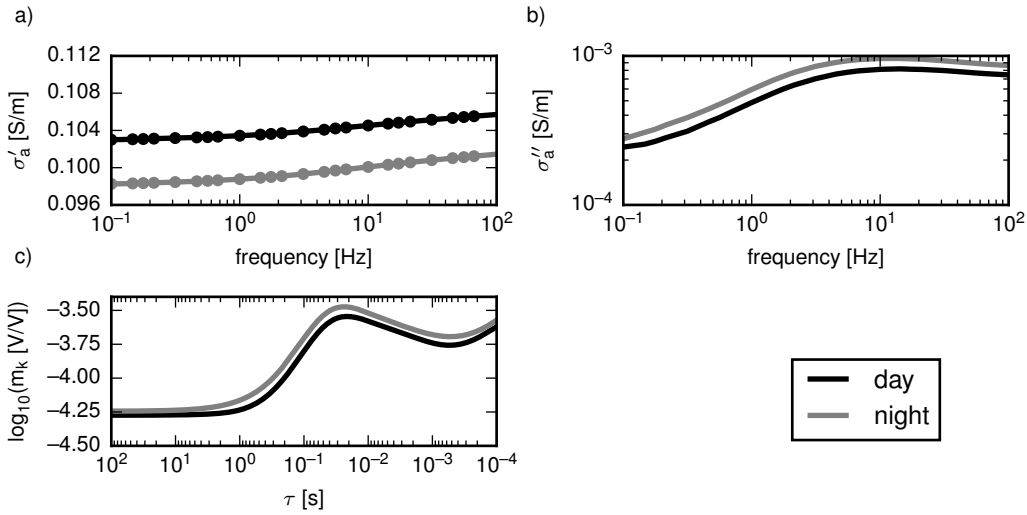

Figure 6.21: Apparent conductivity spectra measured at night (gray) and day (black). a) σ'_a, b) σ''_a, c) Relaxation time distribution recovered from the Debye decomposition of the SIP signatures.

High temporal EIS monitoring of crop roots uncovers very small polarization responses in response to light influence (Fig. 6.21). This suggests that physiological processes, induced and fueled by photosynthesis, change the electrical characteristics of the EDLs in the root tissue. Interestingly, larger polarization responses were observed in the night time, when active energy production is suspended and nutrients are stored within the root system (Delhon et al., 1995). However, although nutrients are accumulated in dark periods in the root elements, effective inflow is also reduced during these times. An effective ion flow across membranes can reduce the EDL thickness by reducing the size of the layers, and thus also reduce effective polarization signals. Nutrient translocation towards the leaf area is only initiated during light exposure, as is corresponding evaporation in the leaf areas. This evaporation then leads to a negative water potential gradient towards the leaf area, resulting in a net water/nutrient flow in this direction. It can thus be assumed that the additional nutrients that are stored in the root system over night strengthen EDLs (by means of increased

ion concentrations), which leads to larger measurable polarization signals. Increased ion flows (active or passive) in daylight hours probably decrease concentration gradients, thus leading to smaller EDL thickness. Changes in characteristic relaxation times could either indicate these changes within the EDL structure, or changes in the overall polarization responses for day and night times. This line of reasoning is supported by the fact that cyclic variations in polarization and relaxation time parameters vanish after the plant is decapitated, and thus deprived of any means of effective hydraulic flow mechanism. The small changes in in-phase conductivity can be explained by warming/cooling due to small heat emission from the LED growth lamp.

The binary behavior of τ^1_{peak} can be explained by the granularity of the underlying discrete relaxation time distribution: The measured SIP signatures exhibit only small changes (Fig. 6.21), and the resulting peak relaxation times differ only in neighboring relaxation times. Nonetheless, the observed behavior is consistent over all days.

Changes in polarization magnitude and relaxation times take place well before changes in the light environment (Figs. 6.18b,c). This can either be related to the previous light cycle, or be the result of some kind of memory effect in the plant. Interestingly, similar, but weaker reactions are observed in the dark period even for the period of prolonged darkness (Fig. 6.19b,c).

Polarization dynamics are quite small, which on one hand can be attributed to the process itself, on the other hand, however, it can be assumed that the high-conductive environment of the nutrient solution has a negative impact on signal strength. Shielding effects will route a larger percentage of the current through the conductive solution, and correspondingly smaller amounts of current polarize the root surface and interior.

In summary, the presented experiment highlights the high accuracy and consistency of the EIT measurement setup. Furthermore, it shows that plant root systems can be monitored over roughly 30 days without any impact on plant health. The previous experiments were all conducted in tap water, which led to a fast decay of the plants due to nutrient deprivation. However, by using nutrient solution as the measurement environment, conductivities and resulting polarization responses were reduced, probably due to shielding effects. Future experiments will have to assess if an imaging of plant roots is possible in this

environment.

6.2.6 Designing future experiments

Experiments conducted on crop root systems in aqueous solutions are far away from realistic field conditions, and correspondingly more complex experimental setups are required to advance method development and assessment. However, aqueous environments can be controlled with ease, and root systems can be introduced as the only source of electrical polarization. This allows for a steady fine tuning of the method, as well as gathering important knowledge of the 'intrinsic' electrical signatures of root systems.

While the presented experiments show that EIT can be used to monitor the reaction of root systems to strong external stress factors, it would be interesting to monitor root systems within a stable environment, that is without external stress factors. One step in this direction is the experiment presented in section 6.2.5, where a plant was monitored under stable conditions using EIS without any imaging.

Another practical problem is that measurements in nutrient solution imply a much larger conductivity of the host medium, compared to tap water. While this environment can sustain plant live over a longer time span, shielding effects reduce EIS and EIT measurement quality and decrease signal-to-noise ratios. Extending this setup to tomographic measurements will be challenging. Thus, additional experiments will be required to assess the optimal nutrient composition that weighs both requirements accordingly.

The stress factors used (nutrient deprivation and decapitation) were easy to control, and physiological reactions could be clearly distinguished from background noise and 'normal' daily variations. By using the large-impact stress factors, certain environmental factors and their impact on the EIT results could be neglected. For example, temperature, humidity, and light directly influence physiological reactions within root systems, and corresponding (small) signal changes can be expected in EIT measurements. Thus, experiments must be designed to screen these environmental factors.

6.3 Imaging of crop roots in soil

6.3.1 Introduction

All previously presented experiments on crop root system use tap water or nutrient solutions as the background medium of the root systems. This type of measurement has multiple benefits: Experiments are much easier to set up and measurement procedures are simplified; root systems can be investigated alone, without interfering background signals. The basic feasibility of using EIT for characterization and monitoring of physiological processes in root systems was established this way. This is an important conclusion, despite numerous previous studies that investigated relationships between electrical and biological properties of root systems in aqueous solutions (e.g., Dalton, 1995; Ozier-Lafontaine and Bajazet, 2005; Dietrich et al., 2013): It is important to keep in mind that the methods used in these studies differ slightly from EIT (e.g., no stem injection, four-point measurements instead with only two electrodes), with the latter introducing the imaging aspect, which has not yet been addressed in this context.

This section presents initial experiments with root systems embedded in two types of substrates, topsoil from a field site and peat substrate. As will be shown in the following sections, another important aspect that is of no concern for measurements in aqueous solution is variable water saturation, which can have manifold influences on electrical impedance measurements. Again, while previous studies observed a high dependence on soil water content (e.g, Dalton, 1995; Aulen and Shipley, 2012, and references therein), these findings have to be reevaluated for EIT measurements.

Rhizotron filling was commenced in an iterative scheme, in which layers of substrate were subsequently introduced into the rhizotron and then compressed using a defined weight (detailed information can be found in Nagel et al., 2012; Pfeifer, 2013).

These experiments were conducted within the subproject 'Non-destructive characterization and monitoring of root structure and function at the rhizotron and field scale using spectral electrical impedance tomography' of the research group FOR 1320 'Crop Sequence and Nutrient Acquisition from the Subsoil' of the DFG

Figure 6.22: Experimental setup for EIT characterization of oilseed rape plants in top soil substrate. Left: Rhizotron filled with top soil, and planted oilseed plants on the upper top. Upper right: Measurement setup with EIT system attached to rhizotron. Lower right: Closeups of the implanted plants. Photographs by J. Pfeifer.

(German Research Foundation). The experiments were jointly conducted with J. Pfeifer, and results of an earlier analysis stage can be found in Pfeifer (2013).

6.3.2 Field roots in top soil

As a first feasibility study three small field grown oilseed rape plants were planted on the left side of a rhizotron filled with topsoil from the same field site (Fig. 6.22). The rhizotron was homogeneously filled up to 60 cm height by successively adding, and compressing, five small layers of substrate (for detailed information on the filling process see Nagel et al., 2012). However, the upper row of substrate was filled by hand to accommodate the root systems taken from the field. This resulted in a less homogeneous density distribution

of the substrate, and an air pocket right below the root system. After planting the rhizotron was watered from the top with 500 ml tap water over the course of 24 hours. Results of preliminary EIT analysis steps were already presented in Kemna et al. (2011) and Pfeifer (2013).

Magnitude and in-phase conductivity images show an increase in resistivity/decrease in conductivity near the bottom of the rhizotron and directly below the plants on the upper left (Figs. 6.23a,c). Polarization responses show a highly polarized anomaly in the location of the root systems, and slightly decreased polarization values at the rhizotron bottom (Figs 6.23b,d). Recovered EIT results show distinct spectral responses in the anomaly of the root systems, while the surrounding soil exhibits slightly smaller polarization magnitudes with a less expressed frequency dependence (Fig. 6.24). Debye decomposition imaging results confirm that the region with roots exhibits large polarization anomalies over the measured frequency range (Fig. 6.25b). Relaxation time patterns show largely decreased relaxation times at the bottom of the rhizotron, and at the location directly below the root systems (Fig. 6.25c).

The presented results show clear evidence that root systems can be imaged if embedded in substrate. However, the surrounding substrate exhibits polarization signatures of its own, and thus it can be expected that the root signatures are partially masked. The detected polarization anomaly does not reach 10 cm depth, which is the approximate rooting depth of the roots. Thus these unresolved lower parts of the root systems are probably masked by the soil response. Problems due to measurement resolution should play only a minor role in this case, given the relatively shallow rooting depth.

The observed spectral behavior of the root systems is clearly distinguishable from the signatures of the surrounding soil (Figs. 6.25a,b). However, relaxation time patterns cannot be clearly interpreted (Fig. 6.25c). One possibility is that the polarization of the substrate is not sufficient enough to reliably determine relaxation times, and observed relaxation times in these low-polarizable regions constitute values determined by the used algorithm. Another possibility is that the root system does not change the underlying length scales of the polarization patterns, i.e., the root system and the surrounding soil exhibit polarization responses on similar length scales (at least in the measured frequency range). If further analysis of relaxation times is sought, a masking approach similar to

the one applied in chapter 5 could be helpful, which selects pixels according to a $m_{\mathrm{tot}}^{\mathrm{n}}$-threshold.
The air pocket introduced during planting can be identified both in in-phase conductivity (σ') and in out-of-phase conductivity (σ''). The phase representation is not clear in this regard. These results are plausible, as air naturally increases resistivity and provides less surface area for EDLs to form, thus reducing polarization signals.

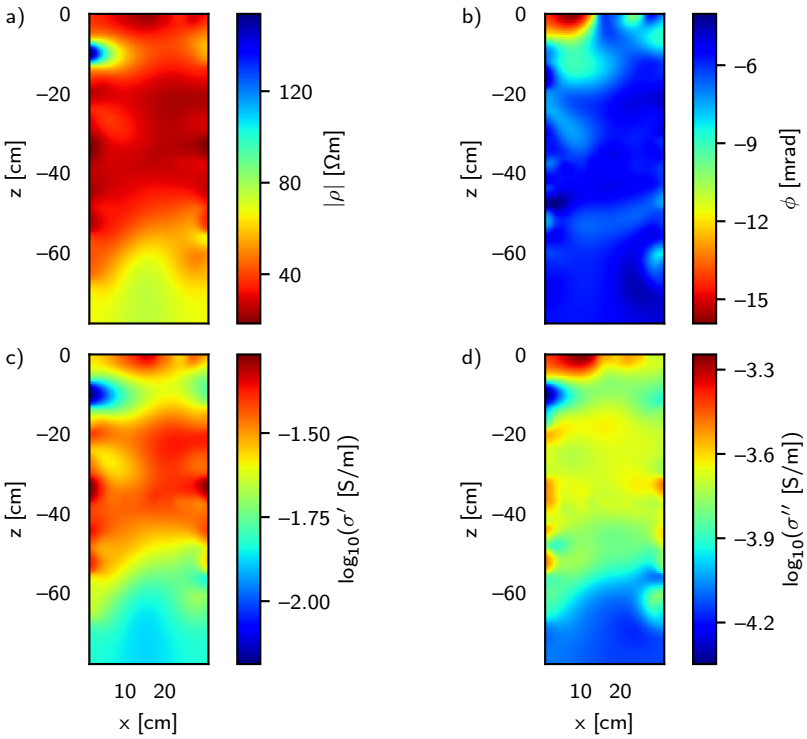

Figure 6.23: Electrical imaging results (21 Hz) of field plant in topsoil.

Irrigation provided water to the top of the rhizotron in relatively small amounts (in total 0.5 l in the 24 hours prior to the EIT measurement). Variations in conductivity patterns (both in the real and imaginary part) at the top and the bottom of the rhizotron can thus be attributed to decreasing water saturation. Effects induced by spatially variable water content are further discussed in sections 6.3.4 and 6.3.5.

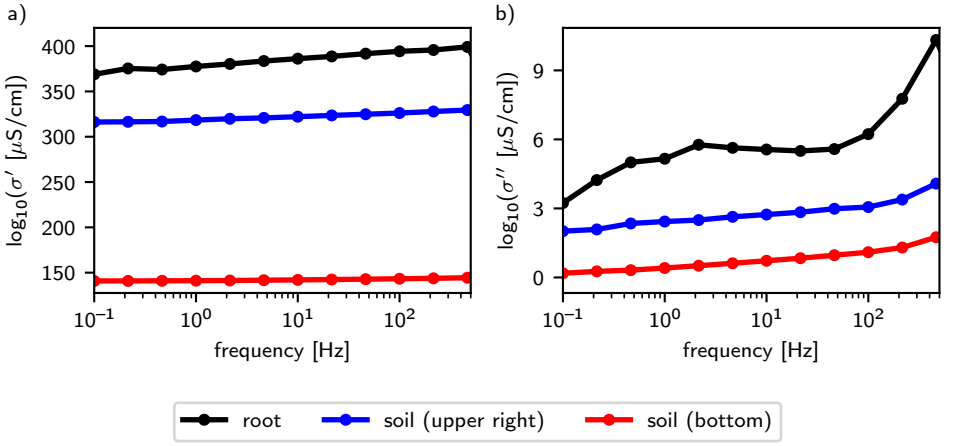

Figure 6.24: Exemplary intrinsic spectra extracted from imaging results. Black: Pixel spectrum from the central location of the root system. Blue: Pixel spectrum from the upper right part of the rhizotron. Red: Pixel spectrum from the lower part of the rhizotron.

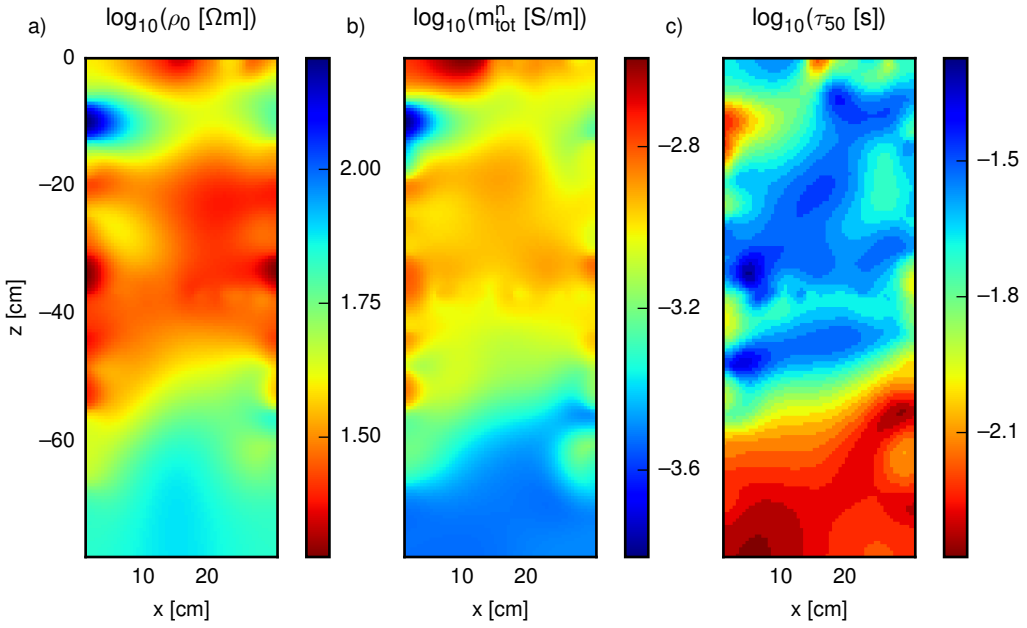

Figure 6.25: Debye decomposition results for field oilseed plant generated from EIT results.

6.3.3 Monitoring root growth in a nutrient deprived environment

The results of section 6.3.2 show the basic capability of EIT to image the spatial extension of crop root systems in a topsoil substrate. This experiment investigates the possibility of using EIT to monitor root growth in a topsoil substrate. Early results of this experiment were already presented in Kemna et al. (2011) and Pfeifer (2013).

Winter wheat was grown in field topsoil (from the Klein-Altendorf test site) for 35 days, irrigated only with de-ionized water. Measurements made on samples taken from the same field site reported between 15 % and 20 % clay content for the topsoil (Gaiser et al., 2012). While initial volumetric water content of the rhizotron lay at approximately 35-38 %, irrigation with de-ionized water was started only two days before seeding with 100-200 ml per day. This amount was reduced to 50 ml per day on day 4 after seeding. The irrigation scheme induced a continuous nutrient stress, given the low nutrient content of the used topsoil substrate. In order to monitor the response of the root system to a sudden spike in nutrient availability, 100 ml of a 0.625 mmolar ammonium nitrate solution were applied to the rhizotron (conductivity of 832 μS/cm) two days before the end of the experiment.

In total 20 EIT measurements were recorded at 18 frequencies between 0.2 Hz and 45 kHz before the tracer application, and another 8 EIT measurements were conducted after the tracer application at 16 frequencies between 1 Hz and 45 kHz.

Filling of the rhizotron was done in a standardized way (Nagel et al., 2012), and plants were sown on the left half of the rhizotron (Fig. 6.26a), and correspondingly a higher root length distribution (RLD) was found on this part of the rhizotron (Fig. 6.26b). However, root elements were found in the complete upper half of the rhizotron, while the bottom was only reached on the left side.

Conductivity patterns before and after seeding exhibit a highly inhomogeneous pattern (Fig. 6.27). Early measurements show low-conductive, high-resistive areas, which increase in conductivity over the following days. However, low-conductive areas remain at the upper boundary of the rhizotron for the first 27 days. High conductive areas can be observed throughout the experiment on the

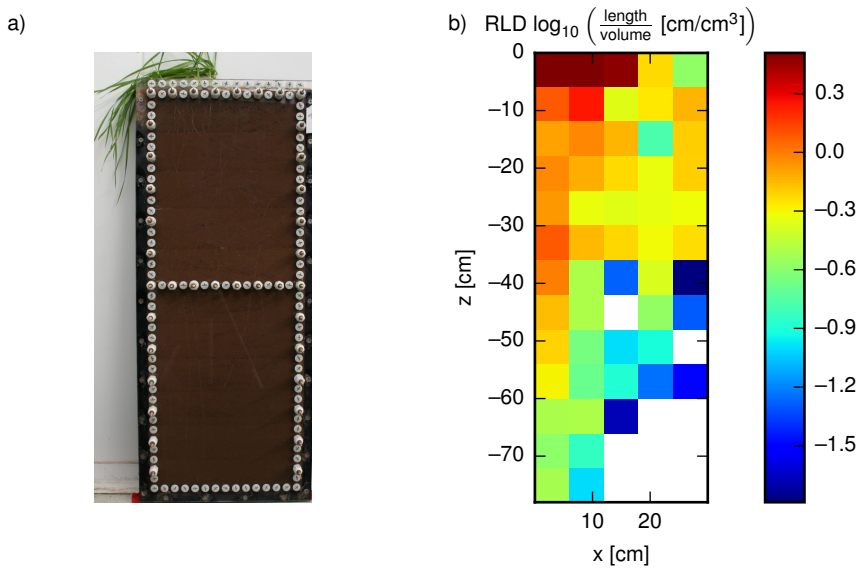

Figure 6.26: Measurement setup for EIT monitoring of wheat growth in a topsoil substrate. Left: Rhizotron filled with topsoil. Wheat plants were sown on the left part of the rhizotron. Picture taken on day 32. Right: Relaxation time distribution of rhizotron on day 32, recovered by destructive sampling (data provided by J. Pfeifer).

left and right sides of the rhizotron. Based on the fact that the observed conductivity patterns are inhomogeneous even before seeding (i.e., cannot be related to root growth or distribution pattern), they are interpreted as proxies to spatially variable water content in the rhizotron. This is also supported by established relationships between water content and electrical conductivity, which in simplified terms relate higher water content to a higher electrical conductivity (e.g., Archie, 1942). The initial distribution of water in the rhizotron certainly depends on the storage history of the material, and subsequent handling during filling. Conductivities increase with increasing duration of irrigation, with the low-resistive zone at the open top of the rhizotron probably created by evaporation and infiltration downwards. Days 23 to 27 show high-resistive areas roughly matching the final root distribution pattern, with a distinct left-right asymme-

try. This could indicate increased water uptake by the root system, and a simultaneous shortage of water to replenish used water. The high-conductive area at the top of the rhizotron on day 30 could be, with high probability, induced by the nutrient tracer, which was applied shortly before this measurement.

Polarization patterns can also be explained using variable water content. Various studies have shown that polarization responses decrease for decreasing water content (within certain limits as, e.g., water content not approaching full saturation) (see, e.g., Breede et al., 2012). Following this line of reasoning, the days before seeding exhibit low polarization patterns due to a corresponding low water content, which is then increased due to irrigation (Fig. 6.28a-d). Polarization responses then more or less show regions of low polarization, corresponding to the assumed region of increased evaporation, and a slowly emerging left-right asymmetry with decreased polarization on the left of the rhizotron. As was observed for σ' this pattern matches nicely with observed root distribution patterns. The tracer application induces a high polarizable region in the upper part of the rhizotron (Fig. 6.28p), which can be explained by increasing water content and increasing fluid conductivity. Increasing fluid conductivity can also increase observed σ'' values (e.g., Comas and Slater, 2004).

With respect to the direct imaging of root distribution patterns, the results of this growing experiment were unsatisfactory. As previously laid out, root distribution patterns map to both σ' and σ'' patterns in later stages of the experiment. However, especially σ'' responses do not fit to the increased polarization responses observed for root systems in aqueous solutions. A plausible alternative is that the root system governs water uptake and translocation within the rhizotron after it reaches a certain critical maturity, that is, a root distribution dense enough to counter water influx. This raises the question if EIT can be used at all to characterize root systems directly, i.e., not only by means of water content. Strong evidence for the possibility of directly characterizing root systems can be found in the results of the tracer application. While the changes in σ' are consistent with the infiltration of the tracer solution into the upper part of the rhizotron, σ'' shows a distinctly asymmetric polarization increase in the left side of the rhizotron (Fig. 6.29). This pattern matches nicely with the root distribution (c.f. Fig. 6.26), and can be interpreted as the 'activation' of the root system in response to the sudden nutrient availability. The asymmetry strongly

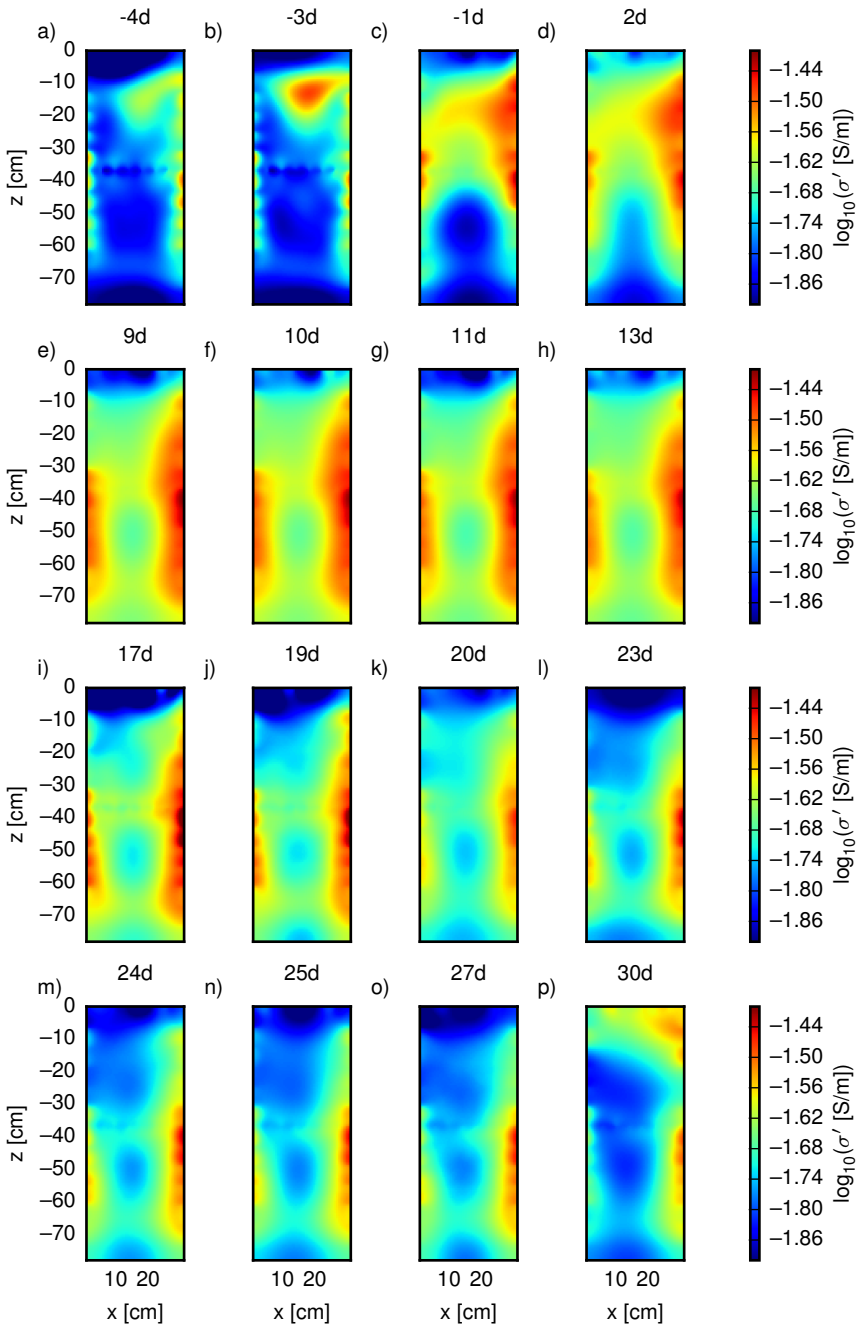

Figure 6.27: Imaging results (10 Hz) of σ' for various growth stages of the experiment. Indicated time spans refer to days after sowing. The last time step (day 30) was measured in parallel to the tracer injection.

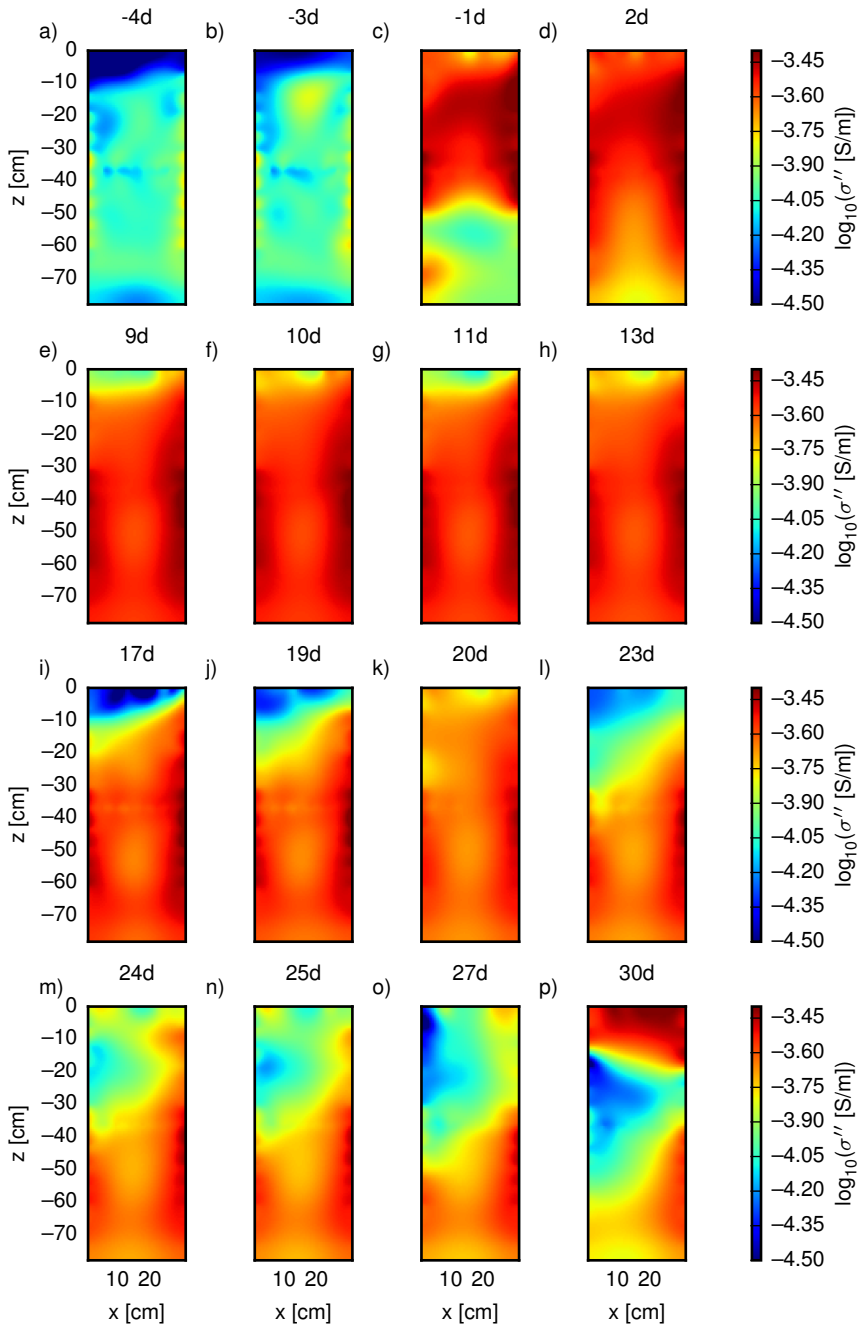

Figure 6.28: Imaging results (10 Hz) of σ'' for various growth stages of the experiment. Indicated time spans refer to days after sowing. The last time step (day 30) was measured in parallel to the tracer injection.

suggests that the observed polarization anomaly does not originate in substrate specific effects, which would be expected to be directly related to water content distribution (i.e., σ' distribution).

Both the increased σ' and σ'' regions fade away over the time of 48 hours, indicating evaporation and infiltration of the tracer solution, as well as a return to previous root polarization responses. The lower part of the rhizotron does not exhibit large changes, which suggests that no large amounts of tracer reached these regions. Polarization values return to the pre-tracer state in the top of the rhizotron, i.e., the region of high root densities. This can have multiple reasons: If the root surfaces are polarized, then the decreasing tracer (ion) concentrations could directly influence EDL strength at the root surface. In the case that the polarization responses were physiologically induced, e.g., through nutrient uptake, and subsequent strengthening of internal EDLs, then decreasing signals could indicate a reduction in physiological activity in response to decreasing nutrient availability.

The observed EIT results exhibit not only variations in the spatial and the temporal domain. Data quality was good enough to capture a limited frequency behavior. Intrinsic spectra, recovered from the imaging results, show depth-dependent polarization responses before and after the application of the tracer, as well as for the left and the right side (c.f. Figs. 6.30 and 6.31). This depth dependence is most pronounced in the upper left region of the rhizotron (Fig. 6.30b), which corresponds with the region of highest root density. For all investigated cases, depth dependence decreases after the tracer application. At this stage it cannot be clearly said if these observed changes in frequency dependence are related to the root systems or to changes in the pore chemistry/water saturation of the substrate. Changes in characteristic relaxation times, indicative for a change of SIP spectra, were reported earlier in this thesis, and changes of peak relaxation times were reported in dependence on water saturation for various sand/clay mixtures by Breede et al. (2012).

In conclusion, the growth of wheat plants was monitored for 30 days in a topsoil substrate using EIT. Root system extension could not be clearly mapped by means of polarization signatures. However, σ' distribution, as a proxy to water content, showed a good correlation to the final root length distribution. A subsequent tracer application of nutrient solution, however, provided strong

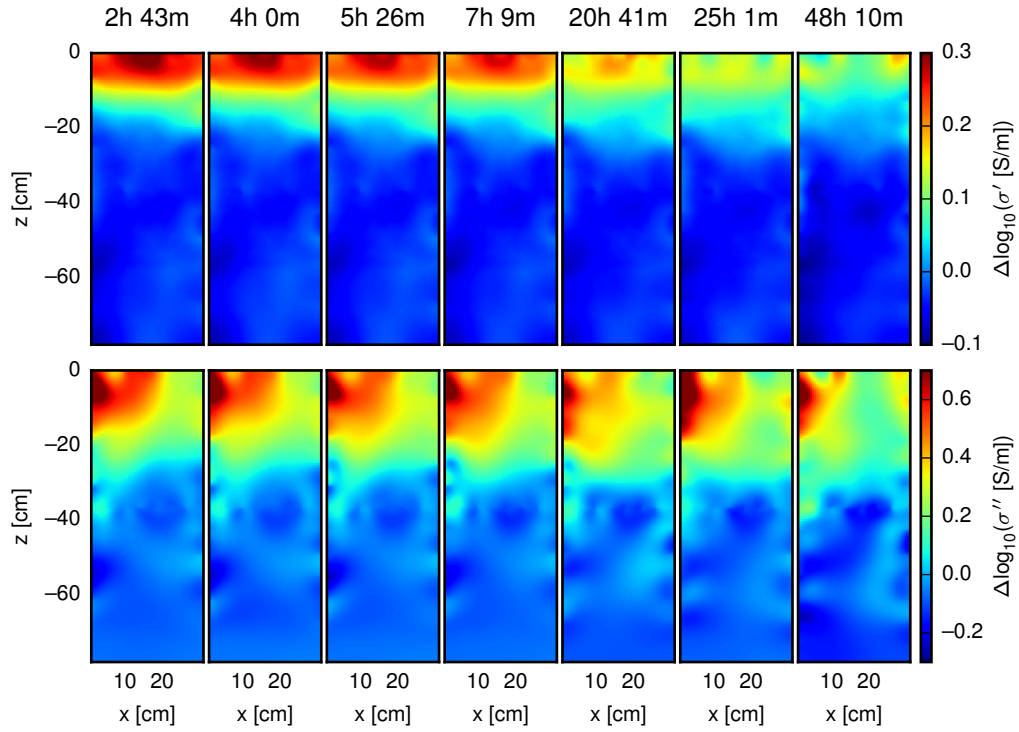

Figure 6.29: Difference images at 10 Hz of the tracer experiment. Differences are shown relative to the base measurement two days prior to the tracer application. Top row: $\Delta \log_{10}(\sigma'_i) = \log_{10}(\sigma'_i) - \log_{10}(\sigma'_0)$, with σ'_i the σ' distribution at the i-th time step and σ'_0 the base measurement. Bottom row: $\Delta \log_{10}(\sigma''_i) = \log_{10}(\sigma''_i) - \log_{10}(\sigma''_0)$, with σ''_i the σ'' distribution at the i-th time step and σ''_0 the base measurement. Time differences refer to time after application of the tracer solution.

evidence that the roots exhibited strong polarization signals in reaction to the sudden nutrient availability, suggesting the possibility of using EIT to characterize these physiological processes. Future work should be focused towards assessing whether the root densities were just too small (nutrient deprived environment) to produce strong enough polarization responses, or whether perhaps measurements procedures could be adapted to yield a better sensitivity in these types of substrate experiments.

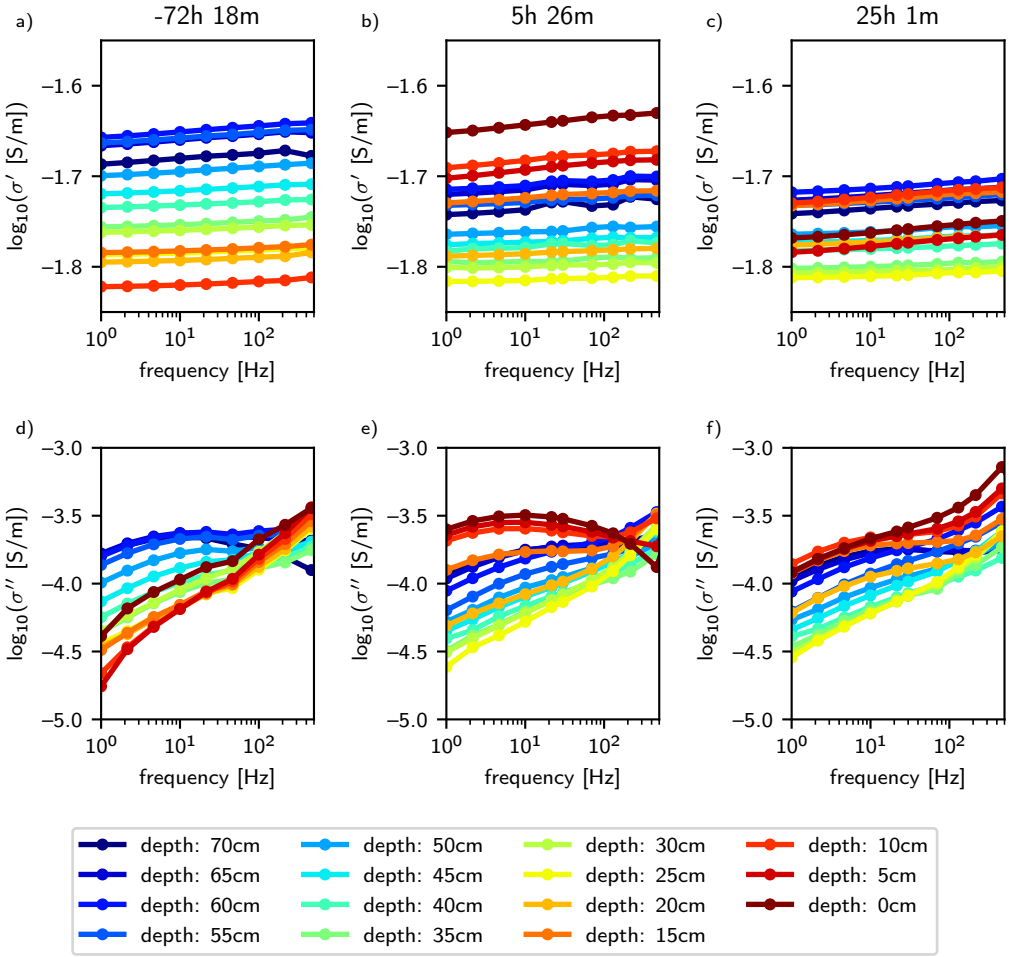

Figure 6.30: Complex conductivity spectra (x=4cm) for different depth locations recovered from imaging results. Wheat plants were sowed in this region of the rhizotron, cf. Fig. 6.26. Time differences refer to time after application of the tracer solution.

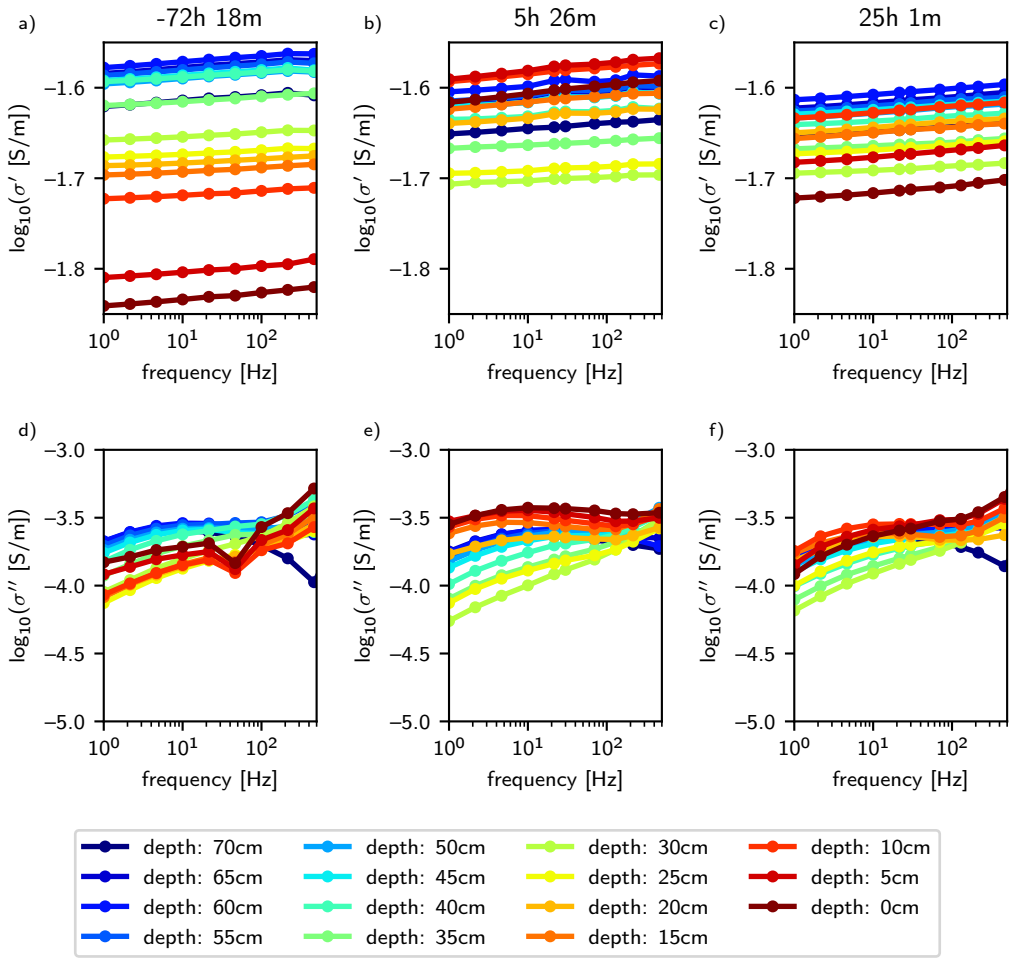

Figure 6.31: Complex conductivity spectra (x=26cm) for different depth locations recovered from imaging results. This half of the rhizotron contained only a limited amount of roots (Fig. 6.26). Time differences refer to time after application of the tracer solution.

6.3.4 Monitoring of oilseed growth in peat substrate: Experiment 1

Following the somewhat inconclusive results of the previous experiment regarding the monitoring of root growth, a follow-up experiment was designed to monitor growth of an oilseed plant with peat as the growth medium (Graberde; Plantaflor Humus, Vechta Germany). The increased nutrient availability of peat, coupled with the expected larger root mass (by means of the tap roots and larger secondary root elements of oilseed), was meant to provide a much more favorable environment for a successful direct imaging of the root distribution using EIT. Plants were seeded on the left half of the rhizotron, and EIT monitoring was conducted for 30 days. Tap water was used for irrigation (ca. 60 ml per day).

Growth and evolution of the root system was monitored using photographs of the roots growing along the transparent rhizotron front plate (Pfeifer, 2013). To promote growth along the transparent front plate of the rhizotron it was inclined by 45°. Visually observed root distribution patterns, however, do not necessarily coincide with total root distribution. In a similar setup, Nagel et al. (2012) observed that only 42 % of the root length of oilseed plants was visible when optically measured root lengths were compared with data obtained via destructive sampling. In addition, no information regarding a possible depth dependence of the ratio between visible and total root length is available. In this light we regard the photographic information only as a qualitative indicator for zones of high growth and high root length densities.

At day 30 of the experiment a nutrient solution was applied to the rhizotron as a tracer (with a preceding increase in tap water irrigation on this day), analogously to the experiment presented in section 6.3.3. This part of the experiment is discussed in appendix 6.A due to somewhat inconclusive results.

Afterwards the rhizotron was destructively sampled in blocks of 6x6 cm. Root properties (length, mass) and volumetric water content were determined for each block (Pfeifer, 2013). See Pfeifer (2013) for detailed information on the biological parameters, as well as for early analysis results of this experiment.

In-phase conductivity decreases steadily from top to bottom during the experiment (Fig. 6.32, top row). The observed patterns of relative change map closely

to the observed root distribution (Fig. 6.32, central row). Changes in the polarization response ($\Delta\sigma''$) show a decrease roughly corresponding to the $\Delta\sigma'$ and RLD patterns, too (Fig. 6.32, bottom row). This behavior is consistent with the results of the previous chapter, indicating that the observed patterns originate in changes of the spatial water content distribution and not in direct polarization signals from the root system. If this was the case, an increase in polarization magnitude would have been expected.
Water content, σ' and σ'' patterns show a certain correlation to each other (Figs. 6.33a - d, f). However, the RLD does not show clear similarities to those parameters (Fig. 6.33e). It is important to keep in mind that these properties were determined after the application of the tracer (cf. appendix 6.A). If the increased water content in the upper part of the rhizotron is assumed to be an indicator for the distribution of the remaining tracer, then the increase in polarization (σ'') in this region could be interpreted as the activation of the root system due to the nutrient supply of the tracer. The slight asymmetry (left/right) observed in σ'' patterns (Fig. 6.33b) is in favor of this interpretation.
The RLDs recovered from optical measurements (Fig. 6.32 central row) and from destructive sampling (Fig. 6.33e) show a good qualitative agreement, although the sampling resolution of the destructive approach is much smaller. No quantitative analysis of both parameters was done.
From this experiment it can thus be concluded that the electrical conduction and polarization mechanisms in the growth phase were primarily controlled by the water saturation in the rhizotron, possibly controlled by root water uptake and evaporation at the top of the rhizotron. However, weak evidence was found that the tracer application led to an increase in polarization signals in the top region of the rhizotron, weakly related to the zone of larger RLD. Here, it is not clear if an increase in polarization of the underlying peat substrate is the cause for the observed patterns.

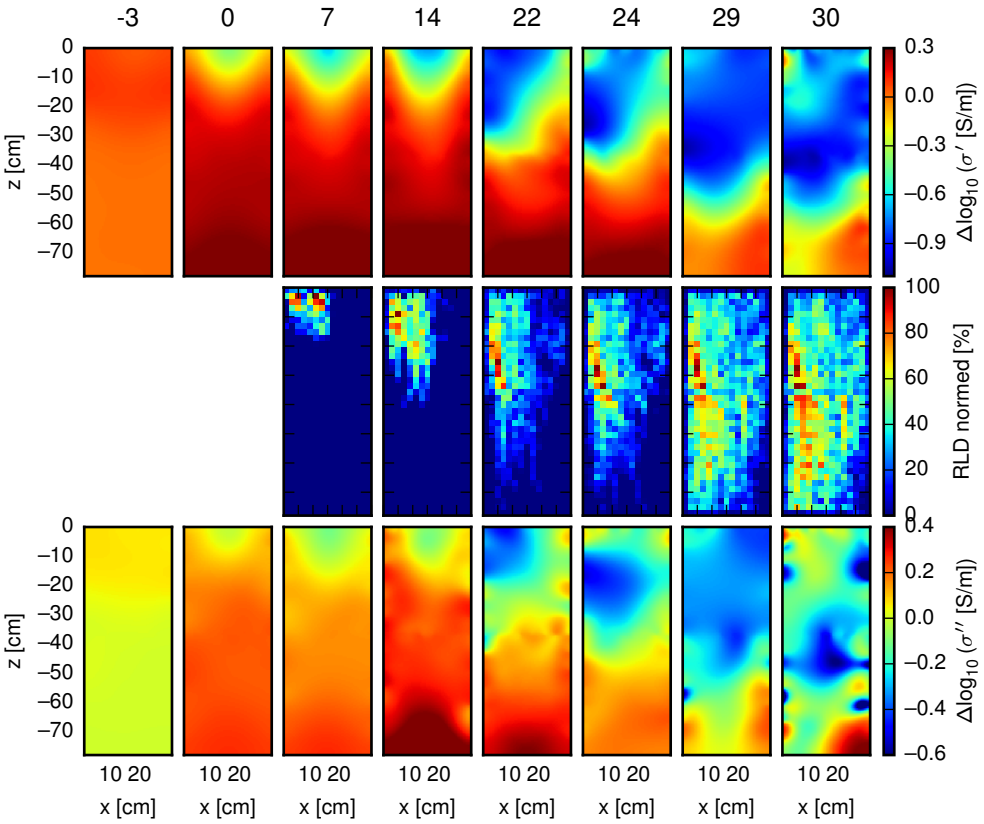

Figure 6.32: Growth experiment with oilseed root system in peat substrate. Shown are log-differences toward the base measurement (not shown) on day -4 at 10 Hz. Top row: $\log_{10} \Delta\sigma'_i = \log_{10}(\sigma'_i) - \log_{10}(\sigma'_0)$, with σ'_i the conductivity distribution of the i-th time step and σ'_0 the base measurement. Central row: relative RLD, as recovered from photographs on the corresponding days (data provided by Pfeifer (2013)). Bottom row: $\log_{10} \Delta\sigma'_i = \log_{10}(\sigma''_i) - \log_{10}(\sigma''_0)$, with σ''_i the imaginary part of the conductivity distribution at the i-th time step and σ''_0 the base measurement.

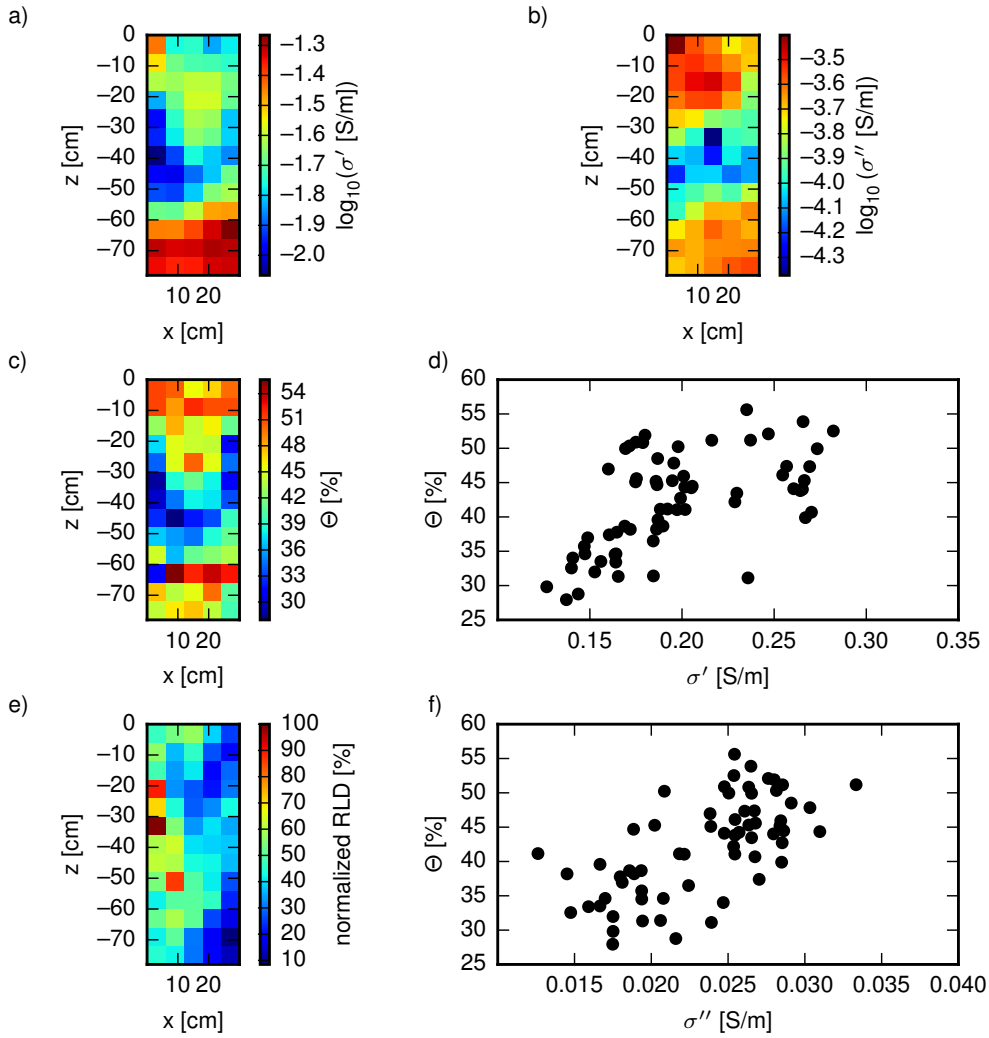

Figure 6.33: Electrical and petrophysical properties determined on day 32 of the experiment. a, b) Absolute σ' and σ'' distributions, upscaled to the resolution of destructive sampling (10 Hz). c) Volumetric water content (VWC) Θ (data provided by Pfeifer (2013)). d) Relationship between Θ and σ'. d) Root length density (RLD), as recovered from destructive sampling (data provided by Pfeifer (2013)). e) Relationship between Θ and σ''.

6.3.5 Monitoring of oilseed growth in peat substrate: Experiment 2

The second growth experiment was inspired by the first growth experiment (described in section 6.3.4): Continuous EIT measurements were conducted on a rhizotron filled with the same peat substrate over the course of 30 days (not including monitoring of the rhizotron before seeding). Oilseed was grown on the left side of the rhizotron (Fig. 6.34), and watering with nutrient solution was increased compared to the previous experiment to two times a day (on average, individual watering times varied due to equipment mode of operation). To promote growth along the transparent front plate of the rhizotron it was inclined by 45°. Due to low germination rates of the used seeds additional seeds were sown 8 days after initial seeding. On average, four full tomographic EIT measurements at 37 frequencies between 0.2 Hz and 45 kHz were completed on each day of the measurements.
On day 22 after initial seeding the water supply was interrupted, resulting in at least 24 hours without irrigation (restored on day 23). On day 30 the rhizotron was destructively sampled in blocks of 6x6 cm (resulting in a 5 times 13 block pattern for the full rhizotron) (Pfeifer, 2013). From each of these blocks root properties (length, mass) and volumetric water content were determined (Pfeifer, 2013).
The analysis of EIT measurements was done as described in chapter 5, and the spectral characteristics were extracted from the imaging results using the Debye decomposition (DD) scheme. The resistivity formulation was used for the DD, resulting in the parameters ρ_0, $m^{\mathrm{n}}_{\mathrm{tot}}$, and τ_{mean}. Due to the massive changes in measured electrical responses due to the interruption of irrigation on day 22, growth patterns are only analyzed up to day 21. Measurements afterwards are separately discussed with respect to the induced changes in the water saturation patterns of the rhizotron.

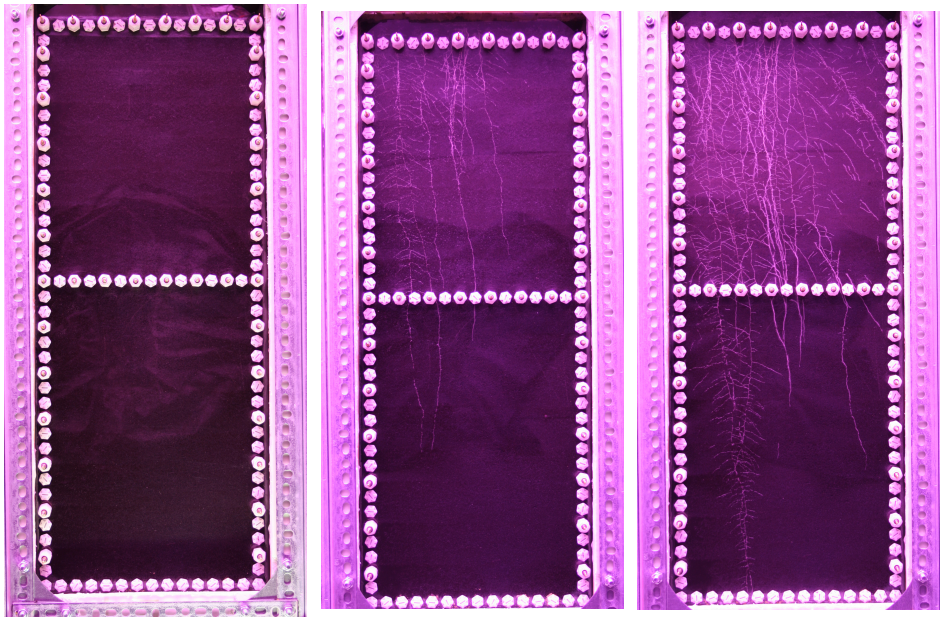

(a) DAS 0 (b) DAS 22 (c) DAS 29

Figure 6.34: Photographs of the rhizotron at various time steps (Pfeifer, 2013). DAS indicates 'days after sowing'. The lower parts of the photographs contain reflections from a cover sheet, and are not related to the root distribution.

Monitoring of root growth

Resistivity results during the growth phase show only minor dynamics between 8 and 14 Ωm, with low-resistive (high-conductive) zones on the sides of the rhizotron (Fig. 6.35). A high-resistive zone forms slowly in the center of the rhizotron and extends to the lower right corner for later time steps. Polarization signals ($m^{\mathrm{n}}_{\mathrm{tot}}$) exhibit generally higher values in the upper third of the rhizotron for the full period, with the maximum polarization in the upper left. This polarization anomaly increases in strength up to day 16, when it starts to decrease again (Fig. 6.36). The polarization anomaly can be observed even before seeding of the oilseed plants, and the lower left region of the rhizotron exhibits small, but stable, polarization magnitudes. Relaxation times show variations in the spatial and temporal domains, too (Fig. 6.37). The resistive zone in the central part of

the rhizotron exhibits increasing relaxation times during the experiment, and the polarization anomaly in the upper left corner shows decreasing relaxation times.
The relatively stable distribution of resistivities shows that the improved irrigation scheme prevented drastic changes in water saturation in the growth phase of the experiment, as was observed in the previous experiment (c.f. Fig. 6.32). The slight decrease in resistivity at the sides of the rhizotron could be related to preferential flow paths at the soil-rhizotron interfaces. Unfortunately, the improvement in the experimental setup did not yield characteristic polarization patterns corresponding to an increase in root distribution during the growth phase (Fig. 6.36). While the observed polarization anomaly on the upper left corner coincides with the area of expected largest root density (plants were seeded on the left part of the rhizotron), it can already be clearly identified four days before seeding. Thus it cannot be related to root growth. While it cannot be excluded that the observed increase in polarization strength originates in increasing root densities, there is no downwards extension of the anomaly in accordance to observed root elongation (c.f. Fig 6.34). One possible explanation for the anomaly lies in the peat substrate itself. Peat has a very high component of organic matter, and exhibits strong polarization signals by itself (e.g., Comas and Slater, 2004; Schwartz and Furman, 2015). This signature varies considerably with water saturation and conductivity. In addition, a nutrient-rich environment with large amounts of organic matter provides a very good growth environment for all kinds of bacteria and fungi, which also exhibit electrical polarization signatures (e.g., Revil et al., 2012a).

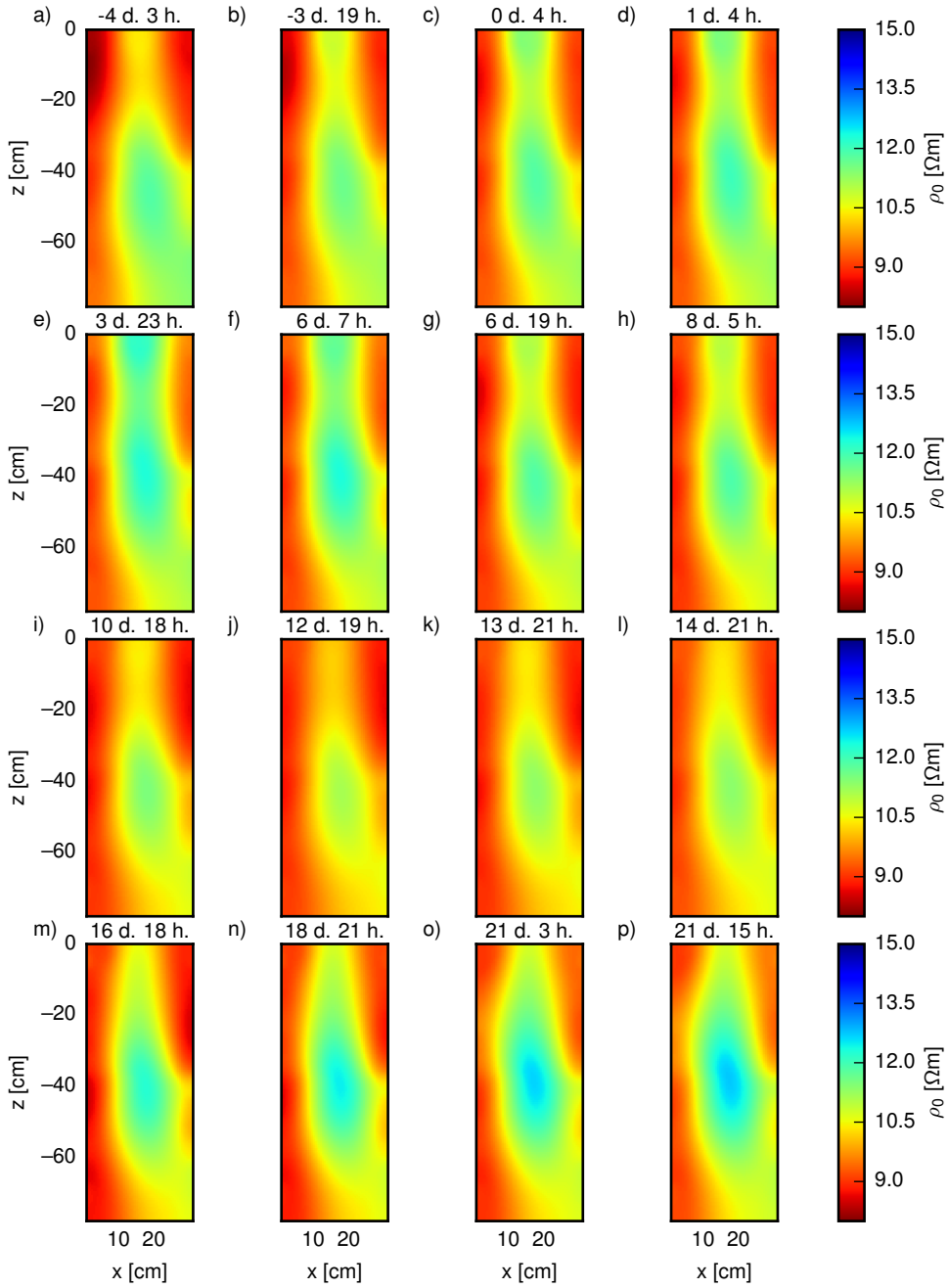

Figure 6.35: Results for ρ_0 for the first 21 days of the growth experiments. DAS refers to 'days after sowing'.

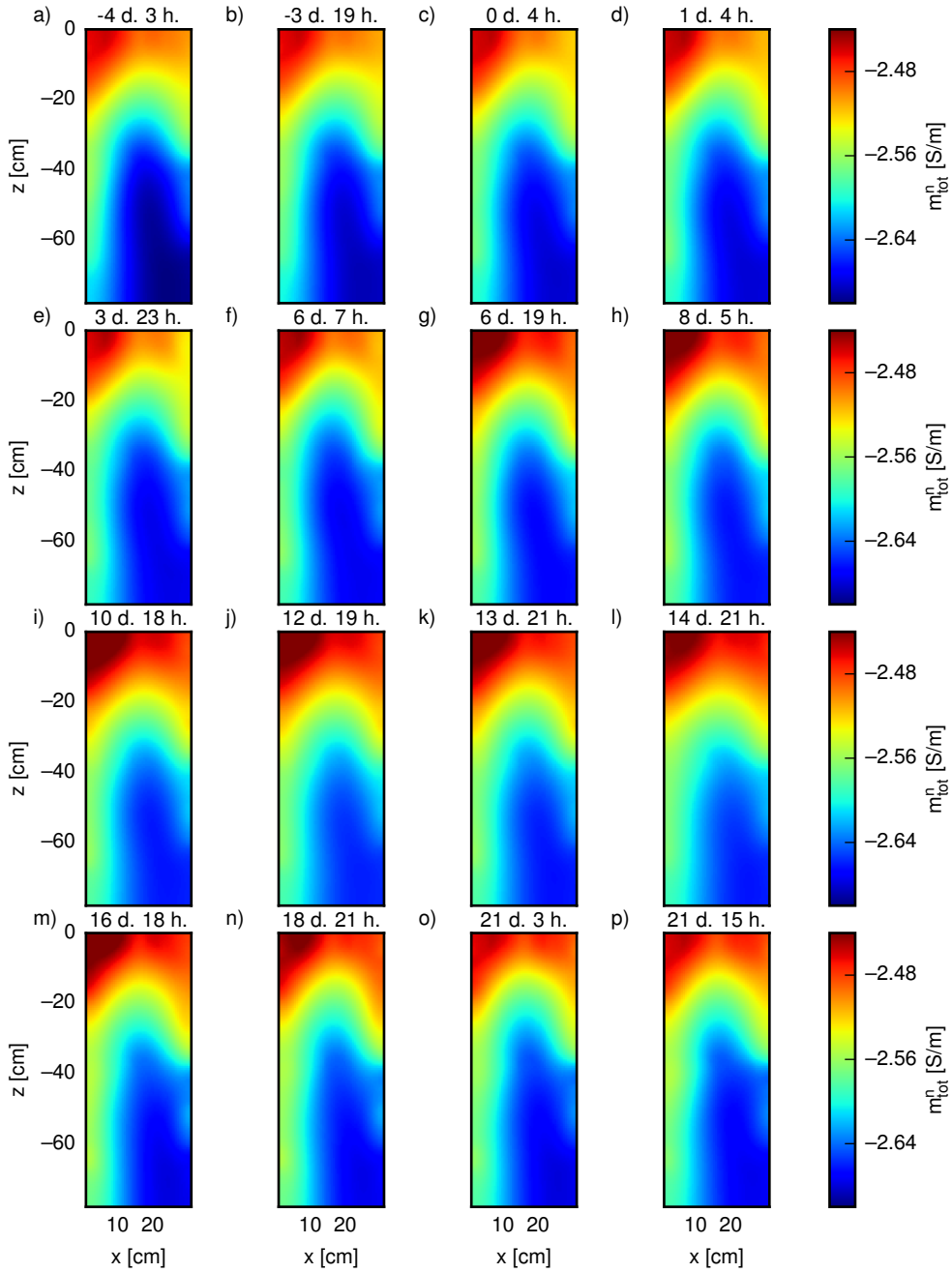

Figure 6.36: Results for m^n_{tot} for the first 21 days of the growth experiments. DAS refers to 'days after sowing'.

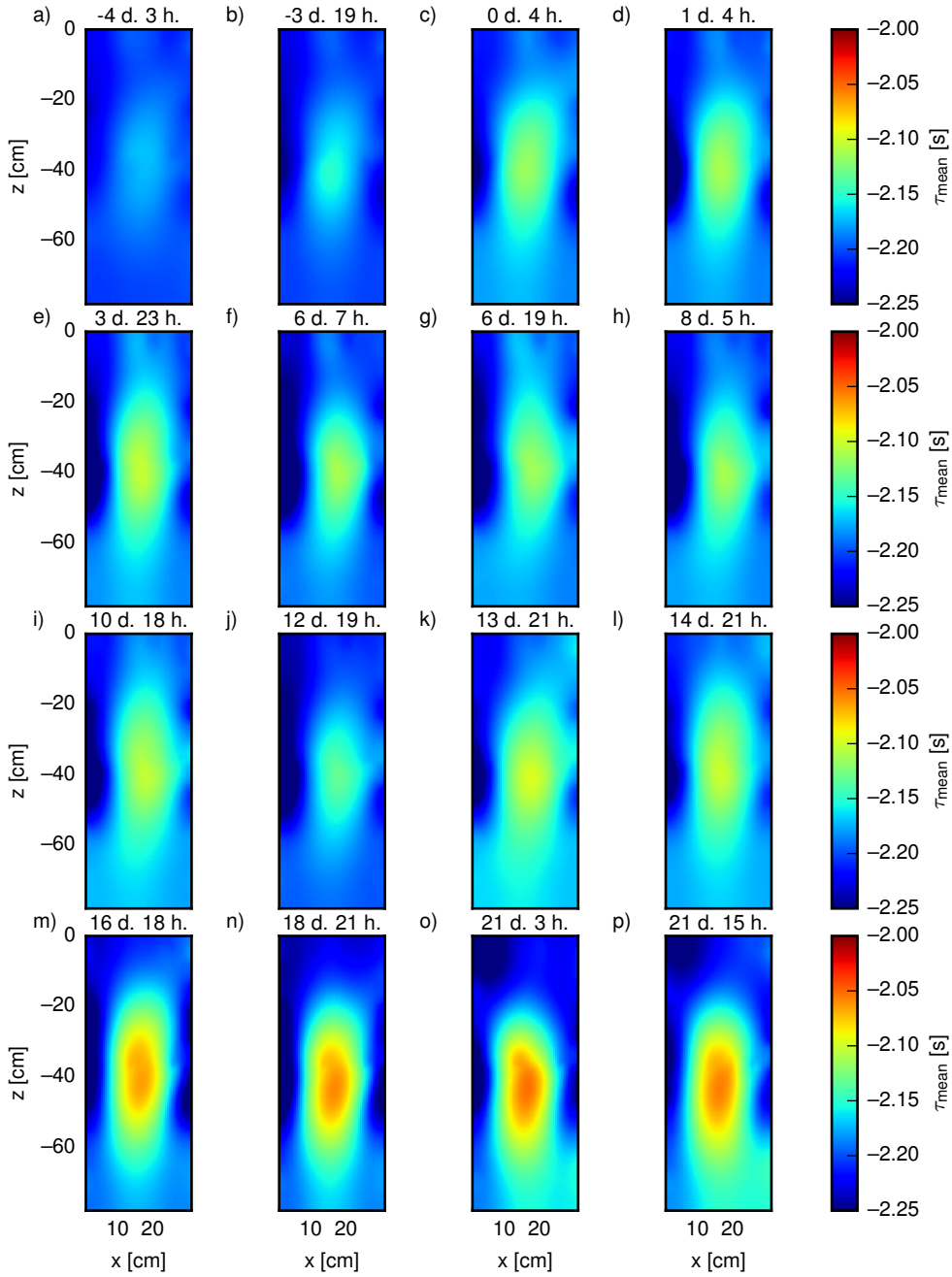

Figure 6.37: Results for τ_{mean} for the first 21 days of the growth experiments. DAS refers to 'days after sowing'.

Interruption of water supply

After the interruption of the irrigation system on day 22 the resistivity distribution of the rhizotron changes significantly, with a high-resistive zone emerging in the upper left part of the rhizotron (Fig. 6.39). This zone maps nicely to the region of highest root density (Fig. 6.38a) and resistivity increases even after restoration of water irrigation. Resistivity values increase to well above 40 Ωm, exceeding the dynamics observed in the early phase of the experiment. Polarization patterns show corresponding decreases in the areas of increasing resistivity (Fig. 6.40), and while relaxation times initially show patterns similar to the ones observed before, in later time steps a zone of small relaxation times emerges in the upper right part of the rhizotron (Fig. 6.41).
These results provide strong evidence that the water budget in the rhizotron is permanently disturbed by the short-term interruption of irrigation. Apparently the simple continuation of the irrigation pattern is not sufficient enough to restore the internal water distribution pattern. One possible cause is the water demand of the root system, which at this point covered almost the whole upper half of the rhizotron. Consequently, if water uptake exceeds water intake, then the lower part of the rhizotron will not be provided with any additional water, and the root system will take up even more of the available water from these regions. This hypothesis is supported by the properties determined by destructive sampling (Pfeifer, 2013). Both RLD and volumetric water content (Fig. 6.38) show weak relationships to σ' and σ'' (Fig. 6.42).

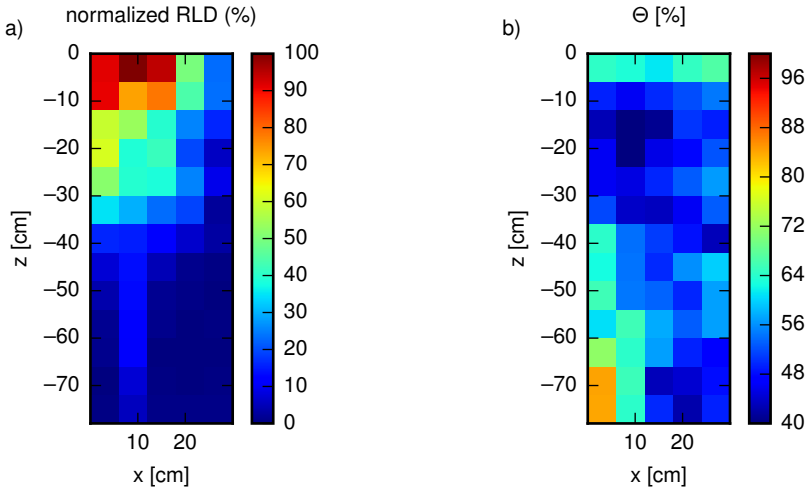

Figure 6.38: Root length density (a) and water content (b) as determined by destructive sampling on day 30 (data provided by J. Pfeifer).

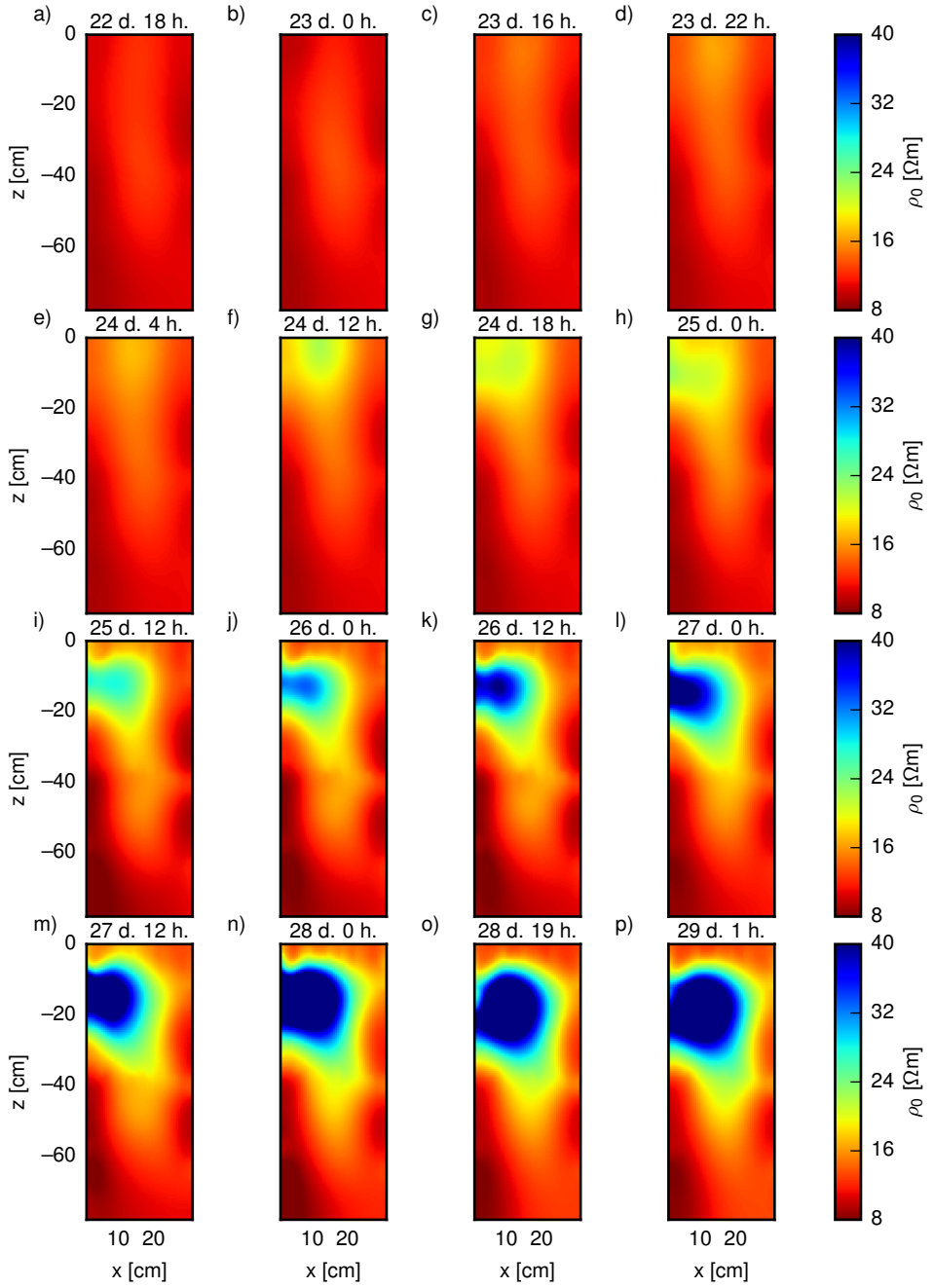

Figure 6.39: Results for ρ_0 for days 21 to 29. DAS refers to days after sowing.

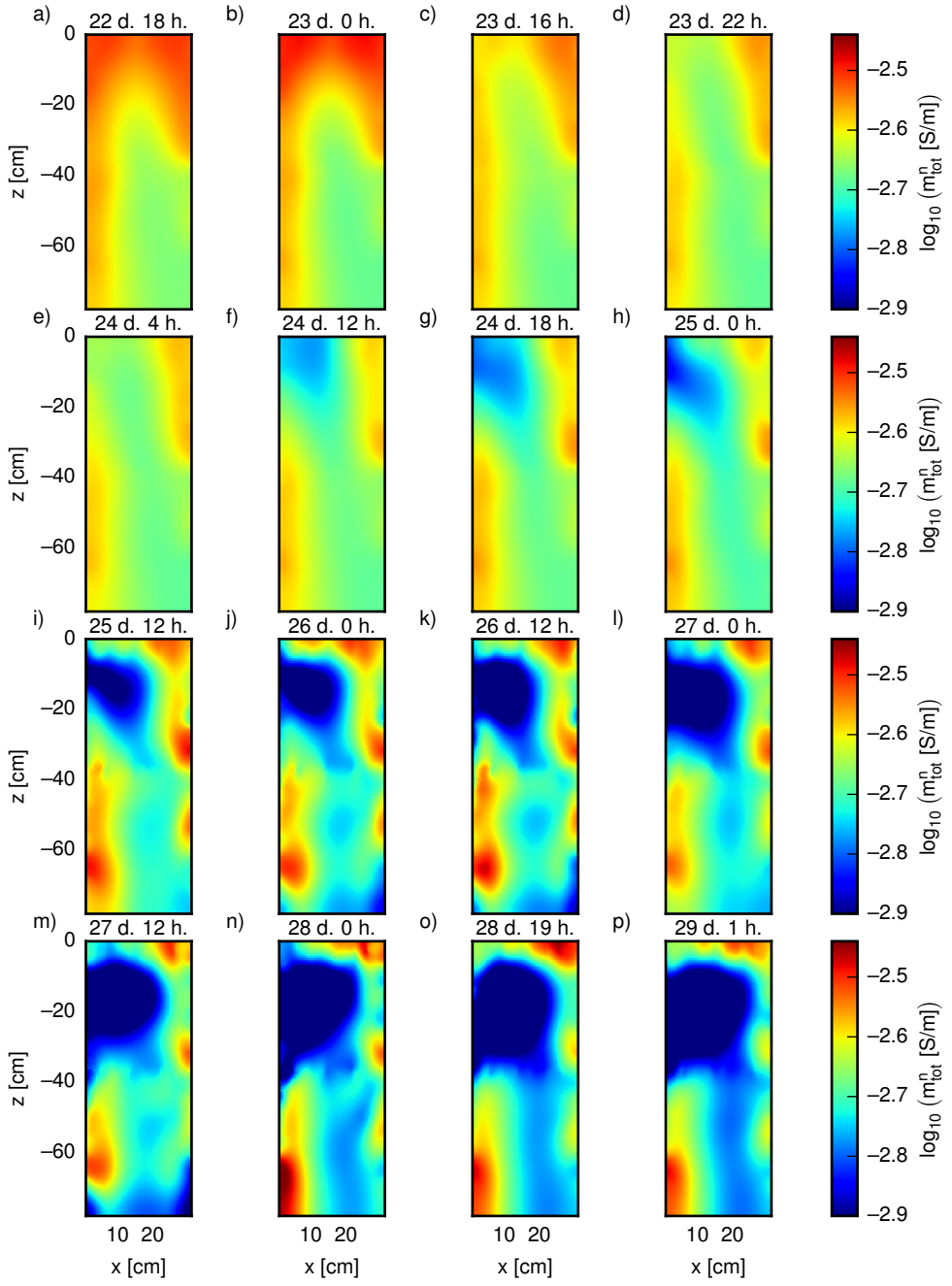

Figure 6.40: Results for $m_{\mathrm{tot}}^{\mathrm{n}}$ for days 21 to 29. DAS refers to days after sowing.

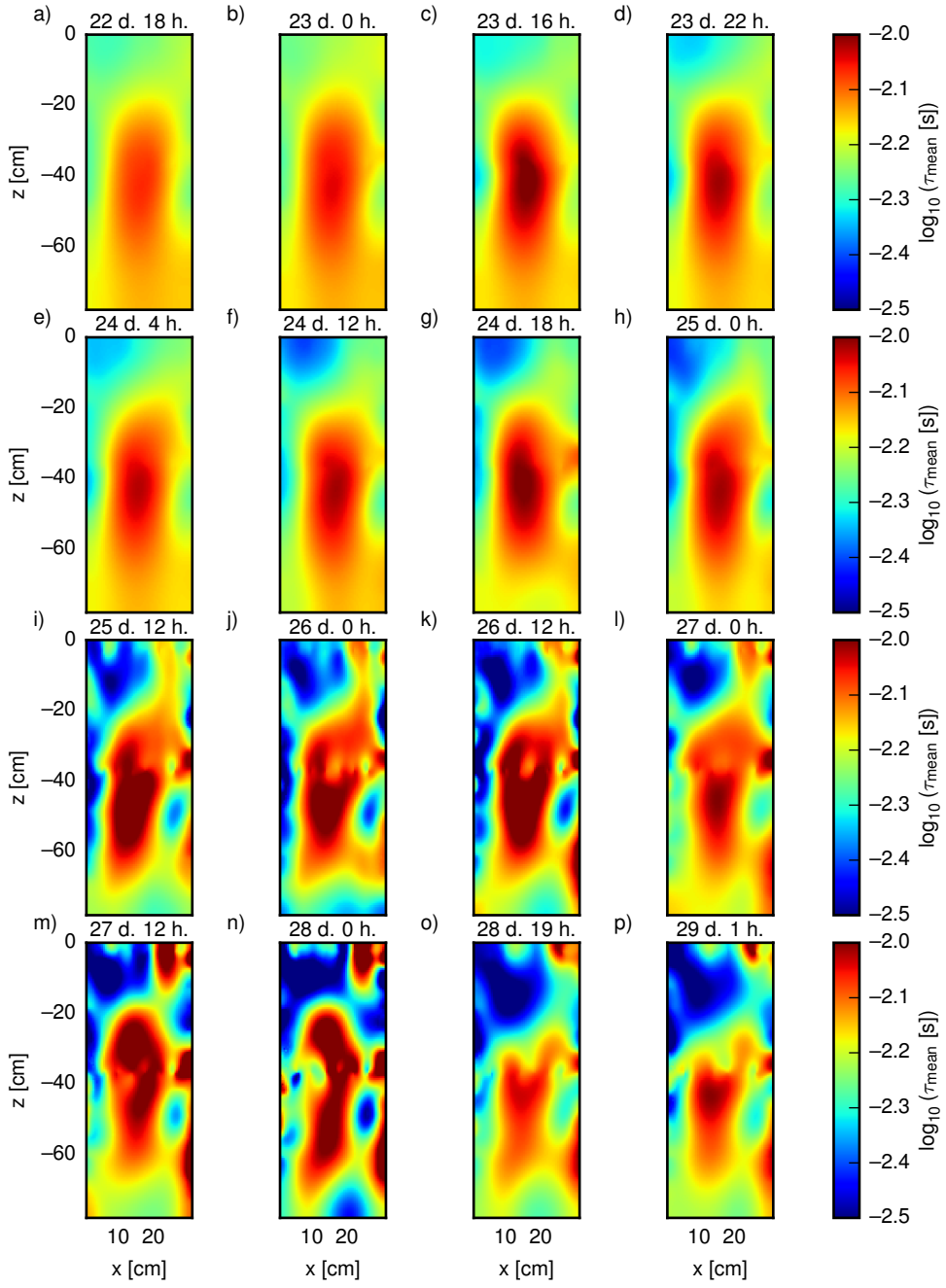

Figure 6.41: Results for τ_{mean} for days 21 to 29. DAS refers to days after sowing.

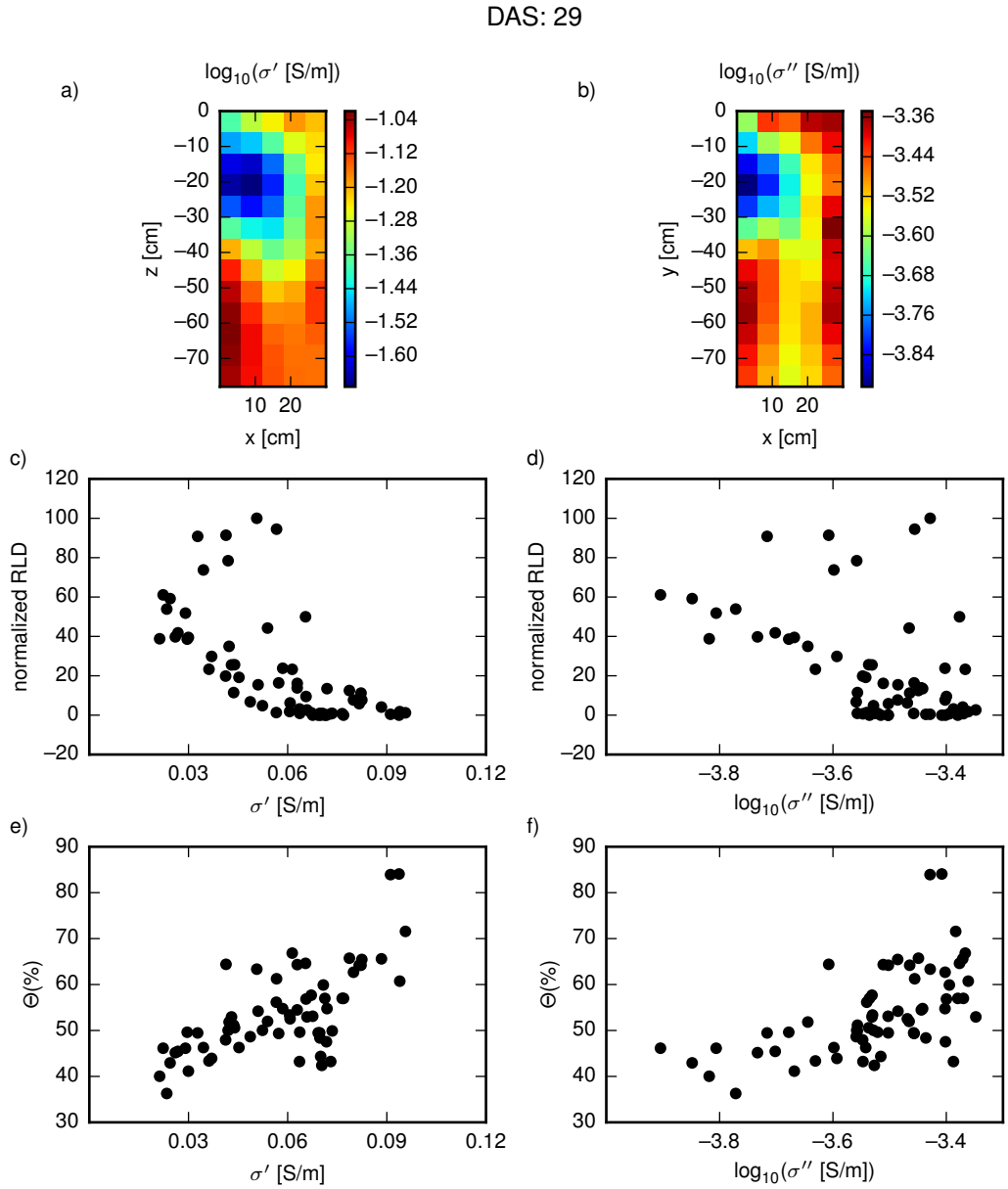

Figure 6.42: Relationships between water content/RLD and electrical parameters (10 Hz) of two time steps. a) σ' as recovered on day 29 from EIT imaging results, upscaled to resolution of destructive sampling (data provided by J. Pfeifer). b) σ'' as recovered on day 29. c-d) RLD as recovered from destructive sampling plotted against the measurements shown in a-b).

6.4 Towards the field scale

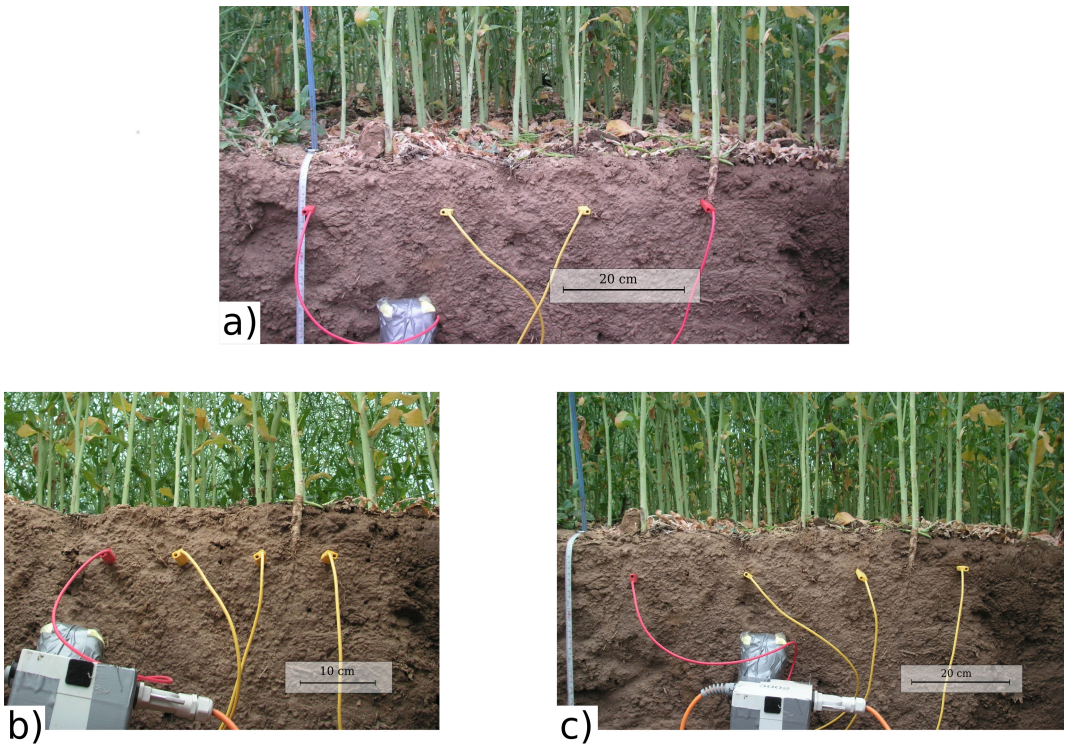

Figure 6.43: Setup SIP field measurements. a) Measurement on soil without tap root in voltage dipole. b) 10 cm spacing with tap root (right). c) 20 cm spacing with tap root.

As presented in chapter 5 and this chapter, crop roots exhibit intrinsic polarization signals that change in accordance to age, root system distribution, and in reaction to physiological changes in the plant system. However, the presented experiments were conducted in aqueous solutions, a simple and accommodating setting to investigate small-scale targets such as crop roots. As shown in section 6.3, introducing any kind of substrate into the measurement setting imposes a significant burden to the successful characterization of crop roots with EIT. Despite of these mixed results the overall objective remains, namely the adaption of EIT to characterize and monitor crop roots on the field scale.

To investigate the small-scale application of EIS/EIT to crop roots on the field scale, EIS measurements were conducted on an oilseed plant in-situ on the field test site Klein-Altendorf. A pit was excavated right next to a plant, and dipole-dipole measurements were made a) on an area with no large root elements in the direct vicinity, b) with the potential dipole of 10 cm spacing enclosing a tap root of oilseed, and c) with the potential dipole of 20 cm spacing enclosing the tap root (Fig. 6.43). Thus, the effect of a single root system in the direct area of sensitivity of the electrode configuration could be assessed, as well as the sensitivity to a larger, more realistic, electrode spacing of 20 cm.
Signatures measured on the dipoles with the tap root between electrodes show a significant increase in polarization signals compared to the surrounding soil (Fig. 6.44). This increase is similar for both the 10 cm and the 20 cm electrode spacings, although the low-frequency response is more pronounced for the smaller electrode spacing.
In many regards this experiment is similar to the experiment shown in section 6.3.2: Plants and topsoil were taken from the same field site. However, the experiment in the field was conducted with an SIP measurement device (Radic Research SIP 256c) intended for field work, which somewhat restricts the measurement capabilities. In addition, topsoil in active agricultural cultivation is highly inhomogeneous with respect to grain size and air enclosures due to weathering effects, earth worm activity, and plowing (among others). This can significantly influence the quality of electrode contact resistances. Also, water content can be controlled even less than in the laboratory experiments (see sections 6.3.3 - 6.3.5). Based on these experiments, the absolute detection of root zones will probably be very hard to accomplish. However, it should be possible to detect changes in the subsoil in reaction to certain environmental events such as drought or rain events (e.g., as was demonstrated in section 6.3.3 using a nutrient tracer).

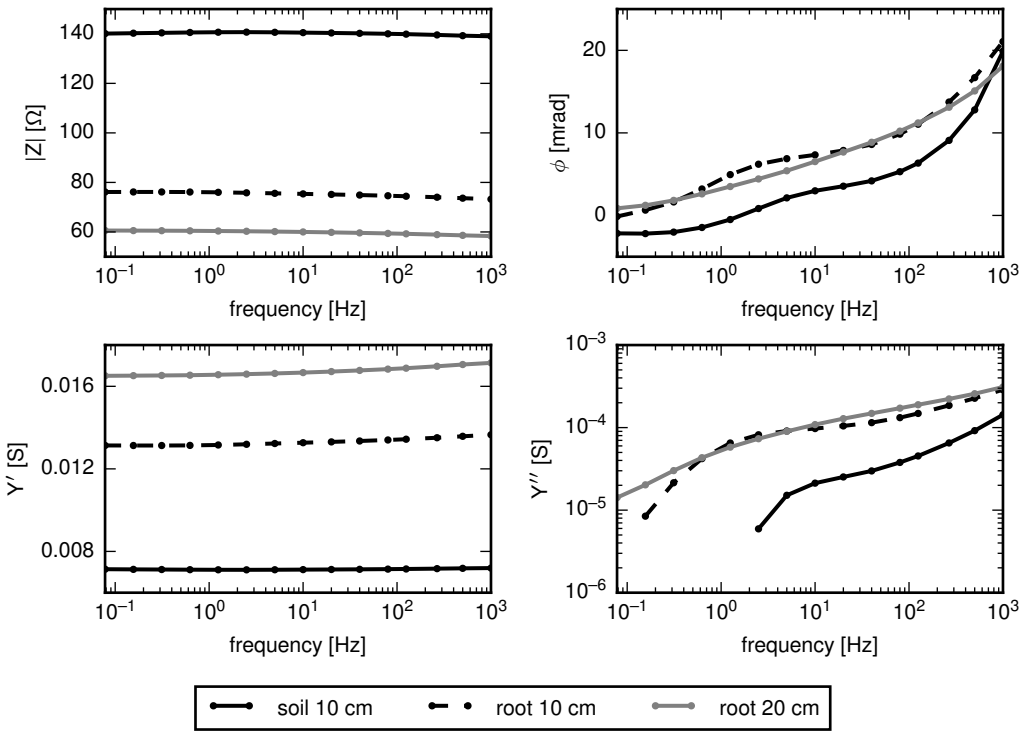

Figure 6.44: Field EIS results. Lengths given in the legend refer to electrode spacing.

6.5 Discussion and conclusions

In this chapter various laboratory experiments on crop root systems are presented that show the variety of physiological responses that can be monitored using electrical methods in aqueous solutions (section 6.2). Characteristic relaxation times can be inferred from multi-frequency measurements, and can be linked to the length scales of the dominant polarization processes. Thus multi-frequency measurements lead to a significant information gain compared to single-frequency measurements. In addition the measurements show a high sensitivity to small temporal changes in the electrical signatures, as evident from the monitoring of night/day cycles in section 6.2.5.

From a methodological point of view, EIT is fully developed and ready to accompany biological experiments on crop root systems in aqueous solutions. However, as soon as solid background media come into play EIT has not yet reached the maturity required to focus on the biological side of the experiments. As presented in section 6.3, the choice of substrate still dominates the electrical measurement results. The use of peat, while being a good growth medium, has proved unfavorable for EIT measurements due to its large inherent EIS signature. Even when electrically 'friendly' substrates are used, the major issue is the spatially variable water content distribution.

So far only a descriptive treatment of EIS signatures has been done, and only basic steps have been made to formulate physico-chemical models that can reliably describe and predict polarization responses of full root systems. However, the multitude of stress factors that influence electrical signatures makes the formulation of these models a high priority. While the intelligent planning of experiments can probably identify certain key components and processes that govern the electrical signals, at some point a theoretical description of the processes must be put forward.

This is even more relevant for the field scale. This highly inhomogeneous and uncontrolled environment still constitutes the ultimate challenge for a meaningful application of EIS/EIT due to the inhomogeneity of the environment and uncontrolled weather situation. Be it temperature, light, or nutrient availability, the laboratory experiments show that all these aspects can influence electrical polarization signals, and thus the analysis of field measurements must untangle

all these factors. It is also hard to gather validation samples with high spatial and temporal resolution without destroying the field environment. This makes a validation of the method much more complicated, and corresponding uncertainties of validation data must be taken into account, too.

Three challenges arise from this chapter: First, improving EIT to the point where those small changes observed in aqueous solutions using EIS can also be imaged, that is captured not only with high temporal, but also with high spatial resolution. This can be achieved by carefully optimizing measurement configurations and measurement setups. In addition, environmental factors such as ambient temperature and light influx must be meticulously controlled and monitored, so that observed patterns can be matched to external stimuli.

Second, the effects of soil must be fully understood on the root polarization signals. Means have to be devised to separate background signals from the primary root signals. Most probably relaxation time analysis will be crucial for this task, as the internal structure of soil and roots differs significantly. This should manifest in different length scales of the polarization signals.

The third challenge is the somewhat broadly formulated establishing of EIT in the field. This includes development of suitable measurement devices, measurement setups and procedures that take into account field cultivation (e.g., plowing). In addition, targets must be clearly defined, i.e., what benefit can be obtained from EIT measurements seen from a farming perspective?

Appendix

6.A Tracer experiment in substrate growth experiment 1

Images of σ' before the tracer application show a continuous decrease, starting on the left half of the rhizotron (Fig. 6.45a-d). This corresponds well to the observed propagation of the root system (Fig. 6.32 top, center). Slight variations in σ' are observed in the upper part of the rhizotron, probably caused by periodic irrigation. Due to an increase in irrigation volume on the day of the tracer injection, Figure 6.45d shows a much larger zone of relatively large conductivities in this upper region. A high-conductive zone emerges after the tracer application in the top region of the rhizotron down to ca. 40 cm depth (Figs. 6.45e-i). Over the next two days this anomaly slowly decreases in strength.
Polarization responses show a somewhat more complicated pattern (Fig. 6.46). It seems that zones of low conductivity coincide with zones of low polarization (cf. Figs. 6.45 and 6.46), although this relationship is not completely clear. However, the high-conductive zone observed due to the tracer application also shows increased polarization signals, which also fade away over the next 2 days. Although the zone of largest changes induced by the tracer is also a zone of high root length density (cf. Fig. 6.32 center), the spatial patterns do not match precisely. One possible cause is an increase in polarization response of the peat substrate, which exhibits highly variable polarization responses with changing water conductivity and content. However, a slight left/right asymmetry can be observed, which could indicate that the polarization increase is indeed partially caused by increased root polarization. We therefore conclude that the observed changes in σ' are primarily caused by changing water distribution and conductivities, and that σ'' patterns are probably caused by changes in the electrical response of the peat substrate, perhaps with a small contribution from increased root polarization, i.e., activity.

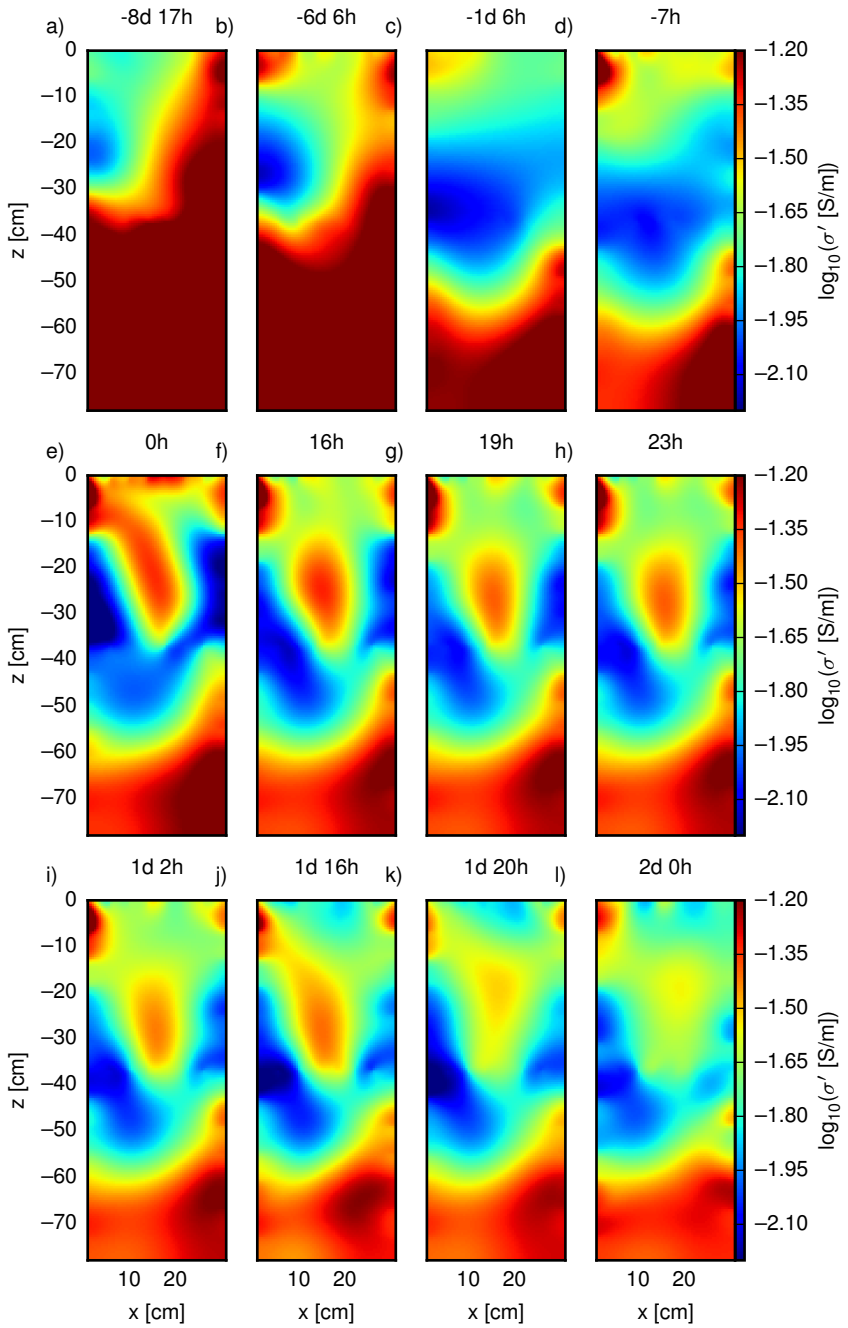

Figure 6.45: Absolute inversion images (10 Hz) of σ' for the time before and after the tracer application. Times refer to time before/after application of the tracer (on day 30 after sowing).

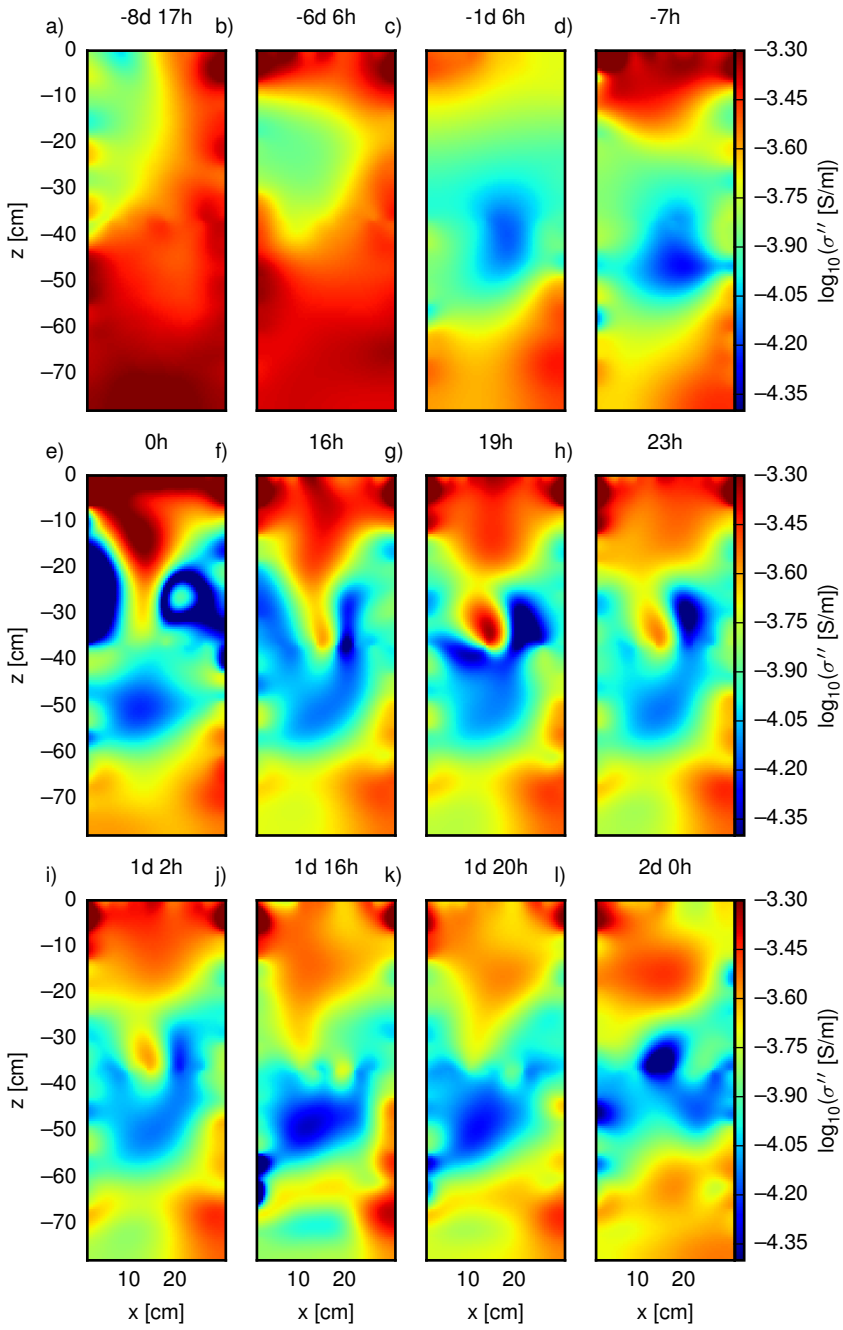

Figure 6.46: Absolute inversion images (10 Hz) of σ'' for the time before and after the tracer application. Times refer to time before/after application of the tracer (on day 30 after sowing).

CHAPTER 7

Conclusions and future research perspectives

The novel contribution of this thesis is the establishment of multi-frequency electrical impedance tomography (EIT) for the direct characterization and monitoring of structural and physiological properties of crop root systems. While electrical polarization properties have been successfully measured on root systems in the past, an imaging approach has not yet been successfully applied, especially not in combination with multi-frequency data acquisition. Multi-frequency data contains information about the dominating relaxation times, which can be linked to characteristic length scales of the underlying polarization processes. The primary challenge in adapting EIT to the measurement of crop root systems is the capturing and processing of small signals in relatively short time frames, which are imposed by the biological processes taking place in crop root systems in response to changes in their environment.

Chapters 2 to 4 present various new aspects of the EIT analysis pipeline that facilitate the application of EIT to crop root systems: A new variant of the Debye decomposition (DD) and its thorough characterization enables the consistent analysis of huge numbers of spectral polarization signatures. As shown in chapter 2, the DD has multiple important tuning parameters that must be carefully controlled. Otherwise, large interpretation errors can be introduced into the analysis. Important examples are the regularization parameter and the choice of relaxation times; both choices can heavily influence the resulting parameters that are later analyzed and interpreted. In a similar manner, chapter 3 highlights the importance of using a consistent analysis scheme by showing large differences between apparently similar parameters of two established SIP models, the

Cole-Cole (CC) model and the Debye decomposition. Chapter 4 examines the reconstruction of SIP parameters in the imaging plane and demonstrates that relaxation times show more stable reconstruction behavior across the image plane than chargeability parameters. Concluding the methodological part of this thesis, the DD is thoroughly characterized and tested for the application to EIT data, i.e., for the unsupervised analysis of tens of thousands of spectra, and proves to be a versatile tool for the analysis of a variety of differently shaped EIS signatures.

The laboratory experiments presented in chapters 5 and 6 show the effectiveness and versatility of EIT with respect to the characterization of crop root systems. Due to the novel nature of the direct imaging of polarization signals of crop roots, only a limited comparison can be made to existing studies. However, there is a large body of existing studies that not only show polarization signals of root systems, but also characteristic changes in response to certain physiological and environmental factors such as growth, herbicide treatment, root mass and age. On a basic level these studies can be compared to those presented in this thesis. However, there exist certain differences in the measurement procedures. Among these differences are different frequency ranges, two- or four-point measurements, measurements of impedances or capacitances, current injection through the stem or only in the rhizosphere. Future work should be directed towards unifying the various measurements types. This could be accomplished by designing common experiments that simultaneously measure with the various electrical procedures.

Previous studies also showed relatively robust relationships to biological parameters of plant root systems for experiments in aqueous solutions or simple substrates, such as sand. In this context the experiments presented in this thesis extend these results by introducing the tomographic, i.e., spatial, analysis of electrical parameters, as well as increased spectral and temporal resolutions. Experiments in peat substrate, which contains a high percentage of organic material, proved to be more of a challenge over the course of this thesis, and although results can be consistently explained, there is only weak evidence that polarization signals of root systems can be measured reliably in such an environment. Also, spatially and temporally variable water contents influenced the results. These findings are in line with findings of previous research, and future

research should be focused on determining if the multi-frequency EIT approach can be adapted to yield robust and useful results in those settings.

Various improvements and extensions to existing inversion algorithms have been proposed and implemented in recent years, but not yet been assessed in the context of the application to root research. Among these are frequency regularization schemes, which impose smoothness constraints on the frequency domain. While somewhat redundant to the frequency regularization built into the DD scheme, they could nevertheless improve multi-frequency EIT results by reducing the impact of noise components. Other extensions include the use of 3D inversion algorithms, which can improve results in inhomogeneous settings if measurement setups are suitably designed. These two, and various other, possible features of inversion algorithms have not yet been assessed in the scope of (crop) root research, and future work should focus on these topics.

Uncertainty estimation will become even more important than it is today. While uncertainties of the measurements can, to a certain extent, be quantified by repeated measurements and the use of reciprocal four-point electrode configurations, uncertainty estimation in the non-linear inversion process used to generate images of the complex resistivity are still hard to come by. Contributing to this topic, chapter 4 highlights certain aspects of the inherent uncertainties and variable resolution inherent to this process. However, it is still hard to transfer these insights into 'error bars', i.e., definitive uncertainties of the final parameters that are analyzed. Future work must be directed towards a consistent and reliable treatment and quantification of uncertainties in each step of the analysis pipeline, starting from the measurements and ending with the finally derived biological parameters.

Another aspect that could help to reduce ambiguities in the data and its interpretation is joint inversion. Here, the electrical inversion could be coupled to hydraulic models of the subsurface and to root growth models that simulate the spatial growth and evolution of root systems. This, however, requires the formulation of electrical models that can parameterize the root geometry with an electrical response, which can be matched with the measured electrical data.

The experiments in this thesis highlight an emerging trend in contemporary electrical measurements: The monitoring aspect together with the acquisition of tomographic and multi-frequency data leads to a huge amount of data and

corresponding meta data. These data must be processed and analyzed in an automated way, while the analysis of a single experiment could be easily managed using manual tasks a few years back. Nowadays experiments must be processed and interpreted in a timely manner by means of automation to avoid drowning in new data piling up. This requires a thoughtful design and review of the computer programs developed for this automation process. While the automation required for the experiments in this thesis is not new, future work should be directed to creating computing frameworks that can be used across experiments and disciplines, and reduce the need to build specialized solutions for all experiments.

Automation and quality control will become even more important as the method in its specific application to crop root systems matures and the biological use increases. As soon as the investigation of biological issues dominates over the development aspect of the method itself, that is, as soon as EIT is ready to be used by biologists and root researchers, (near) real-time applications will move into focus. This will enable not only a post-experimental analysis, but also an in-experiment reaction in response to certain events. One example would be the increase of irrigation frequency in response to the imaging of decreasing water content during a given experiment to prevent long-term penalties in root growth and plant evolution.

This leads directly to the ultimate objective that can be formulated for the use of EIT with crop roots: The application on the field scale. From a biological point of view, the undisturbed field is the natural environment of root systems, and it is always questionable to what extent laboratory conditions can mirror the wide diversity of environmental factors found in nature. Eventually, all insights gained in the laboratory are applied in the field, be it to improve crop yields, crop resilience to certain stress factors, or just to further understand the global ecosystem. From a methodological point of view, the field scale is the ultimate challenge as the environment cannot be controlled, which requires a full understanding of all influences on the measurement process.

In summary, EIT has the potential to become a unique tool of crop research, both in the laboratory and on the field scale. While the current state of research looks promising, future research has to address many remaining challenges.

Acknowledgements

This thesis has come a long way since I started it almost six years ago. While initially integrated in the work of the 'Forschergruppe FOR1320', it soon became clear that the work required more time to carefully put together all the pieces required to make an initial assessment of the EIT method in the context of root research. My special thanks go to my supervisor Prof. Dr. Andreas Kemna who not only ensured that I would have the time to do this, but he also constantly encouraged me to take no shortcuts and look into all the details that came up. His profound knowledge and deep understanding of the matters involved is an unlimited source of help and motivation.
I want to thank Adrián Flores Orozco and Egon Zimmermann for numerous valuable discussions on EIT techniques and field procedures. Thanks for the patience you showed with all my questions! Thanks Egon for building this incredible EIT system, which has been at the heart of this whole endeavor.
I'm very grateful for all members of the PhD commission for their help and flexibility during the organization of the defense: Prof. A. Kemna, Prof. J.A. Huisman, Prof. W. Amelung, Prof. J Garcke.
My parents and my sister showed constant support during the long years that it took to put this thesis together, thank you for the motivational discussions, both in good and bad times! Thank you for the endless hours you lent me a should to cry on when things looked bad. I also want to single out my sister for not being discouraged to pursue her own PhD, may it get together smoothly!
Finally, thank you Jule for the support and motivation you gave me in the final days of this work, your motivation kept me straight on the finish line!
Parts of chapter (2) were conducted in the framework of the SFB TR32 "Patterns in soil-vegetation-atmosphere systems: monitoring, modeling and data assimilation" funded by the Deutsche Forschungsgemeinschaft (DFG). We thank Adrian Flores Orozco and Matthias Kelter for valuable discussions on the Debye decomposition scheme, and Nicolas Florsch along with two anonymous reviewers for their valuable review comments during review process of the accompanying publication.
Parts of chapter (3) were conducted in the framework of the SFB TR32 "Patterns in soil-vegetation-atmosphere systems: monitoring, modelling and data assim-

ilation" funded by the Deutsche Forschungsgemeinschaft (DFG). We thank the editor Jörg Renner and two anonymous referees for their very constructive reviews during the publication process of the accompanying publication.
Parts of chapter (4) were conducted in the framework of the SFB TR32 "Patterns in soil-vegetation-atmosphere systems: monitoring, modeling and data assimilation" funded by the Deutsche Forschungsgemeinschaft (DFG). We thank the two anonymous referees for their very constructive reviews during the review process of the accompanying publication.
Parts of chapter (5) were funded by the Deutsche Forschungsgemeinschaft (DFG) in the framework of the project "Non-destructive characterization and monitoring of root structure and function at the rhizotron and field scale using spectral electrical impedance tomography" (KE 1138/1-1) and the collaborative research centre "Patterns in soil-vegetation-atmosphere systems: monitoring, modeling and data assimilation" (SFB/TR 32). We are especially grateful to Egon Zimmermann and Matthias Kelter for valuable discussions regarding the measurement setup. We also thank Achim Walter, Johannes Pfeifer and Kerstin Nagel for technical support and discussions on root physiology in the initial phase of the work.

Bibliography

Abdel Aal, G., Atekwana, E., Slater, L., and Atekwana, E.: Effects of microbial processes on electrolytic and interfacial electrical properties of unconsolidated sediments, Geophysical Research Letters, 31, doi:10.1029/2004GL020030, 2004.

al Hagrey, S.: Geophysical imaging of root-zone, trunk, and moisture heterogeneity, Journal of Experimental Botany, 58, 839–854, doi:10.1093/jxb/erl237, 2007.

al Hagrey, S. and Petersen, T.: Numerical and experimental mapping of small root zones using optimized surface and borehole resistivity tomography, Geophysics, 76, G25–G35, doi:10.1190/1.3545067, 2011.

Alumbaugh, D. and Newman, G.: Image appraisal for 2-D and 3-D electromagnetic inversion, Geophysics, 65, 1455–1467, doi:10.1190/1.1444834, 2000.

Amato, M., Basso, B., Celano, G., Bitella, G., Morelli, G., and Rossi, R.: In situ detection of tree root distribution and biomass by multi-electrode resistivity imaging, Tree Physiology, 28, 1441–1448, doi:10.1093/treephys/28.10.1441, 2008.

Amato, M., Bitella, G., Rossi, R., Gómez, J. A., Lovelli, S., and Gomes, J. J. F.: Multi-electrode 3D resistivity imaging of alfalfa root zone, European Journal of Agronomy, 31, 213–222, doi:10.1016/j.eja.2009.08.005, 2009.

Anderson, S. and Hopmans, J., eds.: Soil-water-root Processes: Advances in Tomography and Imaging, Soil Science Society of America, doi:10.2136/sssaspecpub61, 2013.

Anderson, W. and Higinbotham, N.: Electrical resistances of corn root segments, Plant physiology, 57, 137–141, doi:10.1104/pp.57.2.137, 1976.

Archie, G.: The Electrical Resistivity Log as an Aid in Determining Some Reservoir Characteristics, Petroleum Technology, pp. 54–62, doi:10.2118/942054-G, 1942.

Aster, R., Borcher, B., and Thurber, C.: Parameter estimation and inverse problems – 2nd ed., Academic Press, doi:10.1016/B978-0-12-385048-5.00031-8, 360 pp., 2013.

Atekwana, E. and Slater, L.: Biogeophysics: A new frontier in Earth science research, Reviews of Geophysics, 47, doi:10.1029/2009RG000285, 2009.

Attwa, M. and Günther, T.: Spectral induced polarization measurements for predicting the hydraulic conductivity in sandy aquifers, Hydrology & Earth System Sciences, 17, 4079–4094, doi:10.5194/hess-17-4079-2013, 2013.

Aubrecht, L., Staněk, Z., and Koller, J.: Electrical measurement of the absorption surfaces of tree roots by the earth impedance method: 1. Theory, Tree physiology, 26, 1105–1112, doi:10.1093/treephys/26.9.1105, 2006.

Aulen, M. and Shipley, B.: Non-destructive estimation of root mass using electrical capacitance on ten herbaceous species, Plant and soil, 355, 41–49, doi:10.1007/s11104-011-1077-3, 2012.

Barsoukov, E. and Macdonald, J., eds.: Impedance spectroscopy: theory, experiment, and applications, Wiley-Interscience, doi:10.1002/0471716243, 2005.

Bayford, R.: Bioimpedance tomography (electrical impedance tomography), Annual Reviews Biomedical Engineering, 8, 63–91, doi:10.1146/annurev.bioeng.8.061505.095716, 2006.

Beff, L., Günther, T., Vandoorne, B., Couvreur, V., and Javaux, M.: Three-dimensional monitoring of soil water content in a maize field using Electrical Resistivity Tomography, Hydrology and Earth System Sciences, 17, 595–609, doi:10.5194/hess-17-595-2013, 2013.

Benlloch-González, M., Fournier, J., and Benlloch, M.: K+ deprivation induces xylem water and K+ transport in sunflower: evidence for a co-ordinated

control, Journal of Experimental Botany, 61, 157–164, doi:10.1093/jxb/erp288, 2010.

Binley, A. and Kemna, A.: DC resistivity and induced polarization methods, in: Hydrogeophysics, edited by Rubin, Y. and S.S., H., pp. 129–156, Springer Netherlands, doi:10.1007/1-4020-3102-5_5, 2005.

Binley, A., Slater, L., Fukes, M., and Cassiani, G.: Relationship between spectral induced polarization and hydraulic properties of saturated and unsaturated sandstone, Water Resources Research, 41, 1–13, doi:10.1029/2005WR004202, 2005.

Boaga, J., Rossi, M., and Cassiani, G.: Monitoring soil-plant interactions in an apple orchard using 3D electrical resistivity tomography, Procedia Environmental Sciences, 19, 394–402, doi:10.1016/j.proenv.2013.06.045, 2013.

Börner, F., Schopper, J., and Weller, A.: Evaluation of transport and storage properties in the soil and groundwater zone from induced polarization measurements, Geophysical Prospecting, 44, 583–601, doi:10.1111/j.1365-2478.1996.tb00167.x, 1996.

Böttcher, C. and Bordewijk, P.: Theory of Electric Polarization. Vol. 2, Elsevier, New York, doi:10.1002/bbpc.19800841128, 525 pp., 1978.

Breede, K., Kemna, A., Esser, O., Zimmermann, E., Vereecken, H., and Huisman, J.: Spectral induced polarization measurements on variably saturated sand-clay mixtures, Near Surface Geophysics, 10, 479–489, doi:10.3997/1873-0604.2012048, 2012.

Bücker, M. and Hördt, A.: Long and short narrow pore models for membrane polarization, Geophysics, 78, E299–E314, doi:10.1190/GEO2012-0548.1, 2013a.

Bücker, M. and Hördt, A.: Analytical modelling of membrane polarization with explicit parametrization of pore radii and the electrical double layer, Geophysical Journal International, 194, 804–813, doi:10.1093/gji/ggt136, 2013b.

Cao, Y., Repo, T., Silvennoinen, R., Lehto, T., and Pelkonen, P.: An appraisal of the electrical resistance method for assessing root surface area, Journal of Experimental Botany, 61, 2491–2497, doi:10.1093/jxb/erq078, 2010.

Cao, Y., Repo, T., Silvennoinen, R., Lehto, T., and Pelkonen, P.: Analysis of the willow root system by electrical impedance spectroscopy, Journal of Experimental Botany, 62, 351–358, doi:10.1093/jxb/erq276, 2011.

Čermák, J., Ulrich, R., Staněk, Z., Koller, J., and Aubrecht, L.: Electrical measurement of tree root absorbing surfaces by the earth impedance method: 2. Verification based on allometric relationships and root severing experiments, Tree physiology, 26, 1113–1121, doi:10.1093/treephys/26.9.1113, 2006.

Chen, J., Kemna, A., and Hubbard, S.: A comparison between Gauss-Newton and Markov-chain Monte Carlo–based methods for inverting spectral induced-polarization data for Cole-Cole parameters, Geophysics, 73, F247–F259, doi:10.1190/1.2976115, 2008.

Chloupek, O.: The relationship between electric capacitance and some other parameters of plant roots, Biologia Plantarum, 14, 227–230, doi:10.1007/BF02921255, 1972.

Chloupek, O.: Die Bewertung des Wurzelsystems von Senfpflanzen auf Grund der dielektrischen Eigenschaften und mit Rücksicht auf den Endertrag, Biologia Plantarum, 18, 44–49, doi:10.1007/BF02922333, 1976.

Claassen, N. and Barber, S.: A method for characterizing the relation between nutrient concentration and flux into roots of intact plants, Plant Physiology, 54, 564–568, doi:10.1104/pp.54.4.564, 1974.

Clarkson, D., Carvajal, M., Henzler, T., Waterhouse, R., Smyth, A., Cooke, D., and Steudle, E.: Root hydraulic conductance: diurnal aquaporin expression and the effects of nutrient stress, Journal of Experimental Botany, 51, 61–70, doi:10.1093/jexbot/51.342.61, 2000.

Cole, K. and Cole, R.: Dispersion and absorption in dielectrics I. alternating current characteristics, Journal of Chemical Physics, 9, 341–351, doi:10.1063/1.1750906, 1941.

Comas, X. and Slater, L.: Low-frequency electrical properties of peat, Water resources research, 40, doi:10.1029/2004WR003534, 2004.

Cseresnyés, I., Fekete, G., Végh, K., Székács, A., Mörtl, M., and Rajkai, K.: Monitoring of herbicide effect in maize based on electrical measurements, International Agrophysics, 26, 243–247, doi:10.2478/v10247-012-0036-4, 2012.

Cseresnyés, I., Tünde, T., Végh, K., Anton, A., and Rajkai, K.: Electrical impedance and capacitance method: A new approach for detection of functional aspects of arbuscular mycorrhizal colonization in maize, European Journal of Soil Biology, 54, 25 – 31, doi:10.1016/j.ejsobi.2012.11.001, 2013.

Daily, W., Ramirez, A., Binley, A., and LaBrecque, D.: Electrical resistance tomography – theory and practice, in: Near-Surface Geophysics, edited by Butler, D., vol. 154, chap. 17, pp. 525–550, Society of Exploration Geophysicists, Tulsa, OK, doi:10.1190/1.9781560801719.ch17, 2005.

Dalton, F.: In-situ root extent measurements by electrical capacitance methods, Plant and Soil, 173, 157–165, doi:10.1007/BF00155527, 1995.

Davis, C., Atekwana, E., Atekwana, E., Slater, L., Rossbach, S., and Mormile, M.: Microbial growth and biofilm formation in geologic media is detected with complex conductivity measurements, Geophysical Research Letters, 33, doi:10.1029/2006GL027312, 2006.

Day-Lewis, F., Singha, K., and Binley, A.: Applying petrophysical models to radar travel time and electrical resistivity tomograms: Resolution-dependent limitations, Journal of Geophysical Research, 110, doi:10.1029/2004JB003569, 2005.

Debye, P.: Polar Molecules, Dover Publications, Inc., New York, doi:10.1002/jctb.5000484320, 172 pp., 1960 [1929].

Delhon, P., Gojon, A., Tillard, P., and Passama, L.: Diurnal regulation of NO3- uptake in soybean plants I. Changes in NO3- influx, efflux, and N utilization in the plant during the day/night cycle, Journal of Experimental Botany, 46, 1585–1594, doi:10.1093/jxb/46.10.1585, 1995.

Dias, C.: Developments in a model to describe low-frequency electrical polarization of rocks, Geophysics, 65, 437–451, doi:10.1190/1.1444738, 2000.

Dietrich, R., Bengough, A., Jones, H., and White, P.: Can root electrical capacitance be used to predict root mass in soil?, Annals of Botany, 112, 457–464, doi:10.1093/aob/mct044, 2013.

Dukhin, S., Shilov, V., and Bikerman, J.: Dielectric phenomena and double layer in disperse systems and polyelectrolytes, Journal of the Electrochemical Society, 121, 154C–154C, doi:10.1002/bbpc.19760800223, 1974.

Dunbabin, V., Postma, J., Schnepf, A., Pagès, L., Javaux, M., Wu, L., Leitner, D., Chen, Y., Rengel, Z., and Diggle, A.: Modelling root-soil interactions using three-dimensional models of root growth, architecture and function, Plant and Soil, 372, 93–124, doi:10.1007/s11104-013-1769-y, 2013.

Dvořák, M., Černohorská, J., and Janáček, K.: Characteristics of current passage through plant tissue, Biologia Plantarum, 23, 306–310, doi:10.1007/BF02895374, 1981.

Ellis, T., Murray, W., and Kavalieris, L.: Electrical capacitance of bean (Vicia faba) root systems was related to tissue density—a test for the Dalton Model, Plant and soil, 366, 575–584, doi:10.1007/s11104-012-1424-z, 2013.

Eshel, A. and Beeckman, T.: Plant roots: The hidden half, Fourth Ed., CRC Press, iSBN: 9781439846490, 2013.

Fixman, M.: Charged Macromolecules in External Fields. 2. Preliminary Remarks on the Cylinder, Macromolecules, 13, 711–716, doi:10.1021/ma60075a043, 1980.

Flores Orozco, A., Williams, K., Long, P., Hubbard, S., and Kemna, A.: Using complex resistivity imaging to infer biogeochemical processes associated with bioremediation of an uranium-contaminated aquifer, Journal of Geophysical Research, 116, doi:10.1029/2010JG001591, 2011.

Flores Orozco, A., Kemna, A., Oberdörster, C., Zschornack, L., Leven, C., Dietrich, P., and Weiss, H.: Delineation of subsurface hydrocarbon

contamination at a former hydrogenation plant using spectral induced polarization imaging, Journal of Contaminant Hydrology, 136, 131–144, doi:10.1016/j.jconhyd.2012.06.001, 2012a.

Flores Orozco, A., Kemna, A., and Zimmermann, E.: Data error quantification in spectral induced polarization imaging, Geophysics, 77, E227–E237, doi:10.1190/geo2010-0194.1, 2012b.

Flores Orozco, A., Williams, K., and Kemna, A.: Time-lapse spectral induced polarization imaging of stimulated uranium bioremediation, Near Surface Geophysics, 11, 531–544, doi:10.3997/1873-0604.2013020, 2013.

Flores Orozco, A., Velimirovic, M., Tosco, T., Kemna, A., Sapion, H., Klaas, N., Sethi, R., and Bastiaens, L.: Monitoring the injection of microscale zerovalent iron particles for groundwater remediation by means of complex electrical conductivity imaging, Environmental Science & Technology, 49, 5593–5600, doi:10.1021/acs.est.5b00208, 2015.

Florsch, N., Camerlynck, C., and Revil, A.: Direct estimation of the distribution of relaxation times from induced-polarization spectra using a Fourier transform analysis, Near Surface Geophysics, 10, 517–531, doi:10.3997/1873-0604.2012004, 2012.

Florsch, N., Revil, A., and Camerlynck, C.: Inversion of generalized relaxation time distributions with optimized damping parameter, Journal of Applied Geophysics, 109, 119–132, doi:10.1016/j.jappgeo.2014.07.013, 2014.

Friedel, S.: Resolution, stability and efficiency of resistivity tomography estimated from a generalized inverse approach, Geophysical Journal International, 153, 305–316, doi:10.1046/j.1365-246X.2003.01890.x, 2003.

Fuoss, R. and Kirkwood, J.: Electrical properties of solids. VIII. dipole moments in polyvinyl chloride-diphenyl systems, Journal of the American Chemical Society, 63, 385–394, doi:10.1021/ja01847a013, 1941.

Gaiser, T., Perkons, U., Küpper, P., Puschmann, D., Peth, S., Kautz, T., Pfeifer, J., Ewert, F., Horn, R., and Köpke, U.: Evidence of improved water uptake from

subsoil by spring wheat following lucerne in a temperate humid climate, Field Crops Research, 126, 56–62, doi:10.1016/j.fcr.2011.09.019, 2012.

Ghorbani, A., Camerlynck, C., Florsch, N., Cosenza, P., and Revil, A.: Bayesian inference of the Cole-Cole parameters from time-and frequency-domain induced polarization, Geophysical Prospecting, 55, 589–605, doi:10.1111/j.1365-2478.2007.00627.x, 2007.

Gregory, P.: Plant roots: growth, activity, and interaction with soils, Blackwell Publishing, Oxford, doi:10.1002/9780470995563, 2006.

Gregory, P., Hutchison, D., Read, D., Jenneson, P., Gilboy, W., and Morton, E.: Non-invasive imaging of roots with high resolution X-ray micro-tomography, in: Roots: The Dynamic Interface between Plants and the Earth, pp. 351–359, Springer, doi:10.1023/A:1026179919689, 2003.

Groff, P. and Kaplan, D.: The relation of root systems to shoot systems in vascular plants, The Botanical Review, 54, 387–422, doi:10.1007/BF02858417, 1988.

Günther, T.: Inversion methods and resolution analysis for the 2D/3D reconstruction of resistivity structures from DC measurements, Ph.D. thesis, Technische Universität Bergakademie Freiberg, 2004.

Günther, T. and Martin, T.: Spectral two-dimensional inversion of frequency-domain induced polarization data from a mining slag heap, Journal of Applied Geophysics, 135, 436–448, doi:10.1016/j.jappgeo.2016.01.008, 2016.

Gurin, G., Titov, K., Ilyin, Y., and Tarasov, A.: Induced polarization of disseminated electronically conductive minerals: a semi-empirical model, Geophysical Journal International, 200, 1555–1565, doi:10.1093/gji/ggu490, 2015.

Hansen, P.: The discrete Picard condition for discrete ill-posed problems, BIT Numerical Mathematics, 30, 658–672, doi:10.1007/BF01933214, 1990.

Heege, H.: Precision in Crop Farming: Site Specific Concepts and Sensing Methods: Applications and Results, Springer Science & Business Media, iSBN: 9400767617, 2013.

Heřmanská, A., Středa, T., and Chloupek, O.: Improved wheat grain yield by a new method of root selection, Agronomy for Sustainable Development, 35, 195–202, doi:10.1007/s13593-014-0227-4, 2015.

Hördt, A., Blaschek, R., Kemna, A., and Zisser, N.: Hydraulic conductivity estimation from induced polarisation data at the field scale—the Krauthausen case history, Journal of Applied Geophysics, 62, 33–46, doi:10.1016/j.jappgeo.2006.08.001, 2007.

Hose, E., Clarkson, D., Steudle, E., Schreiber, L., and Hartung, W.: The exodermis: a variable apoplastic barrier, Journal of Experimental Botany, 52, 2245–2264, doi:10.1093/jexbot/52.365.2245, 2001.

Huisman, J., Zimmermann, E., Esser, O., Haegel, F., Treichel, A., and Vereecken, H.: Evaluation of a novel correction procedure to remove electrode impedance effects from broadband SIP measurements, Journal of Applied Geophysics, doi:10.1016/j.jappgeo.2015.11.008, 2015.

Javaux, M., Couvreur, V., Vanderborght, J., and Vereecken, H.: Root water uptake: From three-dimensional biophysical processes to macroscopic modeling approaches, Vadose Zone Journal, 12, doi:10.2136/vzj2013.02.0042, 2013.

Johnson, T., Slater, L., Ntarlagiannis, D., Day-Lewis, F., and Elwaseif, M.: Monitoring groundwater-surface water interaction using time-series and time-frequency analysis of transient three-dimensional electrical resistivity changes, Water Resources Research, 48, doi:10.1029/2012WR011893, 2012.

Keery, J., Binley, A., Elshenawy, A., and Clifford, J.: Markov-chain Monte Carlo estimation of distributed Debye relaxations in spectral induced polarization, Geophysics, 77, E159–E170, doi:10.1190/GEO2011-0244.1, 2012.

Kelter, M.: Charakterisierung von Wurzelsystemen mit Hilfe der elektrischen Impedanzspektroskopie, Diploma thesis, Universität Bonn, 2011.

Kelter, M., Huisman, J., Zimmermann, E., Kemna, A., and Vereecken, H.: Quantitative imaging of spectral electrical properties of variably

saturated soil columns, Journal of Applied Geophysics, 123, 333–344, doi:10.1016/j.jappgeo.2015.09.001, 2015.

Kemna, A.: Tomographic inversion of complex resistivity – theory and application, Ph.D. thesis, Ruhr-Universität Bochum, doi:10.1111/1365-2478.12013, 2000.

Kemna, A., Vanderborght, J., Kulessa, B., and Vereecken, H.: Imaging and characterisation of subsurface solute transport using electrical resistivity tomography (ERT) and equivalent transport models, Journal of Hydrology, 267, 125–146, doi:10.1016/S0022-1694(02)00145-2, 2002.

Kemna, A., Binley, A., and Slater, L.: Crosshole IP imaging for engineering and environmental applications, Geophysics, 69, 97–107, doi:10.1190/1.1649379, 2004.

Kemna, A., Weigand, M., Kelter, M., Pfeifer, J., Zimmermann, E., and Walter, A.: Imaging and characterizing root systems using electrical impedance tomography, in: AGU Fall Meeting Abstracts, vol. 1, p. 1191, 2011.

Kemna, A., Binley, A., Cassiani, G., Niederleithinger, E., Revil, A., Slater, L., Williams, K., Flores Orozco, A., Haegel, F., Hoerdt, A., Kruschwitz, S., Leroux, V., Titov, K., and Zimermann, E.: An overview of the spectral induced polarization method for near-surface applications, Near Surface Geophysics, 10, 453–468, doi:10.3997/1873-0604.2012027, 2012.

Kemna, A., Huisman, J., Zimmermann, E., Martin, R., Zhao, Y., Treichel, A., Flores Orozco, A., and Fechner, T.: Broadband electrical impedance tomography for subsurface characterization using improved corrections of electromagnetic coupling and spectral regularization, in: Tomography of the Earth's Crust: From Geophysical Sounding to Real-Time Monitoring, pp. 1–20, Springer, doi:10.1007/978-3-319-04205-3_1, 2014.

Kinraide, T.: Use of a Gouy-Chapman-Stern model for membrane-surface electrical potential to interpret some features of mineral rhizotoxicity, Plant physiology, 106, 1583–1592, 1994.

Kinraide, T. and Wang, P.: The surface charge density of plant cell membranes (σ): an attempt to resolve conflicting values for intrinsic σ, Journal of Experimental botany, 61, 2507–2518, doi:10.1093/jxb/erq082, 2010.

Kinraide, T., Yermiyahu, U., and Rytwo, G.: Computation of surface electrical potentials of plant cell membranes correspondence to published zeta potentials from diverse plant sources, Plant physiology, 118, 505–512, doi:10.1104/pp.118.2.505, 1998.

Kormanek, M., Głąb, T., and Klimek-Kopyra, A.: Modification of the tree root electrical capacitance method under laboratory conditions, Tree physiology, pp. 121–127, doi:10.1093/treephys/tpv088, 2015.

Kruschwitz, S., Binley, A., Lesmes, D., and Elshenawy, A.: Textural controls on low-frequency electrical spectra of porous media, Geophysics, 75, WA113–WA113, doi:10.1190/1.3479835, 2010.

Kyle, A., Chan, C., and Minchinton, A.: Characterization of three-dimensional tissue cultures using electrical impedance spectroscopy, Biophysical journal, 76, 2640–2648, doi:10.1016/S0006-3495(99)77416-3, 1999.

LaBrecque, D. and Ward, S.: Two-dimensional cross-borehole resistivity model fitting, Geotechnical and environmental geophysics, 1, 51–57, 1990.

LaBrecque, D., Miletto, M., Daily, W., Ramirez, A., and Owen, E.: The effects of noise on Occam's inversion of resistivity tomography data, Geophysics, 61, 538–538, doi:10.1190/1.1443980, 1996a.

LaBrecque, D., Ramirez, a., Daily, W., Binley, A., and Schima, S.: ERT monitoring of environmental remediation processes, Meas. Sci. Technol., 7, 375–383, doi:10.1088/0957-0233/7/3/019, 1996b.

Leroy, P., Revil, A., Kemna, A., Cosenza, P., and Ghorbani, A.: Complex conductivity of water-saturated packs of glass beads, Journal of Colloid and Interface Science, 321, 103–117, doi:10.1016/j.jcis.2007.12.031, 2008.

Lesmes, D. and Frye, K.: Influence of pore fluid chemistry on the complex conductivity and induced polarization responses of Berea sandstone, Journal of Geophysical Research, 106, 4079–4090, doi:10.1029/2000JB900392, 2001.

Lesmes, D. and Morgan, F.: Dielectric spectroscopy of sedimentary rocks, Journal of Geophysical Research, 106, 13 329–13 346, doi:10.1029/2000JB900402, 2001.

Li, Z., Liu, Y., Zheng, Y., and Xu, R.: Zeta potential at the root surfaces of rice characterized by streaming potential measurements, Plant and Soil, 386, 237–250, doi:10.1007/s11104-014-2259-6, 2015.

Loke, M., Chambers, J., Rucker, D., Kuras, O., and Wilkinson, P.: Recent developments in the direct-current geoelectrical imaging method, Journal of Applied Geophysics, 95, 135–156, doi:10.1016/j.jappgeo.2013.02.017, 2013.

Luo, Y. and Zhang, G.: Theory and application of spectral induced polarization, Society of Exploration Geophysicists, Tulsa, doi:10.1190/1.9781560801856, 1998.

Lyklema, J.: Fundamentals of interface and colloid science: solid-liquid interfaces, vol. 2, Academic press, 2005.

Lyklema, J., Dukhin, S., and Shilov, V.: The relaxation of the double layer around colloidal particles and the low-frequency dielectric dispersion: Part I. Theoretical considerations, Journal of Electroanalytical Chemistry and Interfacial Electrochemistry, 143, 1–21, doi:10.1016/S0022-0728(83)80251-4, 1983.

Macdonald, J.: Dielectric dispersion in materials having a distribution of relaxation times, The Journal of Chemical Physics, 20, 1107–1111, doi:10.1063/1.1700675, 1952.

Mancuso, S.: Measuring roots: an updated approach, Springer Science & Business Media, iSBN: 978-3-642-22067-8, 2012.

Martin, T. and Günther, T.: Complex resistivity tomography (CRT) for fungus detection on standing oak trees, European Journal of Forest Research, 132, 765–776, doi:10.1007/s10342-013-0711-4, 2013.

Martínez-Ballesta, M., Rodríguez-Hernández, M., Alcaraz-López, C., Mota-Cadenas, C., Muries, B., and Carvajal, M.: Plant hydraulic conductivity: The aquaporins contribution, Hydraulic conductivity—issues, determination and applications. Rijeka: In Tech, pp. 103–21, doi:10.5772/18580, 2011.

Menke, W.: Geophysical data analysis: discrete inverse theory, Academic Press, doi:10.2138/am-2017-671, 2012.

Metzner, R., Eggert, A., van Dusschoten, D., Pflugfelder, D., Gerth, S., Schurr, U., Uhlmann, N., and Jahnke, S.: Direct comparison of MRI and X-ray CT technologies for 3D imaging of root systems in soil: potential and challenges for root trait quantification, Plant methods, 11, 1, doi:10.1186/s13007-015-0060-z, 2015.

Morgan, F. and Lesmes, D.: Inversion for dielectric relaxation spectra, Journal of Chemical Physics, 100, 671–681, doi:10.1016/S0022-3093(98)00634-6, 1994.

Mwakanyamale, K., Slater, L., Binley, A., and Ntarlagiannis, D.: Lithologic imaging using complex conductivity: Lessons learned from the Hanford 300 Area, Geophysics, 77, E397–E409, doi:10.1190/GEO2011-0407.1, 2012.

Nagel, K., Putz, A., Gilmer, F., Heinz, K., Fischbach, A., Pfeifer, J., Faget, M., Blossfeld, S., Ernst, M., Dimaki, C., et al.: GROWSCREEN-Rhizo is a novel phenotyping robot enabling simultaneous measurements of root and shoot growth for plants grown in soil-filled rhizotrons, Functional Plant Biology, 39, 891–904, doi:10.1071/FP12023, 2012.

Nguyen, F., Kemna, A., Antonsson, A., Engesgaard, P., Kuras, O., Ogilvy, R., Gisbert, J., Jorreto, S., and Pulido-Bosch, A.: Characterization of seawater intrusion using 2D electrical imaging, Near Surface Geophysics, 7, 377–390, doi:10.3997/1873-0604.2009025, 2009.

Nordsiek, S. and Weller, A.: A new approach to fitting induced-polarization spectra, Geophysics, 73, F235–F245, doi:10.1190/1.2987412, 2008.

Ntarlagiannis, D., Williams, K., Slater, L., and Hubbard, S.: Low-frequency electrical response to microbial induced sulfide precipitation, Journal of Geophysical Research, 110, doi:10.1029/2005JG000024, 2005.

Oldenburg, D. and Li, Y.: Estimating depth of investigation in DC resistivity and IP surveys, Geophysics, 64, 403–416, doi:10.1190/1.1444545, 1999.

Ozier-Lafontaine, H. and Bajazet, T.: Analysis of root growth by impedance spectroscopy (EIS), Plant and Soil, 277, 299–313, doi:10.1007/s11104-005-7531-3, 2005.

Pelton, W., Ward, S., Hallof, P., Sill, W., and Nelson, P.: Mineral discrimination and removal of inductive coupling with multifrequency IP, Geophysics, 43, 588–609, doi:10.1190/1.1440839, 1978.

Pfeifer, J.: Elucidation of root-soil interactions of crops in space and time by establishment and application of novel image based non-invasive root phenotyping methods, Ph.D. thesis, Eidgenössische Technische Hochschule ETH Zürich, doi:10.3929/ethz-a-010216588, nr. 21676, 2013.

Pierret, A., Doussan, C., Garrigues, E., and Mc Kirby, J.: Observing plant roots in their environment: current imaging options and specific contribution of two-dimensional approaches, Agronomie, 23, 471–479, doi:10.1051/agro:2003019, 2003.

Prodan, C. and Prodan, E.: The dielectric behaviour of living cell suspensions, Journal of Physics D: Applied Physics, 32, 335–343, 1999.

Prodan, E., Prodan, C., and Miller Jr, J.: The dielectric response of spherical live cells in suspension: an analytic solution, Biophysical journal, 95, 4174–4182, doi:10.1529/biophysj.108.137042, 2008.

Razilov, I. and Dukhin, S.: Simultaneous influence of concentration polarization of the diffuse layer and polarization of the Stern layer according to the mechanism of bound counterions at arbitrary magnitudes of the relaxation parameter, Colloid Journal of the Russian Academy of Sciences, 57, 364–371, 1995.

Repo, T., Cao, Y., Silvennoinen, R., and Ozier-Lafontaine, H.: Electrical impedance spectroscopy and roots, in: Measuring Roots, edited by Mancuso, S., pp. 25–49, Springer, doi:10.1007/978-3-642-22067-8_2, 2012.

Repo, T., Korhonen, A., Laukkanen, M., Lehto, T., and Silvennoinen, R.: Detecting mycorrhizal colonisation in Scots pine roots using electrical impedance spectra, Biosystems Engineering, 121, 139–149, doi:10.1016/j.biosystemseng.2014.02.014, 2014.

Revil, A. and Florsch, N.: Determination of permeability from spectral induced polarization in granular media, Geophysical Journal International, 181, 1480–1498, doi:10.1111/j.1365-246X.2010.04573.x, 2010.

Revil, A., Atekwana, E., Zhang, C., Jardani, A., and Smith, S.: A new model for the spectral induced polarization signature of bacterial growth in porous media, Water Resources Research, 48, doi:10.1029/2012WR011965, 2012a.

Revil, A., Karaoulis, M., Johnson, T., and Kemna, A.: Review: Some low-frequency electrical methods for subsurface characterization and monitoring in hydrogeology, Hydrogeology Journal, 20, 617–658, doi:10.1007/s10040-011-0819-x, 2012b.

Revil, A., Florsch, N., and Camerlynck, C.: Spectral induced polarization porosimetry, Geophysical Journal International, 198, 1016–1033, doi:10.1093/gji/ggu180, 2014.

Revil, A., Binley, A., Mejus, L., and Kessouri, P.: Predicting permeability from the characteristic relaxation time and intrinsic formation factor of complex conductivity spectra, Water Resources Research, doi:10.1002/2015WR017074, 2015.

Roose, T., Keyes, S., Daly, K., Carminati, A., Otten, W., Vetterlein, D., and Peth, S.: Challenges in imaging and predictive modeling of rhizosphere processes, Plant and Soil, pp. 1–30, doi:10.1007/s11104-016-2872-7, 2016.

Rossi, R., Amato, M., Bitella, G., Bochicchio, R., Ferreira Gomes, J., Lovelli, S., Martorella, E., and Favale, P.: Electrical resistivity tomography as a non-destructive method for mapping root biomass in an orchard, European Journal of Soil Science, 62, 206–215, doi:10.1111/j.1365-2389.2010.01329.x, 2011.

Schraut, D., Heilmeier, H., and Hartung, W.: Radial transport of water and abscisic acid (ABA) in roots of Zea mays under conditions of nutrient deficiency, Journal of Experimental Botany, 56, 879–886, doi:10.1093/jxb/eri080, 2005.

Schwan, H.: Electrical Properties of Tissue and Cell Suspensions, vol. 5 of *Advances in Biological and Medical Physics*, pp. 147 – 209, Elsevier, doi:10.1016/B978-1-4832-3111-2.50008-0, 1957.

Schwartz, N. and Furman, A.: On the spectral induced polarization signature of soil organic matter, Geophysical Journal International, 200, 589–595, doi:10.1093/gji/ggu410, 2015.

Schwarz, G.: A theory of the low-frequency dielectric dispersion of colloidal particles in electrolyte solution, The Journal of Physical Chemistry, 66, 2636–2642, doi:10.1021/j100818a067, 1962.

Singha, K., Day-Lewis, F., Johnson, T., and Slater, L.: Advances in interpretation of subsurface processes with time-lapse electrical imaging, Hydrological Processes, doi:10.1002/hyp.10280, 2014.

Slater, L.: Near surface electrical characterization of hydraulic conductivity: From petrophysical properties to aquifer geometries – A review, Surveys in Geophysics, 28, 169–197, doi:10.1007/s10712-007-9022-y, 2007.

Slater, L. and Binley, A.: Synthetic and field-based electrical imaging of a zerovalent iron barrier: Implications for monitoring long-term barrier performance, Geophysics, 71, B129–B137, doi:10.1190/1.2235931, 2006.

Slater, L. and Lesmes, D.: Electrical-hydraulic relationships observed for unconsolidated sediments, Water Resources Research, 38, 31–1, doi:10.1029/2001WR001075, 2002.

Srayeddin, I. and Doussan, C.: Estimation of the spatial variability of root water uptake of maize and sorghum at the field scale by electrical resistivity tomography, Plant and soil, 319, 185–207, doi:10.1007/s11104-008-9860-5, 2009.

Stamm, M., Weigand, M., and Kemna, A.: EIS monitoring of day-night cycles of plant root activity, in: Jahrestagung der DGG, vol. 76, 2016.

Tarantola, A.: Inverse problem theory and methods for model parameter estimation, siam, doi:10.1137/1.9780898717921, 2005.

Tarasov, A. and Titov, K.: Relaxation time distribution from time domain induced polarization measurements, Geophysical Journal International, 170, 31–43, doi:10.1111/j.1365-246X.2007.03376.x, 2007.

Tarasov, A. and Titov, K.: On the use of the Cole-Cole equations in spectral induced polarization, Geophysical Journal International, 195, 352–356, doi:10.1093/gji/ggt251, 2013.

Tarasov, A., Titov, K., Münch, M., and Kemna, A.: Induced polarization spectra of sands and clays measured in the time domain, in: Proc. Int. Conf. Geophysics of the 21st Century – a Leap into the Future, SEG / EAGE, September 1-4, 4p., 2003.

Tinker, P. and Nye, P.: Solute movement in the rhizosphere, Oxford University Press, Inc., New York, doi:10.1046/j.1365-2389.2001.00418-2.x, 2000.

Titov, K., Komarov, V., Tarasov, V., and Levitski, A.: Theoretical and experimental study of time domain-induced polarization in water-saturated sands, Journal of Applied Geophysics, 50, 417–433, doi:10.1016/S0926-9851(02)00168-4, 2002.

Tong, M., Weinan, W., Li, L., Yizhong, J., and Deqin, S.: Estimation of permeability of shaly sand reservoir from induced polarization relaxation time spectra, Journal of Petroleum Science and Engineering, 45, 31–40, doi:10.1016/j.petrol.2004.05.004, 2004.

Uhlmann, D. and Hakim, R.: Derivation of distribution functions from relaxation data, Journal of Physics and Chemistry of Solids, 32, 2652–2655, doi:10.1016/S0022-3697(71)80114-2, 1971.

Urban, J., Bequet, R., and Mainiero, R.: Assessing the applicability of the earth impedance method for in situ studies of tree root systems, Journal of Experimental Botany, pp. 1857––1869, doi:10.1093/jxb/erq370, 2011.

v. Schweidler, E.: Studien über die Anomalien im Verhalten der Dielektrika, Annalen der Physik, 24, 711–770, doi:10.1002/andp.19073291407, 1907.

Vanhala, H.: Mapping oil-contaminated sand and till with the spectral induced polarization (SIP) method, Geophysical prospecting, 45, 303–326, doi:10.1046/j.1365-2478.1997.00338.x, 1997.

Wagner, K.: Zur Theorie der unvollkommenen Dielektrika, Annalen der Physik, 345, 817–855, doi:10.1002/andp.19133450502, 1913.

Walker, J.: Electrical AC resistance and capacitance of Zea mays L, Plant and Soil, 23, 270–274, doi:10.1007/BF01358354, 1965.

Wang, P., Zhou, D.-M., Li, L.-Z., and Li, D.-D.: What role does cell membrane surface potential play in ion-plant interactions, Plant signaling & behavior, 4, 42–43, doi:10.4161/psb.4.1.7270, 2009.

Wang, P., Kinraide, T., Zhou, D., K., P. M., and Peijnenburg, W.: Plasma membrane surface potential: dual effects upon ion uptake and toxicity, Plant physiology, 155, 808–820, doi:10.1104/pp.110.165985, 2011.

Wang, Y.-M., Kinraide, T., Wang, P., Zhou, D., and Hao, X.: Modeling rhizotoxicity and uptake of Zn and Co singly and in binary mixture in wheat in terms of the cell membrane surface electrical potential, Environmental science & technology, 47, 2831–2838, doi:10.1021/es3022107, 2013.

Weigand, M. and Kemna, A.: Multi-frequency electrical impedance tomography as a non-invasive tool to characterize and monitor crop root systems, Biogeosciences Discussions, 2016, 1–31, doi:10.5194/bg-2016-154, URL http://www.biogeosciences-discuss.net/bg-2016-154/, 2016a.

Weigand, M. and Kemna, A.: Debye decomposition of time-lapse spectral induced polarisation data, Computers and Geosciences, 86, 34–45, doi:10.1016/j.cageo.2015.09.021, 2016b.

Weigand, M. and Kemna, A.: Relationship between Cole-Cole model parameters and spectral decomposition parameters derived from SIP data, Geophysical Journal International, 205, 1414–1419, doi:10.1093/gji/ggw099, 2016c.

Weller, A., Nordsiek, S., and Debschütz, W.: Estimating permeability of sandstone samples by nuclear magnetic resonance and spectral-induced polarization, Geophysics, 75, E215–E226, doi:10.1190/1.3507304, 2010a.

Weller, A., Slater, L., Nordsiek, S., and Ntarlagiannis, D.: On the estimation of specific surface per unit pore volume from induced polarization: A robust empirical relation fits multiple data sets, Geophysics, 75, WA105–WA112, doi:10.1190/1.3471577, 2010b.

Weller, A., Breede, K., Slater, L., and Nordsiek, S.: Effect of changing water salinity on complex conductivity spectra of sandstones, Geophysics, 76, F315–F327, doi:10.1190/GEO2011-0072.1, 2011.

Weller, A., Slater, L., and Nordsiek, S.: On the relationship between induced polarization and surface conductivity: Implications for petrophysical interpretation of electrical measurements, Geophysics, 78, D315–D325, doi:10.1190/GEO2013-0076.1, 2013.

Weller, A., Slater, L., Binley, A., Nordsiek, S., and Xu, S.: Permeability prediction based on induced polarization: Insights from measurements on sandstone and unconsolidated samples spanning a wide permeability range, Geophysics, 80, D161–D173, doi:10.1190/GEO2014-0368.1, 2015.

Whalley, W., Binley, A., Watts, C., Shanahan, P., Dodd, I., Ober, E., Ashton, R., Webster, C., White, R., and Hawkesford, M. J.: Methods to estimate changes in soil water for phenotyping root activity in the field, Plant and Soil, pp. 1–16, doi:10.1007/s11104-016-3161-1, 2017.

White, P., George, T., Gregory, P., Bengough, A., Hallett, P., and McKenzie, B.: Matching roots to their environment, Annals of Botany, 112, 207–222, doi:10.1093/aob/mct123, 2013.

Willatt, S., Struss, R., and Taylor, H.: In situ root studies using neutron radiography, Agronomy Journal, 70, 581–586, doi:10.2134/agronj1978.00021962007000040016x, 1978.

Williams, K., Kemna, A., Wilkins, M., Druhan, J., Arntzen, E., N'Guessan, A., Long, P., Hubbard, S., and Banfield, J.: Geophysical monitoring of coupled microbial and geochemical processes during stimulated subsurface bioremediation, Environmental Science & Technology, 43, 6717–6723, doi:10.1021/es900855j, 2009.

Wong, J.: An electrochemical model of the induced-polarization phenomenon in disseminated sulfide ores, Geophysics, 44, 1245–1265, doi:10.1190/1.1441005, 1979.

Zanetti, C., Weller, A., Vennetier, M., and Mériaux, P.: Detection of buried tree root samples by using geoelectrical measurements: a laboratory experiment, Plant and soil, 339, 273–283, doi:10.1007/s11104-010-0574-0, 2011.

Zhao, Y., Zimmermann, E., Huisman, J., Treichel, A., Wolters, B., van Waasen, S., and Kemna, A.: Broadband EIT borehole measurements with high phase accuracy using numerical corrections of electromagnetic coupling effects, Measurement Science and Technology, 24, 085 005, doi:10.1088/0957-0233/24/8/085005, 2013.

Zhdanov, M.: Geophysical Inverse Theory and Regularization Problems, vol. 36, Elsevier, 2002.

Zimmermann, E., Kemna, A., Berwix, J., Glaas, W., and Vereecken, H.: EIT measurement system with high phase accuracy for the imaging of spectral induced polarization properties of soils and sediments, Measurement Science and Technology, 19, 094 010, doi:10.1088/0957-0233/19/9/094010, 2008.

Zisser, N., Kemna, A., and Nover, G.: Relationship between low-frequency electrical properties and hydraulic permeability of low-permeability sandstones, Geophysics, 75, E131–E141, doi:10.1190/1.3413260, 2010a.

Zisser, N., Kemna, A., and Nover, G.: Dependence of spectral-induced polarization response of sandstone on temperature and its relevance to permeability estimation, Journal of Geophysical Research, 115, doi:10.1029/2010JB007526, 2010b.

Technical details

This thesis is set in the fonts Linux Libertine (serif) and Linux Biolinum (sans serif). Compiled using LaTeX and XeLaTeX
Figures were created using Python, Matplotlib, Numpy and Pandas.

The root system on the cover and back pages is modified from Weaver, J.E.: The ecological relations of roots, 1919, Fig. 38 (page 93). doi:10.5962/bhl.title.79315.

Software developed during the writing of this thesis can be found under https://github.com/m-weigand.

Please cite as:

Weigand, Maximilian: Monitoring structural and physiological properties of crop roots using spectral electrical impedance tomography, Ph.D. thesis, University of Bonn, doi:10.5281/zenodo.400833, urn:nbn:de:hbz:5n-46750, 2017

Revision of this thesis:
Wed, 22 Mar 2017 18:30:41 +0100,
hash: 2997fed862345cdb3f68b921a94f15876d865179

Non- or minimally invasive methods are urgently needed to characterize and monitor crop root systems, both on the laboratory and the field scale. Traditional research methods still overwhelmingly rely on manual labor, which slows down phenotyping and breeding programs.

This thesis investigates electrical impedance tomography (EIT) as a non-invasive method for the characterization and monitoring of crop root systems. First, various improvements to the analysis methodology of electrical polarization measurements, required to investigate the small signal strengths encountered in biological tissue, are implemented and discussed. Second, multiple laboratory experiments with EIT on crop root systems are presented. Measurements were conducted in aqueous solutions, as well as in various substrates. Root system extension could be successfully imaged with EIT in aqueous solutions, as were systematic electrical polarization responses in reaction to physiological stress situations. Substrates, however, still pose significant challenges for EIT measurements due to their inherent polarizability and a strong influence of variable water content on polarization signals.

In summary, EIT is successfully applied to characterize and monitor structural and physiological properties of crop root systems in a laboratory environment. Although many challenges remain, establishing EIT as a reliable tool on the field scale is within reach.

urn:nbn:de:hbz:5n-46750
doi:10.5281/zenodo.400833

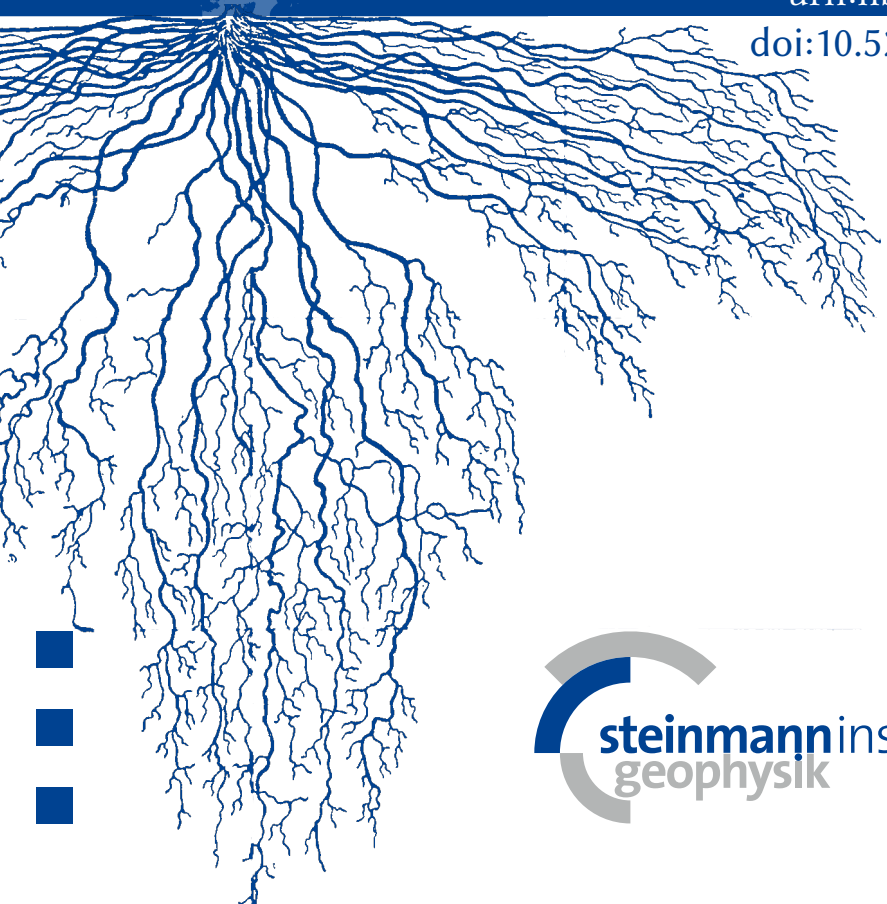

steinmann institut geophysik